Protection of Buried Flexible Pipes with a Geosynthetic:

Experimental and Numerical Studies

By

Ryan Corey

Submitted to the graduate degree program in Civil, Environmental, and Architectural Engineering and the Graduate Faculty of the University of Kansas in partial fulfillment of the requirements for the degree of Doctor of Philosophy.

_____

Chairperson Dr. Jie Han

_____

Dr. Caroline R. Bennett

_____

Dr. Yaozhong Hu

_____

Dr. Anil Misra

_____

Dr. Robert L. Parsons

Date Defended: August 28th, 2015

The Dissertation Committee for Ryan Corey

certifies that this is the approved version of the following dissertation:

Protection of Buried Flexible Pipes with a Geosynthetic:

Experimental and Numerical Studies

_____

Chairperson: Dr. Jie Han

Date approved: August 28th, 2015

Table of Contents

List of Figures viii

List of Tables xxi

Abstract xxiii

Acknowledgments xxiv

Chapter 1 Introduction 1

1.1 Background 1

1.2 Objective and Scope 4

1.3 Organization of this Dissertation 4

Chapter 2 Literature Review 5

2.1 Overview 5

2.2 Basic Pipe Mechanics 6

2.3 Pipe-Soil Interaction 9

2.3.1 Marston and Anderson's Soil Arching 10

2.3.2 Spangler's Equation 11

2.3.3 Vertical Arching Factors for Flexible Pipes 13

2.4 Pipe Design 16

2.4.1 Pipe Deflections 16

2.4.2 Thrust in Pipe Wall 17

2.4.3 Buckling 19
2.4.4 Plastic Pipe Design 22
2.4.5 Local Buckling 26
2.5 Surface Loads 28
2.6.0 Numerical Modeling 31
2.6.1 Constitutive Soil Models 32
2.6.3 Construction steps in numerical modeling 41
2.6.4 Numerical modeling of wheel loads 43
2.6.5 Numerical modeling of plastic pipes 44
2.7 Geosynthetics 48
2.7.1 Geosynthetic Functions 48
2.7.2 Geosynthetics in Pipe Applications 50
2.8.0 Summary 62
Chapter 3 Laboratory Tests 65
3.1 Overview 65
3.2 Steel-Reinforced HDPE Pipe 67
3.2.1 Pipe Materials 67
3.2.2 Pipe Instrumentation 70
3.3 Subgrade 72
3.4 Backfill 74

3.4.1 Backfill Material Properties 74
3.4.2 Backfill Placement 79
3.4.3 Backfill Instrumentation 81
3.5 Base Course 82
3.6 Geogrid 83
3.6.1 Geogrid Material Properties 83
3.6.2 Geogrid Instrumentation 84
3.7 Load Application 85
3.7.1 Static Plate Load Tests 85
3.7.2 Cyclic Plate Load Tests 86
3.8 Laboratory Results 88
3.8.1 Plate Settlement 88
3.8.2 Pipe Deflection 92
3.8.3 Earth Pressures 104
3.8.4 Pipe Strain 125
3.8.5 Geogrid Strain 146
3.9 Analysis of Laboratory Results 159
3.9.1 Pipe Deflections 159
3.9.2 Earth Pressures 161
3.10 Conclusions of Laboratory Results 166

Chapter 4 Numerical Analysis 169
4.1 Overview 169
4.2 Material Parameters 170
4.2.1 Orthotropic Pipe Stiffness 170
4.2.2 Pipe Local Buckling 174
4.2.3 Fat Clay 179
4.2.4 Sand and Crushed Stone 180
4.2.5 AB-3 Aggregate 184
4.2.6 Geogrid 186
4.3 Numerical Model Mesh and Boundary Conditions 187
4.4 Numerical Simulation of Installation and Compaction 192
4.4.1 Kansas River Sand Backfill 192
4.4.2 Crushed Stone Aggregate Backfill 199
4.5 Numerical Results of Plate Loading Tests 200
4.5.1 Base Course Compaction 200
4.5.2 Plate Load Tests on Aggregate Backfill 204
Chapter 5 Parametric Study 222
5.1 Introduction 222
5.2 Selection of Parameters 222
5.3 Effect of Pipe Stiffness 228

5.3.1 Pipe Deflections and Plate Settlements 228
5.3.2 Earth Pressures 232
5.3.3 Pipe Moments and Thrusts 234
5.3.4 Geogrid Strain 237
5.4 Effect of Pipe Hoop Stiffness 239
5.4.1 Pipe Deflections and Plate Settlements 239
5.4.2 Earth Pressures 246
5.4.3 Pipe Moments and Thrusts 251
5.4.4 Geogrid Strain 256
5.5 Conclusions 258
Chapter 6 Conclusions and Recommendations 260
6.1 Introduction 260
6.2 Experimental Study 260
6.3 Numerical Calibration 262
6.4 Parametric Study 263
6.5 Recommendations 265
References 266

List of Figures

Figure 2.1 Parallel Plate Load Test 8

Figure 2.2 Soil Arching 11

Figure 2.3 Spangler's Soil Pressure Distributions (Spangler 1941) 12

Figure 2.4 Pipes under Internal Pressure 18

Figure 2.5 Thrust due to External Pressures 19

Figure 2.6 CSP Column Buckling 21

Figure 2.7 HDPE Tensile Failure and Slow Crack Growth 23

Figure 2.8 Cross Section of Profile Pipe Wall 27

Figure 2.9 Influence of H-20 Load and Weight of Soil on Buried Pipe 29

Figure 2.10 FLAC 3D Mohr-Coulomb Failure Surface 35

Figure 2.11 Yield Surface for Cap Yield Constitutive Model 38

Figure 2.12 Yield Surface in the Principal Stress State (Schanz et al., 1999) 38

Figure 2.13 Peaking of Flexible Pipe during Installation 41

Figure 2.14 Geosynthetic Tension (T) Membrane and Anchorage over a Void 49

Figure 2.15 Geosynthetic Confinement of a Base Course Showing Tension (T) and Compression (C) Forces 50

Figure 2.16 Trench Reinforcement for Flexible Pipes (Jeypalan, 1983) 51

Figure 2.17 Soil-Steel Bridge with Reinforced Backfill (Kennedy et al., 1988) 52

Figure 2.18 Single Reinforcement Layer over a Pipe (Pearson and Milligan, 1991) 53

Figure 2.19 Geovala Method (Bueno et al, 2005) 55

Figure 2.20 Dynamic Load Tests (Moghaddas Tafreshi and Khalaj, 2011) 58

Figure 2.21 Geosynthetic Protection of Pipes from Penetrating Loads (Palmeira and Andrade, 2010) 60
Figure 3.1 Test Pipe Buried in the Big Box 66
Figure 3.2 Parallel Plate Load Test for 610 mm Diameter SRHDPE (Khatri, 2012) 68
Figure 3.3 Pipe Stiffness (PS) of Different Types of Pipe 69
Figure 3.4 Displacement Transducer setup 70
Figure 3.5 Pipe Wall Section and Strain Gauge Orientation 71
Figure 3.6 Circumferential and Radial Strain Gauge Locations 72
Figure 3.7 Longitudinal Strain Gauge Locations 72
Figure 3.8 Fat Clay Trench 73
Figure 3.9 Triaxial Compression Test of Sand at D_r = 25% 75
Figure 3.10 Triaxial Compression Test of Sand at D_r = 40% 76
Figure 3.11 Triaxial Compression Test of Sand at D_r = 77% Sand 76
Figure 3.12 Isotropic Compression Sand D_r = 25% and 77% 77
Figure 3.13 Triaxial Compression Test of Aggregate 77
Figure 3.14 Backfill Placement 79
Figure 3.15 Pipe Deflections during Sand Backfill Placement 80
Figure 3.16 Pipe Deflections during Crushed Aggregate Placement 80
Figure 3.17 Earth Pressure Cell Locations 81
Figure 3.18 Strain gauges on two geogrid layers 84
Figure 3.19 Cyclic Wave Form 87
Figure 3.20 Cyclic loading for Tests 6, 8, and 10 87
Figure 3.21 Loading Plate Settlements in Tests 1 and 4 89

Figure 3.22 Loading Plate Settlements in Tests 2 and 3 89
Figure 3.23 Loading Plate Settlements in Tests 5, 7, and 9 90
Figure 3.24 Plate Settlements in Test 6 90
Figure 3.25 Plate Settlements in Test 8 91
Figure 3.26 Plate Settlements in Test 10 91
Figure 3.27 Vertical Deflection of Pipe – Tests 1 and 4 93
Figure 3.28 Vertical Deflection of Pipe – Tests 2 and 3 93
Figure 3.29 Vertical Deflections at 305 mm from Plate – Tests 1 and 4 94
Figure 3.30 Vertical Deflections at 305 mm from Plate – Tests 2 and 3 94
Figure 3.31 Horizontal Deflection of Pipe -Tests 1 and 4 95
Figure 3.32 Horizontal Deflection of Pipe - Tests 2 and 3 96
Figure 3.33 Vertical to Horizontal Deflection Ratio – Tests 1 through 4 96
Figure 3.34 Vertical Deflections of Pipe - Tests 5, 7, and 9 97
Figure 3.35 Vertical Deflections at 305mm from Plate – Tests 5, 7, and 9 98
Figure 3.36 Horizontal Pipe Deflections –Tests 5, 7, and 9 98
Figure 3.37 Vertical to Horizontal Deflection Ratios – Tests 5, 7, and 9 99
Figure 3.38 Vertical Pipe Deflections with U.R. - Test 6 99
Figure 3.39 Vertical Pipe Deflections with S.L. - Test 8 100
Figure 3.40 Vertical Pipe Deflections with D.L. - Test 10 100
Figure 3.41 Vertical Pipe Deflections at 305 mm from Loading Plate with U.R. - Test 6 101
Figure 3.42 Vertical Pipe Deflections at 305 mm from Loading Plate with S.L. - Test 8 101
Figure 3.43 Vertical Pipe Deflections at 305 mm from Loading Plate with D.L. - Test 10 102
Figure 3.44 Horizontal Pipe Deflections with U.R. - Test 6 102

Figure 3.45 Horizontal Pipe Deflections with S.L. - Test 8 103

Figure 3.46 Horizontal Pipe Deflections with D.L. - Test 10 103

Figure 3.47 Measured Pressures at Crown (C_1) - Tests 1 and 4 104

Figure 3.48 Measured Pressures at Crown (C_1) - Tests 2 and 3 105

Figure 3.49 Measured Vertical Pressures at Crown (C_2) - Tests 1 and 4 105

Figure 3.50 Measured Vertical Pressures at Crown (C_2) - Tests 2 and 3 106

Figure 3.51 Vertical Pressures at Crown (C_1) - Tests 5, 7, and 9 107

Figure 3.52 Vertical Pressures at Crown (C_2) -Tests 5, 7, and 9 107

Figure 3.53 Vertical Pressures at Crown (C_3) -Tests 5, 7, and 9 108

Figure 3.54 Crown Pressure Distributions at Maximum Applied Pressure - Tests 5, 7, and 9 .. 108

Figure 3.55 Vertical Pressures at Crown (C_4) - Tests 5, 7, and 9 109

Figure 3.56 Vertical Pressures at Crown (C_1) with U.R. - Test 6 110

Figure 3.57 Vertical Pressures at Crown (C_1) with S.L. - Test 8 110

Figure 3.58 Vertical Pressures at Crown (C_1) with D.L. - Test 10 111

Figure 3.59 Maximum Vertical Pressures at Crown (C_1) - Tests 6, 8, and 10 111

Figure 3.60 Vertical Pressures at Crown (C_2) with U.R. - Test 6 112

Figure 3.61 Vertical Pressures at Crown (C_2) with S.L. - Test 8 112

Figure 3.62 Vertical Pressures at Crown (C_2) with D.L. - Test 10 113

Figure 3.63 Vertical Pressures at Crown (C_3) with U.R. -Test 6 113

Figure 3.64 Vertical Pressures at Crown (C_3) with S.L. - Test 8 114

Figure 3.65 Vertical Pressures at Crown (C_3) with D.L. - Test 10 114

Figure 3.66 Maximum Vertical Pressures at Crown (C_2) – Tests 6, 8, and 10 115

Figure 3.67 Maximum Vertical Pressures at Crown (C_3) - Tests 6, 8, and 10 115

Figure 3.68 Vertical Pressures under Base Course (C_4) with U.R. - Test 6 116

Figure 3.69 Vertical Pressures under Base Course (C_4) with S.L. - Test 8 117

Figure 3.70 Vertical Pressures under Base Course (C_4) with D.L. - Test 10..... 117

Figure 3.71 Pressures at Springline (S_1) - Tests 1 and 4..... 118

Figure 3.72 Pressures at Springline Shoulder (S_2) - Tests 1 and 4 119

Figure 3.73 Pressures at Springline (S_1) - Tests 2 and 3..... 119

Figure 3.74 Pressures at Springline (S_2) - Tests 2 and 3..... 120

Figure 3.75 Pressure Distributions at Springline - Tests 1, 2, 3, and 4 120

Figure 3.76 Pressures at Invert (I_1) - Tests 1 and 4..... 121

Figure 3.77 Pressures at Invert (I_1) - Tests 2 and 3..... 121

Figure 3.78 Springline Pressure Distributions at Maximum Applied Pressure – Tests 5, 7 and 9 122

Figure 3.79 Vertical Pressures at Springline – Tests 5, 7, and 9 123

Figure 3.80 Pressures at Invert – Tests 5, 7, and 9 123

Figure 3.81 Springline Pressure Distributions at the Maximum Applied Pressure – Tests 5, 7, and 9..... 124

Figure 3.82 Maximum Pressures at Invert Tests 6, 8, and 10..... 124

Figure 3.83 Maximum Vertical Pressures at Springline Tests 6, 8, and 10..... 125

Figure 3.84 Circumferential and Radial Strain Gauge Locations..... 126

Figure 3.85 Longitudinal Strain Gauge Locations..... 126

Figure 3.86 Circumferential Strains at Springline - Test 5..... 127

Figure 3.87 Circumferential Strains at Springline – Test 7 127

Figure 3.88 Circumferential Strains at Springline - Test 9..... 128

Figure 3.89 Circumferential Strains at Springline Cp1 in Test 1 and 4 129
Figure 3.90 Circumferential Strains at Springline Cp2 in Test 1 and 4 129
Figure 3.91 Circumferential Strains at Springline Cs1 in Test 1 and 4 130
Figure 3.92 Circumferential Strains at Crown Cs5 in Test 1 and 4 130
Figure 3.93 Circumferential Strains at Springline Cp1 131
Figure 3.94 Circumferential Strains at Springline Cp2 132
Figure 3.95 Circumferential Strains at Springline Cs1 132
Figure 3.96 Circumferential Strains at Springline Cs2 133
Figure 3.97 Circumferential Strains at Crown C_{s5} 133
Figure 3.98 Circumferential Strains at Springline – Plastic Cp1 134
Figure 3.99 Circumferential Strains at Springline – Steel C_{s1} 135
Figure 3.100 Circumferential Strains at Springline – Steel Cs2 135
Figure 3.101 Circumferential Strains – Steel Cs5 136
Figure 3.102 Maximum Circumferential Strains at the Springline (Cp1) 137
Figure 3.103 Maximum Circumferential Strains at Springline (Cs1) 137
Figure 3.104 Maximum Circumferential Strains at Springline (Cs2) 138
Figure 3.105 Maximum Circumferential Strains at the Crown (Cs5) 138
Figure 3.106 Longitudinal Strains at Crown Lp7 139
Figure 3.107 Longitudinal Strains at Crown Lp8 140
Figure 3.108 Longitudinal Strains at Crown - Lp7 140
Figure 3.109 Longitudinal Strains at Crown - Lp8 141
Figure 3.110 Longitudinal Strains – Plastic Lp7 142
Figure 3.111 Longitudinal Strains – Plastic Lp8 142

Figure 3.112 Maximum Longitudinal Strains at the Crown (Lp7) 143
Figure 3.113 Maximum Longitudinal Strains at the Crown (Lp8) 143
Figure 3.114 Radial Strains at Crown Rs4 in Test 5, 7, and 9 144
Figure 3.115 Radial Strains at Crown Rp3 in Test 5, 7, and 9 145
Figure 3.116 Radial Strains at Crown Rp4 in Test 5, 7, and 9 145
Figure 3.117 Geogrid Strain Gauges on Single and Double Layers 146
Figure 3.118 Longitudinal Strains in Geogrid 147
Figure 3.119 Cross-machine Direction Strains in Geogrid 148
Figure 3.120 Strain in Geogrid at Maximum Applied Pressure (345 kPa) 148
Figure 3.121 Plate Load Pressure Distributions in Test 3 149
Figure 3.122 Longitudinal Strains in Geogrid – Double Layer in Test 4 150
Figure 3.123 Cross Direction Strains in Geogrid – Double Layer in Test 4 150
Figure 3.124 Longitudinal Strains in Geogrid – Double Layer in Test 4 151
Figure 3.125 Cross Direction Strains in Geogrid – Double Layer in Test 4 151
Figure 3.126 Lower Layer Geogrid Strains at Maximum Applied Pressure (689 kPa) 152
Figure 3.127 Upper Layer Geogrid Strains at Maximum Applied Pressure (689 kPa) 152
Figure 3.128 Plate Load Distributions in Test 4 153
Figure 3.129 Cross Direction Strains in Geogrid – Single Layer in Test 7 154
Figure 3.130 Longitudinal Strains in Geogrid – Single Layer in Test 7 154
Figure 3.131 Strains in Geogrid at Maximum Applied Pressure (689 kPa) in Test 7 155
Figure 3.132 Longitudinal Strains in Geogrid – Double Layer in Test 9 156
Figure 3.133 Cross-machine Direction Strains in Geogrid – Double Layer in Test 9 156
Figure 3.134 Longitudinal Strains in Geogrid – Double Layer in Test 9 157

Figure 3.135 Cross-machine Direction Strains in Geogrid – Double Layer in Test 9..... 157

Figure 3.136 Lower Geogrid Strains at Maximum Applied Pressure (689 kPa)..... 158

Figure 3.137 Upper Geogrid Strains at Maximum Applied Pressure (689 kPa) 158

Figure 3.138 Backfill Constrained Modulus Test Data 160

Figure 3.139 Recorded and Estimated Earth Pressures at Crown in Tests 1 and 2 162

Figure 3.140 Recorded and Estimated Earth Pressures at Crown in Test 9 163

Figure 3.141 Recorded and Estimated Soil Pressure Distributions at the Springline..... 164

Figure 3.142 Recorded and Estimated Soil Pressure Distributions at the Springline..... 165

Figure 4.1 Steel Reinforced HDPE Pipe Walls of 25.4 mm on Centers..... 170

Figure 4.2 Simulated Parallel Plate Load Test Results..... 174

Figure 4.3 Simply Supported Plates on all four sides..... 175

Figure 4.4 Simply Supported Plates with One Side Free 176

Figure 4.5 Abaqus ™ Boundary Conditions and Loads 177

Figure 4.6 Typical Abaqus ™ Buckling Results 178

Figure 4.7 Buckling Coefficient k 179

Figure 4.8 Triaxial Data and Numerical Triaxial Model - Loose Sand (Dr = 25%)..... 182

Figure 4.9 Triaxial Data and Numerical Model - Dense Sand (Dr = 77%) 182

Figure 4.10 Isotropic Compression Data and Numerical Model - Dense and Loose Sand 183

Figure 4.11 Triaxial Data and Numerical Model – Crushed Stone Aggregate..... 183

Figure 4.12 Triaxial Tests of Compacted AB-3 Aggregate..... 184

Figure 4.13 Failure Envelope of AB-3 Aggregate..... 185

Figure 4.14 FLAC 3D Mesh..... 188

Figure 4.15 Pressure Applied to the Free-Field State (Burns and Richard 1964) 189

Figure 4.16 Axial Thrust in Pipe Wall 190
Figure 4.17 Moments in the Pipe Wall 190
Figure 4.18 Earth Pressure at Springline with a Full Slip 191
Figure 4.19 Earth Pressure at Springline with No Slip 191
Figure 4.20 Applications of Typical Stresses to a Compacted Layer 194
Figure 4.21 Measured and Computed Pipe Deflections during Installation 196
Figure 4.22 Earth Pressure Cell Locations 196
Figure 4.23 Earth Pressure at Spring Line (S_1) 197
Figure 4.24 Earth Pressure at Shoulder (S_2) 198
Figure 4.25 Earth Pressure at Crown (C_1) 198
Figure 4.26 Earth Pressure at Crown (C_2) 199
Figure 4.27 Vertical Displacement at Center Line of model 203
Figure 4.28 Vertical Displacements at the Crown of the Pipe 204
Figure 4.29 Vertical Settlements of the Loading Plate 205
Figure 4.30 Vertical Deflections of the Pipe 206
Figure 4.31 Horizontal Deflection of the Pipe 206
Figure 4.32 Vertical Pressures at the Crown (C_1) 207
Figure 4.33 Vertical Pressures at the Crown (C_2) 208
Figure 4.34 Vertical Pressures at the Crown (C_3) 208
Figure 4.35 Distributions of Vertical Pressures at the Crown 209
Figure 4.36 Vertical Pressures at Crown (C_4) 209
Figure 4.37 Vertical Pressures at Springline 210
Figure 4.38 Horizontal Pressures at Haunch 211

Figure 4.39 Horizontal Pressures at the Springline 211
Figure 4.40 Horizontal Pressures at the Shoulder vs. Applied Pressure..... 212
Figure 4.41 Distributions of Horizontal Pressures at the Springline 212
Figure 4.42 Horizontal Pressures at the Trench Wall 213
Figure 4.43 Thrust in Pipe Wall at Maximum Applied Pressure..... 214
Figure 4.44 Moment in Pipe Wall at Maximum Applied Pressure..... 214
Figure 4.45 Longitudinal Strains at Crown on the Outside of Pipe..... 215
Figure 4.46 Longitudinal Strains at Crown on Inside of Pipe 216
Figure 4.47 Longitudinal Strains at the Crown under the Maximum Applied Plate Load..... 216
Figure 4.48 Geogrid Strain Top Layer Cross Direction 217
Figure 4.49 Strain of Top Geogrid Layer in the Longitudinal Direction..... 218
Figure 4.50 Strain of the Top Geogrid Layer in the Machine Direction under Maximum Applied Pressure 218
Figure 4.51 Strain of Geogrid in Cross-Machine Direction under the Maximum Applied Pressure 219
Figure 4.52 Strain of Lower Geogrid in the Machine Direction..... 219
Figure 4.53 Lower Geogrid Strain of Lower Geogrid in the Cross-Machine Direction..... 220
Figure 4.54 Strain of Lower Geogrid Layer under the Maximum Applied Pressure 220
Figure 4.55 Strain of the Lower Geogrid Layer under the Maximum Applied Pressure 221
Figure 5.1 Vertical Arching Factor vs Hoop Stiffness Factor (McGrath 1998) 224
Figure 5.2 Pipe Stiffness of different Pipe Materials..... 226
Figure 5.3 Unreinforced and Reinforced Sections for the Parametric Study 227
Figure 5.4 Pipe Vertical Deflections versus Applied Pressure 229

Figure 5.5 Pipe Horizontal Deflections versus Applied Pressure 229
Figure 5.6 Maximum Vertical Pipe Deflections vs. Relative Pipe Stiffness 230
Figure 5.7 Maximum Horizontal Pipe Deflections vs. Relative Pipe Stiffness 230
Figure 5.8 Plate Settlements versus Applied Pressure 231
Figure 5.9 Maximum Plate Settlements vs. Relative Pipe Stiffness 231
Figure 5.10 Vertical Pressures at Crown vs. Relative Pipe Stiffness 232
Figure 5.11 Maximum Vertical Pressures at Crown vs. Relative Pipe Stiffness 233
Figure 5.12 Horizontal Pressures at the Springline 233
Figure 5.13 Maximum Horizontal Pressure at Springline vs Relative Pipe Stiffness 234
Figure 5.14 Pipe Moments at the Maximum Applied Plate Load 235
Figure 5.15 Pipe Thrusts at the Maximum Applied Plate Load 236
Figure 5.16 Maximum Moments vs Relative Pipe Stiffness 236
Figure 5.17 Maximum Thrusts vs. Relative Pipe Stiffness 237
Figure 5.18 Distribution of Machine Direction Geogrid Strains at the Maximum Applied Pressure 238
Figure 5.19 Distribution of Cross-machine Direction Geogrid Strains at the Maximum Applied Pressure 238
Figure 5.20 Pipe Vertical Deflections under an Unreinforced Condition 240
Figure 5.21 Pipe Vertical Deflections under a Reinforced Condition 240
Figure 5.22 Maximum Vertical Pipe Deflections versus Hoop Stiffness Factor 241
Figure 5.23 Vertical Plate Displacements under an Unreinforced Condition 241
Figure 5.24 Vertical Plate Displacements under a Reinforced Condition 242

Figure 5.25 Maximum Plate Displacements at Surface versus Ratio of Soil to Pipe Hoop Stiffness..... 242

Figure 5.26 Permanent Plate Displacements versus Ratio of Soil to Pipe Hoop Stiffness..... 243

Figure 5.27 Vertical Soil Displacements between Loading Plate and Crown of Pipe 244

Figure 5.28 Horizontal Pipe Deflections under an Unreinforced Condition 244

Figure 5.29 Horizontal Pipe Deflections under a Reinforced Condition..... 245

Figure 5.30 Maximum Horizontal Pipe Deflections versus Ratio of Soil to Pipe Hoop Stiffness 245

Figure 5.31 Vertical Pressures at Crown of Pipe under an Unreinforced Condition..... 246

Figure 5.32 Vertical Pressures at the Crown under a Reinforced Condition..... 247

Figure 5.33 Vertical Crown Pressure vs Ratio of Soil to Pipe Hoop Stiffness..... 247

Figure 5.34 Vertical Pressure Distributions at the Bottom of the Base Course ($S_H = 0.001$) 248

Figure 5.35 Vertical Pressure Distributions at the Bottom of Base course ($S_H = 10$) 248

Figure 5.36 Vertical Pressure Distributions at the Crown of the Pipe ($S_H = 0.001$)..... 249

Figure 5.37 Vertical Pressure Distributions at the Crown of the Pipe with..... 249

Pipe Hoop Stiffness Factor of 10 249

Figure 5.38 Horizontal Pressures at Springline under an Unreinforced Condition 250

Figure 5.39 Horizontal Pressures at Springline under a Reinforced Condition..... 250

Figure 5.40 Maximum Horizontal Pressures at the Springline versus Ratio of Soil to Pipe Hoop Stiffness..... 251

Figure 5.41 Bending Moments in the Pipe Wall for Varying Hoop Stiffness at the Maximum Applied Pressure under an Unreinforced Condition..... 252

Figure 5.42 Bending Moments in the Pipe Wall for Varying Hoop Stiffness under a Reinforced Condition..... 252

Figure 5.44 Maximum Bending Moments vs. Ratio of Soil to Pipe Hoop Stiffness..... 253

Figure 5.44 Thrust in Pipe for Varying Hoop Stiffness under an Unreinforced Condition..... 254

Figure 5.45 Thrust in Pipe for Varying Hoop Stiffness under a Reinforced Condition..... 254

Figure 5.46 Thrust at Crown vs Ratio of Soil to Pipe Hoop Stiffness..... 255

Figure 5.47 Thrust at Shoulder vs. Ratio of Soil to Pipe Hoop Stiffness..... 255

Figure 5.48 Longitudinal Strains at Crown vs. Ratio of Soil to Pipe Hoop Stiffness..... 256

Figure 5.49 Distribution of Machine Direction Geogrid Strains at the Maximum Applied Pressure..... 257

Figure 5.50 Distribution of Cross-machine Direction Geogrid Strains at the Maximum Applied Pressure..... 257

List of Tables

Table 2.1 Reviewed Numerical Models Methods for Buried Pipes 47

Table 2.2 Buried Pipe Reinforcement by Geosynthetic Effects 62

Table 3.1 Pipe Structural Properties 67

Table 3.2 Fat Clay Properties..... 74

Table 3.3 Properties of Kansas River Sand 78

Table 3.4 Properties of Aggregate 78

Table 3.5 Properties of Aggregate Base Course 82

Table 3.6 Static Load Tests..... 86

Table 3.7 Cyclic Load Tests 87

Table 3.8 Constrained Modulus of Backfill..... 160

Table 3.9 Reductions (%) by Reinforcement (Single Layer or Double Layer) Compared to Unreinforced Condition 167

Table 3.10 Reductions (%) by Reinforcement (Single Layer or Double Layer) Compared to Unreinforced Condition under Cyclic Loads..... 167

Table 4.1 FLAC 3D Pipe Shell Properties..... 172

Table 4.2 FLAC 3D Pipe Shell Bending Stiffness Properties 173

Table 4.3 FLAC 3D Pipe Shell Membrane Stiffness Properties 173

Table 4.4 Material Properties for Analysis..... 176

Table 4.5 Elastic Soil Properties of Fat Clay..... 180

Table 4.6 Cap-Yield Soil Parameters of Kansas River Sand..... 181

Table 4.7 Cap-Yield Soil Parameters of Crushed Stone Aggregate 181

Table 4.8 Properties of AB-3 Aggregate 185

Table 4.9 AB-3 Elastic Properties of AB-3 186

Table 4.10 FLAC 3D Geogrid Membrane Stiffness Properties..... 187

Table 5.1 Pipe Parameters..... 225

Table 5.2 Bending Stiffness Parameters 226

Table 5.3 Hoop Stiffness Factors..... 227

Abstract

Geosynthetic materials have been used in a wide variety of ways to enhance the performance of buried pipes and conduits. Attenuation of surface loads to protect the pipe include methods such as induced trenches, soil enhancement for cyclic loading, and protection from penetration during construction or accidents. Geosynthetic materials have also been used to reinforce the in situ walls of trenches and to reinforce the backfill of buried pipes The previous studies have shown that geosynthetic materials can improve pipe performance by reducing strains and deflections. There appears to be an opportunity to improve the body of research in this area and to give practical guidance to engineers and designers.

This study concentrates on pipes subjected to near surface loads, and includes full scale experimental studies of a steel reinforced high density polyethylene pipe (SRHDPE) in a trench condition with low cover. Two base course and backfill conditions were run with and without geogrid at the interface of the base course and in the trench. The experimental results showed that the geogrid reinforced base course can reduce deflections and strains in the pipe for the conditions tested. A non-linear three dimensional model of the static load experiments was generated to simulate the test conditions. The cap-yield soil model was used for the trench backfill and the geogrid and pipe were analyzed with orthotropic plates. With the calibrated models a parametric study was conducted to study the effects of various pipes based on bending stiffness and hoop stiffness. Results of the parametric study indicate that the most appreciable enhancement of geogrid reinforcement for pipes in near surface loads conditions, happens for pipes with low bending and hoop-stiffness.

Acknowledgments

I would like to take this opportunity to thank the Faculty and Staff of the University of Kansas Department of Civil, Environmental, and Architectural Engineering, especially my advisor Dr. Jie Han and the other geotechnical engineering Professors, Dr. Anil Misra, and Dr. Robert Parsons, and the other Committee Members, Dr. Caroline Bennett and Dr. Yaozhong Hu from the mathematical department, for their instruction and mentorship. I would like to also thank my employer and supervisor Mark Campbell at RTE Technologies, Inc. for support and mentorship of my academic and professional endeavors. I was honored and privileged to receive the 2011 Geosynthetic Institute (GSI) Fellowship, of which I am thankful for their generous support. I would also like to express my gratitude for the support and research opportunities provided by the Mid-American Transportation Center.

My co-researchers Dr. Deep Khatri, Dr. Fei Wang and the other past and present researchers in the Geotechnical program have encouraged and challenged me, and for that I thank them. I am very appreciative of all the staff at the University of Kansas, School of Engineering for outstanding experience and excellent support.

I would also like to thank Kathy, Owen, Natalie, and Joshua who sacrificed for me, and sustained me through this process.

Chapter 1 Introduction

1.1 Background

Buried conduits: water and natural gas pipelines, sewage, utilities and culverts play a critical part of our modern infrastructure. Existing and new pipes and similar buried infrastructure are being subjected to greater scrutiny, and society will rely more on our buried infrastructure, to last longer, and to protect the public and the environment better than in the past. Many of the new and existing pipe systems will share space with other infrastructure and be subjected to traffic and construction loads in addition to the dead weight of the soil. Unfortunately, it is not uncommon for buried pipelines, conduits, and utilities to fail, causing deaths, injuries, and economic losses. To properly serve the public, pipe systems will be relied on to protect the environment and the humans that they serve.

As often stated, the infrastructure of the United States is aging and in need of improvement. In the 2013 ASCE Report Card for America's Infrastructure (American Society of Civil Engineers 2013) the categories of bridges, drinking water, wastewater and energy were given a grade of C+, D, D and D+ respectively. Overall, the infrastructure of the United States was graded at a D+. This is a generalized overview of conditions, but improvements in buried pipe design, construction and knowledge will help with innovative methods of cost effectively addressing these problems.

In the United States alone between 1999 and 2009 there were over 5,000 significant pipe incidents that resulted in 364 fatalities, 3406 injuries, and 4.4 billion dollars of property damage. Of those serious incidents 25 percent were caused by excavation damage (Pipeline and Hazardous Materials Safety Administration (PHMSA 2011). Currently there are approximately 2.5 million miles of hazardous liquid and natural gas lines in the Unites States (PHSMA). As energy needs increase worldwide and people inhabit areas around pipelines there will continue to be accidents and deaths. Protection of other utilities such as water, effluent, electric lines, and fiber optic cables would be beneficial as well. Although damage of these utilities does not necessarily result in catastrophic events there is a significant economic impact of damaged utilities.

There are many technologies used to prevent pipeline accidents such as pipeline locating technologies, call before you dig programs (811 in the United States), and electronic warning systems. Geosynthetics, factory-manufactured polymer materials in sheets (e.g., geotextiles and geogrids) or cells (e.g., geocells), can be used as a single protection, or as a supplement to one of the other mentioned protection systems. Geosynthetics have been used extensively to reinforce soil in retaining walls, embankments, and pavement applications. It is theorized that geosynthetics can also be used above a pipe or underground utility line to reduce surface loading (such as footings, highway traffics, and rails), lower settlement, and prevent damage by excavation equipment.

Buried pipe design is highly dependent on the interaction of pipes and the surrounding soil. The relative stiffness of the backfill soil, the pipe wall stiffness in bending and compression, the loading history, and proximity to the surface can significantly change how the pipe-soil system behaves. Currently there has not been enough evidence of significant

improvement in the pipe-soil system with the inclusion of geosynthetics to warrant widespread adoption of geosynthetic reinforcement. This is partially due to the complex nature of the pipe-soil interaction, and limitations of the simplified design procedures for buried pipe. Adding the third facet of geosynthetics obviously increases the difficulty of the analysis. The availability of numerical methods has alleviated some of the problems with the difficulty of the analysis of pipe-soil systems, but most systems are still designed with simplified procedures.

There are times when both geosynthetics and conduits are used on the same project. Is there an improvement for these conditions? Is there enough benefit to warrant the increase of geosynthetic uses with buried pipes? Methods of pipe protection have been investigated for buried pipe design. Much of the previous work shows promising results for the use of geosynthetics in protecting pipes and enhancing the strength and serviceability of the pipe-soil system.

Although there is a tremendous amount of research on pipes and geosynthetics separately, it appears that the use of geosynthetics with pipes and its related research are limited, especially for pipe protection. The opportunity exists to expand the use of geosynthetics in conjunction with buried pipes, and to further the understanding of geosynthetic-pipe-soil interaction.

1.2 Objective and Scope

The objectives of this Ph.D. study are to investigate the mechanics, benefits, and interactions of including geogrid in shallowly buried flexible pipe design. This study will concentrate on investigating the mechanisms of pipe performance from near surface loads with the inclusion of geosynthetics. The intent is to provide answers to questions including: are there measurable improvements with the inclusion of geosynthetic, what methods and system characteristics lend itself best to the application of geosynthetics, are there existing pipe design methods that can be augmented to include geosynthetics, and can these new observations lead to new design aids? The objectives of this study will be achieved by performing a series of numerical analysis on a pipe-soil system with and without the inclusion of geosynthetics. The numerical analysis was calibrated based on full scale tests of steel reinforced HDPE pipes in a large geotechnical box. In the full scale tests, pipe was placed into a large geotechnical box, and loaded with a plate load representing a wheel load. The depth of the pipe was held constant, and a layer of base-course was changed and different layers of geosynthetics were included.

1.3 Organization of this Dissertation

This dissertation has been divided into five chapters. The first chapter is the introduction. The second chapter is a literature review and up to date synopsis of pipe and geosynthetic design, specifically with pipe and geosynthetic materials that were used in the lab tests. The third

chapter presents the results of the laboratory full scale tests conducted in this study. Chapter four presents the numerical analysis, and Chapter five draws the conclusions.

Chapter 2 Literature Review

2.1 Overview

To achieve the goals stated in the introduction of this dissertation it is important to have an understanding of the mechanics of pipe design, the mechanics of geosynthetics, and an understanding of the current design methods for both. Pipe design methods began nearly a century ago and have been evolving with current focuses on new pipe technologies and new pipe analysis techniques. To make sense of the current design methods it is certainly important to understand the advancement of pipe design from its beginning to its current status. Pipe design has changed dramatically over the past century, but the observations and early work set the foundation for all of the subsequent work. A literature review of the applicable design methods was completed and is documented here. This literature review focused on the critical points of pipe design and examined those areas that are especially applicable to this study. Those areas that were specifically investigated are flexible corrugated steel and plastic pipe design, and the numerical analysis of pipes.

The literature review of this dissertation is organized in the following manner; basic pipe structural mechanics, a discussion of how the soil loads are applied to the pipe structure (soil

structure interaction), the limit state behavior of buried pipes, and the numerical analysis of pipe-soil systems. The review is concluded with a discussion on previous research where geosynthetics have been used with buried pipes. As will be shown, the soil structure interaction and the limit states are interrelated. Generally this is how pipes are designed, the appropriate load applied to the pipe is determined, and then the pipe behavior from that load is determined and checked versus appropriate limit states. Investigating and documenting how the design methods for determining loads and the pipe behavior were developed is a logical means of understanding buried pipe behavior. Finally, with the advent and ubiquitous spread of numerical methods, and because a numerical analysis is the main impetus of this study, it is critical to understand how and what methods lead to an effective numerical analysis.

2.2 Basic Pipe Mechanics

Buried pipes and their design methods have historically been identified and segregated into two approaches, rigid and flexible pipe design. This separation of the two pipe methods is natural as the behavior and limit states of the pipes vary significantly. Rigid pipes carry the weight of the soil column above the pipe and have very little deflection. With rigid pipes, such as reinforced concrete pipe or vitrified clay pipes, it is critical to avoid cracking in the pipe wall. In contrast, flexible pipes share the weight of the soil column above the pipe with the surrounding soil and can deflect significantly. Deflection and stability of the pipe-soil system becomes more significant for flexible pipes. Both buried pipe behavior and design methods are important to

understand but the majority of this review concentrates on flexible pipe design as it is more relevant to this study.

The behavior of the pipe without soil is an important method of examining pipe behavior, setting limit states, and testing the pipe for quality control. The tests are easily observed and do not require the effort to bury and exhume the specimen. A discussion and examination of these tests can demonstrate some of the most basic concepts of the pipe design. One of the first and most widely used test methods created to understand the behavior of pipes was the Ames standard testing machine created by Marston and Anderson (1913). The Ames Standard Testing machine, originally made for rigid pipes, has gone through some adaptations over time but the purpose essentially has remained the same, which is testing the wall strength of the pipe in compression and bending.

In the Ames Standard Testing machine, a pipe sample is placed below a loading plate and compressed with a force (F) to generally simulate the buried condition and expected shape that the pipe will take during the life of the pipe (Figure 2.1a). The pipe deflects into an oval shape as stresses and strains are generated in the pipe wall. It should be noted that the Ames Standard Testing machine and other rigid pipe tests have slightly different pipe loading and supports than the parallel plate test shown. The parallel plate, a derived test of the Ames Standard Testing device, is still used today to check stability of flexible pipe and the serviceability under a maximum assumed deflection. Likewise, rigid pipes are subjected to a three-point testing to check for cracking. Early design methods simply relied on the estimated load on the pipe (W) to be less than the design capacity (F) determined by the Ames Standard Testing machine with an appropriate factor of safety.

A similar testing device was used to investigate flexible pipes by Spangler (1941). An opposing force (F) was applied to flexible sections of corrugated steel pipes, and the deflection of the pipe (ΔY) was recorded.

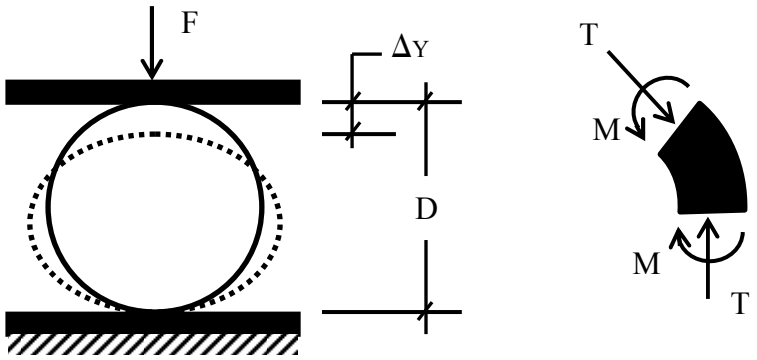

a. Parallel Plate Load Test **b. Pipe Section Free Body Diagram**

Figure 2.1 Parallel Plate Load Test

The pipe stiffness (PS) is determined from the results of the test and plotted as force versus deflection, and simply represented by Equation 2.1. The pipe stiffness is given in force per unit of deflection per unit length of pipe, and is often noted with a unit of kPa (or psi).

$$PS = \frac{F}{\Delta Y} \qquad \textbf{2.1}$$

Spangler (1941) also derived a pipe stiffness equation for thin elastic rings based on the elastic properties of the pipe wall and Castiglione's Theorem (Equation 2.2). The modulus of elasticity and moment inertia of the pipe wall could then be used for analysis. It was demonstrated that the resulting equation closely matched the results of the experiments for small pipe deflections. For deflections larger than 5% of the diameter there was some divergence of the plotted experimental pipe stiffness and the relationship represented by Equation 2.2:

$$PS = \frac{EI}{0.149R^3} \qquad \textbf{2.2}$$

where E is the modulus of elasticity of the pipe, I is the moment of inertia, and R is the radius of pipe. The linear relationship in Equation 2.2 does not consider geometric nonlinearity, which is the secondary effect of the pipe displacement.

Spangler (1941) presented us with the basic equations to analyze the pipe as a structure, providing solutions (not shown here) to determine the moment and thrust for any location on the circumference of the pipe using Castiglione's theorem. A simple free body diagram (Figure 2.1b) shows that the wall section is under a thrust load (T) and bending moment (M) during the parallel plate load test. Knowing the pipe is stable for a known deflection, the maximum thrust and moment can be checked versus the limit states of the pipe wall using fundamental elastic beam and column equations based on the material of the pipe. Spangler (1941) used the concepts of pipe stiffness and the elastic wall properties to develop a rational method for the analysis of flexible pipes to be discussed later.

2.3 Pipe-Soil Interaction

The pipe-soil interaction mechanism in buried pipe design influences both the applied load from the soil and the additional strength provided to the pipe by that same soil. What has been found is that pipes can generally be separated into two categories, rigid and flexible pipes, which are defined by their relative stiffness to the surrounding soil, and how the load is shared between the pipe and the soil. What has also been shown is that the soil stress state and load

path also affect how load is transferred to the pipe. Marston and Anderson's (1913) and Spangler's (1941) research in rigid and flexible pipes respectively, represent the pillars of buried pipe design.

2.3.1 Marston and Anderson's Soil Arching

It can be directly conceived that the load applied to a pipe is simply the weight of the column of soil, and any surface loads directly over the pipe. Marston and Anderson (1913) demonstrated that the load on a pipe in a trench was in some cases lower than the weight of the soil prism above the pipe. Marston and Anderson demonstrated that through arching action, "The side pressures of the filling materials against the sides of the ditch develop frictional resistance, which helps carry part of the weight" and, "The pipe must be strong enough to carry safely the entire weight of the ditch filling materials above the top of the pipe, less the friction of the filling against the sides of the ditch" (Marston and Anderson 1913). Equations 2.3 and 2.4 were provided by Marston and Anderson (1913) for the design load on a rigid pipe considering the beneficial effects of the friction along the trench wall (Figure 2.2a):

$$W = C_d \gamma B_d^2 \qquad \textbf{2.3}$$

$$C_d = \frac{1 - e^{-2K\mu'\left(\frac{H}{B_d}\right)}}{2K\mu'} \qquad \textbf{2.4}$$

where γ is the unit weight of soil, B_d is the width of trench, K is Rankine's lateral earth pressure coefficient, μ' is the coefficient of friction between backfill and trench wall, and H is the height of soil prism above pipe. Note that the B_d value is the entire width of the trench, and the entire

trench width is carried by the rigid pipe. The width of the trench is limited for the benefits of the arching to occur.

Conversely, Marston (1930) also showed that rigid pipes buried in embankment conditions showed negative arching, or additional load, over the pipe caused by the down drag of the soil prism directly over the pipe by the surrounding embankment (Figure 2.2b).

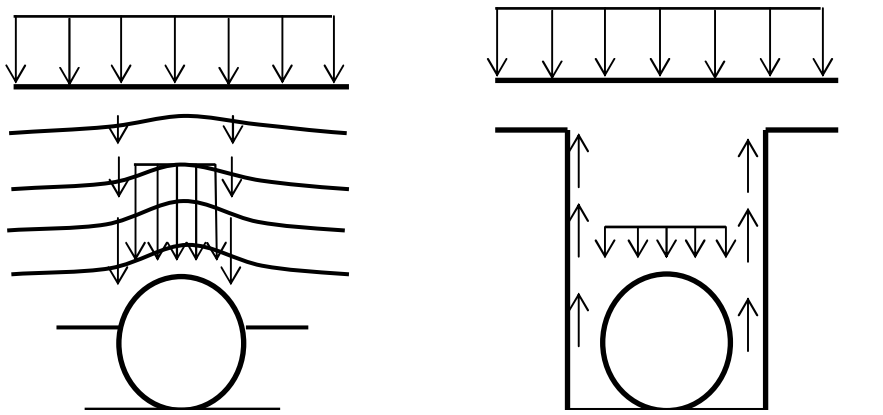

a. Marston trench Load **b. Marston embankment Load**

Figure 2.2 Soil Arching

2.3.2 Spangler's Equation

Prior to Spangler's (1941) work on flexible pipes it was known, based on tests and field observations that buried flexible pipes carried significantly more load than attributable to the pipe strength alone. For example, the buried capacity of a flexible pipe greatly exceeded the strength of the same pipe in an Ames testing machine or similar device unsupported by earth. Spangler (1941) knew that the distribution of load under a flexible pipe was significantly

different than a rigid pipe and that it was assumed that the passive earth pressures at the springline of the pipe helped give the flexible pipe greater strength (Figure 2.3).

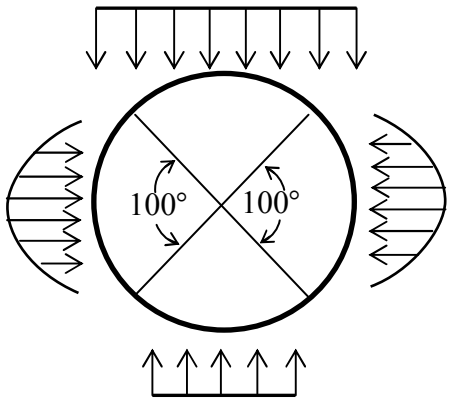

Figure 2.3 Spangler's Soil Pressure Distributions (Spangler 1941)

Based on experimental data Spangler (1941) determined an expected pressure distribution around a buried circular culvert. With the anticipated pressure distribution, and the basic pipe mechanics discussed earlier, Spangler (1941) derived moment distributions around the pipe, and from the resulting strain energy derived a solution for the horizontal deflection of the pipe under a vertical load W_c. Spangler's (1941) original equation was later modified by Watkins and Spangler (1958) and is known as the Iowa formula (Equation 2.5).

$$\Delta x = \frac{D_b D_L W_c}{\frac{EI}{\mathrm{R}^3} + 0.061E'} \qquad \textbf{2.5}$$

Spangler's formula and the Iowa formula were originally provided in the imperial unit format where D_b is the bedding constant, D_L is deflection lag factor, W_c is the vertical load per unit length of pipe (lb/in), R is mean radius of the pipe (in), E is the modulus of elasticity of the

pipe, I is the moment of inertia of the pipe wall per unit length of pipe (in^4/in), and E' is the modulus of soil stiffness (lb/in^2). The resulting deflection can be seen to be a function and the summation of the pipe stiffness and the soil stiffness, given in the left and right hand sides of the denominator.

The stiffness of the soil is a function of the type of soil, its density, and is also a function of the pipe in the soil. It has been noted that E' property cannot be measured in the laboratory or in the field. "This is a soil-pipe system parameter, which could only be obtained from back calculation by knowing the other properties in the modified Iowa equation" (Jeyapalan and Watkins 2004). Howard (1977) did back calculate the modulus of soil stiffness and provided their values based on the soil UCS (Unified Classification System) and specified relative density around the pipe. Regardless of the limitations of Watkins and Spangler's (1958) Iowa formula, it has and still provides a convenient method for designers to estimate the deflection of flexible pipes. The equation also reveals a basic understanding that both the stiffness of the pipe and the soil determine the response of the system.

2.3.3 Vertical Arching Factors for Flexible Pipes

Spangler (1947) (1951) expanded on Marston's equation (1930) to include arching factors for flexible pipes to determine the weight of the soil prism for trench and embankment conditions. For trench conditions the weight of the prism, minus the shear resistance at the sides of the trench, demonstrated that the weight of the prism at the crest of the pipe was carried by the pipe and the backfill equally. Hence the pipe only carries the soil directly over the diameter of

the pipe. In contrast, for rigid pipes the prism of soil is carried by the pipe only and is the width of the trench. For embankment conditions, the direction of the shearing forces is highly dependent on the relative deflection (settlement) of the soil and the pipe. If the pipe is relatively rigid compared to the backfill, the shearing forces at the sides of soil prism will be additive. If the pipe deflects more than the settlement of the backfill, the net weight of the soil prism on the pipe will be less. Because of the "practicality" of an analysis of predicting the settlement ratio, Spangler (1951) recommended that the ratio be empirically derived based on the "observed performance of conduits in service".

It is common in design methods to quantify the ratio of actual vertical thrust in the pipe to the thrust in the pipe wall determined by weight of the soil prism over the pipe. This ratio is called the vertical arching factor (VAF) and is a convenient method of determining the load on a pipe while incorporating the positive or negative effects of soil arching for flexible pipes. White and Layer (1960) suggested no arching action, or a VAF of 1 for corrugated steel pipes based on experimental data, and Watkins (1966) conservatively suggested using a factor of 1.5 times the prism weight based on an elastic solution. Watkins (1966) did recognize that axial shortening of the pipe and other field conditions would likely reduce the arching factor. Watkins (1971) later showed that based on full scale embankment tests for corrugated steel pipes, which are relatively stiff, that a well compacted backfill (greater than 85% relative density) significantly increased the strength of the pipe-soil system with arching action, or the vertical arching factor was less than 1. These experiments and design methodolgies confirmed Spangler's (1941) original findings that the realtive pipe and fill stiffness will determine the load caried by the pipe.

Burns and Richard (1964) provided pipe researchers with a closed form solution of thrust, moment, and deflection of elastic cylinders in an elastic medium due to an overburden pressure.

The modulus of elasticity, constrained modulus, and lateral stress ratio, along with the pipe flexibility (modulus of elasticity, moment of inertia, and diameter) are used to determine moment, thrust, radial and tangential stresses. The method can be used assuming no slippage between the soil and pipe wall, or with full slippage between the soil and the pipe wall. Some basic assumptions are built into the analysis including a homogenous elastic continuum, uniform loads, free-field stresses, and a minimum embedment. While this method is limited to an approximate elastic condition, the method was helpful in demonstrating the general pipe behavior for many conditions.

McGrath et al. (1999) using the Burns and Richard (1964) solution demonstrated that plastic pipes had a greater tendency, than corrugated steel pipes (CSP) in particular, to have positive arching because of the shortening of the pipe circumference. Corrugated steel pipes, while relatively flexible in bending, if properly supported become very stiff axially (tangential to the radius). This circumferential stiffness is proportional to the modulus of elasticity of the steel. If the CSP has a well compacted backfill the pipe deflects very little. Plastic pipes on the other hand have a modulus of elasticity an order of magnitude less than steel pipes. For plastic pipes even with a well compacted backfill a significant positive arching factor can be generated as demonstrated by Hashash and Selig (1990).

A review of current design methodologies such as AASHTO (2012), the National Corrugated Steel Pipe Association (NCSPA 2008), and the American Water Works Association (AWWA 1999), and previous design methods including ASCE No. 60 (1982) and AISI (1983) indicate that for most conditions flexible pipes are designed based on a vertical arching factor of 1 because trench depths are usually limited and trench widths are usually not narrow enough. Generally corrugated steel pipes and thermoplastic pipes are flexible enough that even under

embankments considering no arching is conservative. The NCSPA does have VAF greater than 1 for embankments of very loose soil. The current edition of AASHTO does adopt McGrath's et al. (1999) VAF for plastic pipes because of the relatively low hoop stiffness.

2.4 Pipe Design

Pipe design methods can be generally segregated into two branches, flexible pipes, such as steel and High Density Polyethylene (HDPE) pipes, and rigid pipes, including concrete and vitrified clay pipe. The pipe material properties and limit states, and the response of the pipe in the soil, as shown previously, naturally divide the design methodologies for these two pipe classes. Rigid pipes are generally limited by thrust in the pipe wall and cracking in the pipe which greatly affects its serviceability. Flexible pipes are generally limited by deflection, buckling, and yielding in the pipe wall. This introduction to pipe design and the subsequent sections focuses on flexible pipes. Following is a short discussion of common failure or limits states for the design of flexible pipes.

2.4.1 Pipe Deflections

The earliest design methods for flexible CSP pipes were based on observation and experience. Each manufacturer of metal pipe developed load tables based on the height fill, steel gauge, and a minimum serviceability. George E. Shafer and associates (ARMCO 1955) at

Armco Drainage and Metal Products Inc., prior to 1948 had developed a similar, purely empirical, design method where the deflection could be calculated based on the fill height, diameter of the pipe, standard corrugations, and the thickness of the pipe wall for an "average" installation. An average installation was specified by the manufacturer based on tested backfills and installation procedures. Shafer (ARMCO 1955) noted that the maximum safe deflection of the pipe was 20% of the diameter, to include a safety factor the maximum deflection was limited to 5% of the diameter of the pipe. The pipe deflection would be checked after the installation of the pipe and then backfill or embankment.

Spangler (1941) similarly described a general deflection failure condition in flexible pipes where enough vertical deflection takes places at the crown, that the sidewalls of the pipe begin to move away from the soil at the springline, and the failure is progressive Spangler (1951) also suggested that a 5% vertical deflection limit, calculated by the Iowa formula (Equation 2.5) would give an adequate safety factor versus this mode of failure. In fact, the 5% deflection was the only limit state suggested by Spangler (1951).

2.4.2 Thrust in Pipe Wall

One of the most basic design checks is for pipes that are under internal pressure, which applies to both rigid and flexible pipes. The Barlow formula calculates the hoop stress or circumferential stress in a pipe due to pressure inside the pipe (Roark 1943). One half of a vertically cut pipe, or a half a pipe in any arbitrary plane, has forces balanced in the horizontal direction by pressure multiplied by the diameter in one direction, resisted by the circumferential

stress in the thickness of the pipe in the opposite direction (Figure 2.4), which results in Equation 2.6.

$$\sigma_c = \frac{pr}{t} \qquad \textbf{2.6}$$

where t is the pipe thickness, r is the pipe radius, p is the internal pressure, and s_c= circumferential stress (hoop stress).

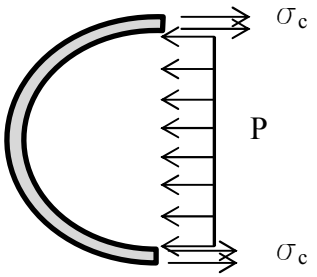

Figure 2.4 Pipes under Internal Pressure

Similarly, for external gravity loads the weight of the soil prism above the pipe and live loads above the pipe are carried through the thickness of the pipe wall. White and Layer (1960) proposed designing corrugated steel pipe by simply checking the wall strength versus wall yielding (or seam strength) against the weight of the soil prism above the pipe, with no positive or negative arching, given that standard pipe wall profiles and a uniform compacted backfill was used in the construction of the pipe soil system (Figure 2.5). The thrust in the pipe wall (Equation 2.7) is checked versus the yield strength of the pipe wall (Equation 2.8) with an appropriate factor of safety.

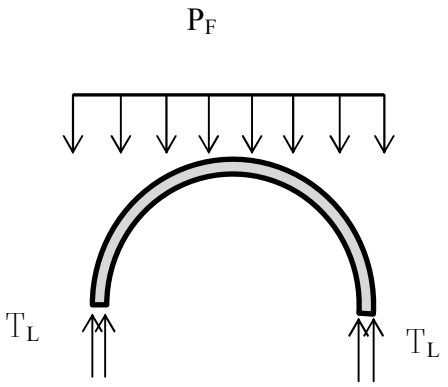

Figure 2.5 Thrust due to External Pressures

$$T_L = P_F\left(\frac{D}{2}\right) \quad \textbf{2.7}$$

$$R_r = A\,F_y \quad \textbf{2.8}$$

where T_L is thrust in force per unit length of pipe, R_r is resistance to thrust, A is the area of the pipe wall per unit length of pipe, F_y is the yield stress of the pipe wall, D is the pipe diameter and P_F is the soil and live load pressures on the crown of the pipe

2.4.3 Buckling

Different buckling design methodologies have been proposed and are currently in use. The current design methods for a given pipe type, CSP or plastic pipe, have been generally predetermined by past use. Pipe materials that have been more recently developed generally have adopted more state-of-the art design methods. Buckling analysis methodologies are generally broken down into column buckling analogy, Winkler Spring design, and continuum models.

The column buckling design analogy is currently in use for corrugated steel pipes. White and Layer (1960) suggested using Timoshenko's buckling of circular rings and tubes hydrostatically loaded as an approximation of the pipe under compressive soil loads (Equation 2.9):

$$f_{cr} = \frac{3EI}{(R)^2} \qquad \textbf{2.9}$$

where f_{cr} is the critical buckling stress in the pipe wall, E is the modulus of Elasticity of the pipe, I is the moment of inertia of the pipe wall, and R is the radius of the pipe.

At approximately the same time, Watkins (1960) proved that in some conditions of backfill stiffness and pipe flexibility, buckling was possible before the 5% vertical deflection threshold was reached. Watkins (1966) and (1971) showed that based on these two parameters (pipe flexibility and soil stiffness) that the pipe was subject to a wall yielding zone and a buckling zone. This confirmed White and Layer's (1966) compression ring theory for conditions with adequate pipe and soil stiffness. Watkins (1966) proposed a buckling load formula based on the hydrostatic buckling of tube modified by a soil stiffness factor K, which was ultimately determined based on experimental results in a lower bound minimum soil stiffness (Equation 2.10). The buckling stress is limited by the yielding of the pipe wall and hyperbolic line approximating inelastic buckling (Figure 2.6). This method is analogous to column buckling, where D is the diameter of the pipe and r is the radius of gyration of the pipe wall. The column method was adopted by the AISI (1983), Wolf and Townsend (1970), and is still used in the recent editions of AASHTO (2012).

$$f_{cr} = \frac{3EI}{K(R)^2} \qquad \textbf{2.10}$$

where K is the soil stiffness factor.

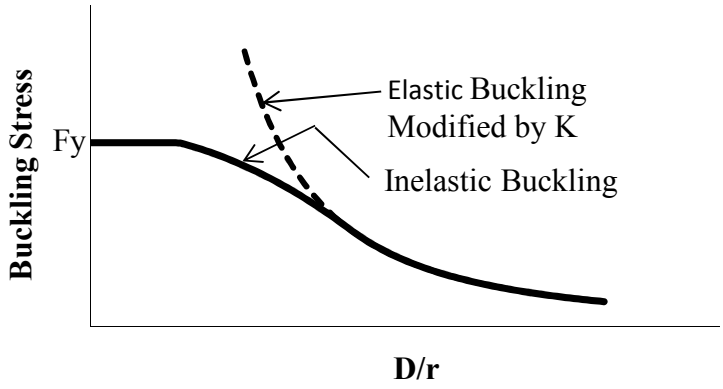

Figure 2.6 CSP Column Buckling

Meyerhof and Baikie (1963) similarly found that buckling was a function of the pipe flexibility and the soil stiffness and were able to provide an elastic buckling solution that included the spring support value k and the coefficient of soil reaction (subgrade modulus). Meyerhof and Baikie (1963) suggested estimating k as a simple function of the soil modulus of elasticity. Luscher (1966) also introduced an equation for the critical buckling of pipes based on the Winkler soil model and included a rational method to calculate the soil spring stiffness based on the soil properties. Modified forms of Luscher's (1966) equations have been used extensively in the design of plastic pipes.

Forrestal and Herrmann (1965) and Moore (1987) have provided elastic continuum solutions for the problem of predicting pipe buckling stresses. In the elastic continuum model the soil is not modeled as spring but as a continuous element with a shear capacity. The

continuum mode has generally shown a closer fit to experimental results (Moore et al., 1988) and to be a more accurate representation of the soil pipe interaction (Moore and Selig, 1990). Currently the AASHTO (2012) design guide for thermoplastic pipes uses the elastic continuum model for predicting global buckling of the pipe system.

2.4.4 Plastic Pipe Design

Plastic pipes were introduced in the 1970s as an alternative to steel pipes and were generally Polyvinylchloride (PVC) and High Density Polyethylene pipes (HDPE). PVC and HDPE pipes have excellent corrosion resistance but added new complexities to the design of buried flexible pipes. Plastic pipes do not have the stiffness of steel pipes, and the plastic does not always behave elastically. In addition plastic gave designers the opportunity to use new innovative pipe wall configurations.

Steel products when kept below yield stress behave consistently and can be modeled as a linearly elastic material. HDPE and PVC materials have visco-elastic properties which result in creep and relaxation of the pipe under stress and strain. Visco-elastic properties are a function of the load duration, the temperature, and the magnitude of the initial stress. To achieve a precise model of viscoelastic materials it is common to model the properties with a variety of spring and dash-pot combinations (Zhang and Moore, 1997). To simplify design methods an apparent modulus of elasticity has been adopted by AASHTO (2012) based on the length of the load duration. Most loads on pipes have a very short duration (wheel loads), or a very long duration (earth loads). Constant tensile stress tests on plastic coupons have been conducted to determine

an apparent modulus of elasticity under a short term load and at 50 years, the design limit for most pipes. Because the viscoelastic nature of the pipe material is based on the temperature and magnitude of the initial stress the values must cover a standard temperature and range of initial stresses. McGrath et al. (1994) by experiment demonstrated well the superposition of short term and long term stresses on HDPE pipe materials. After an initial long term stress, such as when a dead load is applied, the pipe will be undergoing creep or relaxation. In either case when a new short term load, such as a wheel load, is applied the pipe material responds with the apparent short term modulus.

Plastic materials such as HDPE and PVC exhibit two failure modes in tension. The plastic pipe can fail in ductile manner, classic yielding, or the pipe can fail in a brittle mode due to slow crack growth (SCG). Given enough time the plastic can fail in a brittle mode at strain less than the ductile strain. The hydrostatic design basis (HDB) test was an early test method for this condition. The test pipe was placed under constant internal pressure until failure and those failure points plotted on a log time versus a log stress graph. The resulting generic failure line is plotted on the graph in Figure 2.7.

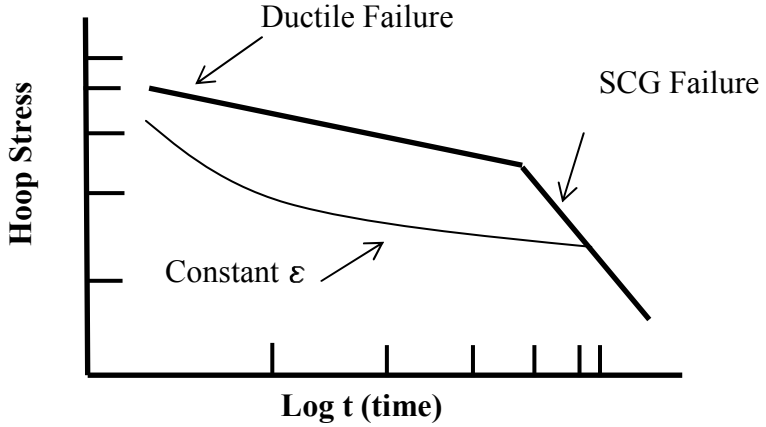

Figure 2.7 HDPE Tensile Failure and Slow Crack Growth

Janson (1981) (1985) plotted the log stress versus log time for constant strain on HDPE pipes and determined that a long term strain of 5% or less resulted in service life of "not less than 50 years". Janson (1981) further surmised, from the deflection strain relationship in an unpressurized pipe wall that a constant thickness pipe is controlled by deflection and not tensile strain. Mruk (1990) and McGrath et al. (2009) have also indicated that while tensile strains are atypical for well-placed, non-pressurized, constant thickness and profile wall pipes, it has been, and should continue to be standard practice to maintain a maximum allowable tensile strain.

HDPE resistance to slow crack growth can also be greatly affected by impurities in the plastic. Hsuan and McGrath (1999) correlated installed cracked pipes with a notched constant tensile load test (NCTL) on the pipe material to determine a minimum NCTL test performance to insure crack resistance. McGrath et al. (2009) also demonstrated that in profile wall pipe, areas of tensile strain can develop due to local effects in the pipe wall. Areas of abrupt change in the pipe wall geometry can cause stress concentrations that crack, thus negatively impacting the function of the pipe.

McGrath and Sagan (2000) recommended that the compressive strain of plastic pipes be limited to 4 to 6 percent, and that compression design should be based on a strain limit, from work performed by Moore and Laidlaw (1997), Selig et al. (1994), and Zhang and Moore (1997). Zhang and Moore (1997) showed clearly that the strain rate on the plastic greatly affected the apparent strength of the material based on compression tests. Quickly applied strains had a much higher influence than slowly applied strains. However, for all strain rates the plastic materials reached their compression limit at around 6% strain.

Due to the strain limits of plastic it has been common practice to design for deflection, buckling, and strain in the pipe wall (Watkins et al. 1974). Similarly many authors, for example, Greatorex (1981), Cole and Timblin (1981), and Leonhardt (1978) attributed much of the early work design methods to Carlstrom and Molin (1966). Knowing the maximum moment in the pipe wall due to equally opposed line loads (Figure 2.1) as provided by Spangler (1941), the pipe stiffness (Equation 2.2), and the relationship between strain and moment in a pipe wall of uniform thickness, the maximum strain in the extreme fiber as a function of pipe deflection in a parallel plate load test can be derived and is given by Equation 2.11.

$$\epsilon_b = 4.28 \frac{\Delta D_v}{D} \frac{t}{D} \qquad \textbf{2.11}$$

where D is the pipe diameter, t is the pipe wall thickness, and ΔD_v is the vertical pipe deflection.

Watkins et al. (1974) proposed a slight variation of Equation 2.11. Watkins proposed that the pipe would deflect in an ellipse shape, resulting in a slightly lower factor from 3 to 4 in lieu of the previously calculated 4.28.

Leonhardt (1978) demonstrated that under certain installations and bedding conditions that the methods proposed by Carlstrom and Molin (1966) would need to be modified to account for stress concentrations. Jeyapalan and Abdelmagid (1984) and Bishop and Lange (1984) also showed that with "very" flexible pipes there were some variations with the proposed Watkins et al. (1974) method. Using a finite element analysis it was demonstrated that with high stiffness backfills and flexible pipes the strain in the pipe wall was much higher than anticipated by the Watkins method. Jeyepalan and Abdelmagid (1984) indicated that the discrepancy was excess strains at areas of low soil stiffness around the pipe, especially below the springline. It was also shown that with a very flexible pipe there was some variation in deflection with respect to the

Watkins formula, as the pipe did not deflect into an elliptical shape, but a box shape. Bishop and Lang (1984) provided a range of D_f deformation value based on the pipe stiffness and the level of compaction around the pipe. Jeyapalan et al. (1987) noted that the bending strain in the pipe wall in ground conditions could be underestimated by the Watkins formula. Based on a two-dimensional finite element analysis it was determined that for certain conditions the strain factor D_f could be as high as 10.

2.4.5 Local Buckling

Local buckling has become an issue in the design of pipes with the introduction of HDPE profile wall pipes and other pipe wall sections with elements. Some of these elements to increase efficiency of material use have high width to thickness ratios. The plastic material is extruded and the fabrication of these sections can come in a wide array of shapes and sizes. A common generic section of profile pipe wall can be seen in Figure 2.8. Selig et al. (1994) observed local buckling in the liner of a profile wall pipe under high hoop loads and Moore and Hu (1995) demonstrated numerically that the cause of the rippling effect was due to local buckling of the liner. Moore and Laidlaw (1997) performed a series of axisymmetric hoop strain experiments and determined that the cold-form plate models used in cold-form design were able to predict critical buckling stresses.

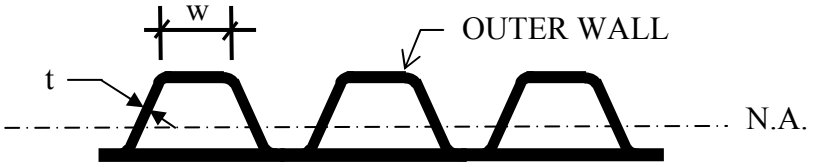

Figure 2.8 Cross Section of Profile Pipe Wall

If the wall width (w) to thickness (t) ratio of individual elements is high enough the element will buckle at lower stresses than the yield stress of the material. The critical buckling stress equation of plates is given in Equation 2.12 (Bryan 1891).

$$\sigma_{cr} = \frac{k\pi^2 E}{12(1-\mu^2)(w/t)^2} \qquad \textbf{2.12}$$

where k is the buckling coefficient, E is the modulus of elasticity, w is the plate width, t is the plate thickness, and μ is the Poisson's ratio of the plate.

The length of the plate element and boundary conditions, whether they are fixed or pinned, control the k value. Local buckling does not lead to an immediate failure of the structural member but does reduce the capacity of the section. Von Karman et al. (1932) and Winter (1946) introduced the concept of effective area to simplify the analysis of post-buckled cross sections. The effective element is reduced by an effective width ratio of ρ and the section is designed per the standard limit states.

Moore and Laidlaw (1997) also gave the local buckling criteria in the form of a critical strain to accommodate plastic design methods. McGrath and Sagan (2000) performed a series of "stub compression" tests to demonstrate that Winter's equations correlated with resulting buckling stresses. McGrath and Sagan (2000) (2001) introduced the local buckling design

method adapted for use with thermoplastic pipe. The effective area of the plastic pipe is taken into consideration when calculating the strains in the pipe wall due to bending and compression in the pipe

2.5 Surface Loads

It was recognized early that often failures of pipes were commonly due to near surface loads such as wheel loads from trucks. Spangler et al. (1926) provided early research into the application of surface loads to buried pipes. This research included full scale tests that measured the static and impact loads to the crown of a buried culvert with varying heights of cover. Spangler et al. (1926) concluded that for static loads, the Boussinesq solution provided an accurate method of predicting the load at the top of the culvert due to a surface load. It was also concluded that surface loads were negligible for height of cover exceeding five feet. Likewise his team suggested using an impact load of 150 to 200 percent of the calculated static load to predict the effects of slow moving trucks. The conclusions were qualified to wheel loads at slow speeds and maximum pipe diameters of three and a half feet.

Early methods of determining the influence of live loads to buried conduits were provided by the corrugated steel pipe manufacturers. The equivalent live load at the crown of the pipe was simply added to the soil prism weight. The standard checks of thrust and deflection were then made. The Handbook of Drainage and Construction Products (ARMCO 1955) and subsequent editions of the Handbook of Steel Drainage and Highway Construction Products

(AISI 1983) graphically provided equivalent pressures to the crown of the pipe based on the axel load and the burial depth based on the Boussinesq method. The influence graph of an H-20 load has been recreated in Figure 2.9 in Si units. The live load portion of the total load, as determined by the Boussinesq method, becomes negligible as compared to the unit weight of the soil 19.2 kN/m^3 (120 pcf) when the depth exceeds 1.8 m (6 ft). Shown in Figure 2.9 is the distribution of an H-20 wheel load applied to a 36"x40" area (AISI 1983).

An alternative method to the Boussinesq solution is to establish the load on the pipe as the trapezoidal distribution of the surface load to the crest of the pipe. The Handbook of Steel Drainage and Highway Construction Products (AISI 1983) allowed a ½ unit horizontal to 1 unit vertical distribution of the live load. Watkins et al. (1974) reasoned that the trapezoidal distribution of the soil load was more accurate because at soil failure the load "punched through" leaving the truncated soil pyramid, thus resulting in the worst case load applied to the pipe. The current AASHTO (2012) allows a 1.15 horizontal distribution for conditions with granular backfill.

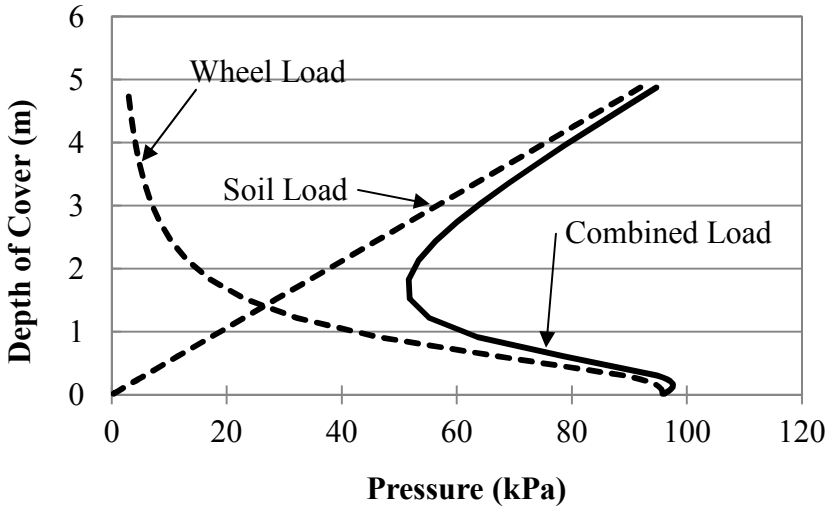

Figure 2.9 Influence of H-20 Load and Weight of Soil on Buried Pipe

Whether the Boussinesq solution or the trapezoidal load method is used the effective stress estimated to be added to the pipe is an average pressure. Both methods transform the surface load into an equivalent uniform load that is simply added to the weight of the soil prism. It can be visualized that if the span of the pipe is significant in relationship to the height of cover or the width of the surface load, that the surface load is not uniform over the pipe. Non-uniformity of load on the pipe creates local deformations of the pipe and can generate higher bending strains in the pipe wall. Non-concentric loads over the pipe have also been demonstrated to create the highest moments. Both Duncan (1979) and Watkins et al. (1987) derived methods of checking the moment in the pipe wall based with surface load offset from directly over the pipe. Minimum covers are required to maintain the confinement and distributive properties of the soil. Without the confinement of the soil the load on the pipe is no longer distributed in the pipe through thrust and the pipe crown must resist the load through bending. Rutting can also reduce the height of cover and should be considered for unpaved applications. Minimum cover heights were established based on observations of field tests and standards of industry practice.

Klaiber et al. (1996) and Phares et al. (1998) performed laboratory tests on HDPE pipes and full scale tests on a 36" diameter (915 mm) profile wall HDPE pipe with the goal of determining the behavior of HDPE pipes subjected to live loads under shallow cover. Their research indicated that in addition to the usual conditions of failure, bending at the crown, longitudinal strain was a significant factor in the performance of the pipe. Phares et al. (1998) even stated that in regards to their tests that "field tests indicate that the pipes failed in the longitudinal direction". Reddy (2002) also observed high longitudinal strains in full scale tests of near surface loads. Watkins (1985) emphasized the importance of longitudinal stress in pipes

and gave several causes of longitudinal stress including: pipe longitudinal expansion due to temperature changes, pipe longitudinal stress due to the pipe spanning a weak area, or even the Poison's effect where the length of the pipe is shortened when the pipe expands under pressure. Although longitudinal strain is not a current design check per the AASHTO (2012) code there is some indication beyond the tests that longitudinal strain is a problem for HDPE pipes.

Gassman et al. (2005) performed a survey of 45 HDPE pipes to evaluate their long-term performance. The pipe's deflection was measured and cameras were used to look for damage on the interior of the pipe. Of the forty-five pipes checked, 18% had circumferential cracking, an indication of longitudinal strain. It was noted that the crack occurred at the inner lining and did not propagate through the profile of the wall. The locations of the cracks along the pipe and load history of the pipes were not provided in the report. The authors also did not provide an explanation of the cracking process.

2.6.0 Numerical Modeling

The inception of finite element and finite difference modeling introduced designers and researchers with a powerful tool to investigate and predict the behavior of buried structures. Prior to the creation of numerical modeling, empirical methods were employed because of the inherent non-linear properties of the soil and indeterminacy of the soil and structure. In addition, the soil around the pipe is not homogenous and the soil does not apply load to the pipe uniformly. Specifically, the stress state of the soil in zones around the pipe greatly affects the

interaction. The variations in stress state around the pipe create areas of varying stiffness. Numerical analysis gives researches a useful method for studying buried pipes.

Katona et al. (1976) introduced the Culvert Analysis and Design "CANDE" software package for the design and analysis of buried pipes. The finite element program gave the authors a powerful tool and method of presenting a "unifying" design process, for almost any type of buried pipe. The design software also gave a convenient method to determine with more insight to how the surface load affected the displacement of the pipe and thrust and moment in the pipe wall. Table 2.1 at the end of this section gives a partial list of the papers studied for this literature review.

2.6.1 Constitutive Soil Models

A wide variety of soil constitutive models have been created for the analysis of embankments, foundations and buried structures. Following is a discussion of those models that are important to the established methods of analyses of buried pipes. Also discussed are the features of the constitutive models that make them of specific use to the analyses of buried structures. This discussion will focus on elastic models, elastic-perfectly plastic models, and non-linear soil models. There are also combinations of each, for instance non-linear plastic soil models.

Prior to the literature review it was known that the three dimensional version of the Fast Lagrangian Analysis of Continua (FLAC 3D) would be used for numerical analysis and numerical studies of geosynthetic protected pipes. The FLAC software by the Itasca Consulting

Group (2009) is designed and well suited for geotechnical analysis. The software has many built in constitutive soil models and structural element models, including shells and geogrid elements. The literature review was completed mindful that the constitutive models used in the study would be those available in the FLAC 3D software, and are used here for discussion and comparison.

Elastic Soil Models

The first constitutive model is the linear elastic model based on Hooke's law. This model follows the basic linear relationship, in one dimensional form, that stress is the product of strain times the modulus of elasticity. In a three dimensional model the shear and elastic moduli will have the same linear properties, and are provided by six equations for the normal and shear forces acting on each face of an element. The elastic constitutive model has several advantages for use in the analysis and design of pipe systems. The elastic method does simplify the numerical modeling for input. The material model can be generated with two inputs (the modulus of elasticity and Poisson's ratio) and the model is ready for analysis. Because all of the stiffness relationships in the model are linear the model is quick to run. The elastic model does have limitations as the model cannot emulate plasticity, dilation, failure, and other non-linear behavior, properties inherent in soil materials. The elastic method with its limitations has very important uses including rudimentary analyses, and analyzing those portions of the model that will be subjected to elastic behavior.

Elastic-Plastic Soil Models

The elastic-plastic soil model takes the elastic soil model and sets a limiting yield state at which point the material continues to strain at a constant stress. The limiting yield state is a function of the material, and for soil type materials it is generally a shear or tension limit state that is used. The shear limit can be set by a number of different yield functions, but the Mohr-Coulomb is discussed here as it is the most well-known failure relationship for soils. The shear and tension yield functions used by FLAC 3D version 4 (Itasca, 2009) are shown in Equations 2.13 through 2.15.

$$f_s = \sigma_1 - \sigma_3 N_\phi + 2c\sqrt{N_\phi} \qquad \textbf{2.13}$$

$$f_t = \sigma_3 - \sigma_t \qquad \textbf{2.14}$$

$$N_\phi = \frac{1 + sin(\phi)}{1 - sin(\phi)} \qquad \textbf{2.15}$$

where $\boldsymbol{\sigma}_1$ and $\boldsymbol{\sigma}_3$ are the maximum and minimum principal stresses, c is the soil cohesion, ϕ is the soil friction angle, and $\boldsymbol{\sigma}_t$ it the tensile strength of the soil.

Plotting the yield functions on the principal stress plot reveals a section of the failure surface for the FLAC 3D Mohr-Coulomb failure plane as shown in Figure 2.10. In the figure positive principal stresses are in compression. As long as the stress state stays below the failure surface the element behaves elastically linear based on Hooke's law. If the stress state goes beyond the failure surface the material becomes plastic and all further deformations are permanent and cannot be recovered.

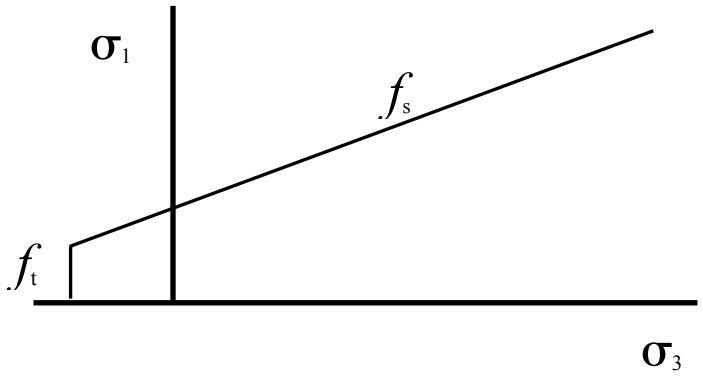

Figure 2.10 FLAC 3D Mohr-Coulomb Failure Surface

Non-Linear Soil Models

Non-linear soil models were developed and introduced as an improvement to the linear models and the on/off behavior of Mohr-Coulomb failure. Duncan and Chang (1970) recognized that with advances in computing power and numerical analyses researchers and designers could utilize non-linear constitutive models to improve analytical models. Konder (1963) had previously established that the deviator stress vs. axial strain relationship of a tri-axial test could be presented as a hyperbolic relationship. Using this basic relationship Duncan and Chang (1970) introduced Equation 2.16 for the Duncan-Chang hyperbolic soil model.

$$\sigma_1 - \sigma_3 = \frac{\epsilon}{\left[\frac{1}{E_i} + \frac{\epsilon R_f}{(\sigma_1 - \sigma_3)_f}\right]} \qquad \textbf{2.16}$$

where E_i is the initial modulus, $(\sigma_1 - \sigma_2)_f$ is the deviator stress at failure, and R_f (the failure ratio) defines the ultimate deviator stress as the limit of hyperbola which is approached

asymptotically. The deviator stress at failure, $(\sigma_1 - \sigma_2)_f$, is calculated by the Mohr-Coulomb failure criterion expressed in Equation 2.17:

$$(\sigma_1 - \sigma_3)_f = \frac{2c\,(\cos\phi) + 2\sigma_3 sin\phi}{1 - sin\phi} \qquad \textbf{2.17}$$

Duncan and Chang (1970) used the power law in Equation 2.18, based on Janbu's research (1963), to describe the relationship between E_i and the initial confining stress $\boldsymbol{\sigma}_3$:

$$E_i = Kp_a\left(\frac{\sigma_3}{p_a}\right)^n \qquad \textbf{2.18}$$

where p_a is the atmospheric pressure and the dimensionless K and n parameters are established with experimental data.

The Duncan-Chang constitutive model can match well the non-linear behavior of soils, and has been used to provide significant studies in pipe design including; Duncan (1976), Duncan (1979), Katona (1990), McGrath (1998), and Kang et al. (2008) to name a few. Large amounts of data on soil parameters (Selig 1988) (Duncan et al. 1980) have been determined and are available for use in the numerical analysis of buried pipes as well. This model does have its limitations in that it cannot capture plasticity. Katona et al. (1976) grouped and described non-linear soil models into two groups; variable modulus, and plasticity models. The Duncan-Chang model would fall into Katona's description of variable modulus. The variable modulus model captures non-linearity, but does not model plasticity as the stress path does not change or deviate from the previously described loading path during unloading. For instance if a load is removed from an element the displacement of the element will follow the loading stress-strain curve back,

ultimately to its original state and does not capture the permanent deformation associated with most soil materials.

Non-Linear Plastic Soil Models

The second non-linear soil model type Katona et al. (1976) discussed was the plasticity model. The plasticity model as the name suggests is able to model the quantity of plastic or permanent strain that a soil element has undergone allowing the stress path to change and model unloading conditions. FLAC 3D version 4 (Itasca, 2009) has the built-in constitutive Cap-Yield soil model (i.e., a plasticity model), which is able to model hardening, softening, and the plastic volumetric strain due to isotropic compression. The Cap-Yield Soil constitutive model includes both non-linear shear yielding and volumetric hardening. Plotting a stress path figure in 2-D space with the mean stress (p) and deviatoric stress (q) for an element the two yield surfaces can be shown in Figure 2.11. A plot of the yield surface in a principal stress state is shown in Figure 2.12.

Stress paths inside the yield surface result in fully recoverable elastic strains. Stress paths outside of the yield surface result in non-recoverable plastic strains. The yield surface is based on the function shown in Equations 2.19 and 2.20, where p' is the effective mean stress, q is the deviatoric stress, p_c is the cap pressure, and α is the parameter to control the shape of the ellipse. The effective stress and deviatoric stress are calculated by Equations 2.21 through 2.23; where σ_1, σ_2, and σ_3 are principal stresses. The value M represents the slope of the shear yield surface based on the mobilized friction angle (ϕ_m) as shown in Equation 2.24.

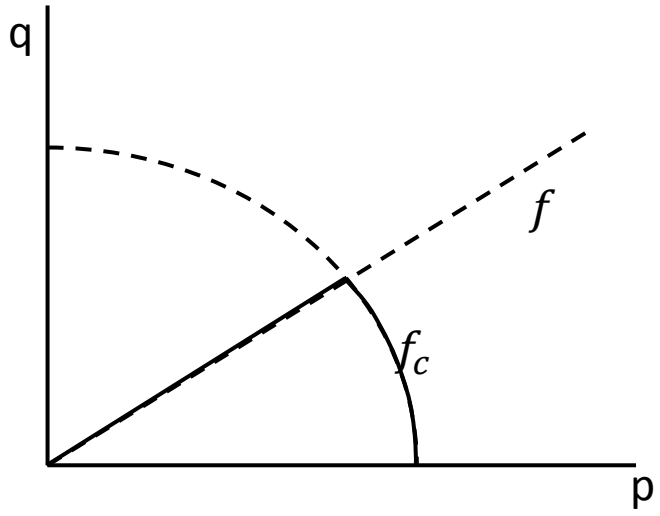

Figure 2.11 Yield Surface for Cap Yield Constitutive Model

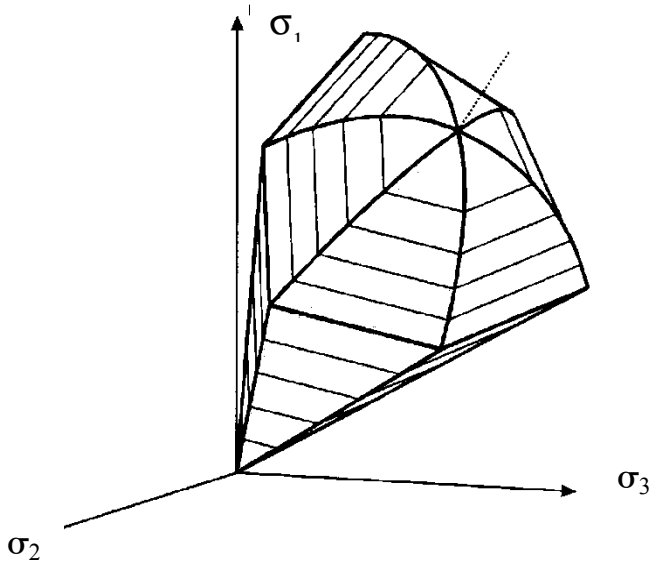

Figure 2.12 Yield Surface in the Principal Stress State (Schanz et al., 1999)

$$f = Mp' - q \quad \textbf{2.19}$$

$$f_c = \frac{q^2}{\alpha^2} + p'^2 + p_c \quad \textbf{2.20}$$

$$p' = \frac{\sigma_1 + \sigma_2 + \sigma_3}{3} \quad \textbf{2.21}$$

$$q = -[\sigma_1 + (\delta - 1)\sigma_2 - \delta\sigma_3] \quad \textbf{2.22}$$

$$\delta = \frac{(3 + sin\phi)}{(3 - sin\phi)} \quad \textbf{2.23}$$

$$M = \frac{6sin\phi_m}{(3 - sin\phi_m)} \quad \textbf{2.24}$$

The Cap Yield soil model in FLAC 3D determines plastic shear strains with the flow rule based on the non-associative plastic potential function given in Equation 2.25. The terms of the potential function are based on the mobilized dilation angle (ψ_m), see Equations 2.26 through 2.28. Plastic strains on the cap are associated with the yield function and are proportional based on a constant R to be discussed later.

$$g = M^* p' - q^* \quad \textbf{2.25}$$

$$M^* = \frac{6\sin\psi_m}{(3 - \sin\psi_m)} \quad \textbf{2.26}$$

$$q^* = [\sigma_1 + (\delta^* - 1)\sigma_2 - \delta^* \sigma_3] \quad \textbf{2.27}$$

$$\delta^* = \frac{(3 + sin\psi_m)}{(3 - sin\psi_m)} \quad \textbf{2.28}$$

To capture the hardening of the material the yield surface must expand as the stress path exceeds the limits of the previous yield surface. The Cap Yield soil model does this by updating the mobilized friction angle (ϕ_m) and the cap pressure (p_c) for Equations 2.24. The mobilized friction angle is updated based on a table of plastic shear strains and associated mobilized friction angles, and the cap pressure is updated by the plastic volumetric strain. FLAC 3D (Itasca, 2009) included Equation 2.29 for generating a table of plastic shear strains (γ^p) and mobilized friction angles (ϕ_m) for typical hardening soils based on the ultimate friction angle (ϕ_f), the reference elastic tangent shear modulus (G^e_{ref}), the failure Ration (R_f), and the constant m. FLAC 3D included Equation 2.30 for generating of a table of plastic volumetric strain (e^p) and cap pressure based on the previously defined terms and the reference bulk modulus (K^{iso}_{ref}).

$$\gamma^p = \frac{p_{ref}}{G^e_{ref}}\left(\frac{p'}{p_{ref}}\right)^{1-m}\frac{sin\phi_f}{R_f}\left[\frac{1}{1-\frac{sin\phi_m}{sin\phi_f}R_f}-1\right] \qquad \textbf{2.29}$$

$$p_c = p_{ref}\left[(1-m)\frac{1+R}{R}\frac{K^{iso}_{ref}}{p_{ref}}e^p\right]^{\frac{1}{1-m}} \qquad \textbf{2.30}$$

The R value is a description of the ratio of plastic volumetric strain rate to the elastic volumetric strain rate. Itasca (2009) assumed that the ratio of upper bound bulk modulus to shear modulus in the Cap Yield soil model is proportional to the elastic portions of the reference bulk and shear modulus as follows:

$$R = \frac{K}{G}\frac{G^e_{ref}}{K^{iso}_{ref}} - 1 \qquad \textbf{2.31}$$

2.6.3 Construction steps in numerical modeling

Although not always necessary for the design of pipes, many researchers have found it necessary to model the construction process of the pipe-soil interaction to effectively duplicate measured field conditions. There are a few reasons why this process is necessary for analysis. As noted in the pipe-soil interaction description in the previous chapter the installation sequence and relative stiffness effects whether forces "flow" towards the pipe or the forces arch over the pipe. Secondly, compaction forces place lateral pressure on the pipe, causing "peaking" or negative deflection of the pipe (Figure 2.13). Likewise these same horizontal loads can generate moments and thrusts in the pipe wall. The same lateral force that generates deflection and pipe forces also generates horizontal pressures in the backfill, that are locked in due to the plasticity of the soil, pre-stressing the backfill, and increasing its initial stiffness.

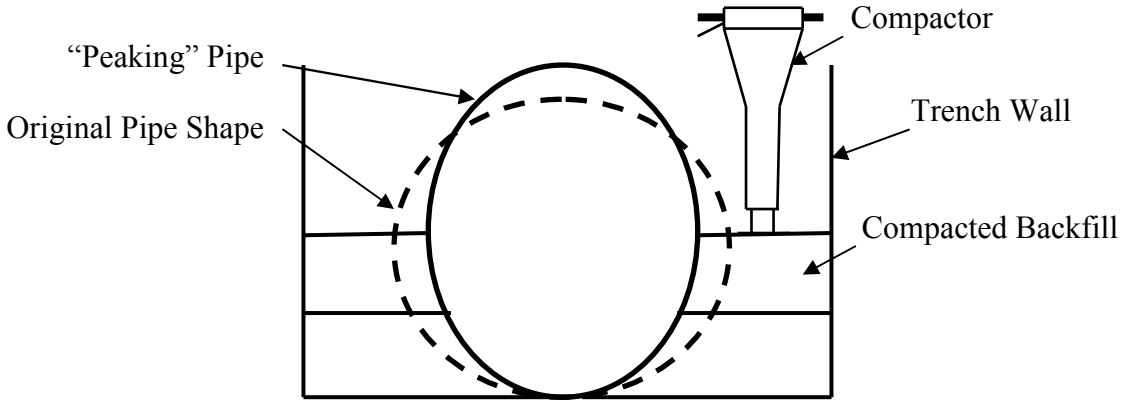

Figure 2.13 Peaking of Flexible Pipe during Installation

Numerical analyses allow researchers to model the construction process. In the recent CANDE manual and in previous versions, Katona et al. (2007) suggested modeling the

construction increment process by placing vertical pressure on each layer as that layer is introduced in the model. This process effectively "squeezes" each layer producing the horizontal forces on the pipe.

Duncan and Seed (1986) and Seed and Duncan (1986) presented methods for determining the residual stresses in soils that have been incrementally compacted. Each soil layer is analyzed as a series of loading and unloading (hysteresis) of the layer of soil. The relationship of the horizontal and vertical loading is a function of K_o and factors presented as α and β, all of which are determined empirically. The resulting horizontal pressure on the wall increases and is "locked in" with each increasing application of vertical stress.

Because of difficulties with the direct application of Duncan and Seed's soil models into a numerical analysis and difficulties in determining the magnitude of stress on the layers, more empirical methods for installation analysis have been examined. While investigating backfill interaction with pipes McGrath et al. (1999) also noted that the densification of the backfill causes peaking of the pipe. The authors measured peaking deflections during the installation of metal and plastic pipes with rammer and vibratory plate compactors. The backfill was also varied with silty-sand and stone. During the installation process in the numerical analysis loads at the level of installation were laterally applied to the nodes of the pipe. The loads were adjusted until the peaking in the numerical analysis matched the observed peaking. The authors then had an empirical method for determining peaking on pipes in other configurations.

Taleb and Moore (1999) approximated the horizontal stress in the compacted soil layer by calculating the horizontal passive earth pressure created by the construction increments of self-weight. The reaction of the pipe, small displacements for rigid pipes and larger

displacements of flexible pipes were predicted by the numerical analysis. Elshimi and Moore (2013) expanded on this method by including a "kneading" factor that combined the effects of plastic strain during the densification process.

Masada and Sargand (2007) provided an equation for predicting peaking during installation based on an empirical solution similar to the Iowa formula. The lateral pressures at the springline from the invert of the pipe to the crown of the pipe are estimated at the end of the installation process before the fill is placed above the crown. Knowing the pipe stiffness and this lateral force the amount of pipe peaking can be estimated. Additional fill placed above the pipe then works against the pipe peaking.

2.6.4 Numerical modeling of wheel loads

Pipe design and analysis conveniently lends itself to plane strain analysis, in which the third dimension (parallel to the pipe) is ignored and the system can be designed two dimensionally. This works because typically there is no differential strain in the longitudinal direction to generate stresses. The pipe is assumed continuous and the loads applied to the pipe do not vary along the length of the pipe.

However, for the case of a point or wheel loads on the pipe a plane strain may not be appropriate. Discrete loads, such as wheel loads or foundations, or variations in soil stiffness in the longitudinal direction of the pipe can create strains and deflections in the longitudinal direction. There are a number of ways that have been used to approximate a surface area load as a continuous load. Both the Boussinesq and trapezoidal distribution of forces have been used to

generate continuous surface loads that generate the same load at the crown of the pipe as the peak load due to the load area of the wheel. This is a good approximation for most pipe conditions and is convenient for the numerical analysis of pipe, as the generation of the mesh and the analysis itself is much quicker. Many numerical analyses have been successfully run with this method. Katona et al. (1976) suggested using the Boussinesq to approximate surface loads and Duncan (1979) used the Boussinesq approximation for the development of the Soil-Culvert Interaction (SCI) method.

For some conditions a more exact analysis may be warranted. New more powerful analysis programs have increased the ease and speed of three-dimensional analysis. Both the pipe and load, can be analyzed in the third dimension parallel to the pipe. When using a three dimensional analysis program it is important to consider the approximation of the model. The pipe system can be built with all of the corrugations or profiles or approximated as a plate similar to approximating the pipe as beam elements in a two dimensional model. When modeling pipes as an equivalent plate it is important to recognize that the pipe likely has unique plate stiffness parallel and perpendicular to the axis of the pipe.

2.6.5 Numerical modeling of plastic pipes

As discussed in the previous sections on plastic pipe design the plastic material and width to thickness ratios of the components of the pipe wall add some unique obstacles to a numerical analysis. Brown and Lytton (1984) showed with the CANDE software that the pipe deflection of plastic pipes could be estimated by numerical methods. Brown and Lytton (1984) used a two

dimensional numerical model with non-linear pipe and soil elements with a fully bonded interface. They demonstrated that the soil properties were more important with flexible pipes. Moore (1994) used numerical modeling to simulate experimental parallel plate load tests on a profiled wall pipe. A three dimensional model, including all pipe wall components, was compared with the analysis of a thin circular ring or shell assumed in most designs. Moore (1994) also used a linearly visco-elastic element and geometric non-linearity during his numerical analysis. Moore (1994) showed that a linearly viscoelastic material model worked reasonably well when simulating the parallel plate load test, and he confirmed that the resulting strain in the extreme fiber of the pipe section was within five to fifteen percent as estimated by Equation 2.11 or similar approximation. Moore also concluded that the thin ring theory approximation worked reasonably well, but that the method could not be used to predict longitudinal loads that were generated in the liner of the pipe.

Dhar and Moore (2006) verified the validity of a two-dimensional finite element model for profile-wall pipes by comparing an analysis to the results of a laboratory test (Dhar et al. 2004). The laboratory results were also compared to simplified design methods. In the numerical analysis the authors used a secant modulus of the plastic pipe based on a time of 6 hours. Two dimensional beam-column elements were used for the analysis, and their bending and axial stiffness were set equivalent to profile wall HDPE and ribbed PVC pipes. The two dimensional analysis worked well in determining pipe deflections and strains in the pipe, and the non-linear soil model used was the most important parameter for creating an accurate model. The results are not an exact representation of strain distribution in the pipe wall, but can give a good estimate at the extreme fibers. Dhar and Moore (2006) described modeling the pipe wall in

axis-symmetric numerical analysis for a more accurate determination of local bending effects in the pipe wall.

As part of the literature review Table 2.1 was compiled and represents a few of many reviewed publications that discuss and provide the results of numerical analysis for buried pipes and conduits. This table is a list of papers that had thorough discussions and explanations of the methodologies used when constructing the numerical models or papers that have been impactful to the research of buried pipes. Although not exhaustive Table 2.1 does give an insight into the methodologies generally adopted by most buried pipe and conduit researchers.

Duncan (1979) stated plainly that the incremental construction and nonlinear soil behavior must be used when trying to replicate field conditions. The literature review supports this statement as many of the analyses have incremental construction, nonlinear soil types. Fully-bonded interfaces are used more often in the numerical analyses of buried pipes as opposed to using interface elements. It can be seen many times that a two-dimensional analysis of the three-dimensional pipe profile is often adequate for research.

Table 2.1 Reviewed Numerical Models Methods for Buried Pipes

	Pipe Material	Non-Linear Geometry	Fully Bonded Interface	Interface Elements	Incremental Construction	Elastic Soil Elements	Non-Linear Soil	Elastic Plastic Soil	Non-Linear Pipe Elem.	Two Dimensional model of complex pipe wall
Arockiasamy et al. (2006)	HDPE, PVC, CSP		✓			✓				✓
Bathurst and Knight (1998)	SSP			✓			✓			
Bishop and Lang (1984)	FG	✓	✓		✓		✓			✓
Brown and Lytton (1984)	HDPE		✓				✓		✓	✓
Dhar and Moore (2006)	HDPE		✓					✓		✓
Dhar et al. (2004)	HDPE		✓				✓	✓		✓
Duncan (1976)	CSP		✓		✓		✓			
Duncan (1978)	CSP		✓		✓		✓			
Duncan (1979)	CSP		✓		✓		✓			
Duns and Butterfield (1971)	NA		✓			✓				
Fernando and Carter (1998)	NA		✓			✓				
Hafez and Abdel-Sayed (1983)	CSP			✓	✓		✓			
Hashash and Selig (1990)	HDPE		✓		✓		✓			
Jeyapalan, and Abdelmagid (1984)	HDPE				✓		✓			
Jeyapalan (1983)	HDPE		✓		✓		✓			✓
Jeyapalan et al. (1987)	HDPE		✓		✓		✓			
Kang et al. (2008)	CSP		✓		✓		✓			
Katona (1990)	HDPE		✓		✓		✓			✓
Kennedy et al. (1988)	CSP			✓	✓		✓			✓
McGrath (1998)	CSP,HDPE, FG, RCP		✓	✓	✓		✓			✓
Moon et al. (2010)	CSP		✓		✓		✓	✓		✓

	Pipe Material	Non-Linear Geometry	Fully Bonded Interface	Interface Elements	Incremental Construction	Elastic Soil Elements	Non-Linear Soil	Elastic Plastic Soil	Non-Linear Pipe Elem.	Two Dimensional model of complex pipe wall
Moore (1994)	HDPE	✓							✓	✓
Moore and Brachman (1994)	CSP		✓			✓				
Moore and Taleb (1999)	CSP, RCP		✓		✓			✓		
Peterson et al. (2010)	HDPE, CSP		✓					✓		
Sargand et al. (2002)	HDPE		✓		✓		✓			✓
Suleiman et al. (2003)	HDPE	✓	✓			✓	✓			✓
Taleb and Moore (1999)	CSP, RCP		✓		✓			✓		
Zaman and Lagurus (1990)	NA			✓	✓					

Notes: FG – Fiber Glass, HDPE - High Density Polyethylene, CSP – Corrugated Steel Pipe, SSP – Stainless Steel Pipe

2.7 Geosynthetics

2.7.1 Geosynthetic Functions

Geosynthetics are man-made materials placed in the earth used to enhance soil properties for engineering applications. Geosynthetics are generally fabricated sheets of plastic materials which are resistant to degradation in the soil. Geosynthetics are manufactured in a variety of ways and come in a wide range of configurations. Each geosynthetic type often has functional advantages depending on how the geosynthetic is fabricated. The functions of geosynthetics are generally broken down into five primary ones (Koerner 2005): separation, reinforcement,

filtration, drainage, and containment. Soil reinforcement, which can be further broken down into confinement, shear resistance, membrane action, and anchorage, is the primary function of interest for this study.

Membrane action and confinement are important reinforcement functions when considering base courses and wheel loads. The flat sheets of geosynthetic have little or no bending capacity but have comparatively great tensile capacity. Geosynthetic membranes can be used to bridge voids as shown by Giroud et al. (1990) (Figure 2.14). For wheel loads it was determined that considerable vertical deflection, or rutting, of the cross section was required for the geosynthetic to develop a tension membrane effect exclusively (Giroud and Noiray, 1981). It was established (Giroud et al. (1985), Giroud and Han (2004a and 2004b)) that confinement, which is the lateral restraint of the soil by the geosynthetic, was a critical aspect of base course reinforcement (Figure 2.15). The following review demonstrates the innovative ways that other researches have used geosynthetic materials to protect pipes and other buried structures.

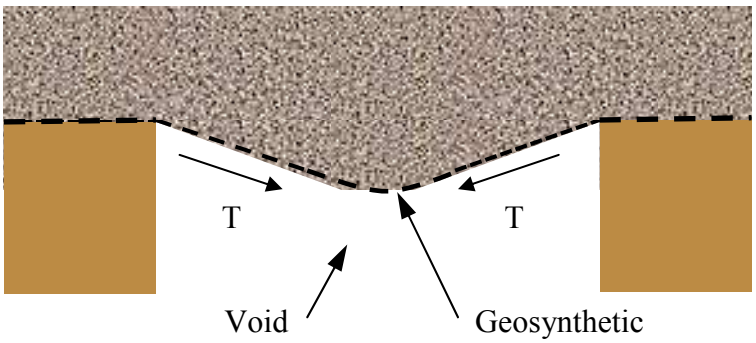

Figure 2.14 Geosynthetic Tension (T) Membrane and Anchorage over a Void

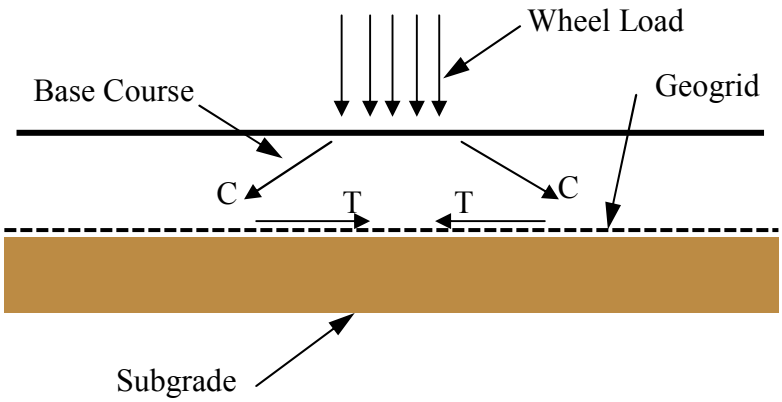

Figure 2.15 Geosynthetic Confinement of a Base Course Showing Tension (T) and Compression (C) Forces

2.7.2 Geosynthetics in Pipe Applications

The literature study revealed several methods of applying geosynthetics with pipe systems, which have been previously used and investigated. The pipe protection research is grouped here into methods of reinforcement including: trench reinforcement, reinforcement for static and repeated loads, utility cut repair, and protection from penetrating loads. Most of the previous research found was limited to model testing, small scale testing, and numerical modeling. Only a few examples of full scale testing or case studies are available. After a description and brief discussion of the previous studies a synopsis of the geosynthetic reinforcement method will be presented.

Trench Reinforcement

Jeypalan (1983) investigated the use of geosynthetic layers along a trench wall (Figure 2.16) to reduce the deflection and bending strains for pipes buried in soft in-situ soil. Jeypalan (1983) had previously studied flexible plastic pipes in varying backfill stiffness. By increasing the overall stiffness at the springline, Jeypalan (1983) showed with numerical analysis, that the pipe performance could be increased to a degree, comparable to improving the quality of the backfill. This would potentially give pipe designers options in addition to increasing the pipe stiffness or providing higher quality backfill. The improved lateral support for the flexible pipe decreased the pipe deflections and pipe wall moments. The inclusion of geosynthetics did increase the axial force in the pipe wall, which was foreseeable, as the stiffer backfill increased "ring compression".

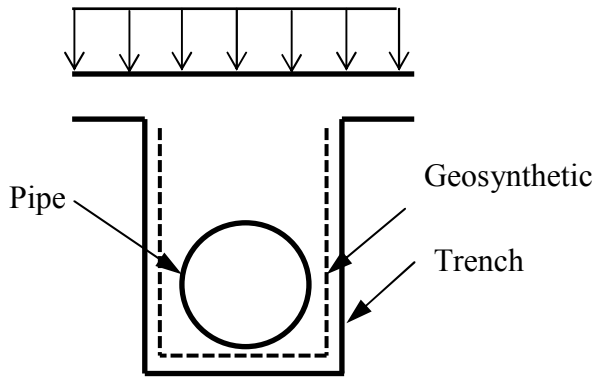

Figure 2.16 Trench Reinforcement for Flexible Pipes (Jeypalan, 1983)

Reinforcement for Static Loads

Kennedy et al. (1988) performed model tests and numerical analysis on reinforced soil-steel bridges, which are a variation of the buried conduit. In soil-steel bridges, the corrugated steel plates that form the span are usually founded on footings and the span to depth of the arch is much greater than a conventional buried pipe. The height of cover is also generally small compared to the span that is wide enough to form a "bridge". In the study, the authors reinforced the layers of the backfill similar to a mechanically stabilized earth retaining wall (Figure 2.17), by attaching steel strip reinforcement to the conduit wall.

In addition to an unreinforced soil-steel bridge, continuous reinforcement above the crown of the arch was excluded in one case, and included in two other cases of varying cover. The authors showed that reinforcing the backfill reduced deflections and increased the shear strength in a manner similar to a geosynthethic reinforced retaining wall. The authors also demonstrated that the redundancy of the system was increased, specifically by including the reinforcement above the soil-steel bridge, significantly reducing the chances of a sudden catastrophic failure.

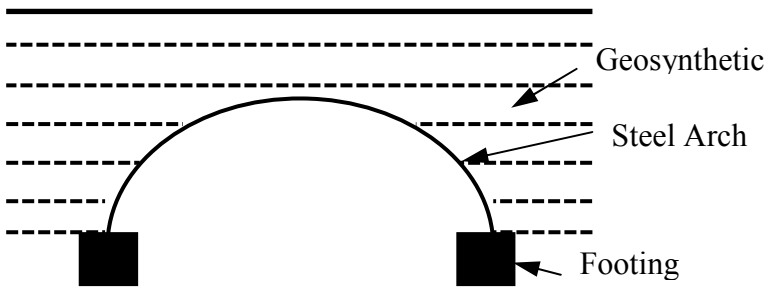

Figure 2.17 Soil-Steel Bridge with Reinforced Backfill (Kennedy et al., 1988)

Pearson and Milligan (1991) performed a parametric scale-model study of a single layer of reinforcement, in this case, steel strips over a long-span flexible steel pipe. The long-span pipe is generally defined as a pipe with a high enough span-to-stiffness ratio that the bending stiffness controls the behavior of the pipe. Although visually the graphic of the test model (Figure 2.18) appears to represent a conventional buried pipe, the investigation was more similar to the research of Kennedy et al. (1988) based on the factors controlling the design of the pipe, bending and deflection at the crown. The height of cover was varied from 1/8 to 1/4 of the span, and the height of the reinforcing layer varied from right on the crown, to the top of the cover. The width of the reinforcement was limited to the span (diameter) of the pipe. The load was applied to a 32 mm wide footing, which was also as long as the pipe, until the pipe soil system failed. It was found that, for a cover of 1/4 the span of the pipe, the optimum location was right at the crown of the pipe and the reinforcing effect diminished with increased height of reinforcement above the crown of the pipe. At the optimum location of the reinforcement, the pipe saw an ultimate capacity increase of 25% and a maximum bending strain and deflection reduction of 50%.

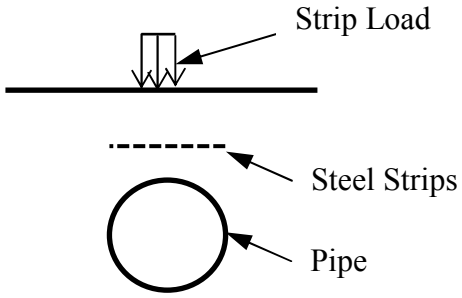

Figure 2.18 Single Reinforcement Layer over a Pipe (Pearson and Milligan, 1991)

As part of a study on geogrid reinforcement of unpaved roads, Bauer (1994) included full scale static load tests on an unpaved roadway condition with a 150 mm diameter steel conduit. The tests for both the unreinforced and reinforced conditions were conducted in a 1.6 m wide by 2 m long sand-filled box. The height of fill over the pipe and the depth of geogrid reinforcement, which covered the entire geotechnical box, were also varied. The static load was applied with a 0.15 m square footing concentrically, directly over the pipe and eccentrically, 150 mm off the center line of the pipe. Bauer (1994) demonstrated a reduction in the pipe and surface deflection due to the inclusion of geogrid.

Kawabata et al. (2003) performed tests in a 2 m wide by 1 m long by 1 m deep sand-filled test pit with a 150 mm diameter aluminum pipe and 450 mm of cover. Three layers of geogrid were placed over the pipe and a uniform load was applied over the entire width and length of the test pit, duplicating an overburden load in a deeply buried condition. 150 mm below the pipe, a movable plate was installed to simulate subsidence below the pipe. After the surface was loaded to 600 kN, the plate below the pipe was lowered 15 mm. The total vertical load on the pipe, as calculated by the prism method, was reduced by 25% by including the geosynthetic layers. Around the pipe, the normal and tangential soil stresses on the pipe were also significantly reduced.

Bueno et al. (2005) investigated combining geosynthetics with the trench condition in an application similar to Marston's early work in which loose fill or compressible materials was placed directly over the pipe to reduce pressures on the pipe. The authors provided a proposed construction method, the "Geovala Method", in which the pipe constructors over-excavate the pipe trench wider above the pipe, and place a geosynthetic in the bottom of the over-excavated trench (Figure 2.19a). The configuration of the geosynthetic develops anchorage which supports

the load of the soil prism with membrane action and improved arching action. The authors suggested a number of backfill conditions can be used, including compacted or loose backfill, and purposefully leaving a gap between the geosynthetic and the pipe. The authors also introduced a similar construction method for embankments where a fabricated channel piece or re-excavation over the pipe acts as the gap for the geosynthetic to bridge (Figure 2.19b).

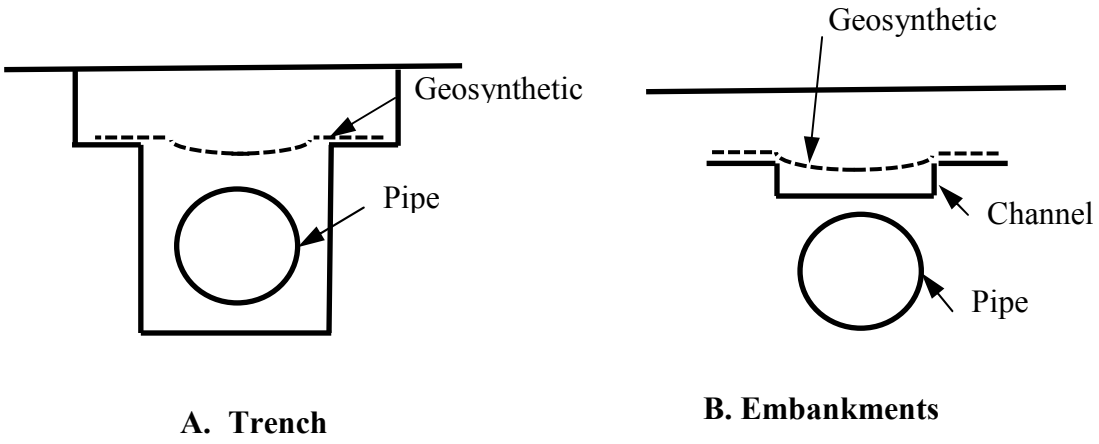

A. Trench **B. Embankments**

Figure 2.19 Geovala Method (Bueno et al, 2005)

Bueno et al. (2005) provided data on a large scale test they performed for a trench condition constructed with their proposed method. A 400 mm diameter pipe was placed in a narrow trench and the over excavation was widened to 600 mm. No backfill was placed in the trench below the geosynthetic layer. Three different non-woven geotextiles were placed in three separate tests and a fill height of 200 mm was placed above the geosynthetic. A standard trench condition was also monitored. Uniform pressures were applied directly to the surface with an air filled bladder. An earth pressure cell measured the pressures above the pipe. In all cases with the proposed construction method, the earth pressures above the pipe were approximately half the standard trench condition.

Bathurst and Knight (1998) performed a series of numerical analysis of geocell geosynthetic reinforcement over long-span culverts. Based on calibrations of full scale and reduced-scale tests, the authors were able to model the 0.2 m thick geocell reinforced soil as a composite material in a two-dimensional plane strain analyses of the pipe and backfill. The 7.62 m diameter pipe with varying heights of cover, from 1 to 0.4 m, was loaded with a 0.2 m wide concentrated load. Analysis of long-span pipe with concentric (loaded at mid-span) and eccentric loading was provided. Failure was considered as bearing failure of the soil and flexure in the pipe resulting in buckling of the pipe wall. The authors showed a marked increase in ultimate capacity and remarkable decrease in deflection of the long-span culvert with the inclusion of the geocell.

Rajkumar and Ilamparuthi (2008) ran tests of a 200 mm wide continuous loading plate on a buried 200 mm diameter PVC buried pipe. The tests were conducted with cover heights of 200, 400, and 600 mm. A comparison of the 400 mm cover condition was run with a single layer of geogrid at 200 mm above the crown of the pipe. The reinforced condition saw a pipe vertical deflection of 1.6 mm at 150 kPa versus 2.3 mm at 150 kPa for the unreinforced condition. The vertical and horizontal deflections of the pipe for the unreinforced and reinforced conditions were similar up to a pipe deflection of about 0.2% of the diameter; the deflections then linearly diverged and were smaller for the reinforced condition. Although the deflections were small (approximately 1% of the diameter), at the maximum applied load the vertical and horizontal deflection of the pipe for the reinforced condition decreased approximately 33% with respect to the unreinforced condition.

Reinforcement for Dynamic Loads

Lundvall and Turner (1997) investigated settlement of roadways over culverts and methods of avoiding this condition. The authors experimentally investigated methods including using geosynthetic reinforced soil for mitigating rutting and settlement over culverts. The tests were run in a 1.4 m by 1.7 m by 1.5 m tall test box. The authors performed model tests on a 200 mm corrugated metal pipe in a uniform clay backfill with the same clay acting as 204 mm of cover. An unreinforced condition and a reinforced condition were run with one layer of geogrid at 102 mm above the pipe. A dynamic load of 16 kN was applied with a 660 mm by 364 mm loading plate at a frequency of 0.204 Hz. The clay was placed in 100 to 120 mm lifts at maximum dry density and optimum moisture content. Results from the cyclic loading tests indicated no appreciable improvement of surface settlement as compared to the unreinforced condition, and for both cases the surface settlement increased with more cycles, indicating that the system was "unstable" and prone to rutting.

Moghaddas Tafreshi and Khalaj (2008) performed laboratory and analysis on small diameter (110 mm) High Density Polyethylene (HDPE) pipes subjected to repeated loads replicating as traffic conditions or similar cyclic loads. The height of fill above the pipe varied from 165 to 330 mm, and the fill above the pipe was reinforced with one to five equally spaced layers of geogrid (Figure 2.20). The densities of the sand backfills were varied in tests at 42%, 52%, and 72%. The width of the geosynthetic cover was 4.5 times the diameter of the pipe, and for the single layer of geosynthetic the width varied from 1 to 5 times the diameter of the pipe. Control runs without geogrid reinforcement were also performed. The dynamic load was applied as 540 kPa pressure on a 100 mm plate at a frequency of 0.3 Hz to simulate heavy traffic loads.

The surface settlement was monitored with a linear variable displacement transducer (LVDT) and the pipe diameter was monitored with an additional eight displacement transducers at the invert crown, springline and quarter points between. Overall, a comprehensive array of 86 tests was run. Moghaddas Tafreshi and Khalaj (2011) expanded on the 2008 research by varying the amplitude of the applied pressure from 550 kPa to 400 kPa and 220 kPa.

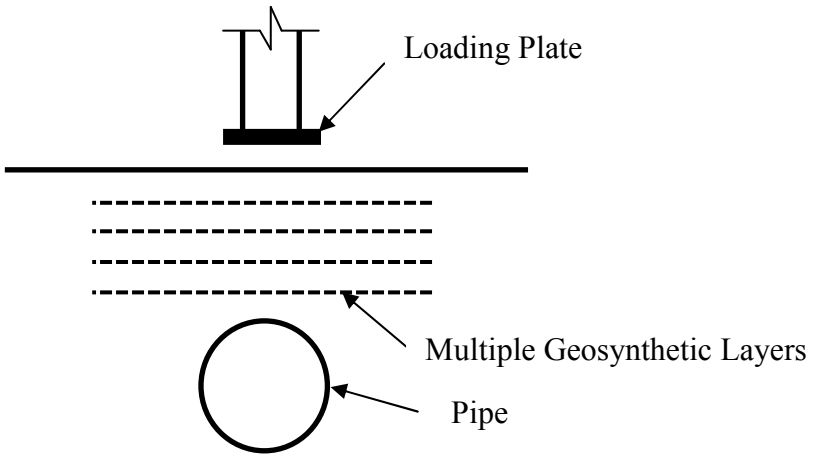

Figure 2.20 Dynamic Load Tests (Moghaddas Tafreshi and Khalaj, 2011)

The authors found that increasing the number of geosynthetic layers, increasing the relative density of the soil, and increasing the depth of cover improved, or decreased, the final surface settlement and the vertical pipe deflection. Maximum deflections were in the vertical axis because of the concentric loads and the rate of deformation decreased with the number of cycles. There was a significant reduction of the surface and pipe deflection with the inclusion of geosynthetic, specifically in lower density sands.

Utility Cut Repair

Kazemian et al. (2010) provided a case study of the use of geosynthetics to remediate improperly backfilled trenches that were also subjected to traffic loading. The original construction consisted of a 1 m wide trench by 3 m deep trench constructed below a roadway. Remediation of the roadway with the geogrid was performed only at two manholes spaced every 100 meters. An unreinforced (control) section was monitored in addition to two locations with two different geogrids. At the locations of the manholes the trench was 2 meters wide. Sand was placed up to the crown of the pipe (approximately 50 mm), in-situ soil was placed into the trench up to 1.25 m below the surface, and the remainder of the fill was crushed gravel. Finally a 20 mm thick base course of crushed rock and a 50 mm layer of asphalt were used. In locations where the geogrid layers were used, the 24 m wide geogrid reinforcement was placed directly on the base course centered over the pipe and manhole. The surface settlement was monitored at 3 months, 6 months, and 12 months. After monitoring, the authors stated that there was no visual distress in the reinforced section while there were visible settlements in the unreinforced section. Measured reductions in the displacements of the reinforced sections, at the end of 12 months, as compared to the unreinforced section were in the range of 40 - 50%.

Protection from Penetrating Loads

Palmeira and Andrade (2010) proposed and performed full scale tests of the protection of buried pipes using geosynthetics (Figure 2.21). In their tests 75 mm diameter pipes were buried

with 150 mm of cover and geosynthetics with varying configurations; single layer, inverted U and complete envelopment around the pipe. The depth of the geosynthetic was placed at 75 mm for all reinforced conditions and additionally in a separate test at 37.5 mm. Penetrating loads in the form of a 20 mm thick continuous plate were used to simulate excavation or similar equipment. The inclination and location of the penetrating load were also varied.

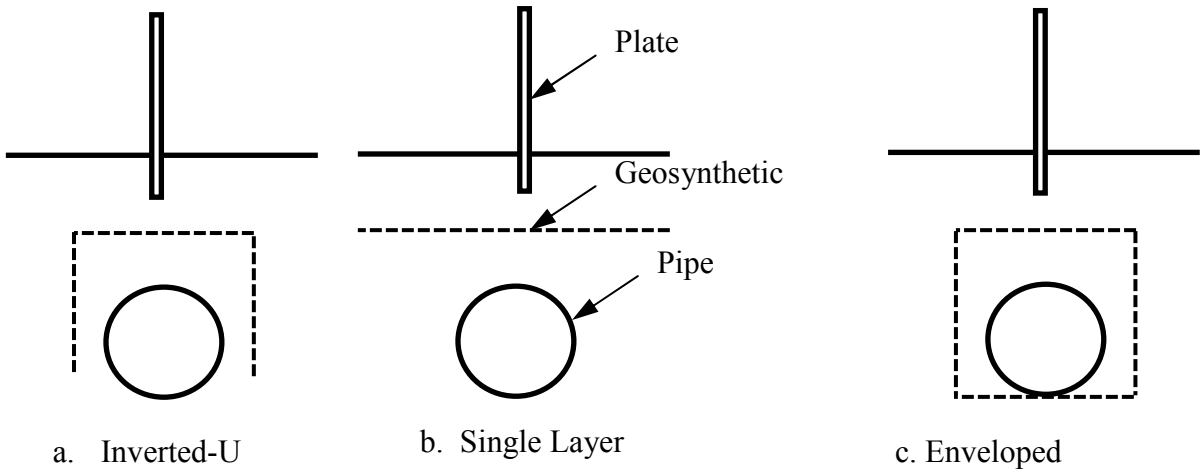

Figure 2.21 Geosynthetic Protection of Pipes from Penetrating Loads (Palmeira and Andrade, 2010)

Plate penetration, earth pressures around crown invert and springline, and pipe strains on the crown invert and springline were monitored. In the full scale tests, the pipe strains were reduced, pressures on the pipe were reduced for the envelopment condition, and most significantly, the force required to achieve the same amount of plate penetration as the unreinforced condition was significantly higher.

Reinforcement Summary

Many of the reinforcement methods used multiple functions, but an attempt has been made to segregate them here. Table 2.2 provides a breakdown of each reviewed study and the geosynthetic effects to improve the performance of the pipe.

In a few of the studies it was clear which geosynthetic effect improved the pipe and soil. For instance in the Bueno et al. (2005) and Kawabata et al. (2003) studies the geosynthetic acted as a tensioned membrane over the pipe reducing the load. The Kennedy et al. (1988) study was unique in that the geosynthetic was used to improve the shear capacity of the block of soil around the pipe, and act as an anchor with the geosynthetic attached to the pipe wall. A large portion of the studies were for the attenuation of the wheel or other small loads over the pipe. In some cases, such as Bauer (1994), Moghaddas Tafreshi and Khalaj (2008), and Rajkumar and Ilamparuthi (2008), the geosynthetic was used to confine the soil particles to reduce surface and pipe settlements. In these cases (Bathurst and Knight, 1998; Pearson and Milligan, 1991), there was not always a clear distinction between confinement and tensioned membrane effects of the geosynthetic, and in many cases there was indication that the improvement of the system was the result of both effects.

Table 2.2 Buried Pipe Reinforcement by Geosynthetic Effects

	Membrane and Anchorage	Confinement	Shear Reinforcement
Bauer (1994)		✓	
Bathurst and Knight (1998)	✓	✓	
Bueno et al. (2005)	✓		
Jeypalan (1983)	✓	✓	
Kawabata et al. (2003)	✓		
Kazemin et al. (2010)	✓	✓	
Kennedy et al. (1988)	✓		✓
Lundvall and Turner (1997)	✓	✓	
Mogohaddas Tafreshi and Khalaj (2008)		✓	
Palmeira and Andrade (2010)	✓	✓	
Pearson and Milligan (1991)	✓	✓	
Rajkumar and Ilamparuthi (2008)		✓	

2.8.0 Summary

Based on the literature review a few comments can be made on the state of research with respect to geosynthetic protection of underground pipes. This assessment and an understanding

of pipe and geosynthetic behavior can be used to deduce which area of pipe design is best suited for a further study. It is also important to recognize the numerical study will be calibrated on full scale laboratory tests, and as such the study will be restricted by the ability to make reasonable conclusions and predictions from those full scale tests.

There appeared to be three basic methods of using geosynthetic with respect to pipes; attenuation of surface loads, attenuation of the soil prism load, and reinforcement of the backfill around the pipe or soil-steel bridge. For attenuation purposes the geosynthetic is placed between the pipe and the surface or near surface load and also used to support the soil prism above the pipe. The method of attenuation of the surface load was attained by both the tensioned membrane and anchorage methods (Bueno et al., 2005) and confinement of the backfill (Bauer, 1994) or a combination of these two. For the reinforcement of the backfill the geosynthetic is placed around the pipe in addition to that above the pipe. There is some overlap between the three effects, and for design purposes it may be helpful to make a rational distinction between them if possible.

The full scale tests used to calibrate the models will be on a moderately sized pipe, 0.61 m in diameter, in a fairly shallow condition (less than 2 m). The pipe will be a steel reinforced high density steel pipe (SRHDPE). Because of this it was decided to concentrate on the attenuation functionality for near surface loads.

For the attenuation of near surface loads the geosynthetic is used to reduce pressure and pipe deflections, which in turn reduces thrust and local bending stresses in the pipe wall. The limit states of thrust failure, buckling failure, or even the deflection limitation will not be reached in these experiments, but it can still be ascertained if there is a benefit from the geosynthetic in

reducing strain in the pipe wall and reduction of deflection. Also secondary benefits normally associated with geosynthetic inclusion, such as rut reduction, can improve the long term performance of the pipe and soil pipe system.

Based on the reviewed literature it was apparent that for near surface loads the response of the system is not a plane strain condition and an analysis in the third dimension is necessary and could be enlightening. Also from the review it was decided that a non-linear plastic soil model would provide the most accurate model to simulate the experimental tests.

Chapter 3 Laboratory Tests

3.1 Overview

Calibration of the numerical models in the following chapters is based on full-scale static plate load tests. In conjunction with the full-scale plate load tests on steel reinforced HDPE (SRHDPE) pipes performed by Khatri (2012), additional static plate load tests were run with geosynthetics placed over the pipe. This test setup simulates a small footing or the application of a wheel load on a pipe in a trench condition with 0.61 m of fill cover. The purpose of the previous work was to investigate the behavior of shallowly buried SRHDPE pipes subjected to surface loads. The geosynthetic was added to investigate the resulting reduction of stress and strain in the pipe and settlement at the surface of the soil as compared to the tests run for the unreinforced section. Following is a synopsis of the laboratory work performed followed by an analysis of the data and conclusions.

Tests were run in a 3 m wide by 2 m long by 2 m deep box at the Department of Civil, Environmental, and Architectural Engineering at the University of Kansas. The load was controlled and monitored by an integrated actuator, hydraulic pump, and software package. The actuator had a maximum 245 kN capacity. The box was extended from a width of 2 m to 3 m specifically for the pipe tests.

For the initial full scale investigation the materials used were chosen based on common conditions in the state of Kansas, available materials, and homogenous soils with known

properties. A 0.61 m diameter 2 m long steel-reinforced SRHDPE pipe was centered in the 3 meter width of the box. The pipe was placed in a 1.22 m wide by 1.14 m deep trench created in a fat clay (CH). Kansas River sand and crushed stone aggregate were used as backfill material in the trench. Finally a compacted well graded gravel (or Kansas River Sand) was used as a top layer to create a base course. The resulting typical cross section of the test is shown in Figure 3.1. Subsequent tests were run by varying the geogrid reinforcement and changing the base course. After each test the base course and backfill in the trench were removed and replaced.

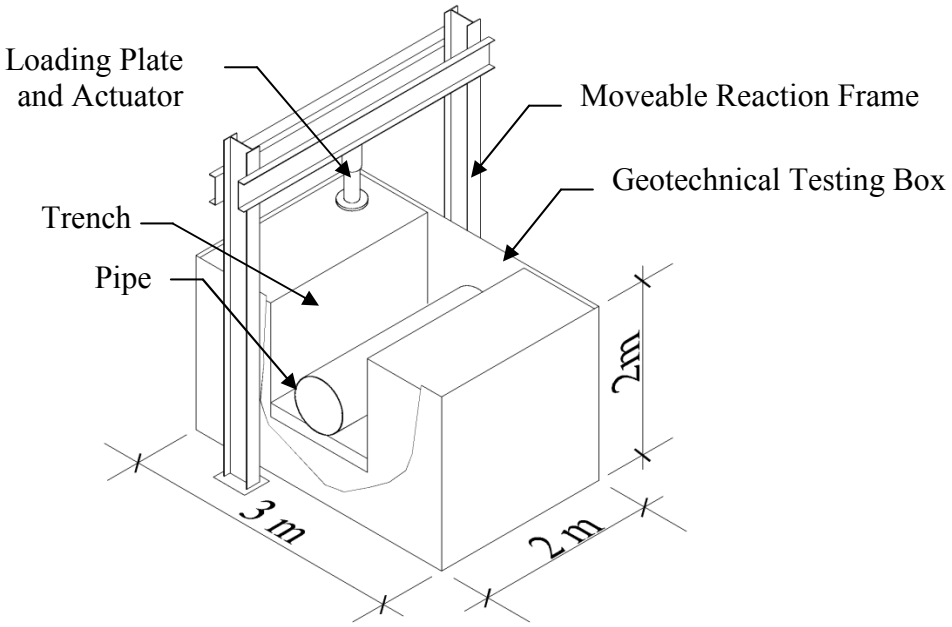

Figure 3.1 Test Pipe Buried in the Big Box

The full scale tests, with and without, the geogrid were run in this study and their results were documented. Geogrid, one type of geosynthetic, was proposed to reduce deflections and

strains of pipes in the test section and reduce settlements in the soil prism above the pipes. The following discussion covers the test set up and the results.

3.2 Steel-Reinforced HDPE Pipe

3.2.1 Pipe Materials

The pipe used for the full-scale tests was a 0.61 m diameter helically-wound SRHDPE pipe. The pipe consisted of an HDPE shell with 13 mm by 1.5 mm steel ribs outstanding from the pipe wall. Each outstanding rib was 25.4 mm on center and encapsulated in HDPE which is integral with the pipe wall. The pipe material properties are shown in Table 3.1.

Table 3.1 Pipe Structural Properties

(Provided by the Manufacturer)

Nominal Pipe Diameter (m)	0.61
Moment of Inertia (Steel Only) (mm^4/mm)	10.5
Modulus of Elasticity Steel E_s (GPa)	200
Steel Yield Strength F_y (MPa)	522
Pipe Wall Area (Steel Only) (mm^2/mm)	0.752
Modulus of Elasticity HDPE E_p (MPa)	441

Khatri (2012) completed parallel plate load tests on the SRHDPE pipe and the results from a typical test are shown in Figure 3.2. Calculating the pipe stiffness (PS) from the parallel plate load tests at a 5% vertical deflection (30.5 mm) yields a stiffness of 295 kPa. Comparatively if the pipe stiffness is calculated by the elastic solution (Equation 2.2) the resulting pipe stiffness is calculated as 478 kPa, demonstrating that the elastic solution does not fully capture the geometric non-linearity and material non-linearity observed in the parallel plate load test.

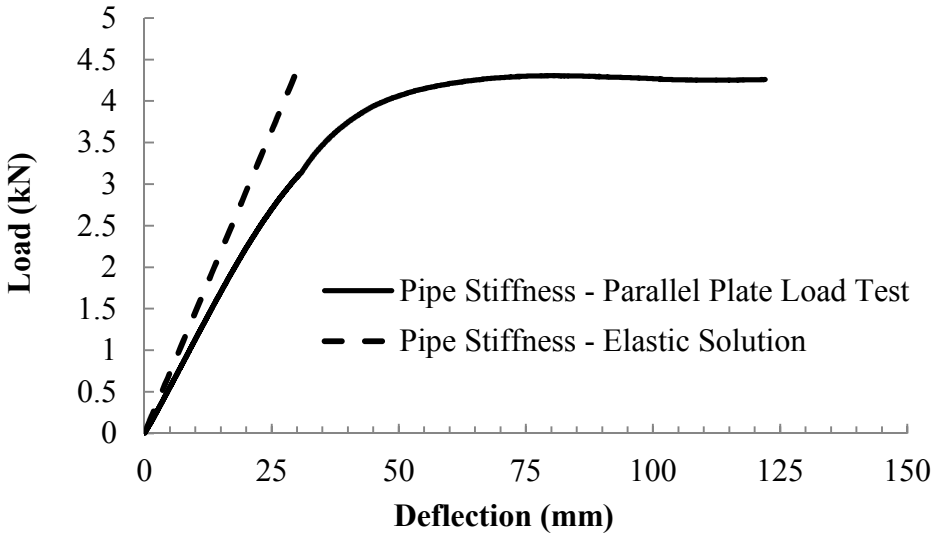

Figure 3.2 Parallel Plate Load Test for 610 mm Diameter SRHDPE (Khatri, 2012)

The pipe used for analysis in the succeeding sections of this dissertation, including the numerical and laboratory tests, is the described SRHDPE pipe. Currently this pipe is a fairly new technology, and an important aspect of this dissertation is the performance and behavior of the pipe selected. A comparison of published pipe stiffness values for HDPE, corrugated steel

pipe (CSP), and reinforced concrete pipe (RCP) to the pipe stiffness for the SRHDPE pipe is shown in Figure 3.3.

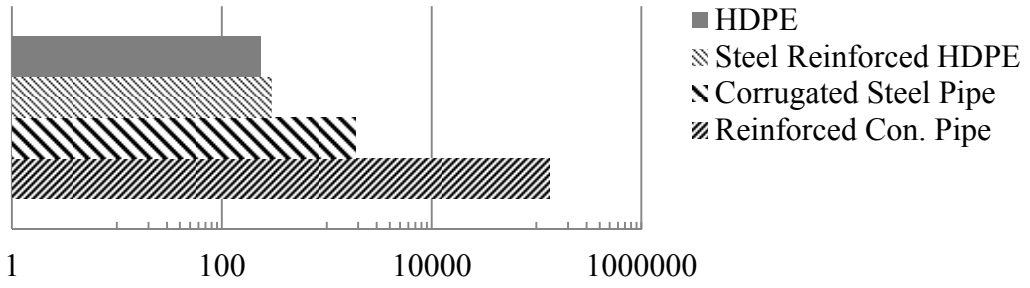

Figure 3.3 Pipe Stiffness (PS) of Different Types of Pipe

It can be seen from the graphic that the SRHDPE pipe stiffness, as measured by the parallel plate loading test, is most comparable to the HDPE pipe. It is important to note however, that the parallel plate loading is primarily a representation of the bending stiffness of the pipe. As discussed in Section 2.3.3, the vertical arching of soil is also dependent on the axial stiffness (hoop stiffness) of the pipe wall. The steel reinforcing of the pipe wall is a magnitude of order greater in stiffness than the HDPE. It is expected that with a well compacted backfill the buried pipe will behave more like a corrugated steel pipe.

3.2.2 Pipe Instrumentation

Two displacement transducers were placed at the center of the pipe directly under the loading plate to measure the relative displacements of the crown, invert, and springline. One transducer was placed vertically to measure the vertical displacements of the pipe, while the second transducer was placed in a horizontal position to measure horizontal displacements of the pipe section. A third displacement transducer was placed vertically at the center line of the pipe, 0.30 m longitudinally from the loading plate. The three displacement transducers DT 1, DT 2, and DT 3 can be seen in Figure 3.4. A tell-tale was attached to the crown of the pipe to measure the movement of the crown of the pipe in relation to a stationary datum.

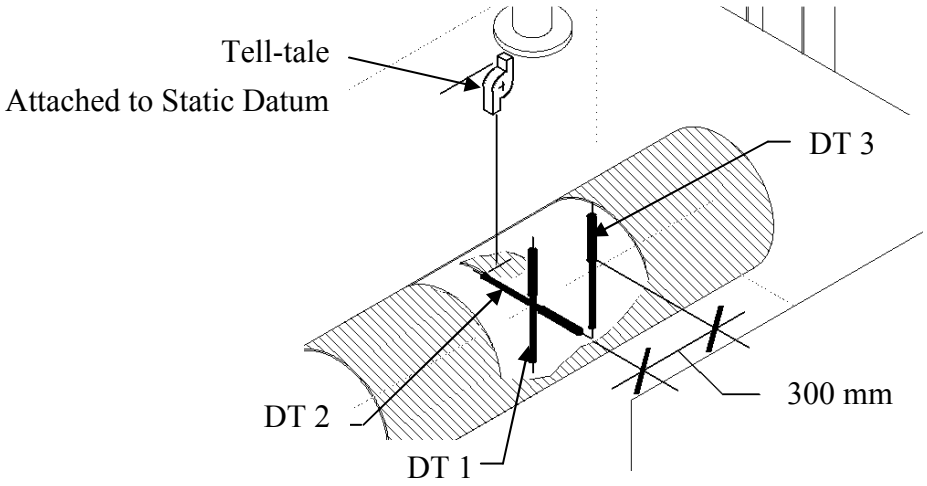

Figure 3.4 Displacement Transducer setup

Strain gauges were placed around the pipe to monitor the strains in the pipe wall during construction of the test section and during loading. The manufacturer's specifications show that

this type of strain gauge has accuracy of 1μ or 0.0001%. Strain gauges were placed at the invert, crown, and the springline of the pipe, directly under the loading plate. The circumferential and radial strain gauges were placed on both sides of the outstanding steel and plastic portions of the ribs, while the longitudinal strain gauges were placed on the inside and outside of the pipe wall. A section of the pipe wall with strain gauges can be seen in Figure 3.5.

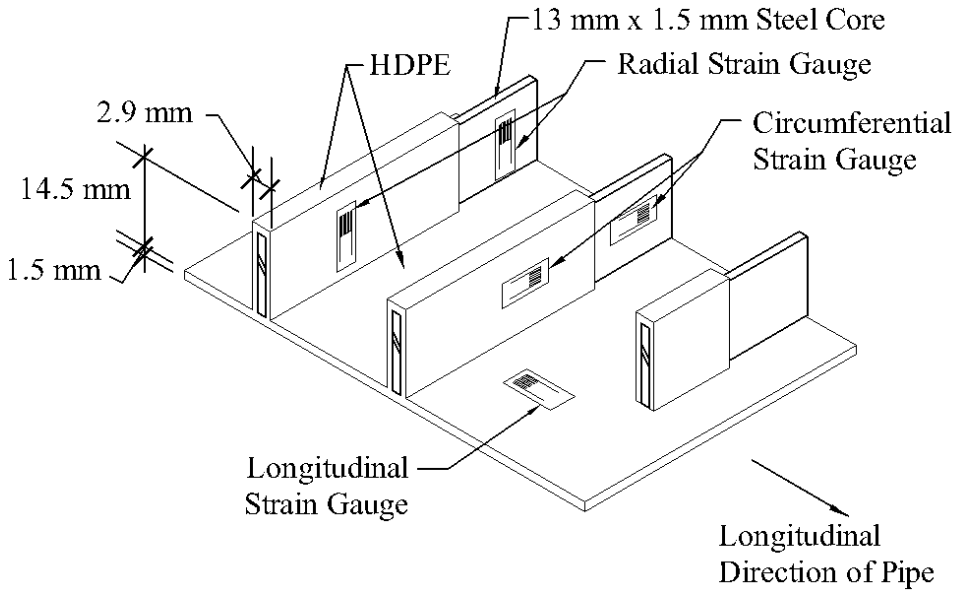

Figure 3.5 Pipe Wall Section and Strain Gauge Orientation

Twenty five strain gauges were placed on the pipe in the radial (R), the circumferential (C), and Longitudinal (L) directions. All strain gauges were placed within 25 mm of the longitudinal centerline of the pipe, directly under the loading plate. Since the pipe is a composite material the strain gauges were placed on the steel (Figure 3.6A) and the plastic covering (Figure 3.6B). In the longitudinal direction there is no steel and the strain gauges were placed on the plastic only (Figure 3.7).

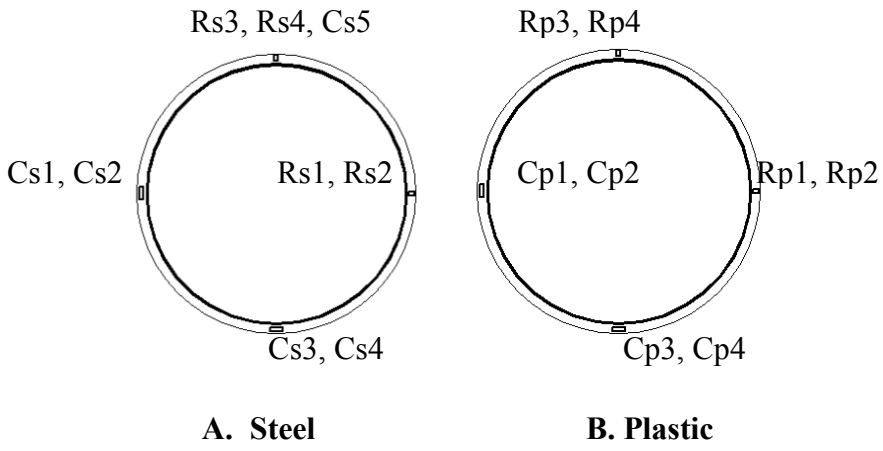

Figure 3.6 Circumferential and Radial Strain Gauge Locations

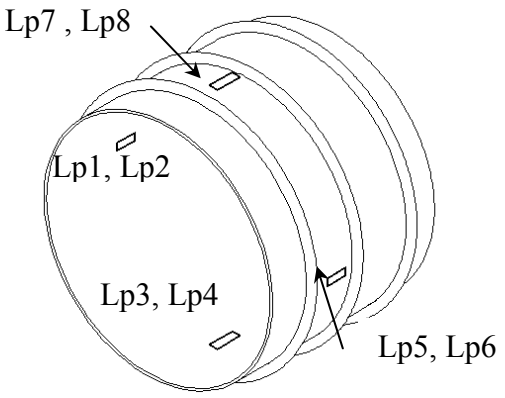

Figure 3.7 Longitudinal Strain Gauge Locations

3.3 Subgrade

The soil in which the pipe and backfill were placed was a fat clay (CH). The fat clay is a locally available soil in Kansas and many pipes have been buried in this type of soil. The properties of this subgrade are provided in Table 3.2. Multiple vane shear tests and California

Bearing Ratio (CBR) tests were run on standard proctor test samples to correlate the fat clay CBRs to undrained shear strengths.

To avoid the need for excavation of a trench in the laboratory, the trench was built from the floor of the box up. A 0.46 m thick fat clay layer was laid across the width of the box. Each side of the trench was shored with plywood walls, and the remainder of the fat clay was placed behind the walls. After the clay was placed and compacted, the shored walls were removed leaving a 1.22 m by 1.14 m trench (Figure 3.8). The lifts were placed at a 26 percent moisture content, with a compacted density of 14.5 kN/m^3, Dynamic cone penetrometer (DCP) and vane shear tests were conducted to maintain the uniformity and strength of the fat clay for each lift.

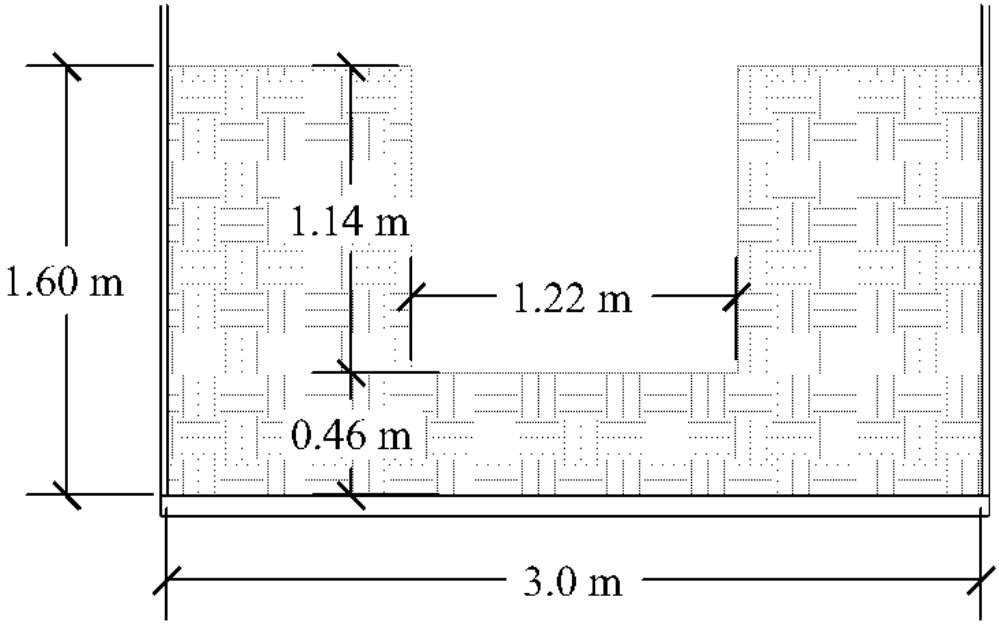

Figure 3.8 Fat Clay Trench

Table 3.2 Fat Clay Properties

	Subgrade
Liquid/Plastic Limit- LL/PL	54/26
Specific Gravity G_s	2.71
Maximum Dry Unit Weight γ_{dmax} (kN/m^3)	15.4
Optimum Moisture Content w_{opt} (%)	24
Unconfined Compressive Strength q_u at As-compacted Density (kPa)	75

3.4 Backfill

3.4.1 Backfill Material Properties

In the large box tests, two backfills were used in the trench; Kansas River sand and a crushed stone aggregate. The sand was chosen as a backfill material for a less than optimal cohesion-less backfill condition, while the crushed stone aggregate was selected as an optimal backfill material. This would give a range of backfill conditions that could be used in subsequent research.

Nine triaxial tests were run on the sand backfill materials at varying densities. Tests for a loose condition, a condition of minimal compaction, and a heavily compacted sample, which had relative densities of 25%, 40% and 77% respectively, were completed. For each density, triaxial shear tests were completed at three confining stresses: 103.4 kPa, 68.9 kPa, and 34.5 kPa. The

deviator strain was applied at a uniform rate of 0.2% per minute. The results of the triaxial tests can be seen in Figures 3.9 through 3.11.

An isotropic compression test was also run on the loose sand condition to capture the bulk modulus of the sand. At the beginning of this test a uniform pressure and equal pressure inside the sample were applied. An external confining pressure was then applied in increments of 13.8 kPa. The change in volume of the test sample was monitored with the burets. An attempt was also made to determine the ratio of plastic volumetric strain to the elastic volumetric strain. At 96.5 kPa the confining pressure was reduced in two 13.8 kPa increments. A positive confining pressure was then applied again in 13.8 kPa steps until a maximum pressure of 151.7 kPa was reached. The results of the isotropic compression test can be seen in Figure 3.12.

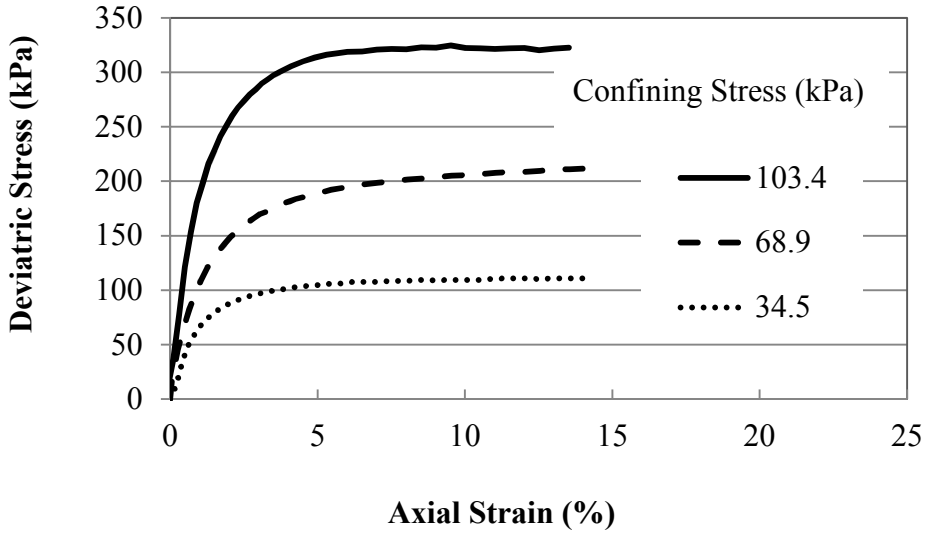

Figure 3.9 Triaxial Compression Test of Sand at D_r = 25%

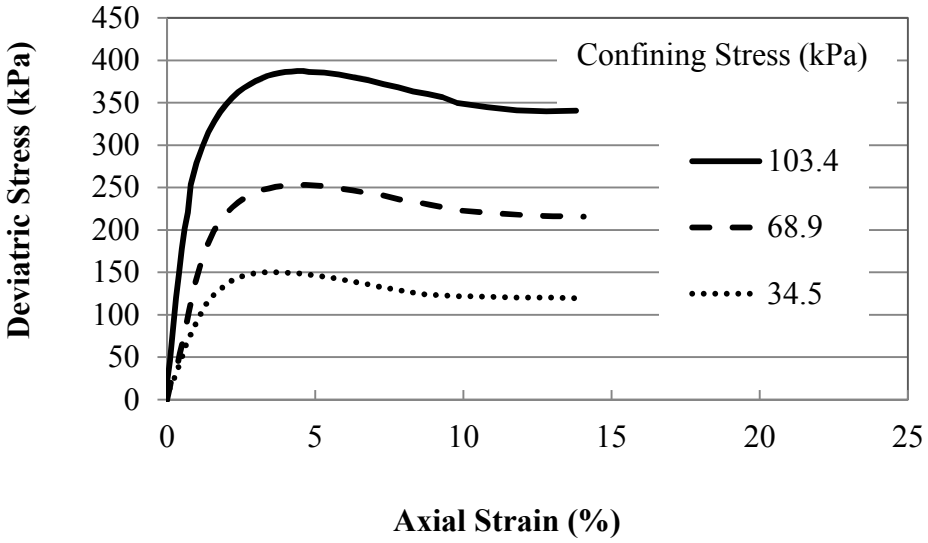

Figure 3.10 Triaxial Compression Test of Sand at D_r = 40%

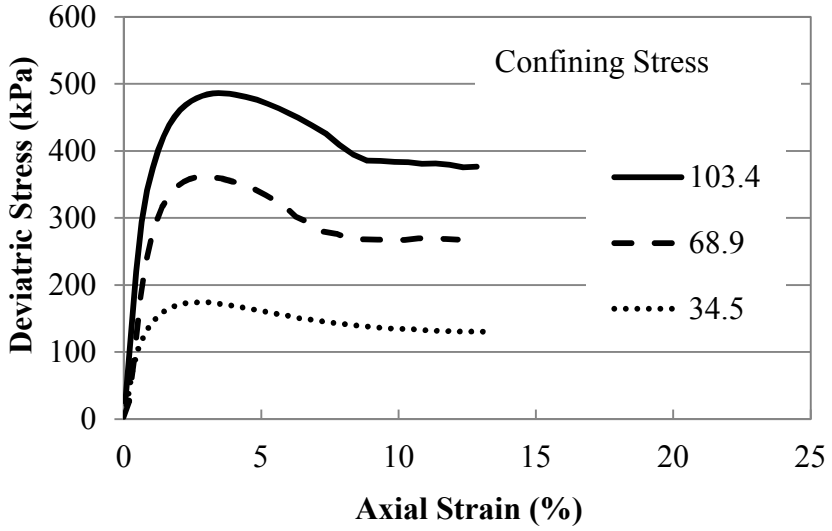

Figure 3.11 Triaxial Compression Test of Sand at D_r = 77% Sand

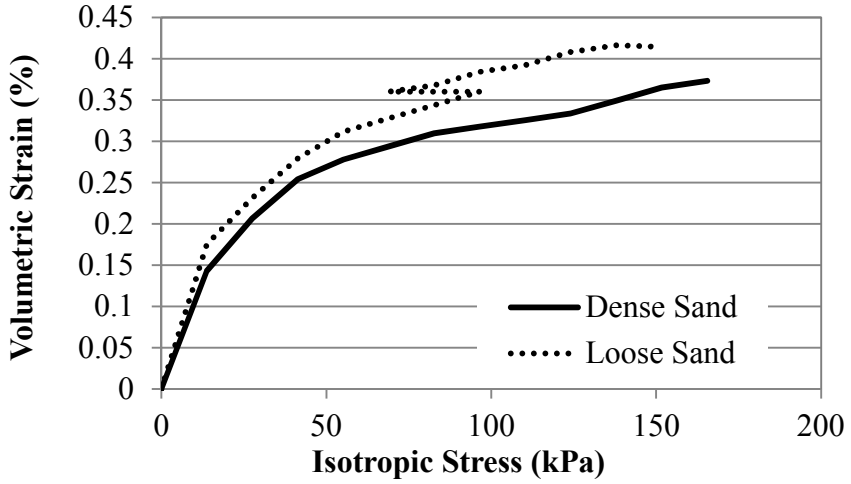

Figure 3.12 Isotropic Compression Sand D_r = 25% and 77%

Triaxial tests were also run on the crushed stone aggregate backfill materials at one density, a dumped condition with no compaction (Dr = 45%). For the triaxial tests three confining stresses (68.9 kPa, 51.7 kPa, and 34.5 kPa) were used. The deviator strain was applied at a uniform rate of 0.2% per minute. The results of the triaxial tests can be seen in Figures 3.13. The backfill material properties can be seen in Tables 3.3 and 3.4.

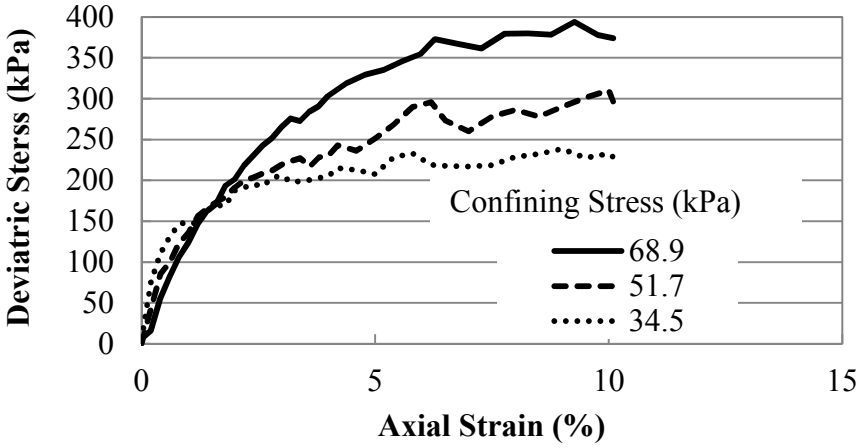

Figure 3.13 Triaxial Compression Test of Aggregate

Table 3.3 Properties of Kansas River Sand

Maximum Dry Unit Weight γ_{dmax} (kN/m^3)	19
Minimum Dry Unit Weight γ_{dmax} (kN/m^3)	16
Coef. of Curvature (Cc)	0.93
Coef. of Uniformity (Cu)	3.18
Mean Particle Size (mm)	0.5
Friction Angle ϕ at D_r = 25% (Triaxial Test)	38°
Peak Friction Angle ϕ_P at D_r = 40% (Triaxial Test)	41.5°
Residual Friction Angle ϕ_R at D_r = 40% (Triaxial Test)	39°
Peak Friction Angle ϕ_P at D_r = 77% (Triaxial Test)	45.5°
Residual Friction Angle ϕ_R at D_r = 77% (Triaxial Test)	41.5°

Table 3.4 Properties of Aggregate

Maximum Dry Unit Weight γ_{dmax} (kN/m^3)	16.2
Minimum Dry Unit Weight γ_{dmax} (kN/m^3)	13.5
Coef. of Curvature (Cc)	1.01
Coef. of Uniformity (Cu)	2.3
Mean Particle Size (mm)	11.2
Max Particle size (mm)	19
Friction Angle ϕ at D_r = 45 % (Triaxial Test)	49°

3.4.2 Backfill Placement

The backfill and bedding used for the first set of tests were Kansas River sand. The bedding for the pipe was placed in a 152 mm lift. The remainder of the backfill sand was placed in 152 mm layers and the last layer, at the top of the trench, was placed in a 76 mm layer. Each layer was compacted to a relative density of 70%, and was controlled by knowing the appropriate weight and volume of sand required for the desired lift thickness and density. The placement of the backfill can be seen in Figure 3.14. The middle third of the bedding was not compacted, consistent with the Kansas Department of Transportation specification (2007), to alleviate a stress concentration at the base of the pipe. Layers 1 through 4 were placed with an electric jack hammer and a vibratory plate compactor was used for the bedding and the remaining layers.

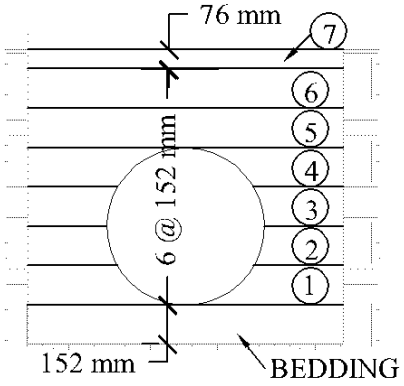

Figure 3.14 Backfill Placement

The second and third sets of tests were run with crushed stone aggregate bedding and backfill. The aggregate backfill was dumped in 152 mm lifts without compaction and with a unit weight of 14.6 kN/m^3. The lifts of aggregate were dumped into the trench simultaneously on

each side of the pipe to prevent the pipe from distorting laterally. A comparison of the pipe deflections during placement of the different backfills can be seen in Figures 3.15 and 3.16. Steps 8 and 9, not shown in Figure 3.14, represent the placement of the base course in two 190 mm layers discussed in a following section.

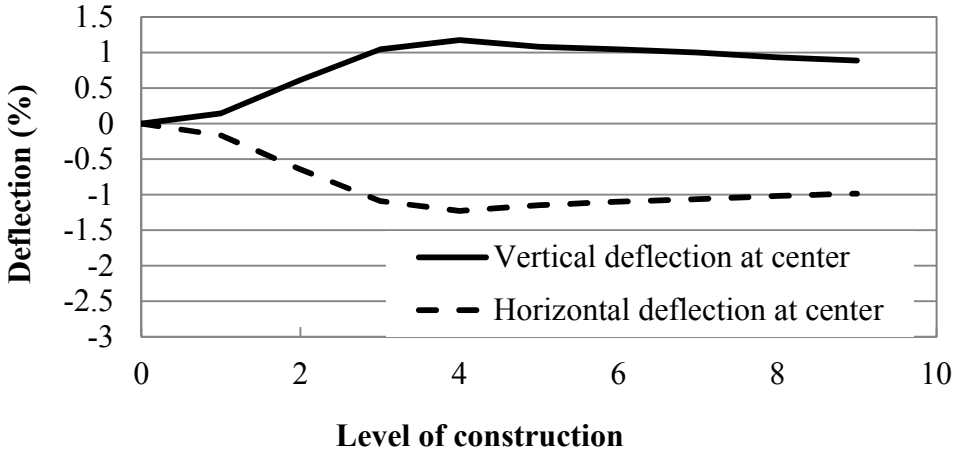

Figure 3.15 Pipe Deflections during Sand Backfill Placement

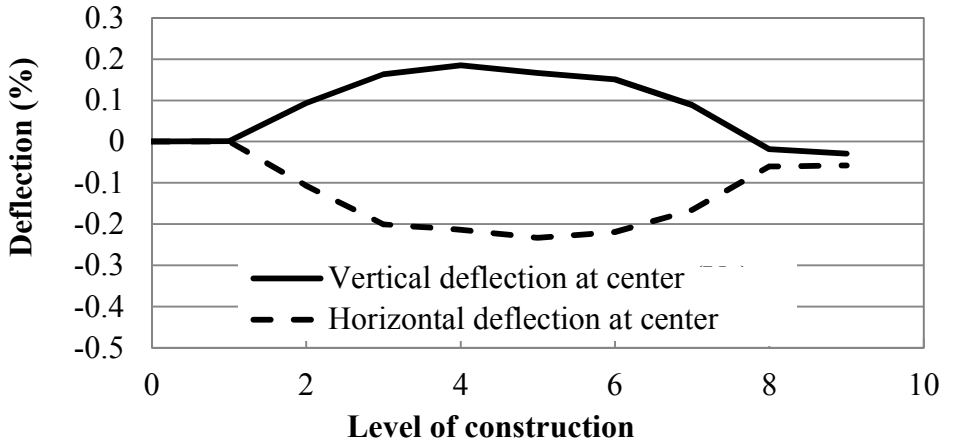

Figure 3.16 Pipe Deflections during Crushed Aggregate Placement

3.4.3 Backfill Instrumentation

During the placement of the backfill, earth pressure cells were placed at the crown, invert, and springline (Figure 3.17). Two models of earth pressure cell were used, one with a 200 kPa (KDE-200) capacity and the second with a 500 kPa (KDE-500) capacity. A total of five earth pressure cells (I_1, S_1, S_2, C_1, and C_2) were placed for the first set of tests, with the sand backfill. For the second set of tests, with aggregate backfill, five additional earth pressure cells were placed for a total of 10 earth pressure cells. All of the earth pressure cells can be seen in Figure 3.17. With the crushed aggregate backfill, the earth pressure cells were protected by sand filled bags.

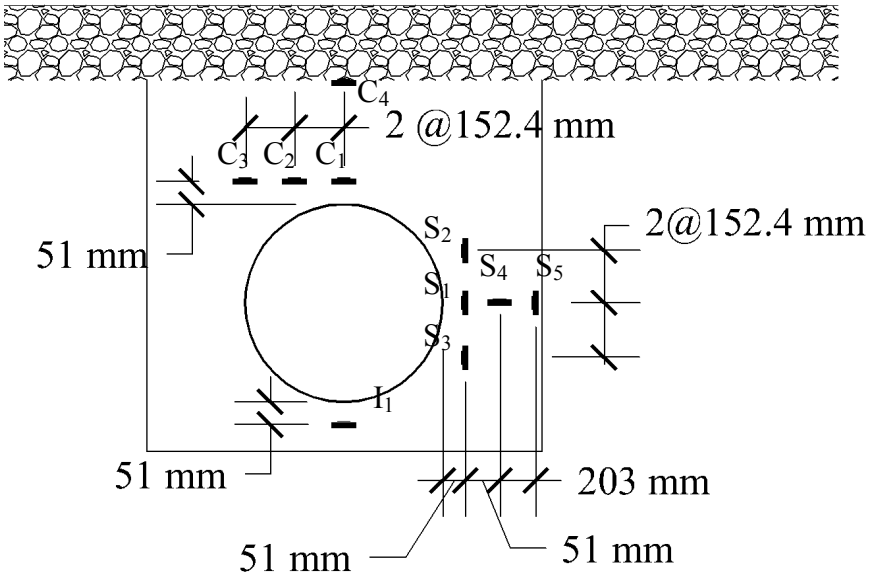

Figure 3.17 Earth Pressure Cell Locations

3.5 Base Course

The first test set used aggregate and sand base courses in separate testing runs while the second and third test sets were run exclusively with a 230 mm thick aggregate base course (AB-3). The properties of the AB-3 base course summarized from Yang (2010) are listed in Table 3.5. The base course was installed and compacted to a 95% maximum dry density from the Standard Proctor Test. Dynamic Cone Penetration tests were conducted at four locations to control the stiffness and consistency of the base course throughout the tests.

The same Kansas River sand that was used as backfill material was also used as a 0.23 m thick base course in two of the tests. The sand was placed in two 115 mm lifts. The density was controlled by knowing the weight and volume of sand necessary to fill the lift and be compacted to a relative density of 70%.

Table 3.5 Properties of Aggregate Base Course

Liquid/Plastic Limit- LL/PL	20/13
Specific Gravity G_s	2.69
Maximum Dry Unit Weight γ_{dmax} (kN/m^3)	20.6
Optimum Moisture Content w_{opt} (%)	10
Coef. of Curvature (Cc)	1.55
Coef. of Uniformity (Cu)	21
Mean Particle Size (mm)	7.0
Peak Friction Angle ϕ_P (Direct Shear)	52°
Residual Friction Angle ϕ_R (Direct Shear)	47°
Cohesion Peak/Residual (kPa)	7.2/4.7

3.6 Geogrid

3.6.1 Geogrid Material Properties

The geogrid used for the protection of the pipe was a biaxial polypropylene geogrid with a 25 mm by 33 mm aperture size, manufactured by Tensar International. The geogrid was chosen such that it would have sufficient strength so that it would not fail during the test. It was also desired to have a relatively high tensile modulus. The geogrid's strengths were published by the manufacturer. Strengths in the cross-machine direction were 9 kN/m at 2% strain and 19.6 kN/m at 5% strain, while the strengths in the machine direction were 6 kN/m at 2% strain and 11.8 kN/m at 5 % strain. The ultimate strengths were 28.8 kN/m in the cross-machine direction, and 19.2 kN/m in the machine direction.

Considering how a geosynthetic layer would be applied in a pipeline project, both layers of the geogrid were laid with the machine direction parallel to the pipe. Conceivably, this would allow the geogrid to be rolled out along the pipe in an application in the field. The lower geogrid, when used, was placed 0.15 m above the pipe crown. The width of the lower geogrid was limited by the trench width for these tests. The upper geogrid was placed at the interface of the base course and the subgrade, allowing the width of coverage to be expanded to 2.4 m. The geogrid covered the length of the pipe and the coverage perpendicular to the pipe length can be seen in Figure 3.18

3.6.2 Geogrid Instrumentation

In each test that included geogrid reinforcement, uniaxial foil-type electrical resistance strain gauges (C2A-13-250 LW-120) were placed on the layers of geogrid in the machine direction and cross-machine direction, parallel to the pipe and perpendicular to the pipe, respectively, as seen in Figure 3.18. Four strain gauges were placed in each direction starting directly under the loading plate and incrementally farther away from the center line of the geogrid. On the lower layer of geogrid, the strain gauges in the cross-machine direction were placed at 150 mm on center to accommodate four strain gauges before reaching the trench wall. All other strain gauges were placed 200 mm on center.

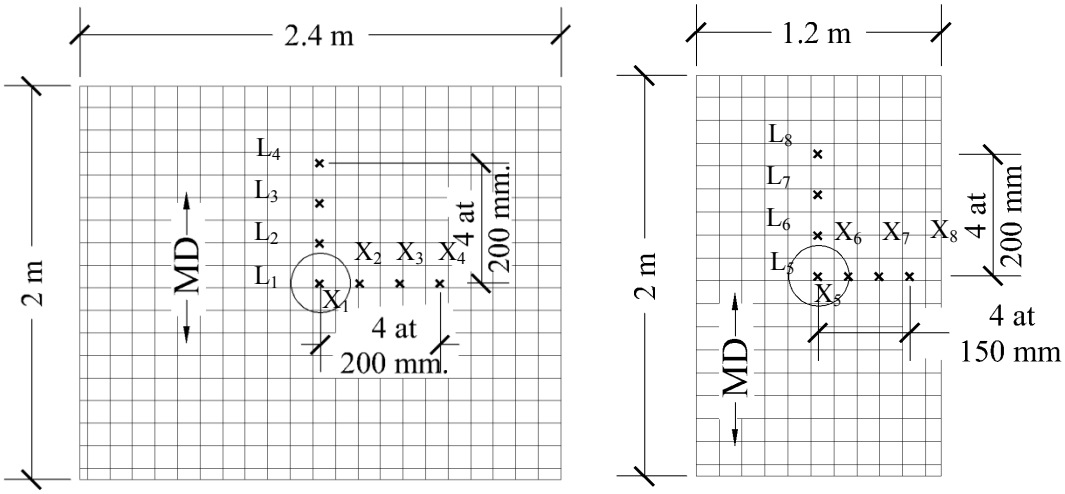

A. Upper Layer **B. Lower Layer**

Figure 3.18 Strain gauges on two geogrid layers

3.7 Load Application

The plate loads were controlled and monitored by an integrated actuator, hydraulic pump, and software package. The actuator had a maximum 245 kN capacity and was attached to a moveable reaction frame. A fourth displacement transducer was used to monitor the displacement of the plate. An actuator was used to apply the load and software was used to monitor the applied loads and displacements of the loading plate.

3.7.1 Static Plate Load Tests

A 0.30 m diameter loading plate with a rubber base was used to apply a static load in the load increments and maximums shown in Table 3.6. The maximum plate pressure of 552 kPa approximates a tire pressure of a wheel in a standard axle of a highway truck. Based on prior experience and observation, however, it was apparent that the sand base course would not be able to support the 552 kPa pressure. Therefore, a reduced load of 345 kPa was chosen. The interval was selected to ensure there were at least eight to ten data points for each pressure-settlement curve. After the maximum pressure was reached, the load was reduced and the data from instrumentation was recorded at three data steps including the removal of all loads from the plate.

Table 3.6 Static Load Tests

Test No.	Backfill	Base Course	Geogrid Reinforcement	Pressure Increment (kPa)	Maximum Pressure (kPa)
1	Sand	AB-3	Unreinforced	68.9	551
2	Sand	Sand	Unreinforced	34.5	345
3	Sand	Sand	Single Layer	34.5	345
4	Sand	AB-3	Double Layers	68.9	551
5	Agg.	AB-3	Unreinforced	68.9	689
7	Agg.	AB-3	Single Layer	68.9	689
9	Agg.	AB-3	Double Layers	68.9	689

3.7.2 Cyclic Plate Load Tests

Cyclic loads (Table 3.7) were applied to simulate the traffic loading with the same 0.3 m loading plate as the static loading test. Each cyclic load had a trough value of 7 kPa, which was applied to keep the plate in contact with the surface and to prevent impact loading on the surface. The loading wave frequency was 0.77 Hz. The cyclic wave form is shown in Figure 3.19 and the numbers of cycles per load are shown in Figure 3.20.

Table 3.7 Cyclic Load Tests

Test No.	Backfill	Base Course	Geogrid Reinforcement	Pressure Increment (kPa)	Peak Pressure (kPa)
6	Agg.	AB-3	Unreinforced	137.8	689
8	Agg.	AB-3	Single Layer	137.8	689
10	Agg.	AB-3	Double Layers	137.8	689

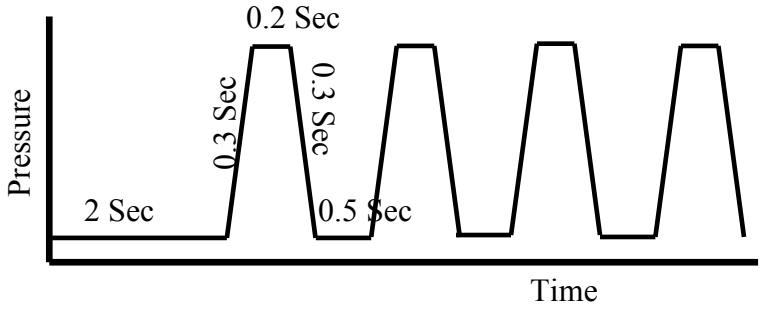

Figure 3.19 Cyclic Wave Form

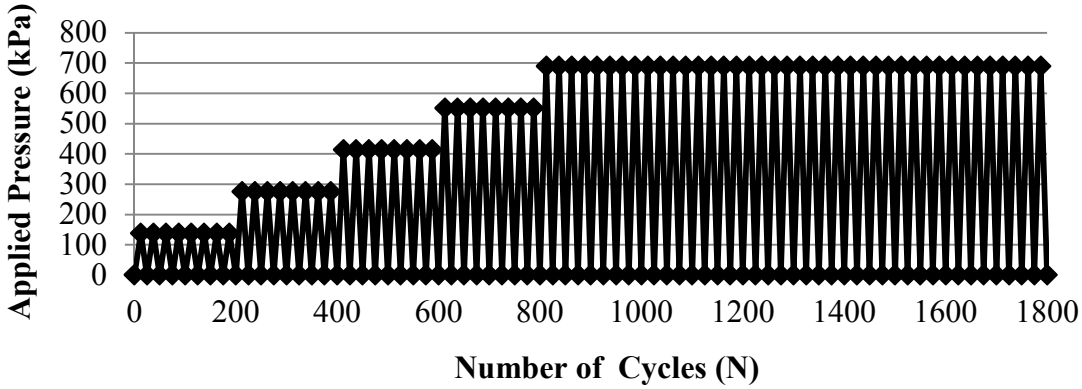

Figure 3.20 Cyclic loading for Tests 6, 8, and 10

3.8 Laboratory Results

3.8.1 Plate Settlement

The settlement of the loading plate at the surface was monitored during loading and unloading of the test section. The effectiveness of the geosynthetic in reducing plate settlement is expected to be a function on the relative stiffness of the base course and geosynthetic composite, and the relative stiffness of the backfill and the pipe. In the case of the AB-3 base course and sand backfill tests (1 and 4), shown in Figure 3.21, there was only a minor reduction in the settlement of the loading plate, 11%, between the unreinforced and reinforced conditions. The relatively stiff AB-3 base course distributes the static load well without the geosynthetic. Comparatively, in the case with the sand backfill and sand base course (tests 2 and 3 shown in Figure 3.22), there was a 25% decrease in plate settlement of the geogrid reinforced section as compared to the unreinforced section. In the remainder of the figures U.R. is short for unreinforced, D.L. is short for double layers of geogrid, and S.L. is short for single layer of geogrid.

In the case of the dumped crushed stone aggregate, the double layers of reinforcement decreased the plate settlement by 38% as compared with the unreinforced condition. Conversely, the single layer of reinforcement in the aggregate backfill appeared to increase the plate settlement by 26% as compared to the unreinforced condition. Both results are shown in Figure 3.23.

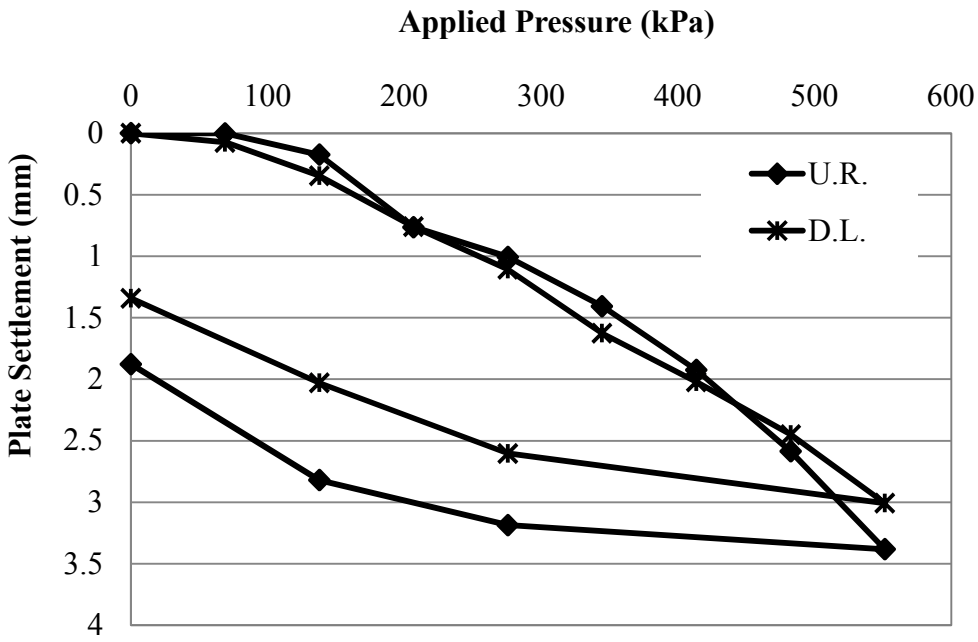

Figure 3.21 Loading Plate Settlements in Tests 1 and 4

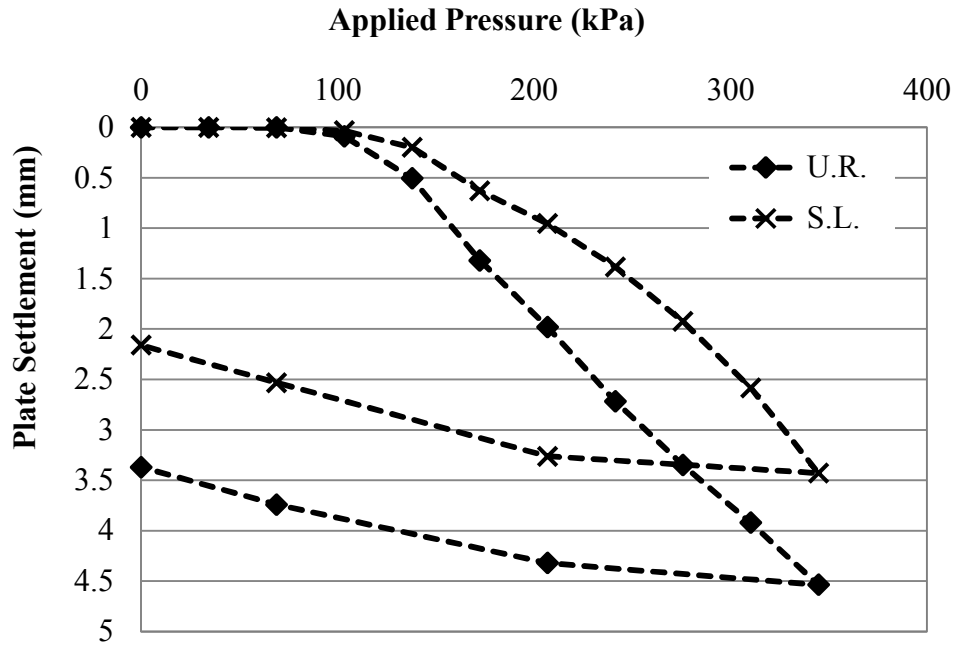

Figure 3.22 Loading Plate Settlements in Tests 2 and 3

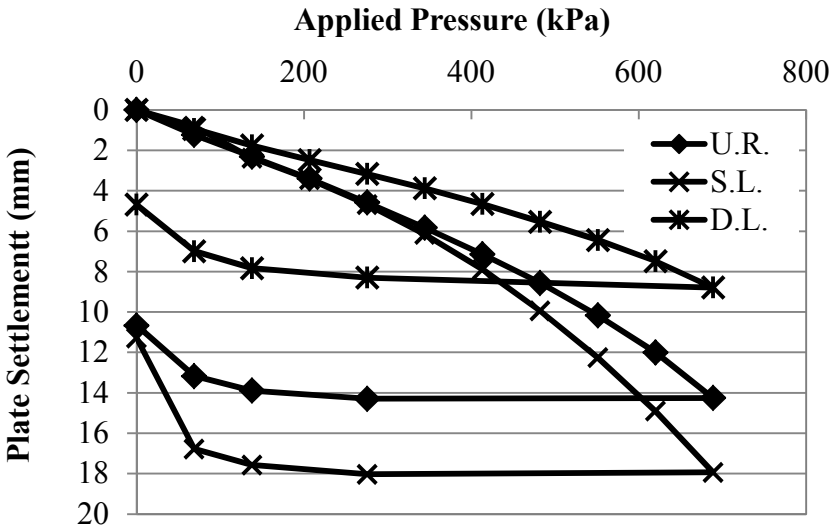

Figure 3.23 Loading Plate Settlements in Tests 5, 7, and 9

Plate settlements were also monitored and recorded during each cyclic loading test. The data recorders took data points every one tenth of a second, continuously. The data points at the beginning and the end of the load step, and the data at 40 cycles are shown in Figures 3.24 through 3.26. At each data point, the minimum and maximum settlements are given.

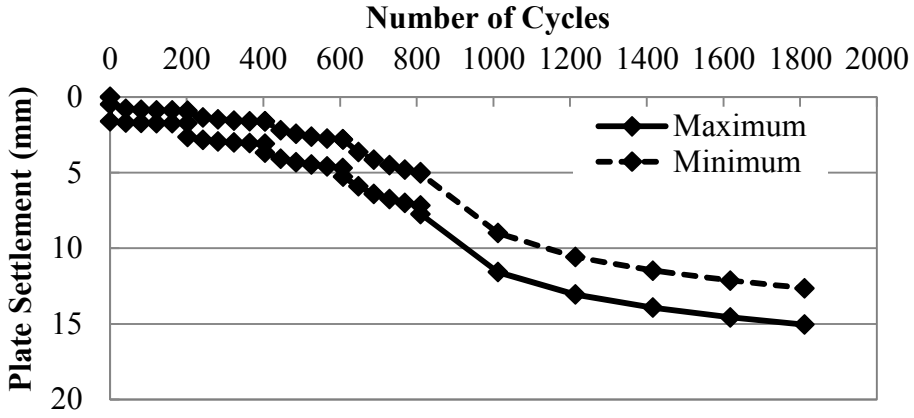

Figure 3.24 Plate Settlements in Test 6

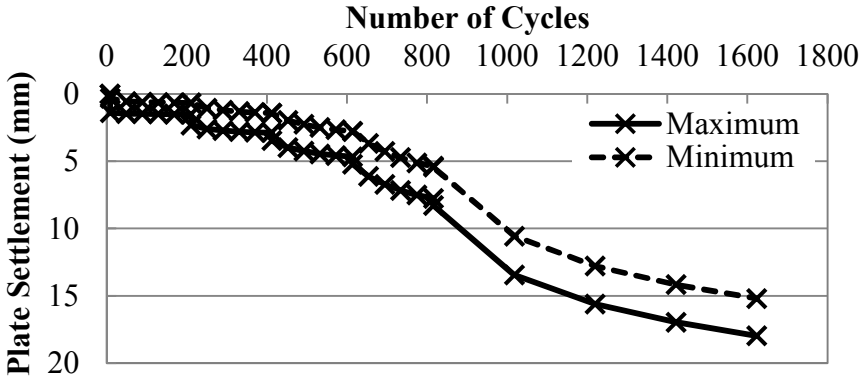

Figure 3.25 Plate Settlements in Test 8

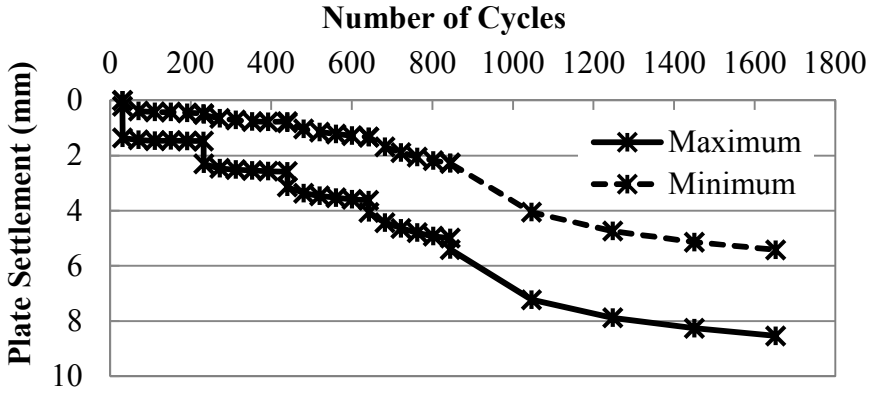

Figure 3.26 Plate Settlements in Test 10

The cyclic load cases confirmed the observations in the static load cases: the single layer of geosynthetic placed at 0.15 m above the pipe crown appeared to slightly increase the plate settlement while the double layers significantly lowered the plate settlement. It is conjectured that there was little to no difference in plate settlements due to the single layer of geogrid, but that differences observed in the tests were the result of slight differences in the modulus of the

base course, which could be the result of differences in compaction energy, moisture content during compaction or moisture changes due to drying during the tests. It was also observed in the cyclic load case that the geogrid increased the rebound of the base course. The magnitude of the maximum plate settlements was similar in the static load and cyclic load cases.

3.8.2 Pipe Deflection

During the plate loading tests, two displacement transducers continuously recorded the movements of the pipe along the vertical and horizontal principal axis. A third displacement transducer continuously recorded the vertical displacements of the pipe at 305 mm from the center of the loading pipe along the longitudinal axis of the pipe. The displacement at the end of each loading step is plotted against the loading steps.

Pipe Deflections in Tests 1 through 4

In the case of the sand backfill, the double layer of reinforcement reduced the vertical deflection of the pipe (Figure 3.27), while the single layer of geogrid reinforcement (Figure 3.28) did not affect or slightly increased the deflection of the pipe. Assuming that deflection of the pipe will control the design, and that the strain in the pipe is proportional to the magnitude of pipe deflection, this would indicate that the second layer near the surface has a greater potential impact on the design of a near surface pipe.

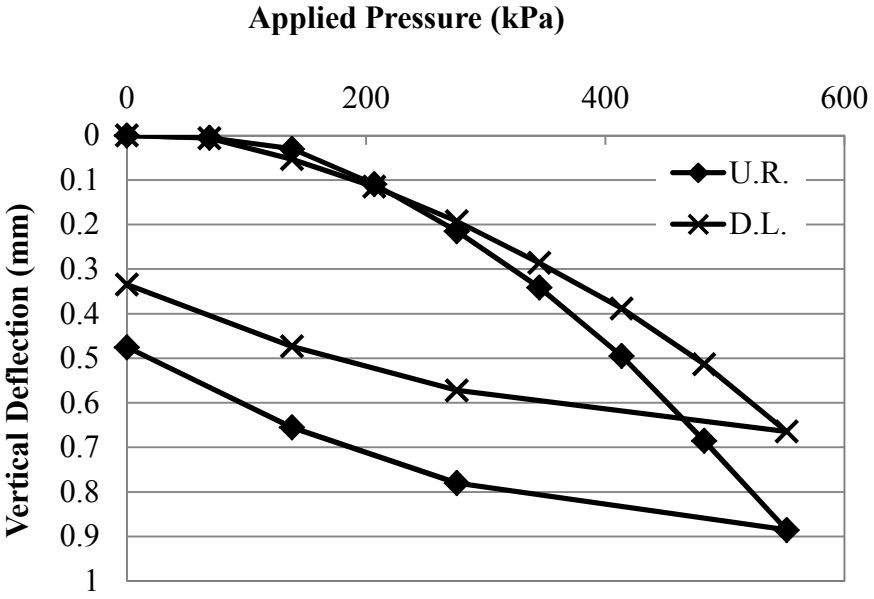

Figure 3.27 Vertical Deflection of Pipe – Tests 1 and 4

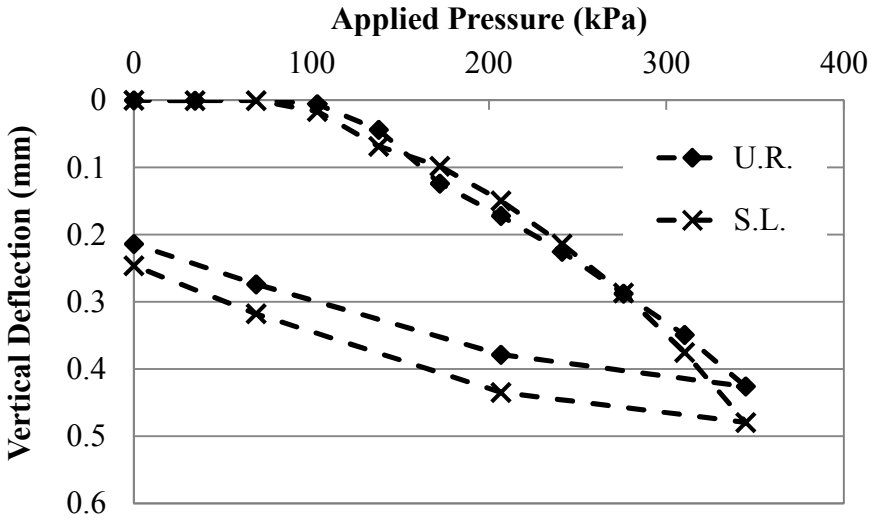

Figure 3.28 Vertical Deflection of Pipe – Tests 2 and 3

As would be expected the deflection of the pipe at 305 mm from the loading plate (Figures 3.29 and 3.30) was less than the deflection directly under the loading plate. The relative deflections between the reinforced and unreinforced conditions matched the displacements directly under the loading plate.

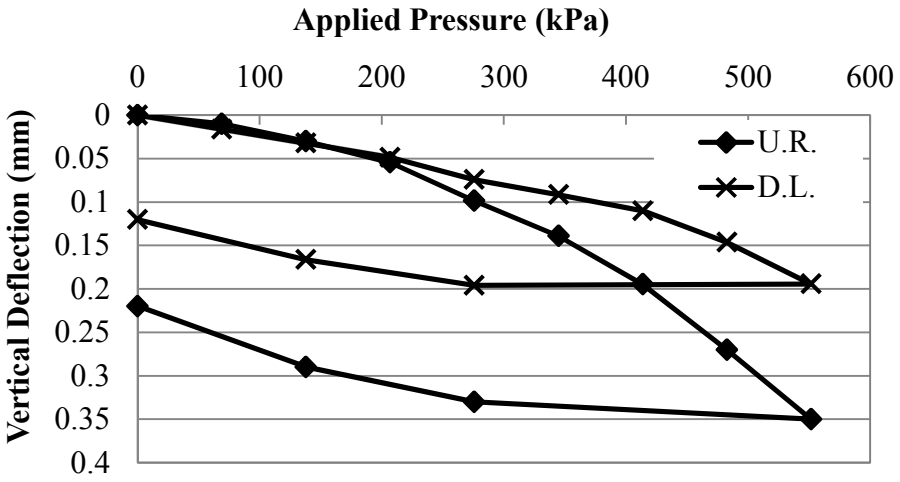

Figure 3.29 Vertical Deflections at 305 mm from Plate – Tests 1 and 4

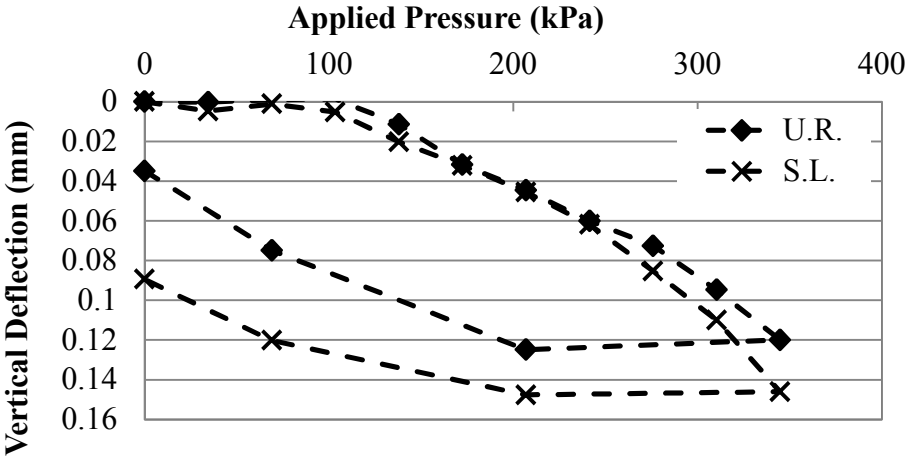

Figure 3.30 Vertical Deflections at 305 mm from Plate – Tests 2 and 3

Horizontal deflections of the pipe were also recorded during the plate load tests directly under the loading plate. The horizontal deflections can be seen in Figures 3.31 and 3.32. Again in the sand base course the single layer of geogrid appeared to increase the pipe deflection while the double layer of geogrid decreased the deflection of the pipe. The ratio of vertical to horizontal deflection underneath the plate is shown in Figure 3.33. This figure demonstrates that in both cases the vertical to horizontal deflection ratio is slightly higher, though the magnitudes of the vertical and horizontal deflections were less for the double layer of geogrid. The closer the ratios of vertical and horizontal deflections of the pipe are to one, the more elliptical the shape of the pipe is and there is potentially less bending strain. It is expected to have a deflection ratio greater than one for concentrated loads.

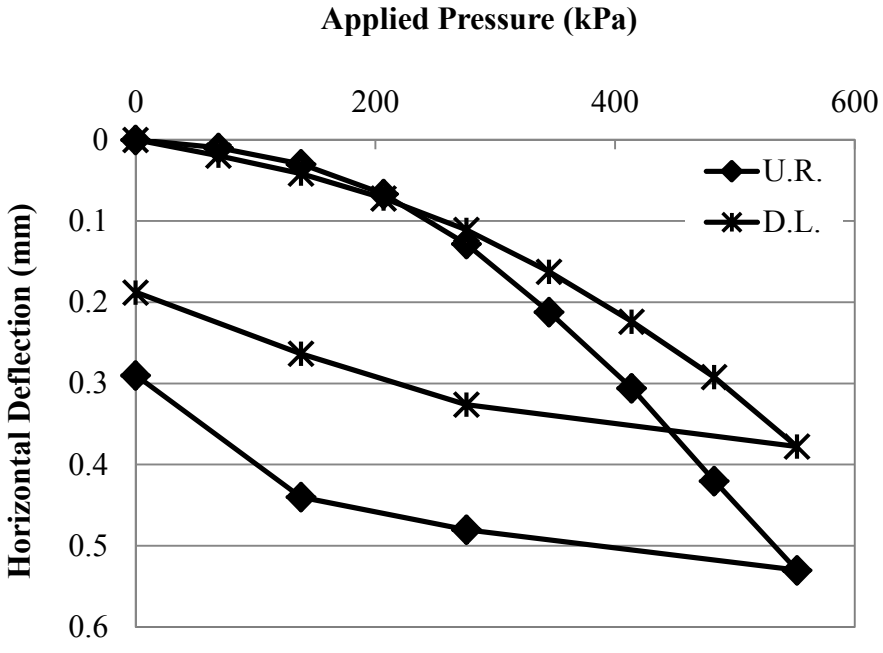

Figure 3.31 Horizontal Deflection of Pipe -Tests 1 and 4

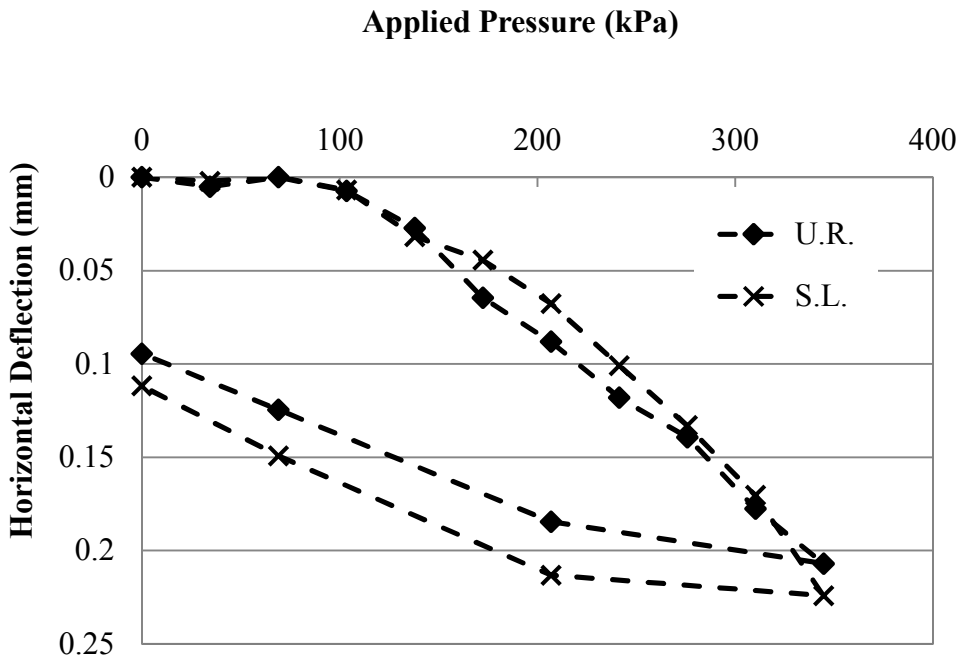

Figure 3.32 Horizontal Deflection of Pipe - Tests 2 and 3

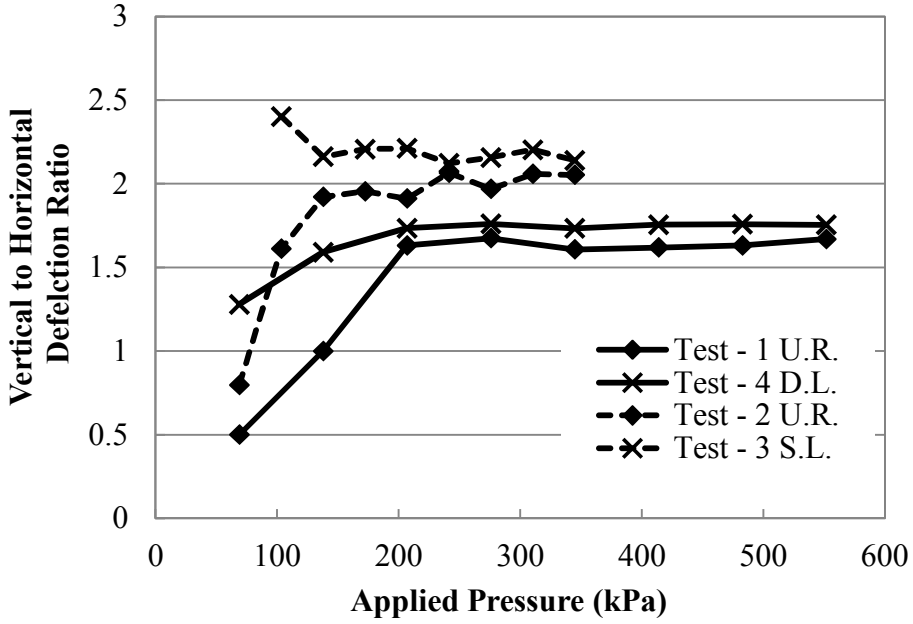

Figure 3.33 Vertical to Horizontal Deflection Ratio – Tests 1 through 4

Pipe Deflections in Tests 5 through 10

In tests 5 through 10, in which the crushed stone aggregate backfill was used, vertical and horizontal pipe deflections were taken with the same set up of displacement transducers as described in the set-up of the previous tests. The vertical deflection under the plate, the vertical deflection at 0.305 m from the plate, and the horizontal deflection under the plate can be seen in Figures 3.34, 3.35, and 3.36 respectively. The ratio of vertical to horizontal deflection directly under the plate can be seen in Figure 3.37.

Again the same general pattern appears, where the single layer of geogrid appeared to possibly cause a small increase of the deflection while the double layer, or specifically the upper layer decreased the pipe deflection. For the single layer of geogrid, the changes in the pipe deflection compared to the changes in the plate displacements seemed to confirm that the changes in stiffness were nearer the plate, possibly from changes in the base course stiffness not the single layer of geogrid.

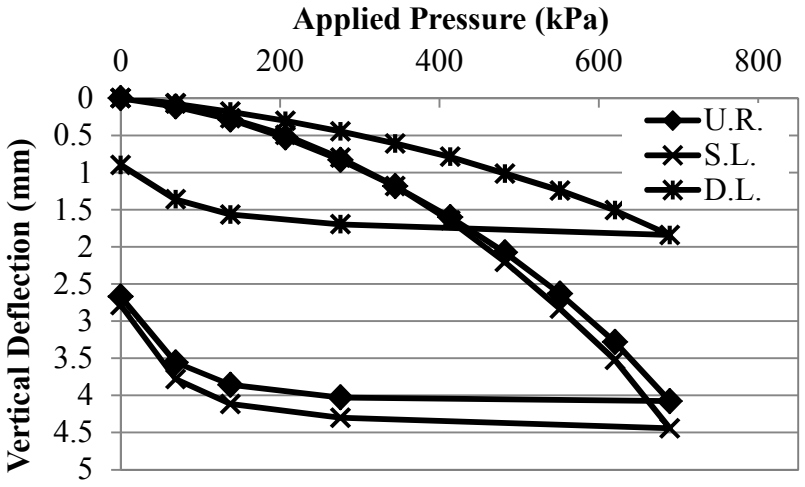

Figure 3.34 Vertical Deflections of Pipe - Tests 5, 7, and 9

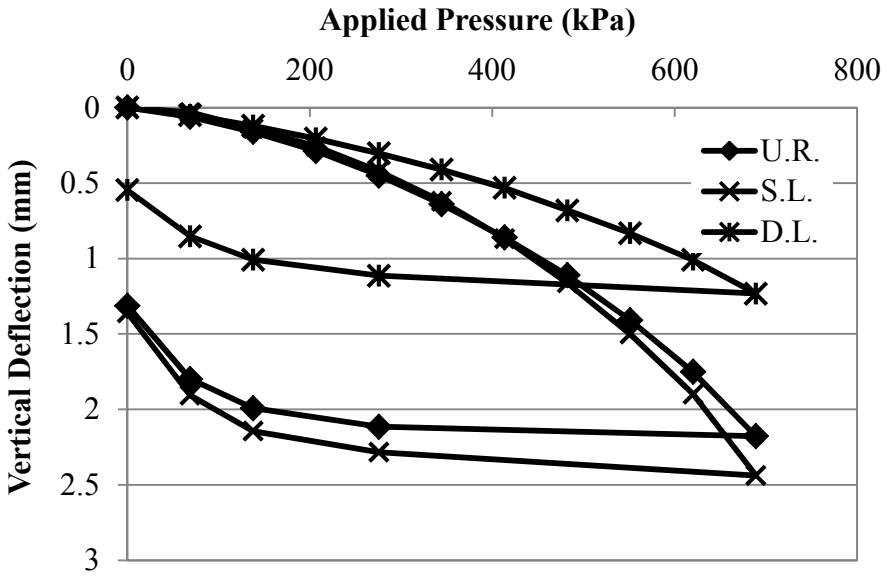

Figure 3.35 Vertical Deflections at 305mm from Plate – Tests 5, 7, and 9

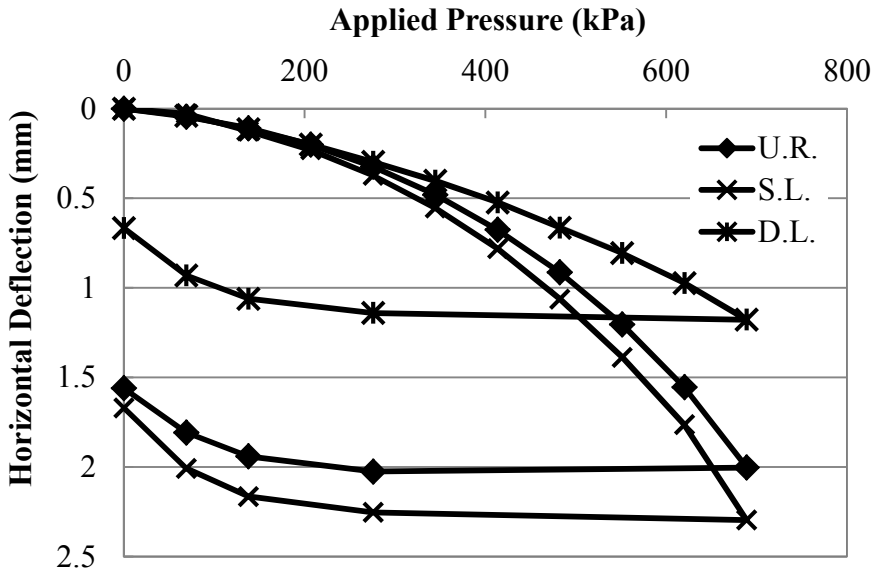

Figure 3.36 Horizontal Pipe Deflections –Tests 5, 7, and 9

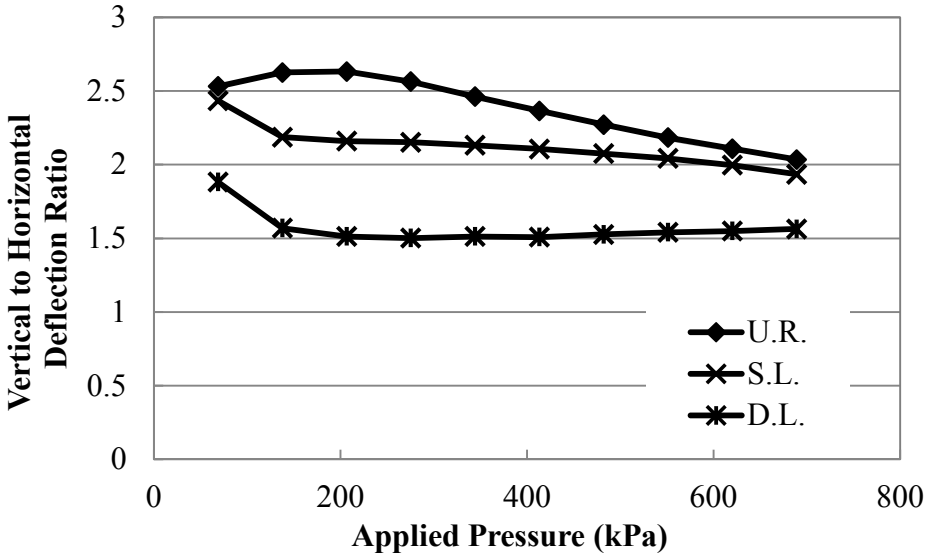

Figure 3.37 Vertical to Horizontal Deflection Ratios – Tests 5, 7, and 9

During the cyclic load test the pipe deflection was monitored again as shown in Figures 3.38 through 3.46. The deflection was affected in the same pattern as established in the previous comparisons. The magnitudes of the pipe deflections were similar in the static load and cyclic load cases.

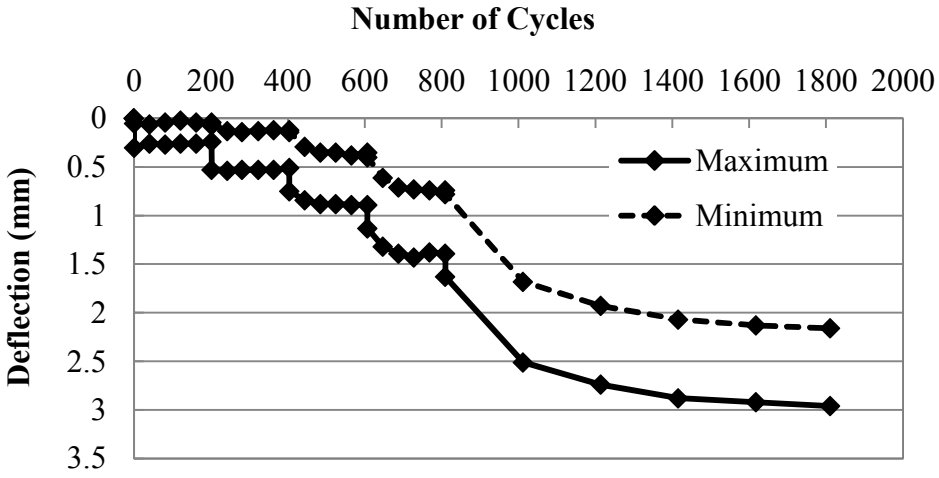

Figure 3.38 Vertical Pipe Deflections with U.R. - Test 6

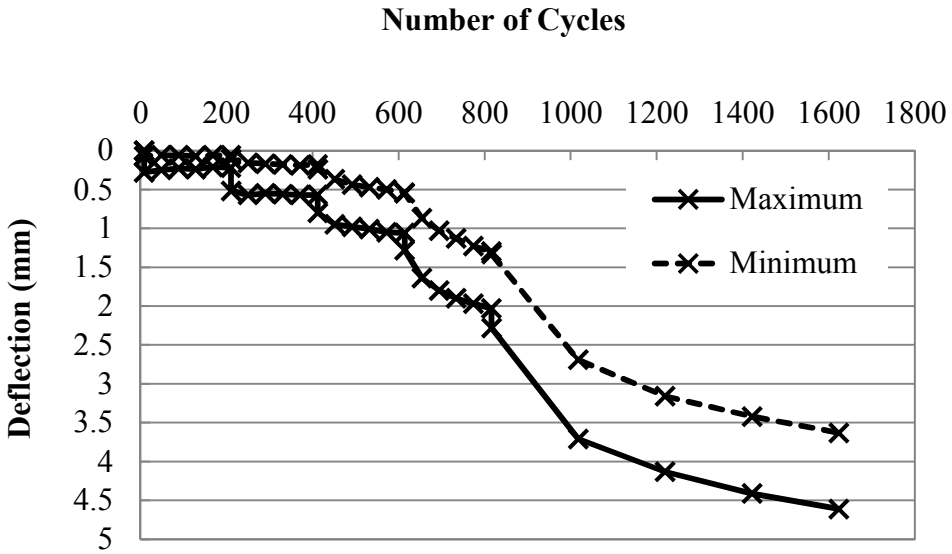

Figure 3.39 Vertical Pipe Deflections with S.L. - Test 8

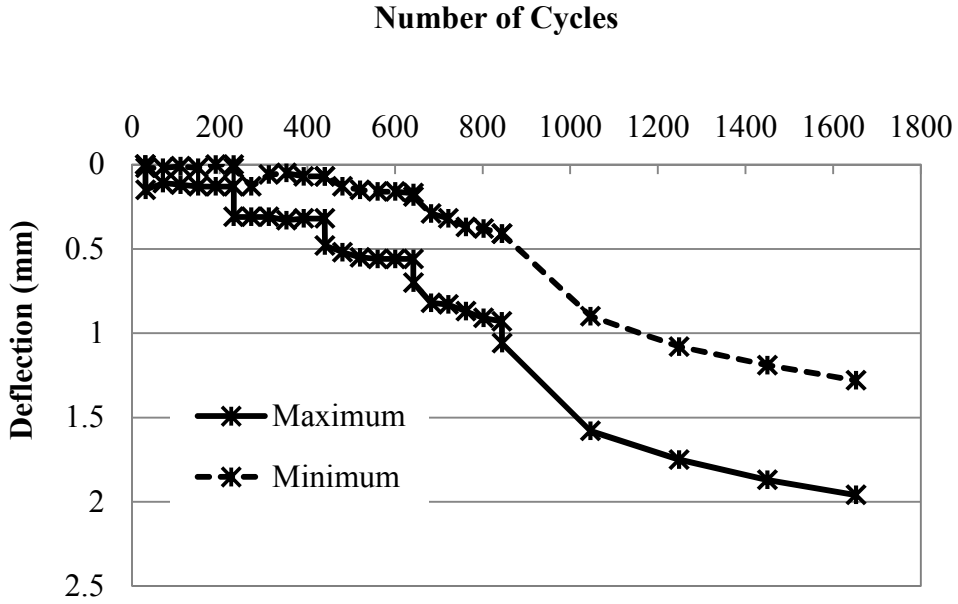

Figure 3.40 Vertical Pipe Deflections with D.L. - Test 10

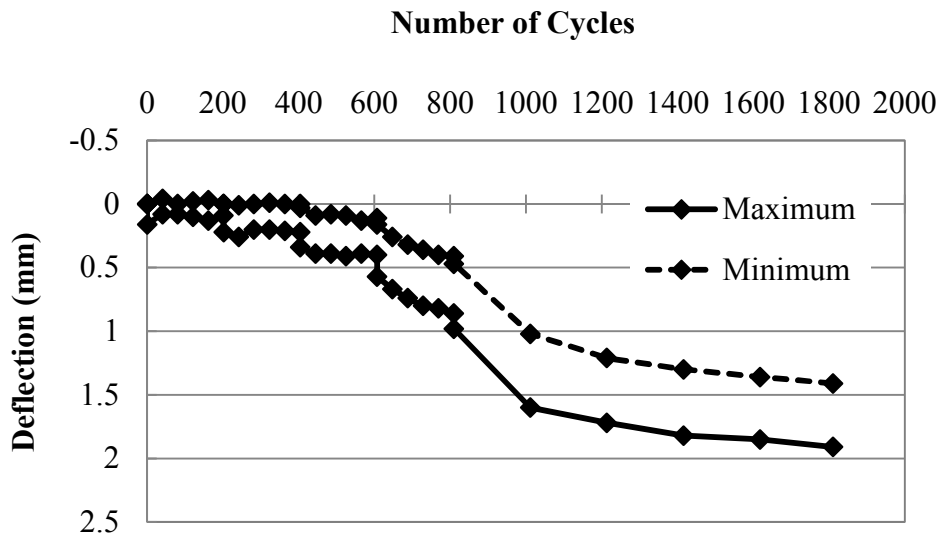

Figure 3.41 Vertical Pipe Deflections at 305 mm from Loading Plate with U.R. - Test 6

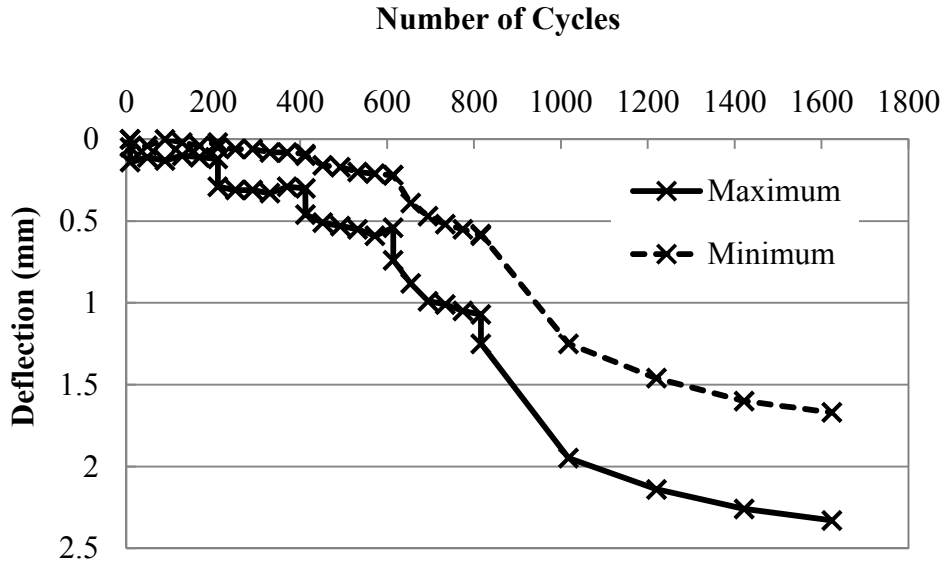

Figure 3.42 Vertical Pipe Deflections at 305 mm from Loading Plate with S.L. - Test 8

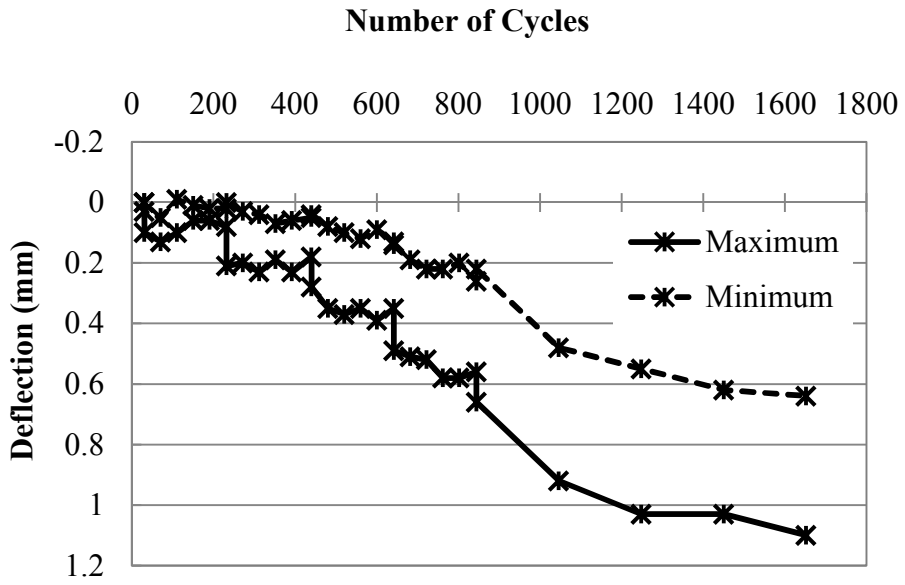

Figure 3.43 Vertical Pipe Deflections at 305 mm from Loading Plate with D.L. - Test 10

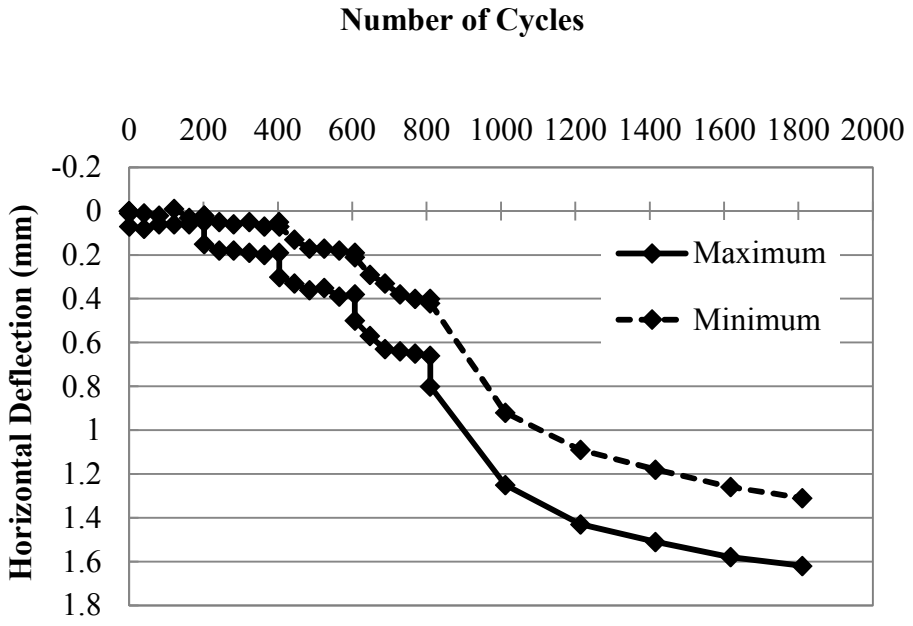

Figure 3.44 Horizontal Pipe Deflections with U.R. - Test 6

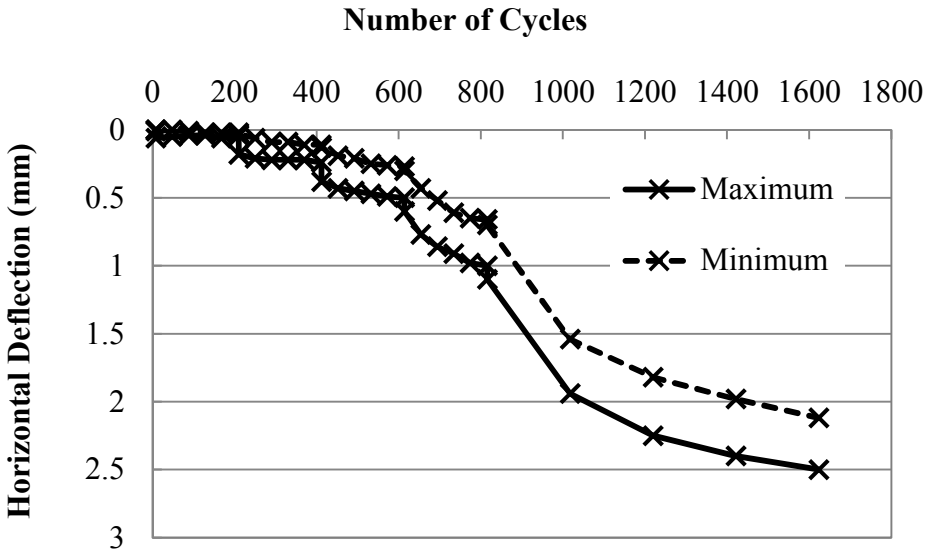

Figure 3.45 Horizontal Pipe Deflections with S.L. - Test 8

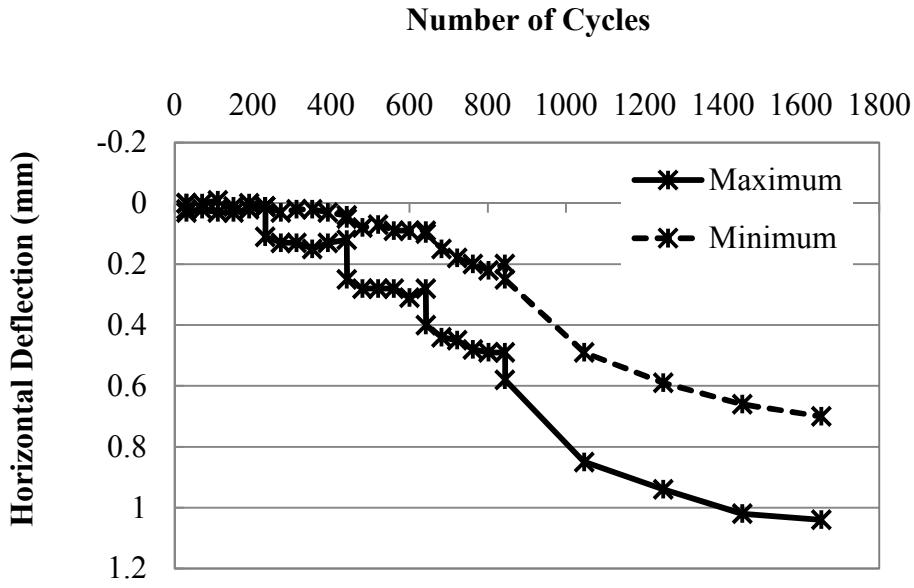

Figure 3.46 Horizontal Pipe Deflections with D.L. - Test 10

3.8.3 Earth Pressures

During the static plate loading tests, earth pressures were monitored and recorded. In the first four tests only pressure cells I_1, S_1, S_2, C_1, and C_2 were included in the backfill. After these tests it was decided to expand the number of pressure cells. The remaining pressure cells were included in tests 5 through 10.

Crown Pressures in Tests 1 through 4 (Sand Backfill)

For the sand backfill conditions (tests 1 through 4) the earth pressures at the crown were measured and are plotted versus the applied plate pressure in Figures 3.47 through 3.50. It is apparent that there was little reduction in earth pressures directly over the crown, or at a distance of 0.152 m from the crown, with the sand backfill.

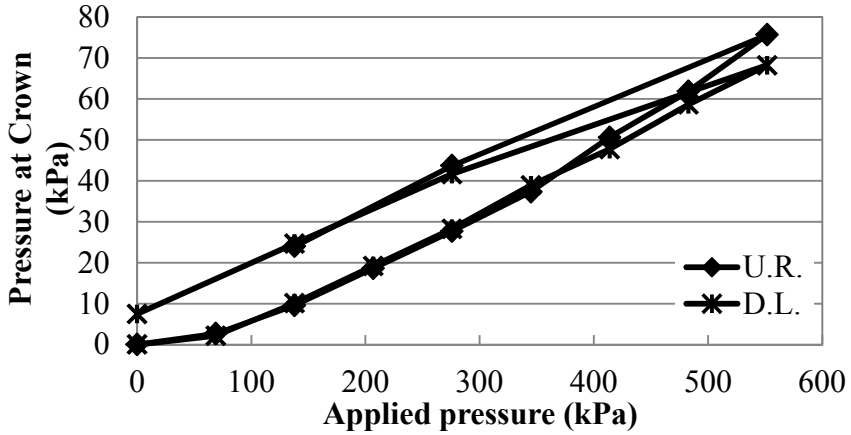

Figure 3.47 Measured Pressures at Crown (C_1) - Tests 1 and 4

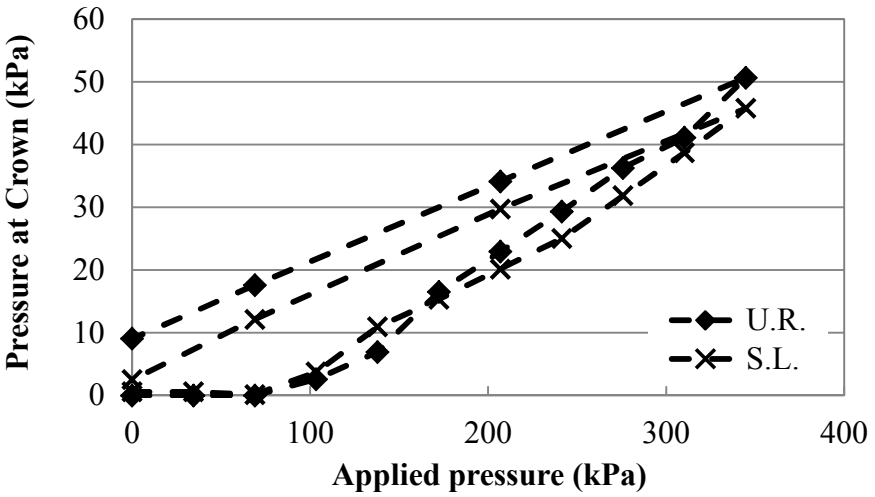

Figure 3.48 Measured Pressures at Crown (C_1) - Tests 2 and 3

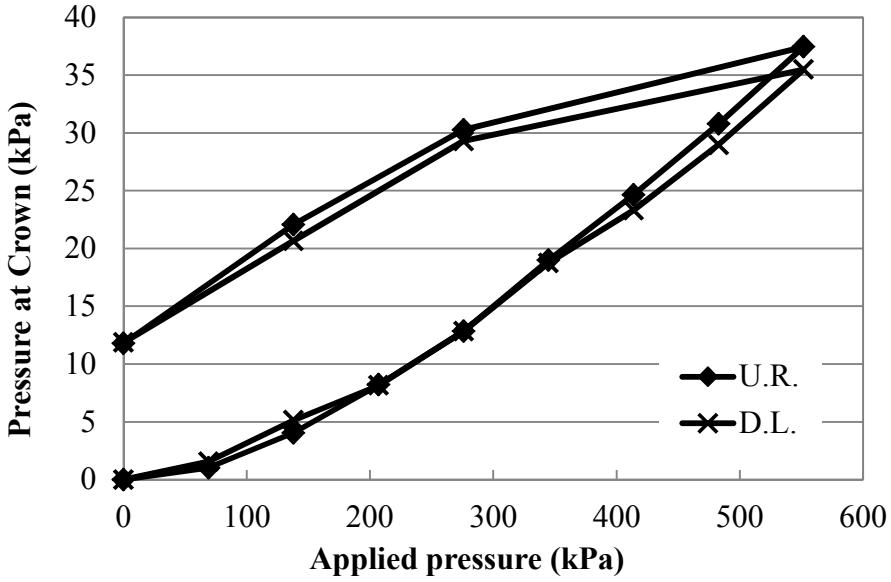

Figure 3.49 Measured Vertical Pressures at Crown (C_2) - Tests 1 and 4

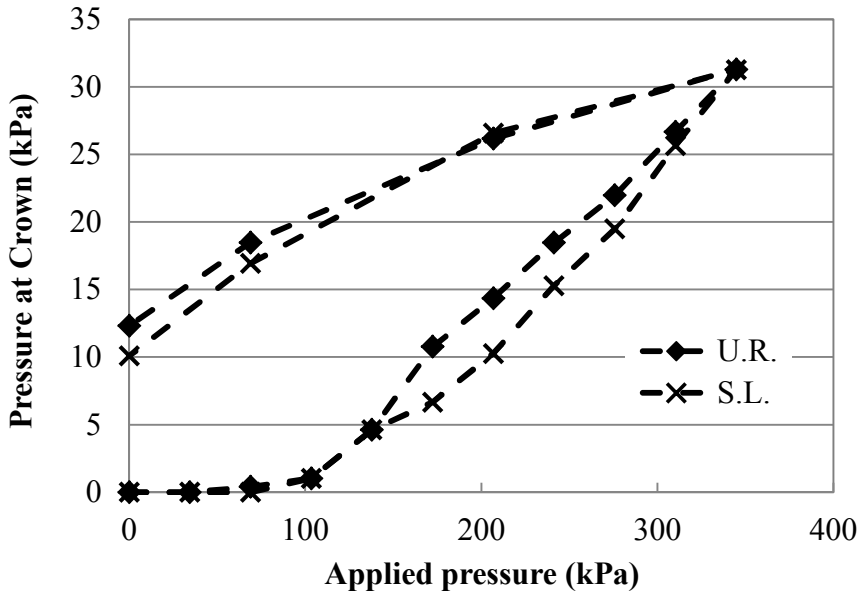

Figure 3.50 Measured Vertical Pressures at Crown (C_2) - Tests 2 and 3

Crown Pressures in Tests 5 through 10 (Aggregate Backfill)

The earth pressures recorded at the crown for tests 5, 7, and 9, at locations (C_1), (C_2), and (C_3) are shown in Figures 3.51 through 3.53. For the crushed stone aggregate backfill the inclusion of geogrid significantly reduced the pressure directly over the crown, but at a distance of 0.152 m from the pipe crown the inclusion of geogrid increased the pressure. The pressure distribution of the aggregate backfill can be seen in Figure 3.54. The addition of the geogrid reinforcement in the aggregate backfill appears to distribute the earth pressures away from the crown and towards the shoulders of the pipe. The earth pressures directly under the base course were significantly affected by the geogrid, i.e., reducing the earth pressures by 26% for the single layer of reinforcement and by 43% for the double layer of reinforcement. The earth pressures directly under the base course are shown in Figure 3.55.

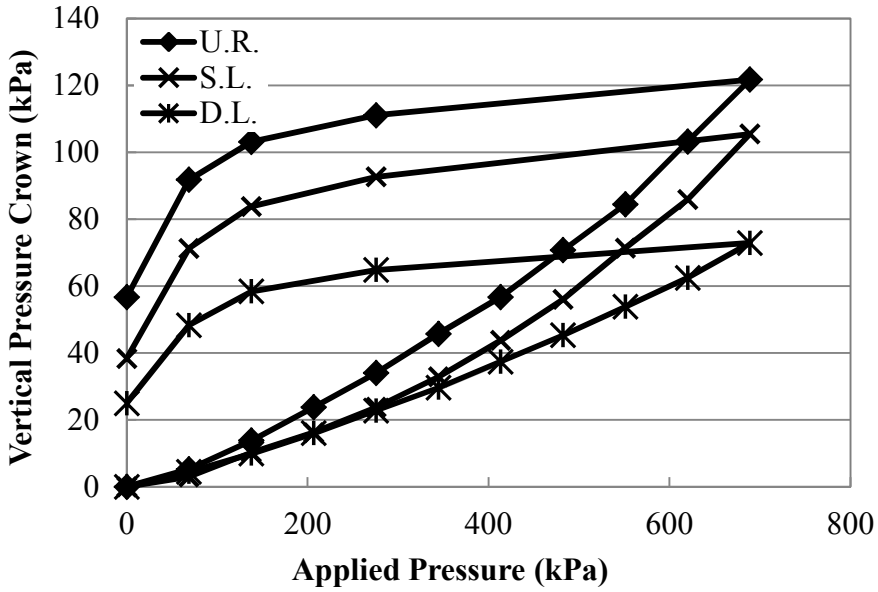

Figure 3.51 Vertical Pressures at Crown (C_1) - Tests 5, 7, and 9

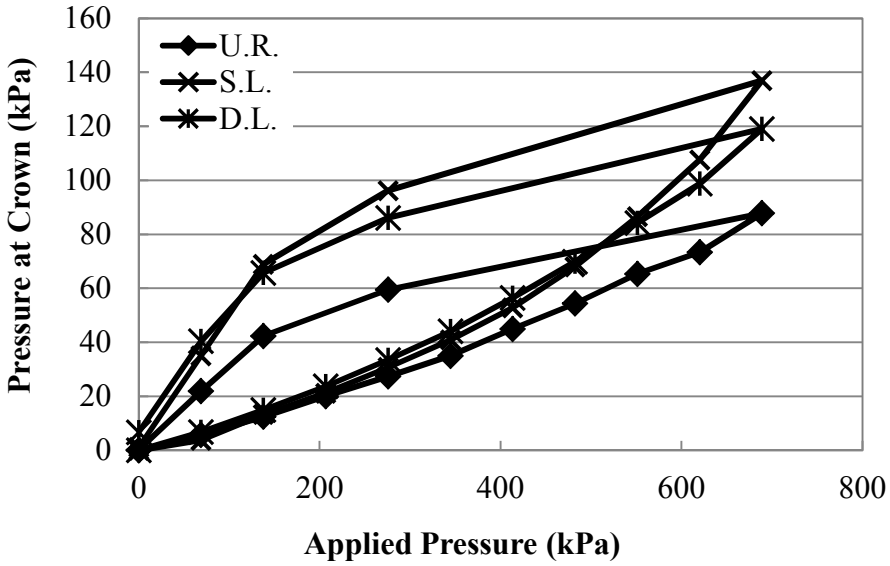

Figure 3.52 Vertical Pressures at Crown (C_2) -Tests 5, 7, and 9

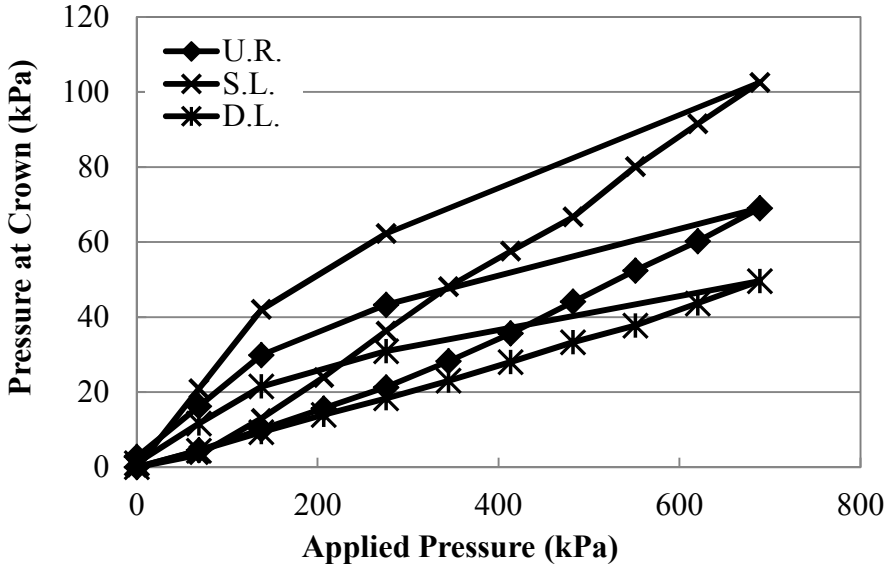

Figure 3.53 Vertical Pressures at Crown (C_3) -Tests 5, 7, and 9

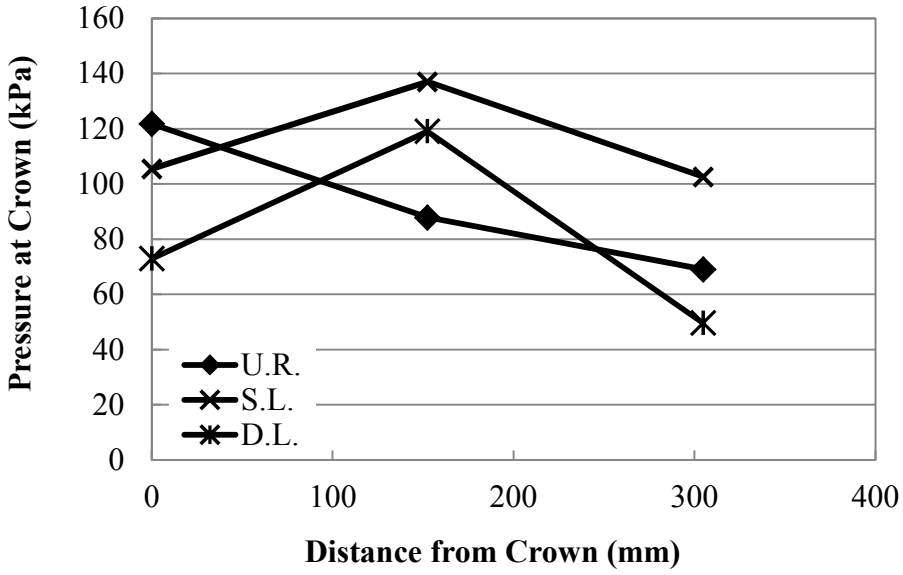

Figure 3.54 Crown Pressure Distributions at Maximum Applied Pressure - Tests 5, 7, and 9

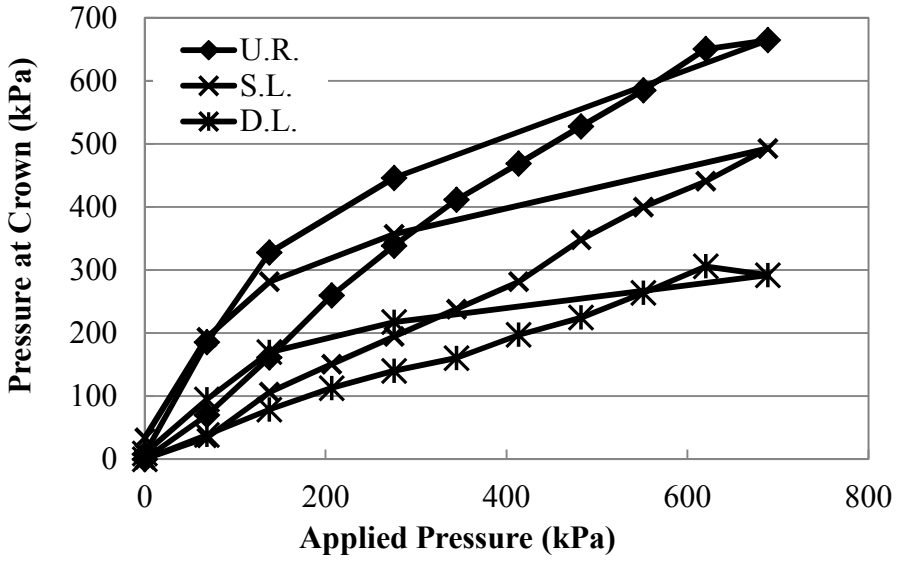

Figure 3.55 Vertical Pressures at Crown (C_4) - Tests 5, 7, and 9

The earth pressures recorded for the cyclic load cases are shown in Figures 3.56 through 3.68. The data points were taken as the minimum and maximum pressures over 40 cycles. The pressures directly over the crown showed a similar maximum magnitude of pressure as the static load cases for the unreinforced, singly reinforced, and doubly reinforced conditions (Figures 3.56, 3.57, and 3.58) in the initial stages of the tests. The single layer however appears to cause an increase in pressure directly over the crown when the applied peak pressure of 413 kPa was reached, or at approximately 400 cycles. A comparison of the maximum recorded pressures at the crown versus the applied peak pressure can be seen in Figure 3.59.

Similarly the pressures recorded by the earth pressure cells C_2 and C_3 are shown in the Figures 3.60 through 3.65. The maximum recorded pressure at the C_2 and C_3 are shown in Figures 3.66 and 3.67.

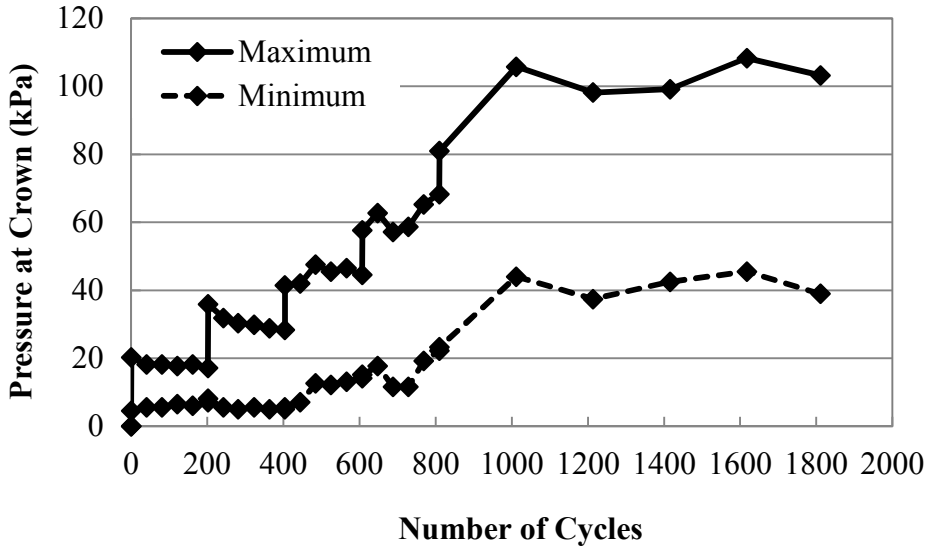

Figure 3.56 Vertical Pressures at Crown (C_1) with U.R. - Test 6

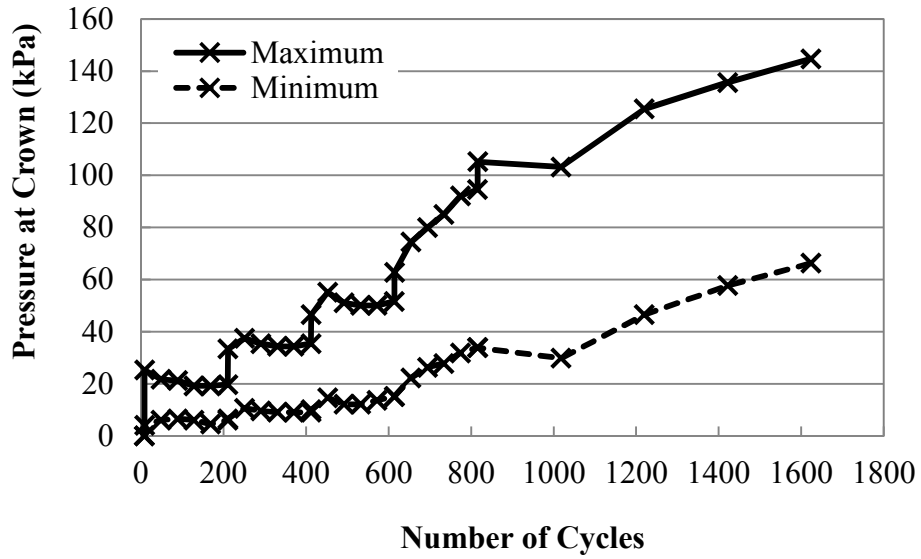

Figure 3.57 Vertical Pressures at Crown (C_1) with S.L. - Test 8

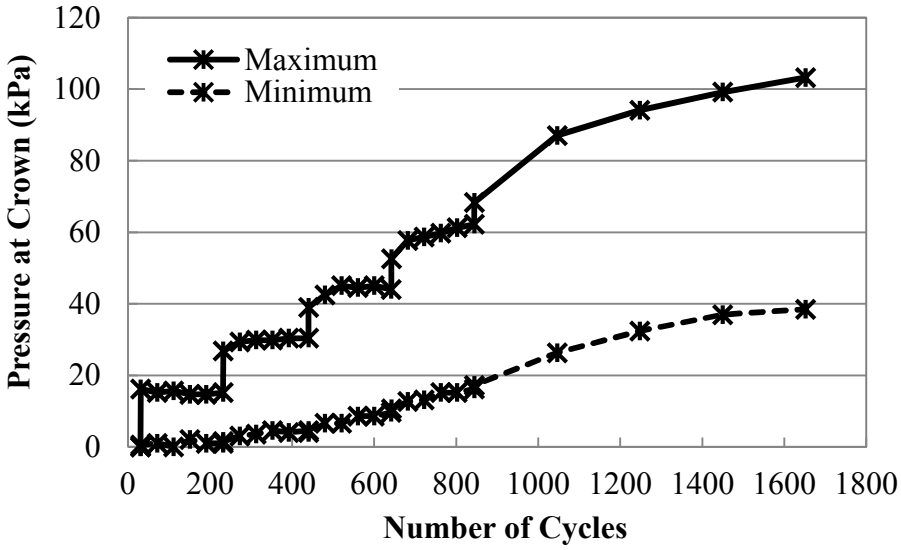

Figure 3.58 Vertical Pressures at Crown (C_1) with D.L. - Test 10

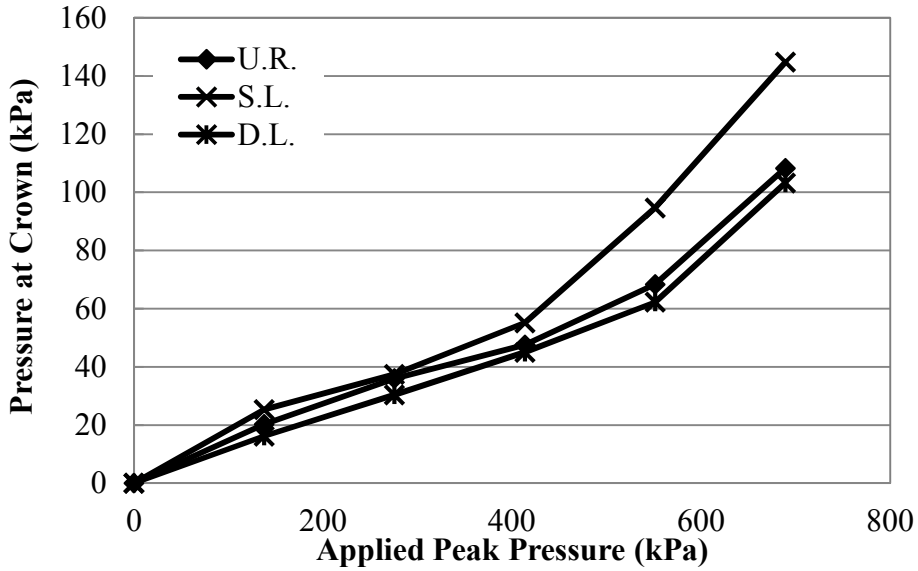

Figure 3.59 Maximum Vertical Pressures at Crown (C_1) - Tests 6, 8, and 10

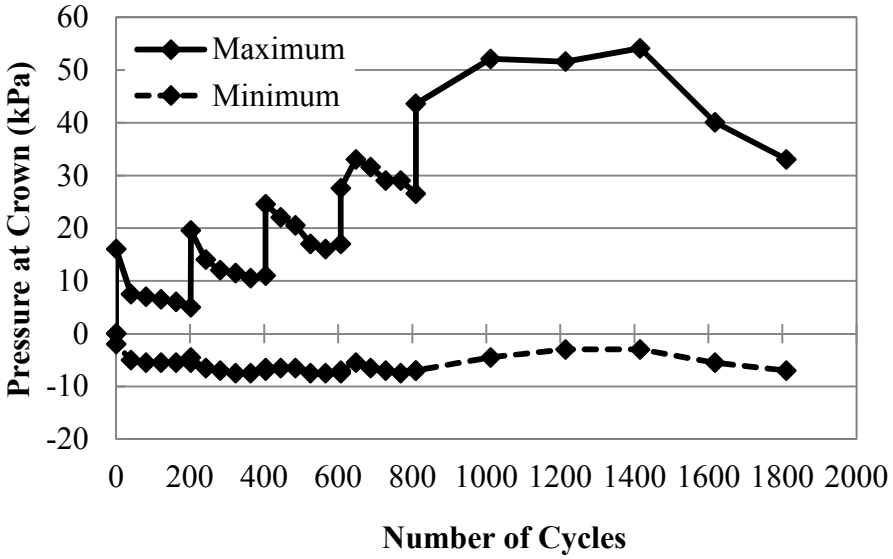

Figure 3.60 Vertical Pressures at Crown (C_2) with U.R. - Test 6

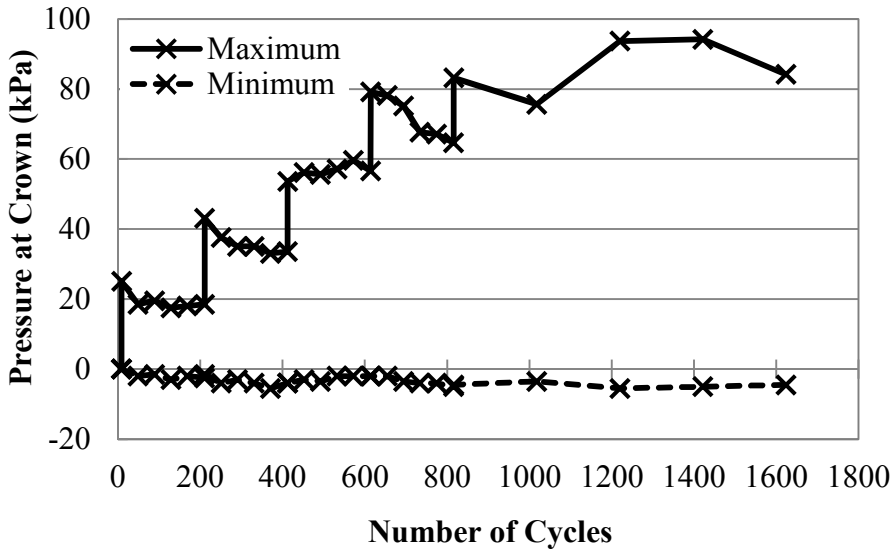

Figure 3.61 Vertical Pressures at Crown (C_2) with S.L. - Test 8

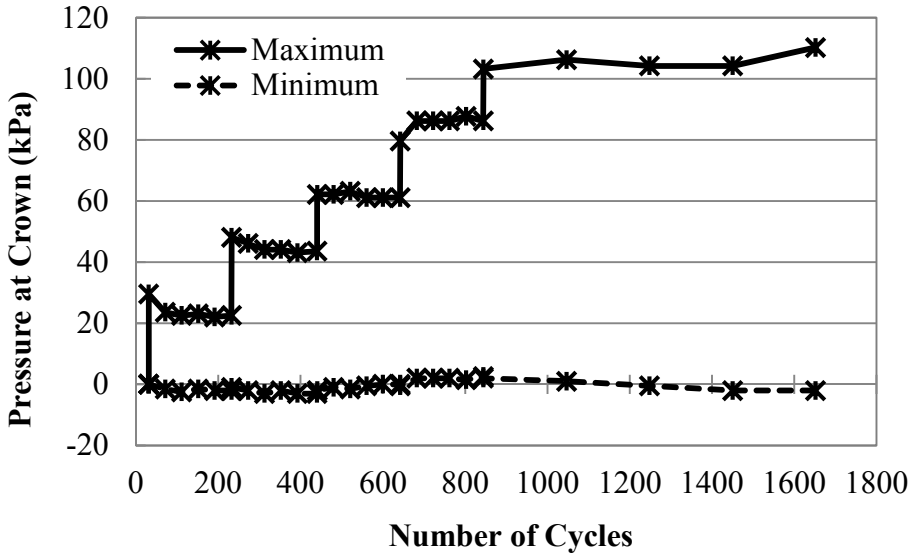

Figure 3.62 Vertical Pressures at Crown (C_2) with D.L. - Test 10

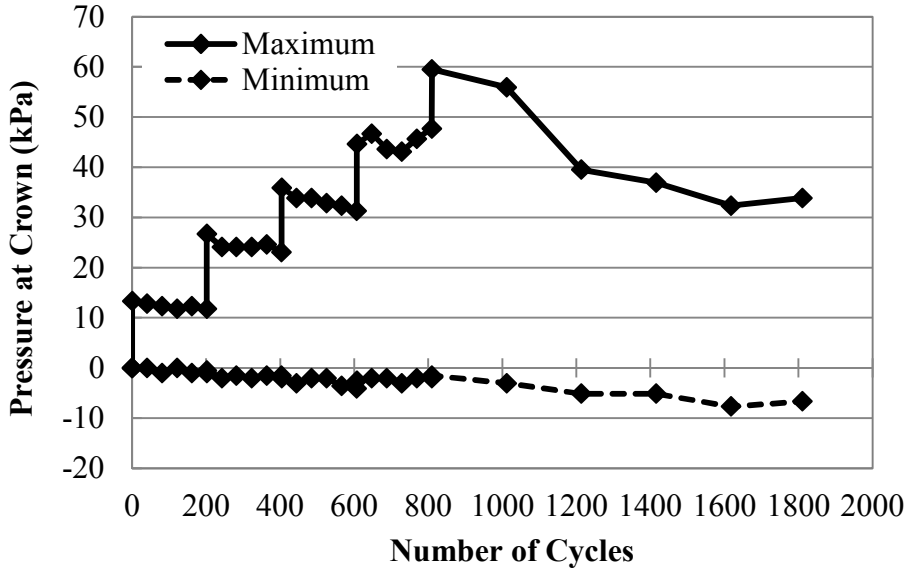

Figure 3.63 Vertical Pressures at Crown (C_3) with U.R. -Test 6

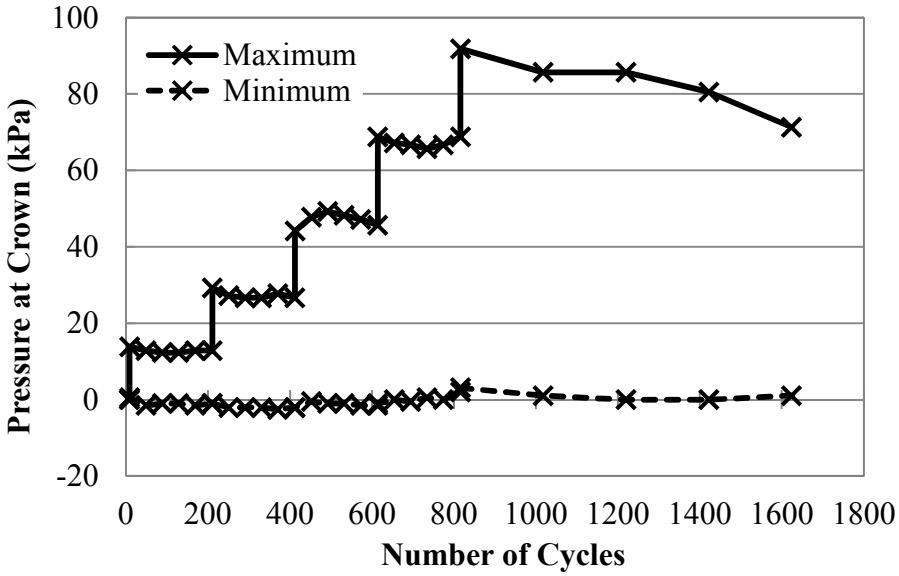

Figure 3.64 Vertical Pressures at Crown (C_3) with S.L. - Test 8

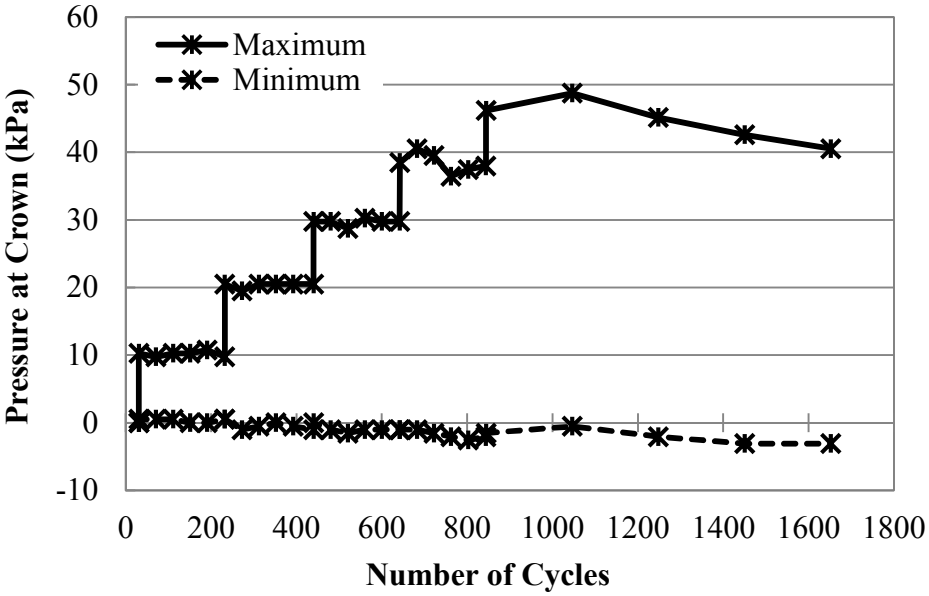

Figure 3.65 Vertical Pressures at Crown (C_3) with D.L. - Test 10

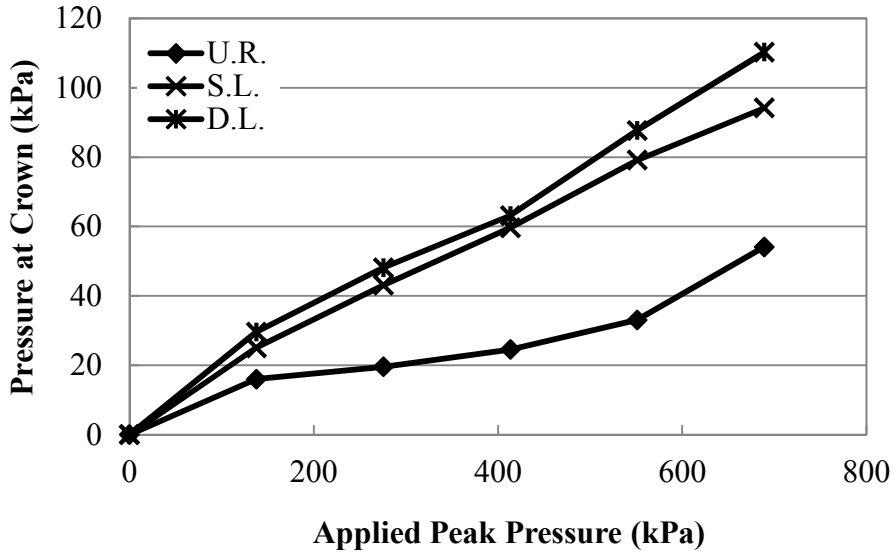

Figure 3.66 Maximum Vertical Pressures at Crown (C_2) – Tests 6, 8, and 10

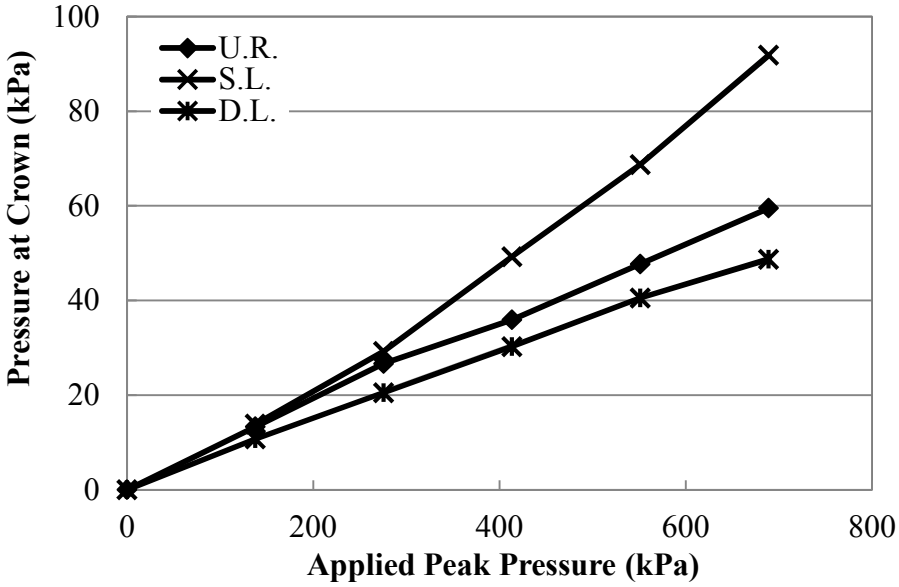

Figure 3.67 Maximum Vertical Pressures at Crown (C_3) - Tests 6, 8, and 10

Data output readings from the earth pressure cell directly under the base course (C_4) (i.e. 0.229 m deep under the loading plate), were recorded every 10^{th} of a second during the test. The data was reduced and the maximum and minimum recorded pressures over forty cycles are plotted in Figures 3.68 through 3.70. For both the singly and doubly reinforced condition the reduction of earth pressures, at the base course to backfill interface, was about 12.5 % from 400 kPa to 350 kPa. The recorded pressures at the earth pressure cell C_4 were less in the cyclic load case than the static load conditions for the unreinforced and singly reinforced conditions. In the doubly reinforced case the recorded pressures were higher in the cyclic load case than in the static load case. In both the static and the cyclic load cases there appears to be more distribution of the plate pressure with both reinforced conditions.

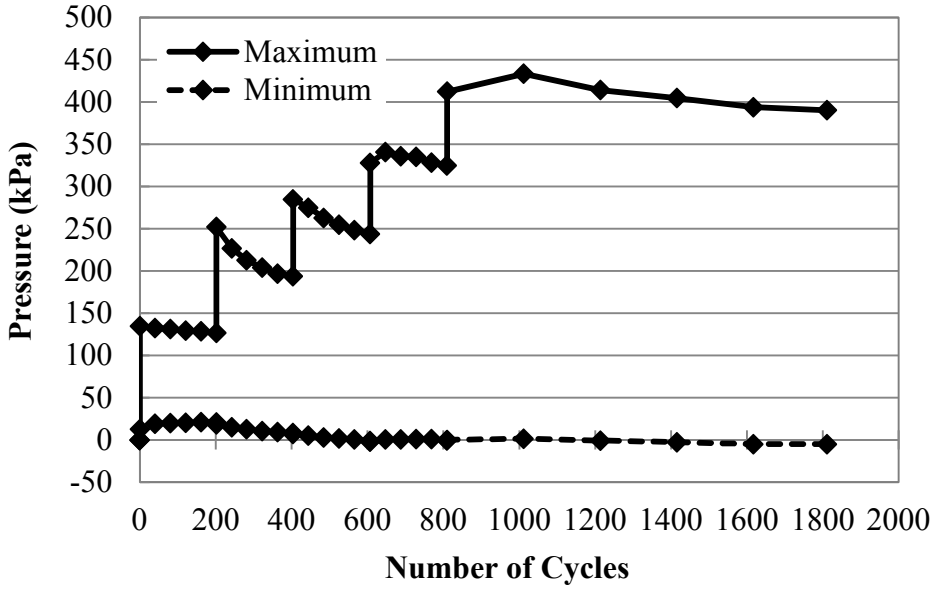

Figure 3.68 Vertical Pressures under Base Course (C_4) with U.R. - Test 6

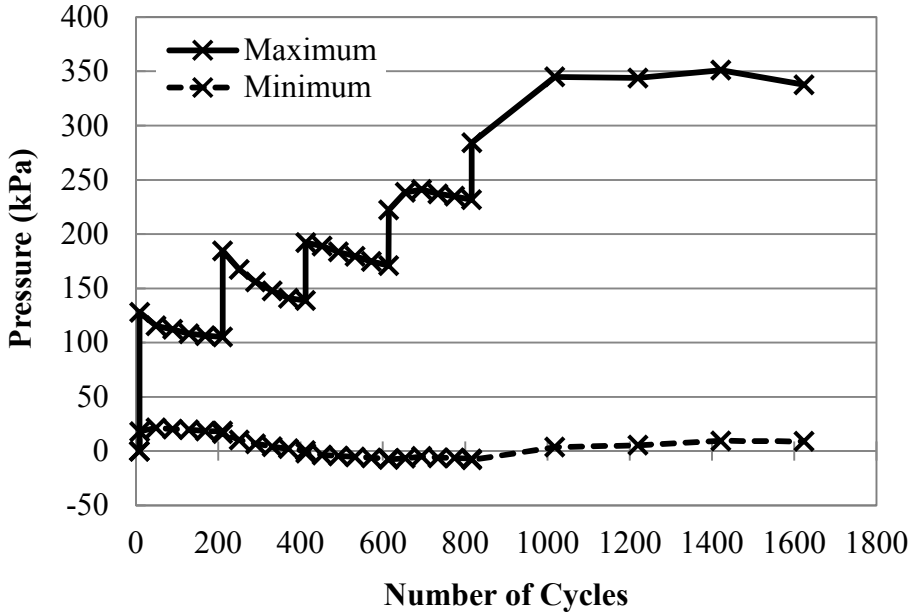

Figure 3.69 Vertical Pressures under Base Course (C_4) with S.L. - Test 8

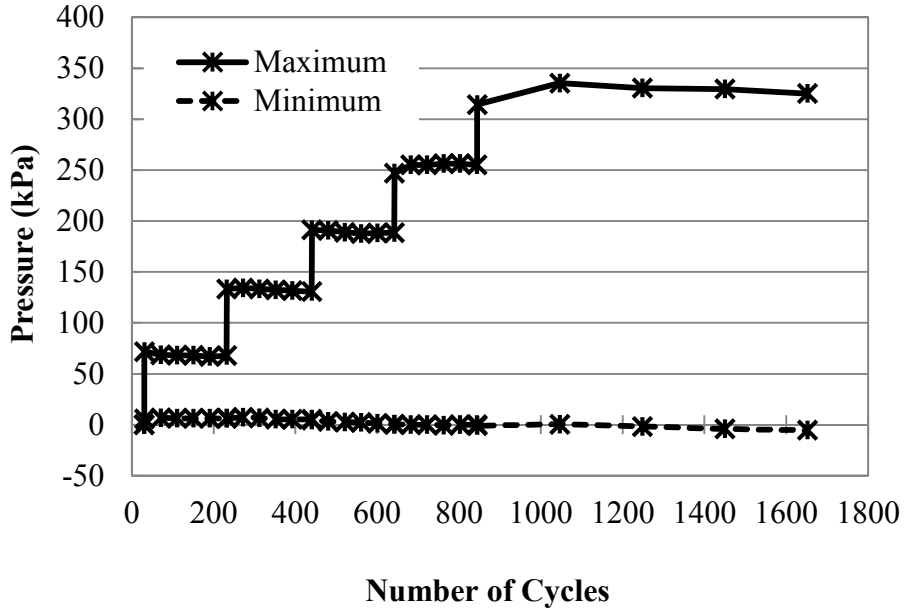

Figure 3.70 Vertical Pressures under Base Course (C_4) with D.L. - Test 10

Springline and Invert Pressures in Tests 1 and 4

Pressures were also recorded at the springline and the invert for tests 1 through 4. The springline and shoulder earth pressures are given in Figures 3.71 through 3.74, and the pressure distribution at the springline for each condition is given in Figure 3.75. It is critical to note that there appears to be no or little difference in the pressures over the pipe between the reinforced and unreinforced conditions at the springline. Figures 3.76 and 3.77 represent the recorded values at the invert for tests 1 through 4.

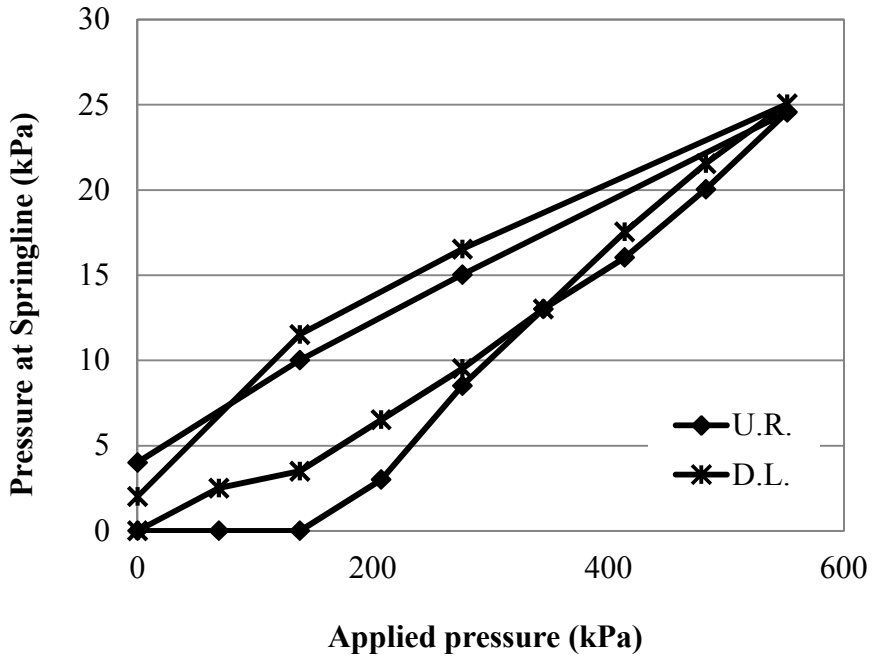

Figure 3.71 Pressures at Springline (S_1) - Tests 1 and 4

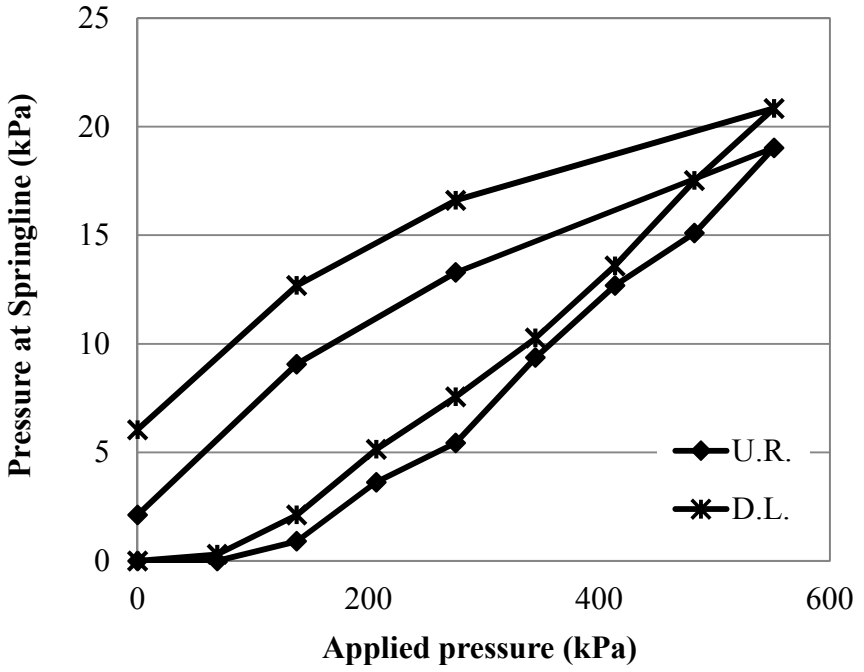

Figure 3.72 Pressures at Springline Shoulder (S_2) - Tests 1 and 4

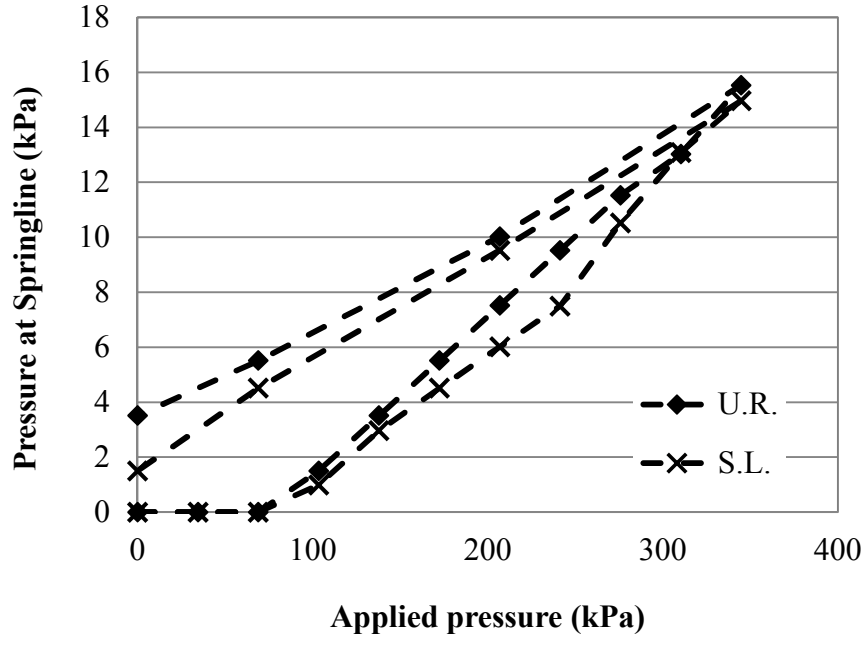

Figure 3.73 Pressures at Springline (S_1) - Tests 2 and 3

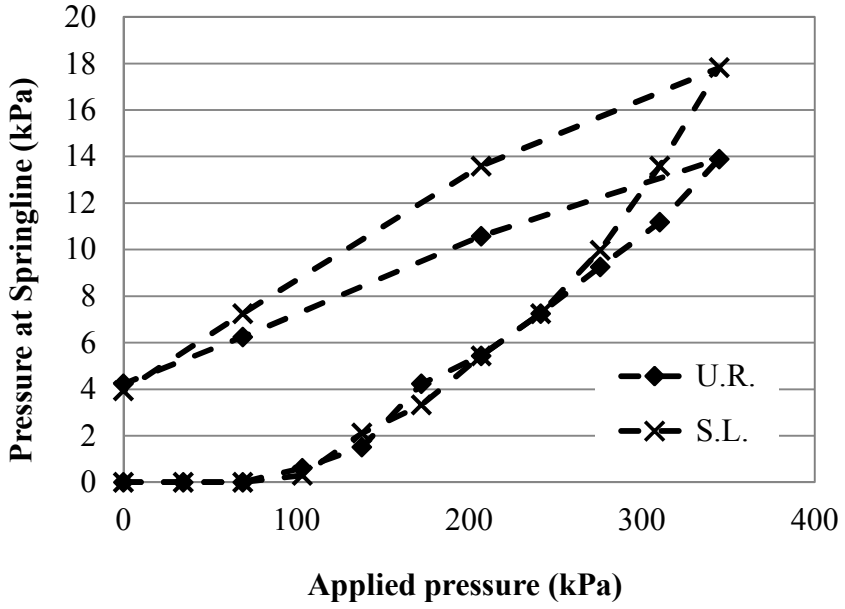

Figure 3.74 Pressures at Springline (S_2) - Tests 2 and 3

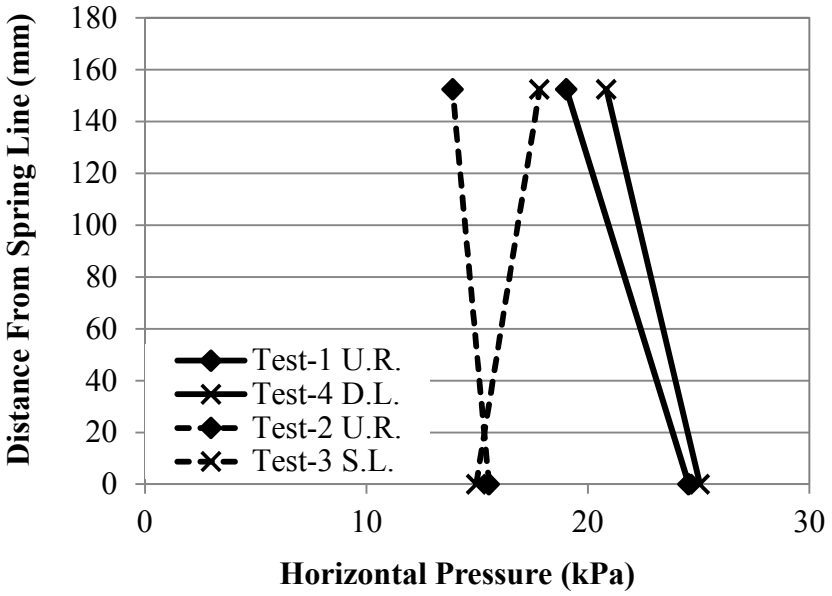

Figure 3.75 Pressure Distributions at Springline - Tests 1, 2, 3, and 4

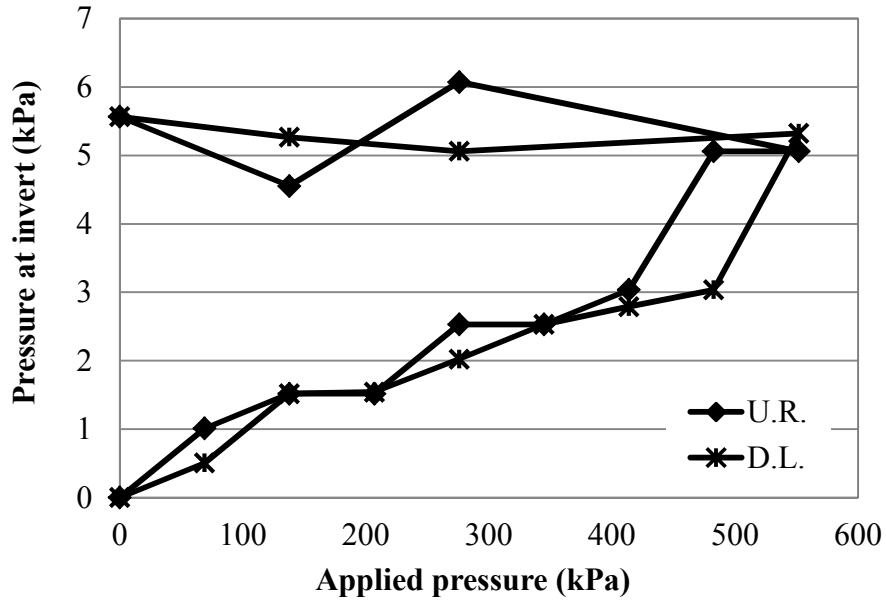

Figure 3.76 Pressures at Invert (I_1) - Tests 1 and 4

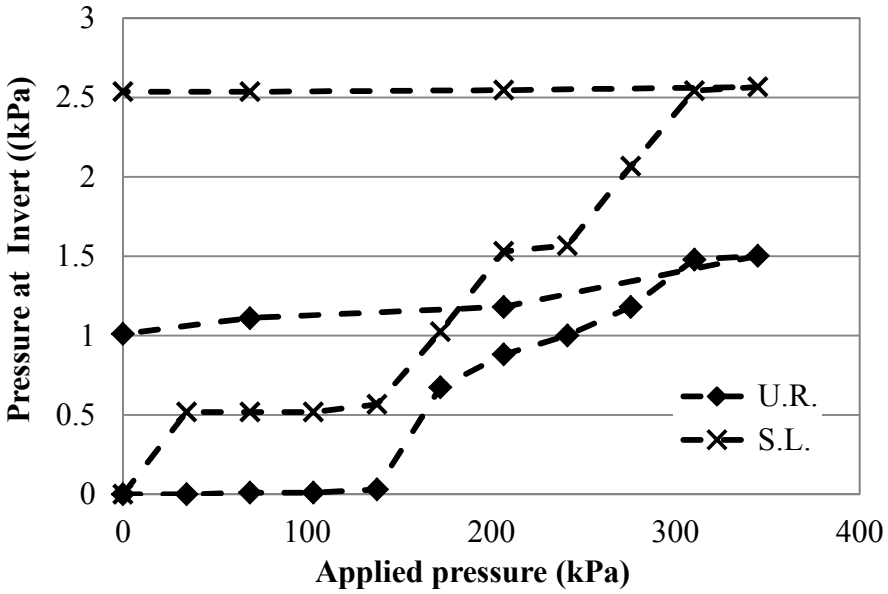

Figure 3.77 Pressures at Invert (I_1) - Tests 2 and 3

Springline and Invert Pressures in Tests 5 through 10

Pressures were also recorded at the springline and the invert for tests 5 through 10. The pressure distributions at the springline for test 5, 7, and 9 are shown in Figure 3.78. Similar to the sand backfill conditions there did not appear to be a significant redistribution of soil pressures except for that at the shoulder. Figures 3.79 and 3.80 represent the recorded vertical pressures at the springline and the invert. For the cyclic load tests the horizontal pressure distribution is shown in Figure 3.81, while the vertical pressures at the invert and at the springline are shown in Figures 3.82 and 3.83 respectively. The maximum recorded pressures in the static load and cyclic load cases appear to be very similar, and the effects of the geogrid are proportional for each case.

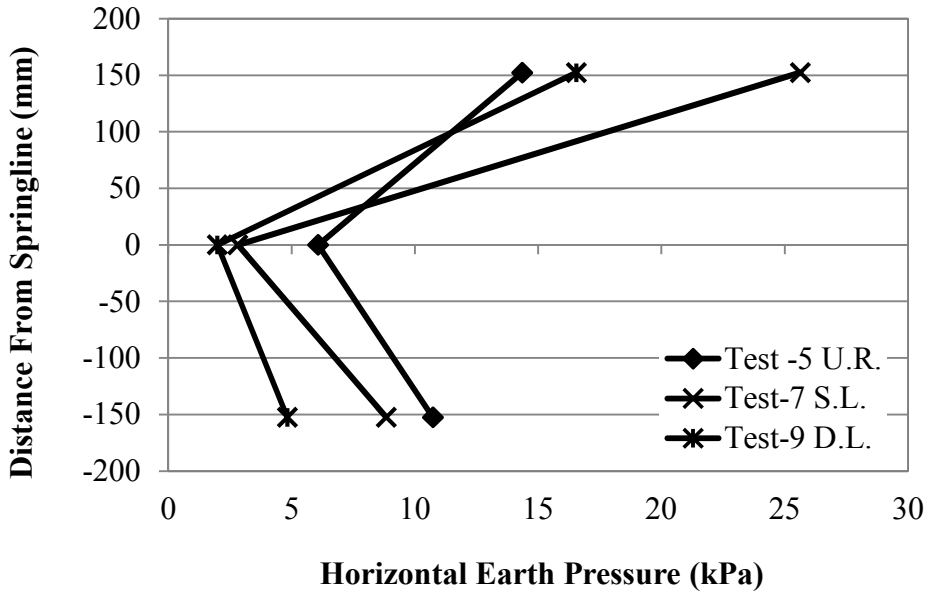

Figure 3.78 Springline Pressure Distributions at Maximum Applied Pressure – Tests 5, 7 and 9

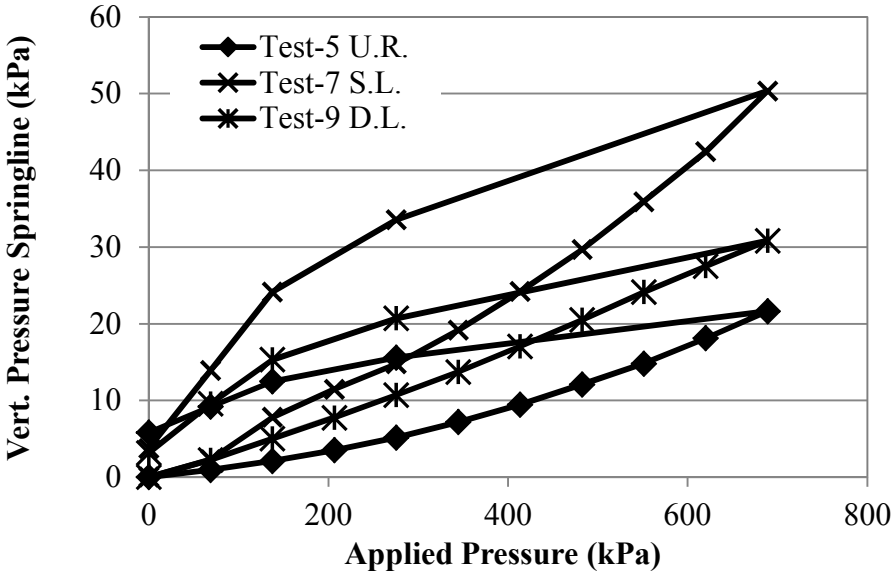

Figure 3.79 Vertical Pressures at Springline – Tests 5, 7, and 9

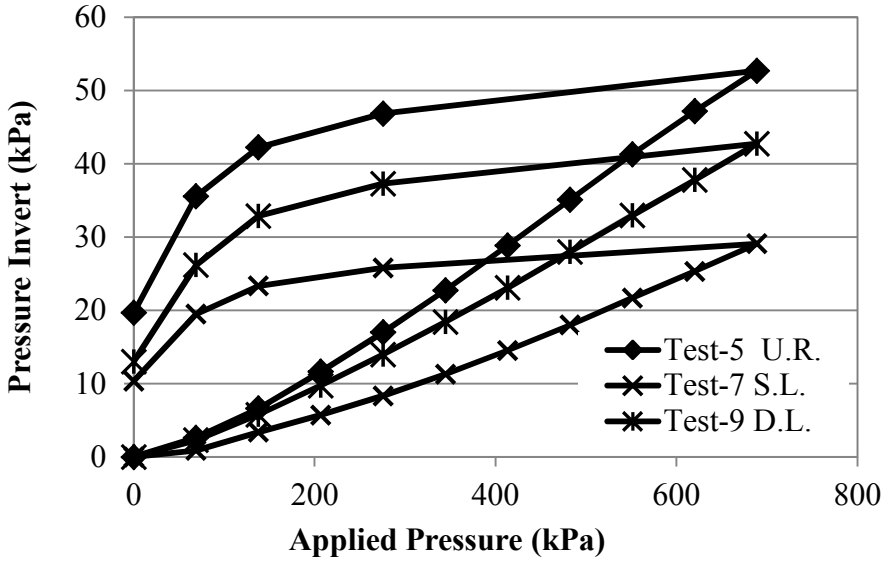

Figure 3.80 Pressures at Invert – Tests 5, 7, and 9

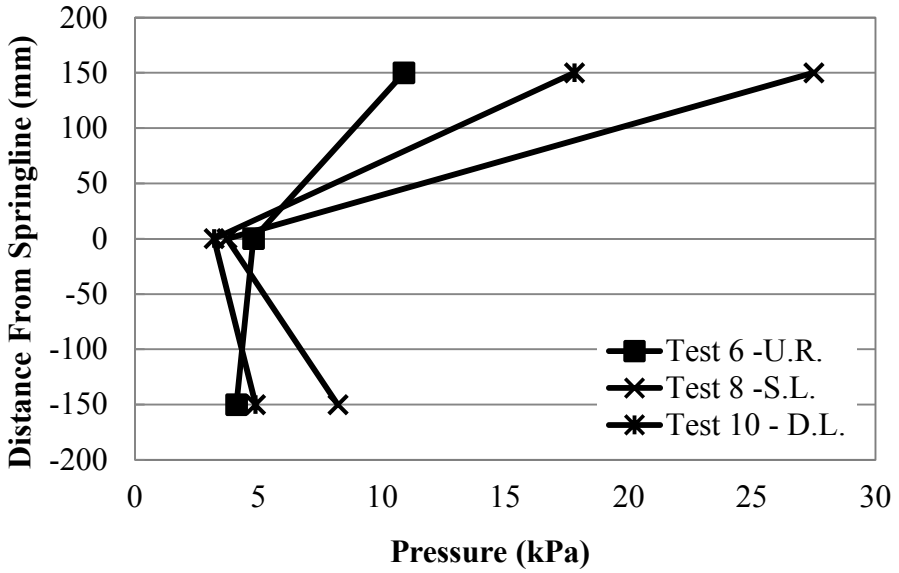

Figure 3.81 Springline Pressure Distributions at the Maximum Applied Pressure – Tests 5, 7, and 9

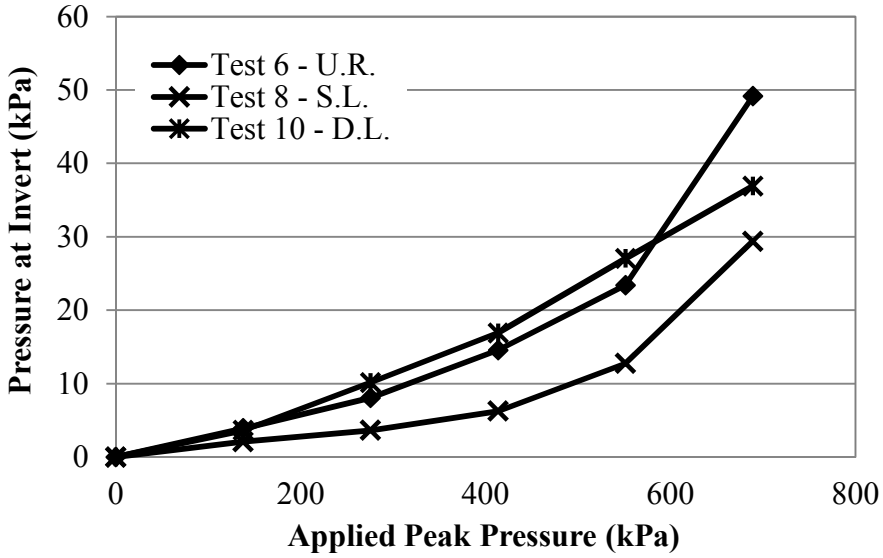

Figure 3.82 Maximum Pressures at Invert Tests 6, 8, and 10

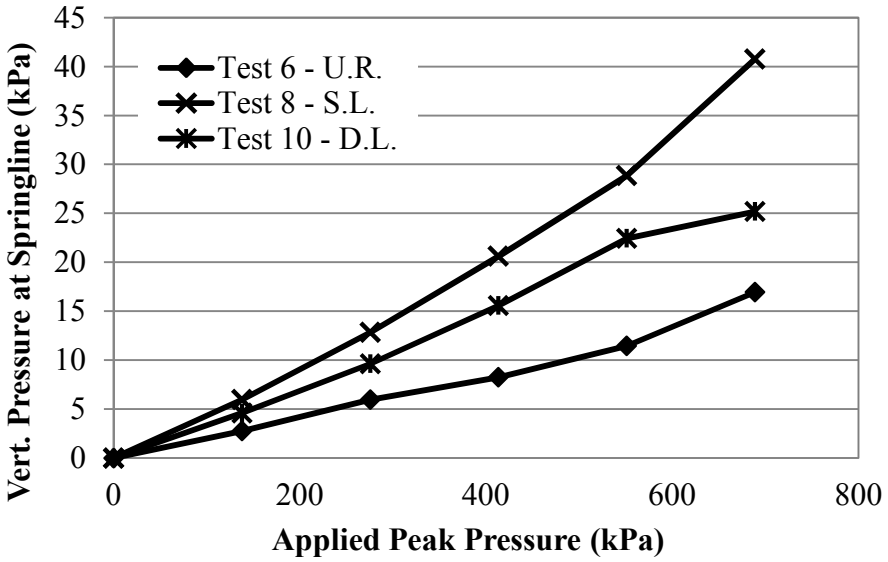

Figure 3.83 Maximum Vertical Pressures at Springline Tests 6, 8, and 10

3.8.4 Pipe Strain

Pipe strains were recorded during loading with 17 strain gauges located at the springline, invert, and the crown for each test (Figures 3.84 and 3.85). Some strain gauges failed or exceeded the allowable range of measureable strains by the gauge. The strains of failed strain gauges or inconclusive data were not included in the following plots and can be seen in the Appendix. Positive strains are tensile and negative strains are compressive.

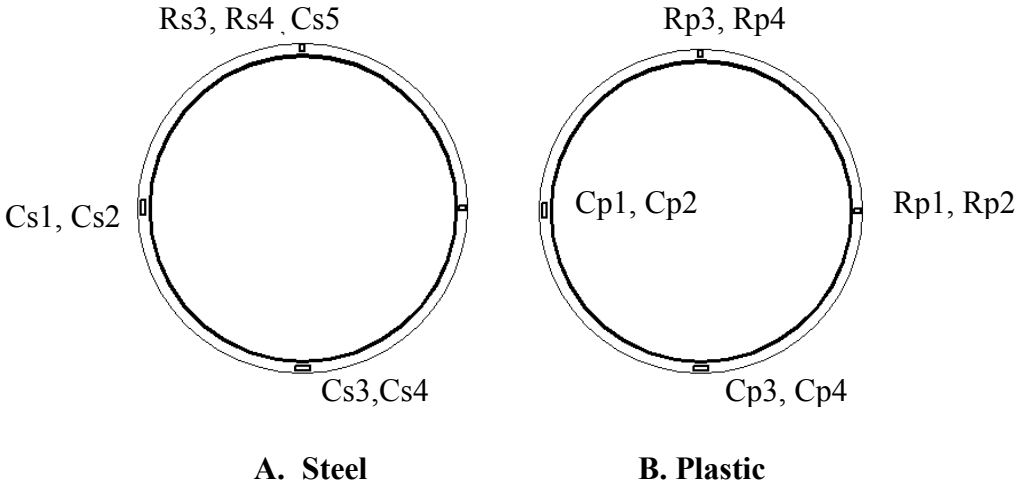

Figure 3.84 Circumferential and Radial Strain Gauge Locations

The composite behavior of the pipe wall, and the very small recorded strains, make interpretation and analysis of the strain results difficult. In many cases, it is difficult to draw any conclusion from the strain gauge response. The strain gauges at locations around the pipe recorded similar behavior, with each strain gauge showing the same apparent haphazard response (Figures 3.86, 3.87, and 3.88). This indicates that the strain gauge response and corresponding plotted data, while seemingly arbitrary, was accurate.

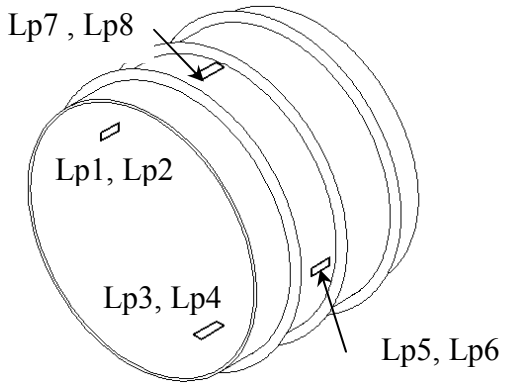

Figure 3.85 Longitudinal Strain Gauge Locations

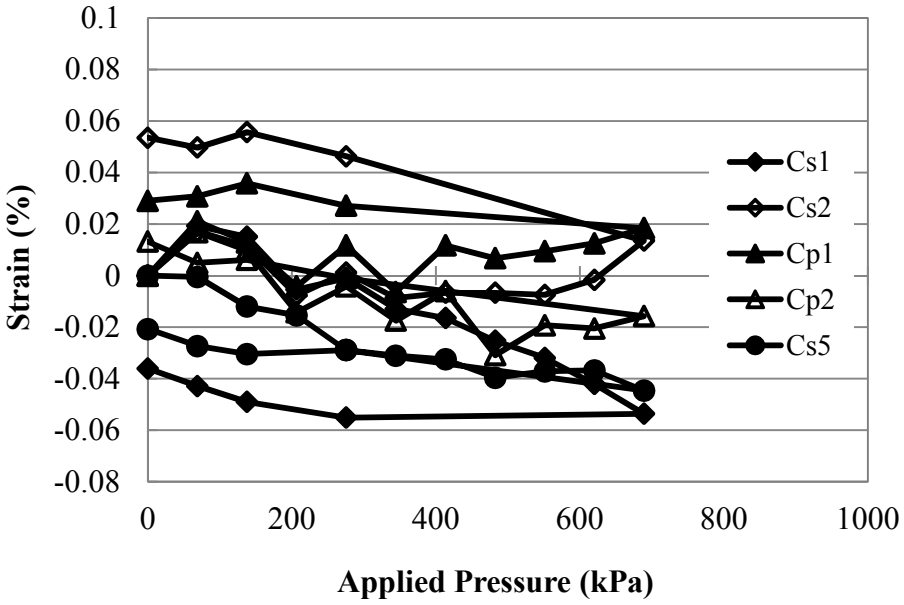

Figure 3.86 Circumferential Strains at Springline - Test 5

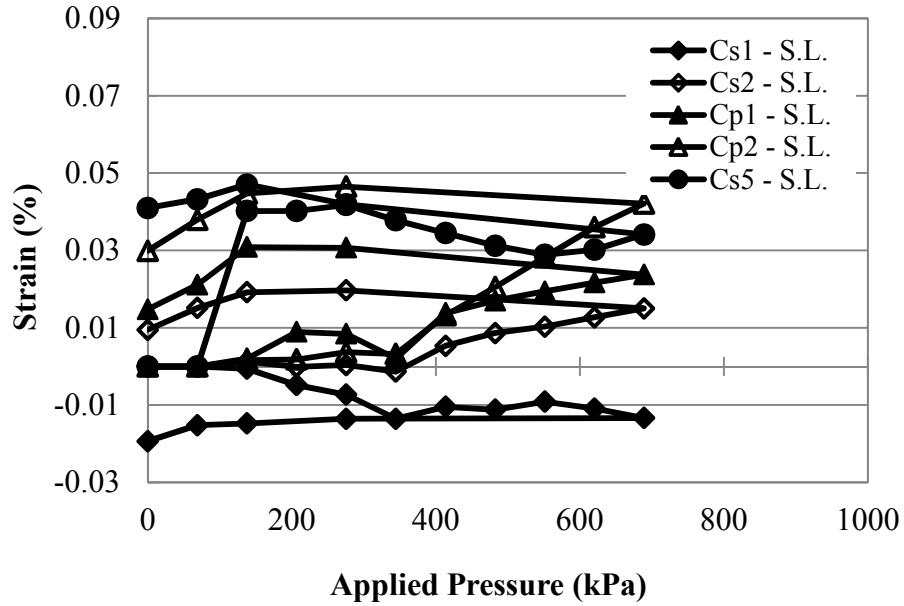

Figure 3.87 Circumferential Strains at Springline – Test 7

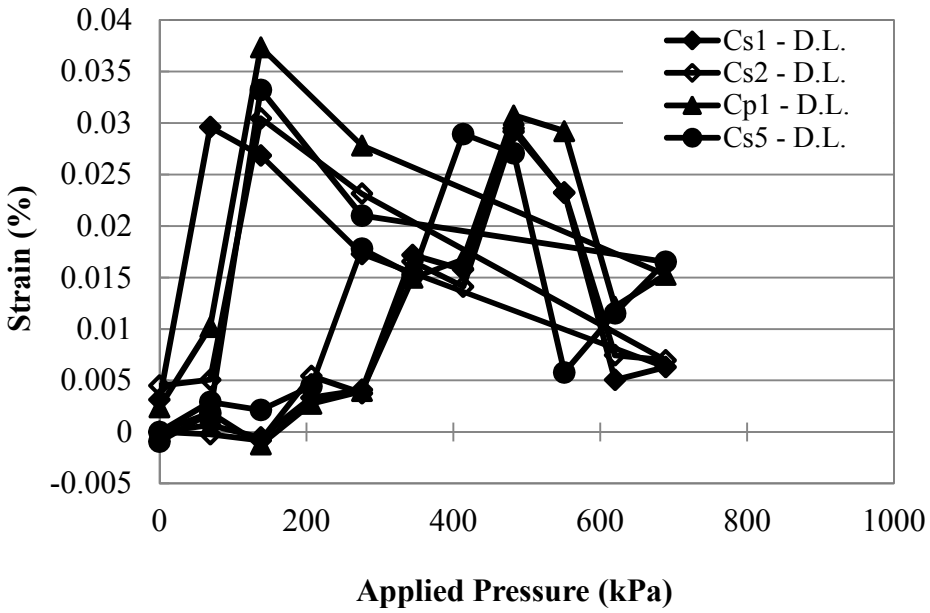

Figure 3.88 Circumferential Strains at Springline - Test 9

Circumferential Strains

Even with the small strain, some strain gauge readings were still straight forward and some conclusions could be drawn from the response of the strain gauge. On tests 1 and 4, for example, the strain gauge Cp1, on the plastic at the springline (Figure 3.89), shows a distinct and smooth transition of strain as the plate pressure was applied. The strain on the plastic shell began as a compressive strain and transitioned to tension. The strain data indicates that the strain gauge was placed on the outside of the neutral axis of the pipe wall, and that as bending occurred at the springline, the strain gauge went into tension. The corresponding strain gauge Cp2 on the other side of the rib (Figure 3.90) showed no clear pattern.

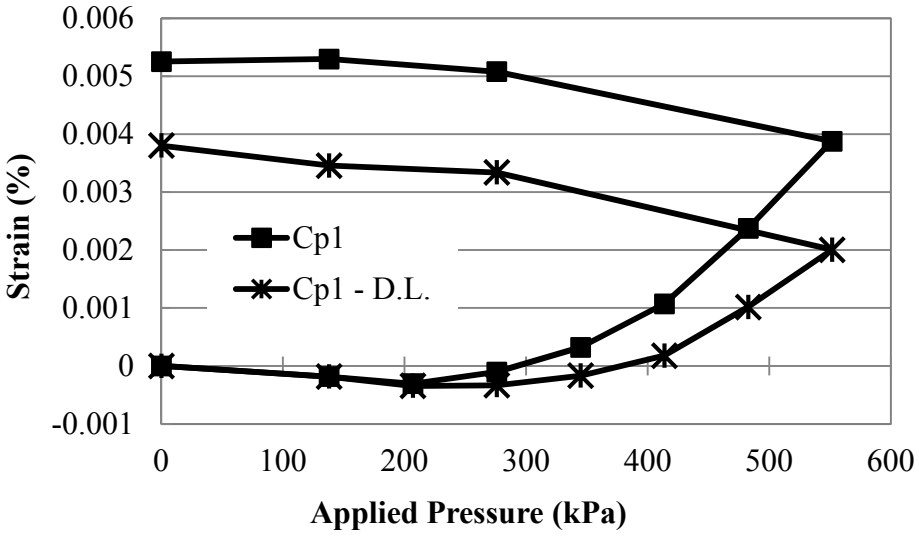

Figure 3.89 Circumferential Strains at Springline Cp1 in Test 1 and 4

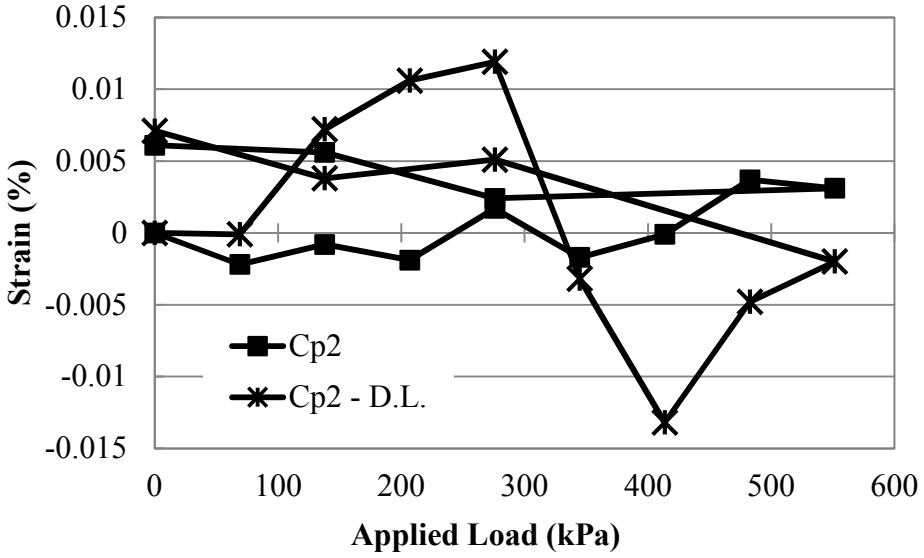

Figure 3.90 Circumferential Strains at Springline Cp2 in Test 1 and 4

Comparatively, the strain recorded at Cs1 (Figures 3.91), which was one rib away at the same location, on the steel, shows only an increase in the compressive strain. Most circumferential strains, for instance at the crown Cs5 (Figure 3.92) showed no clear pattern.

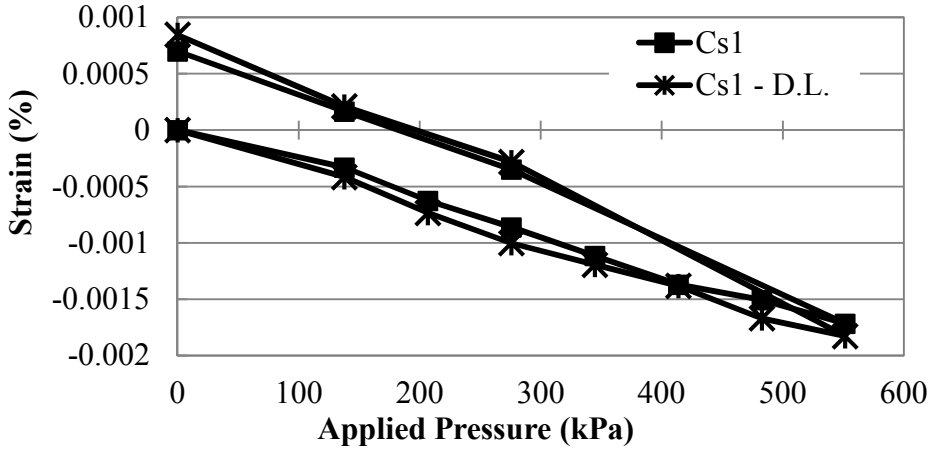

Figure 3.91 Circumferential Strains at Springline Cs1 in Test 1 and 4

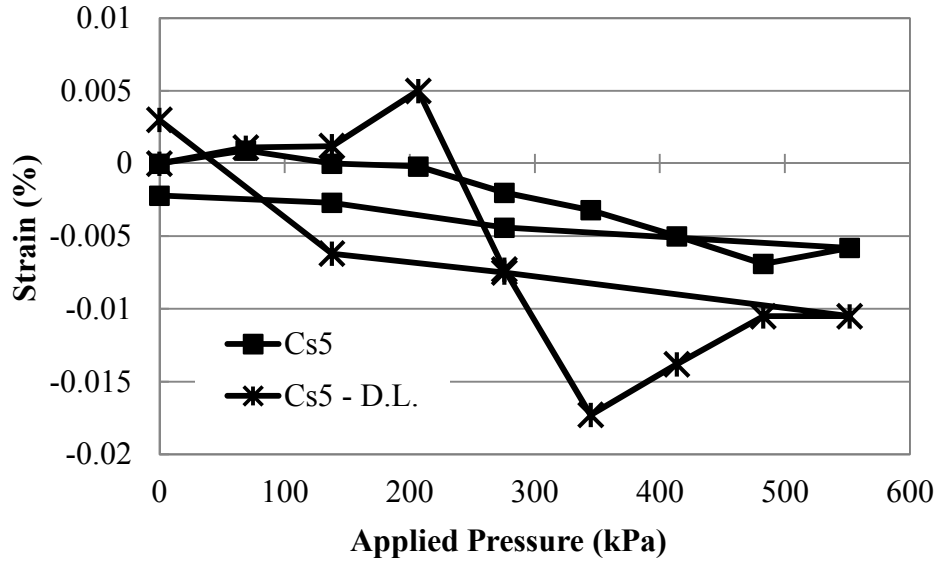

Figure 3.92 Circumferential Strains at Crown Cs5 in Test 1 and 4

Tests 2 and 3 with the sand backfill and sand base course showed a similar pattern. The circumferential strains on the plastic, in some locations showed a clear pattern (Figure 3.93),

while on the other side of the same rib (Figure 3.94), the strain gauge showed a less clear pattern. For the plastic, based on the shape of the strain versus load curve, it again appeared that the most strain came from bending. On the steel rib the circumferential strain was generally in compression as would be expected, and greatest at the crown (Figures 3.95 through 3.97). The strains in the circumferential direction were also linear with respect to the applied pressure. It appears that the single layer of geogrid actually increased strain in the circumferential direction. In the unreinforced cases there was a sudden drop in strain at 310 kPa, when there was a loss of confinement in the backfill and the stress in the backfill redistributed.

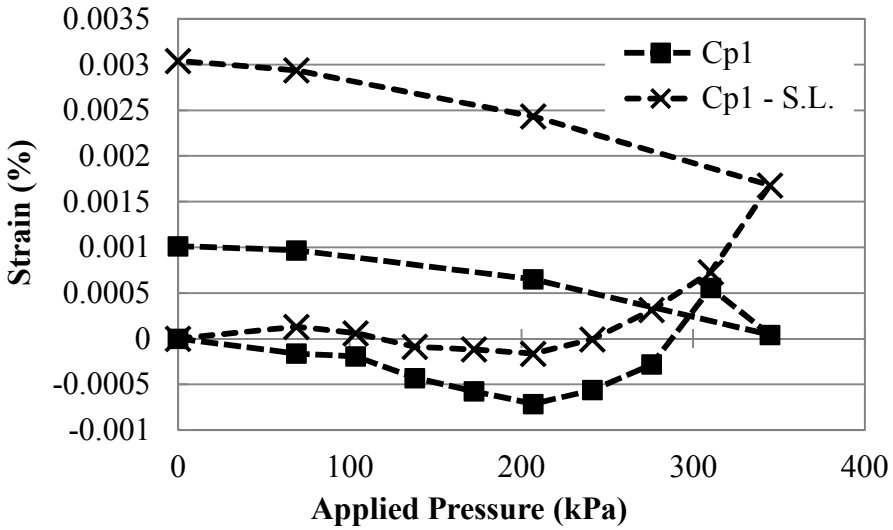

Figure 3.93 Circumferential Strains at Springline Cp1

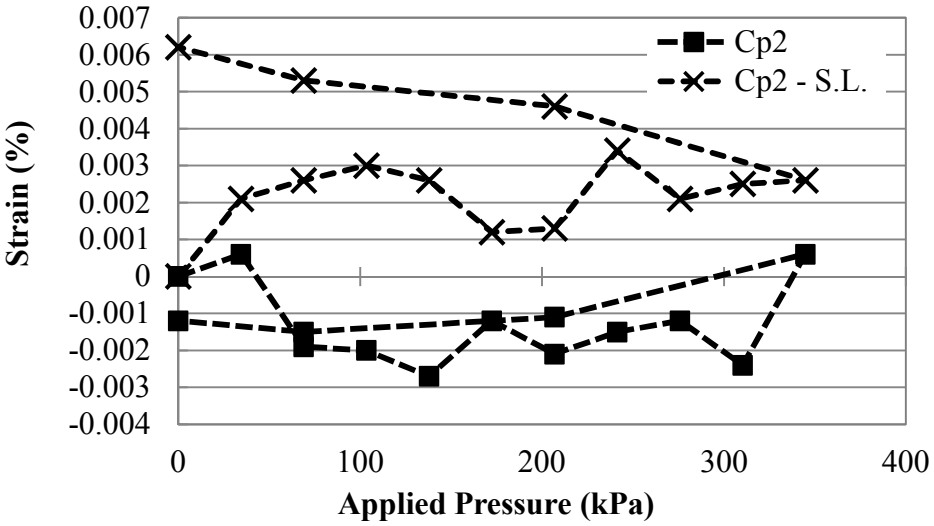

Figure 3.94 Circumferential Strains at Springline Cp2

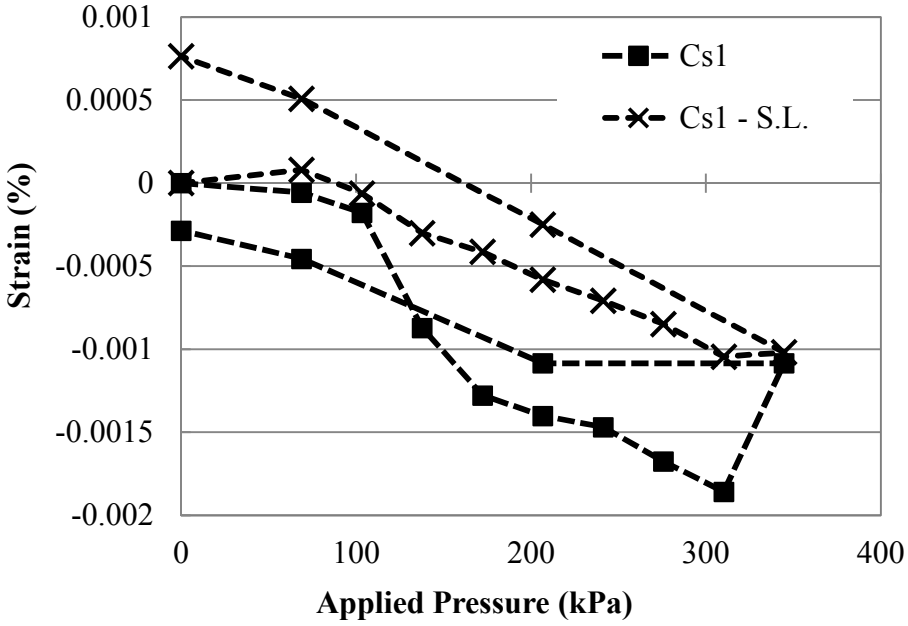

Figure 3.95 Circumferential Strains at Springline Cs1

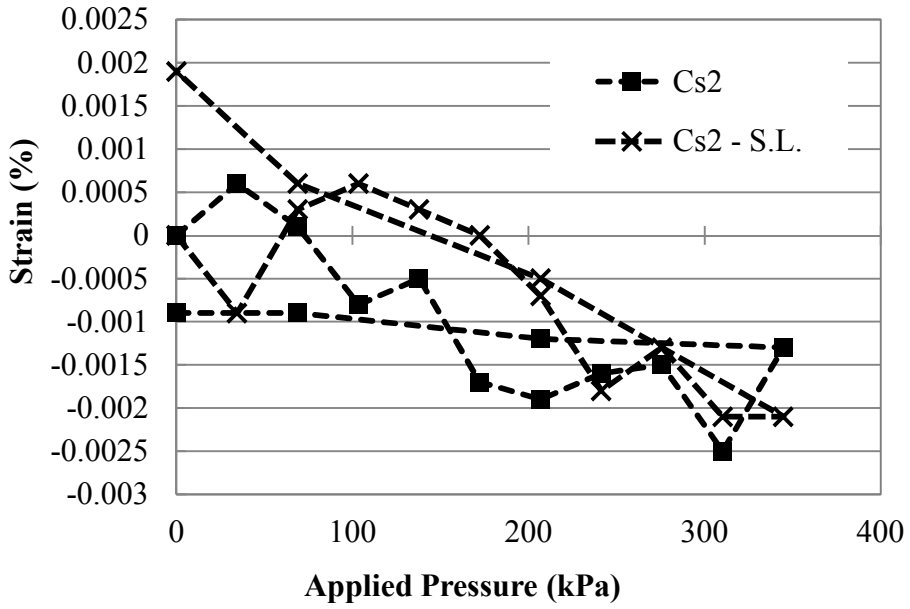

Figure 3.96 Circumferential Strains at Springline Cs2

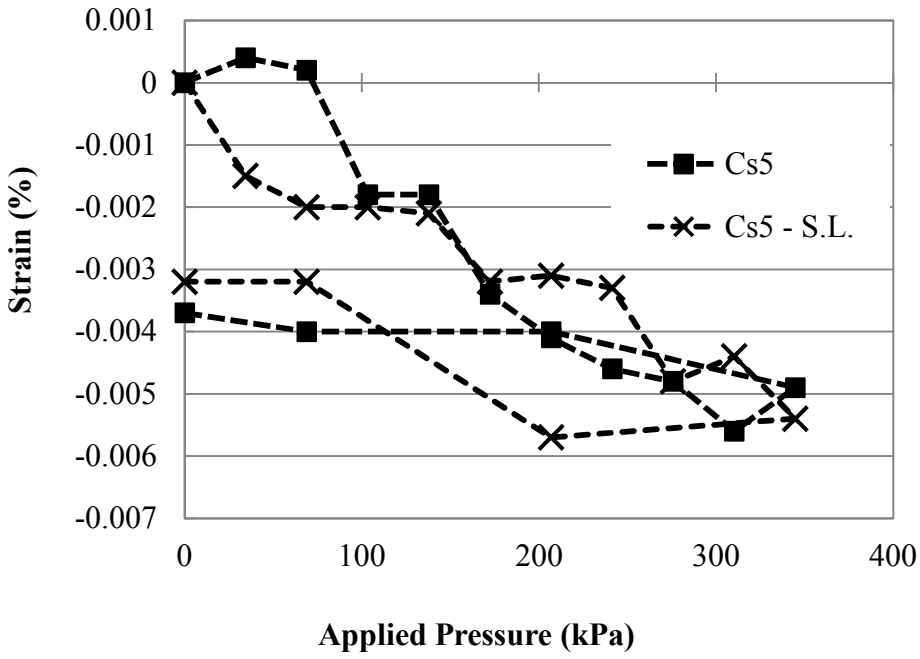

Figure 3.97 Circumferential Strains at Crown C_{s5}

Circumferential strains for the crushed stone backfill during the static tests (Tests 5, 7, and 9) were more difficult to interpret than the strains recorded in the sand backfill conditions. None of the smooth responses like those in the sand condition were recorded. It is assumed that at the recorded small strains the interaction with the aggregate caused a non-uniform or less clear response. Overall there appeared to be no difference in the circumferential plastic strain (Figure 3.98), between the reinforced and unreinforced cases. There did however appear that there was some possible strain reduction in the steel core (Figures 3.99 through 3.101).

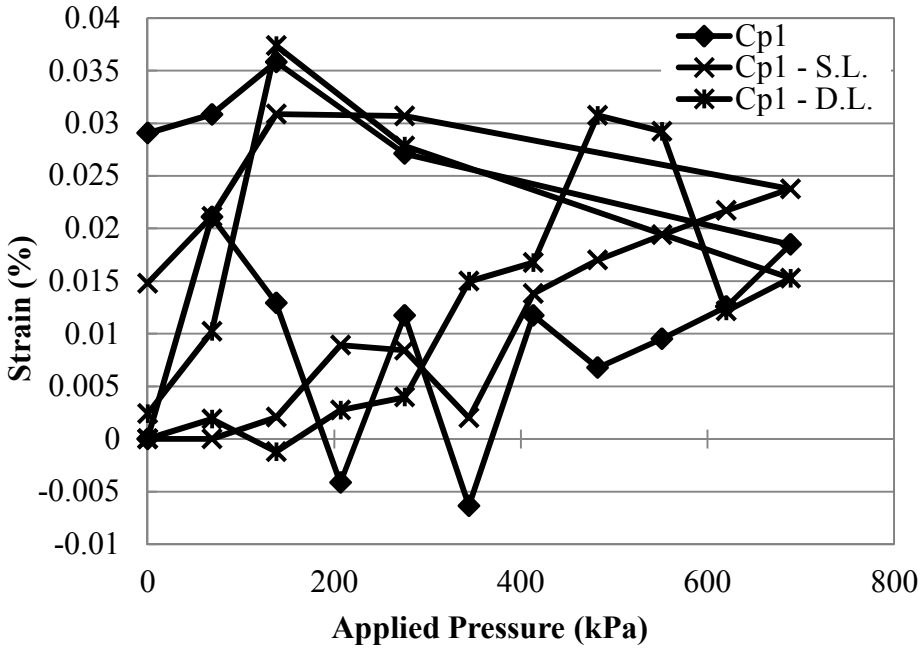

Figure 3.98 Circumferential Strains at Springline – Plastic Cp1

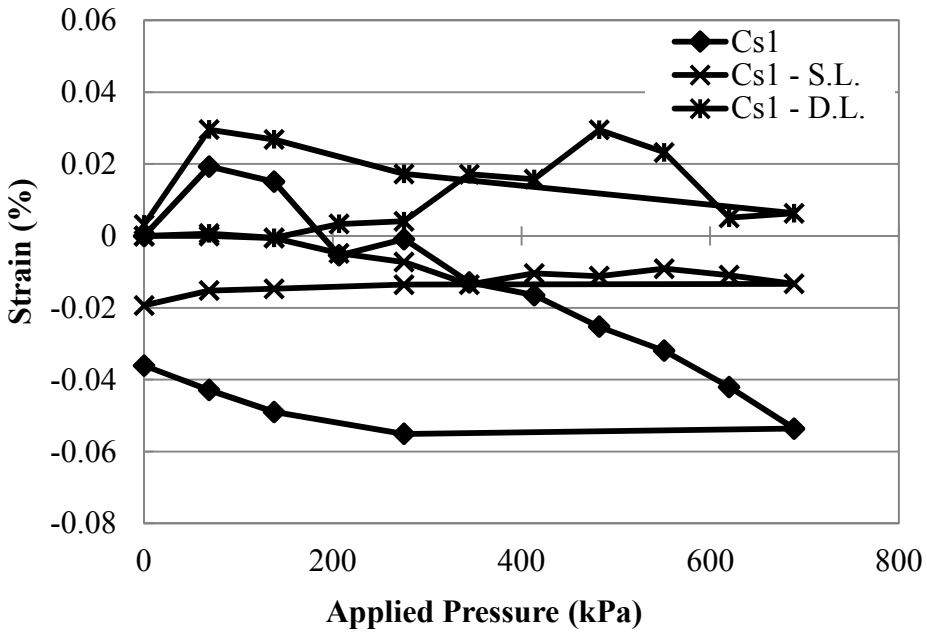

Figure 3.99 Circumferential Strains at Springline – Steel C_{s1}

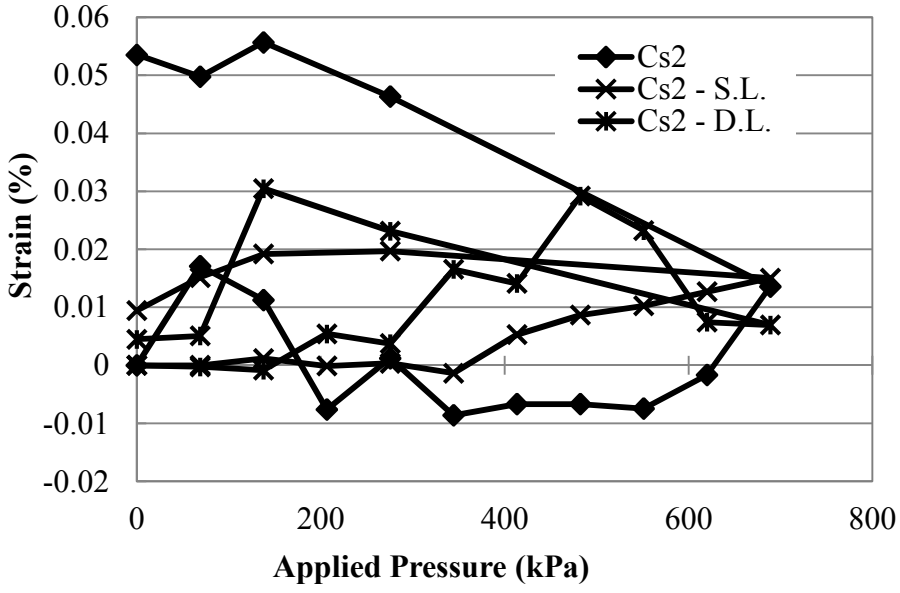

Figure 3.100 Circumferential Strains at Springline – Steel Cs2

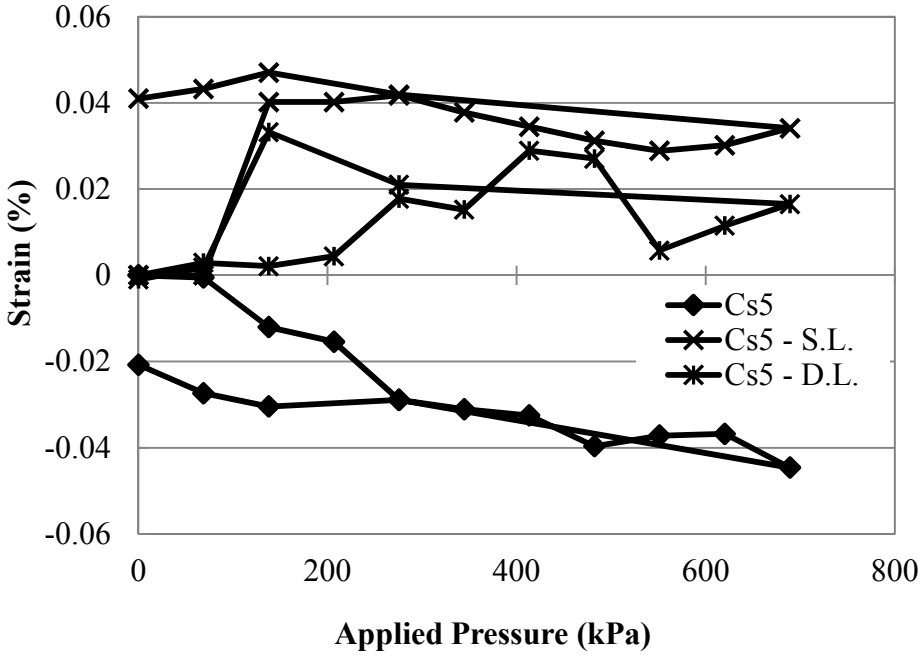

Figure 3.101 Circumferential Strains – Steel Cs5

During the cyclic load tests (Tests 6, 7, and 8) strains were recorded continuously every tenth of a second and the maximum strains, both compression and tension, are plotted versus the peak applied pressure during the cycle in the following graphs. In these figures a clearer picture of the benefit of the inclusion of the geosynthetic can be seen. On the plastic at the springline (Figure 3.102) a dramatic reduction in the plastic strain can be seen with the inclusion of the geogrid. At the springline the circumferential strain on the steel core (Figures 3.103 and 3.104) was also reduced by a minimum of fifty percent for the single layer of reinforcement and up to a seventy percent reduction for the two layers of geogrid. The strain at the crown (Figure 3.105) appeared to increase with the inclusion of geogrid.

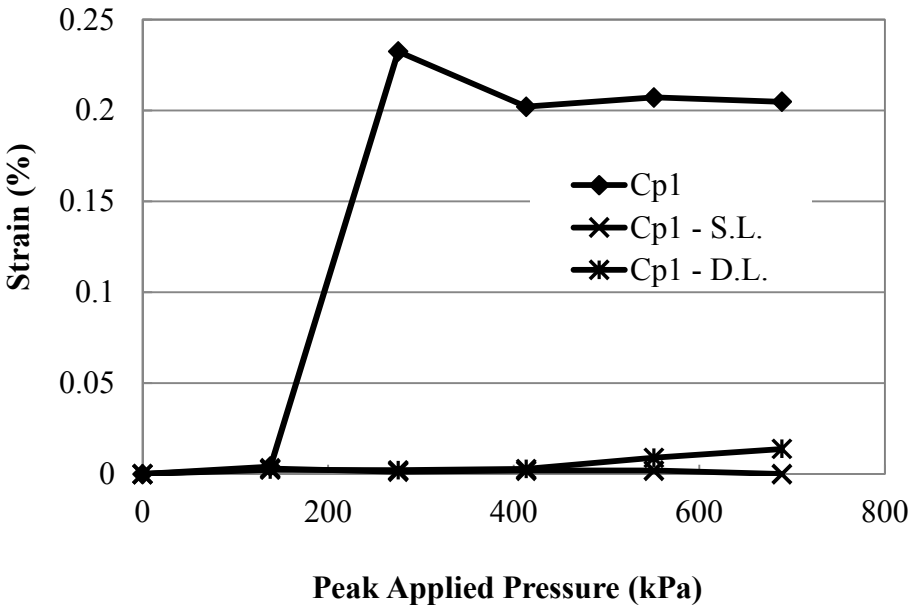

Figure 3.102 Maximum Circumferential Strains at the Springline (Cp1)

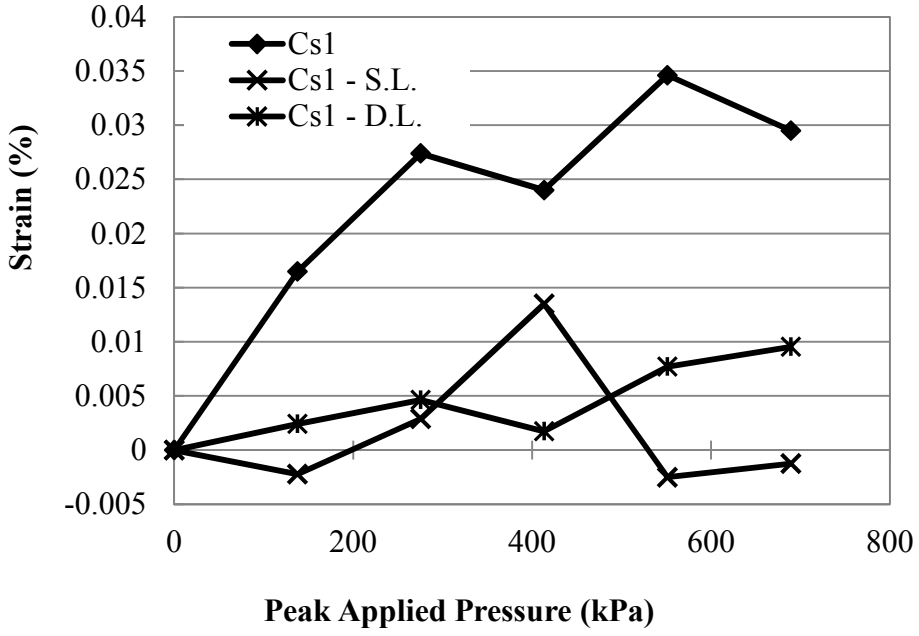

Figure 3.103 Maximum Circumferential Strains at Springline (Cs1)

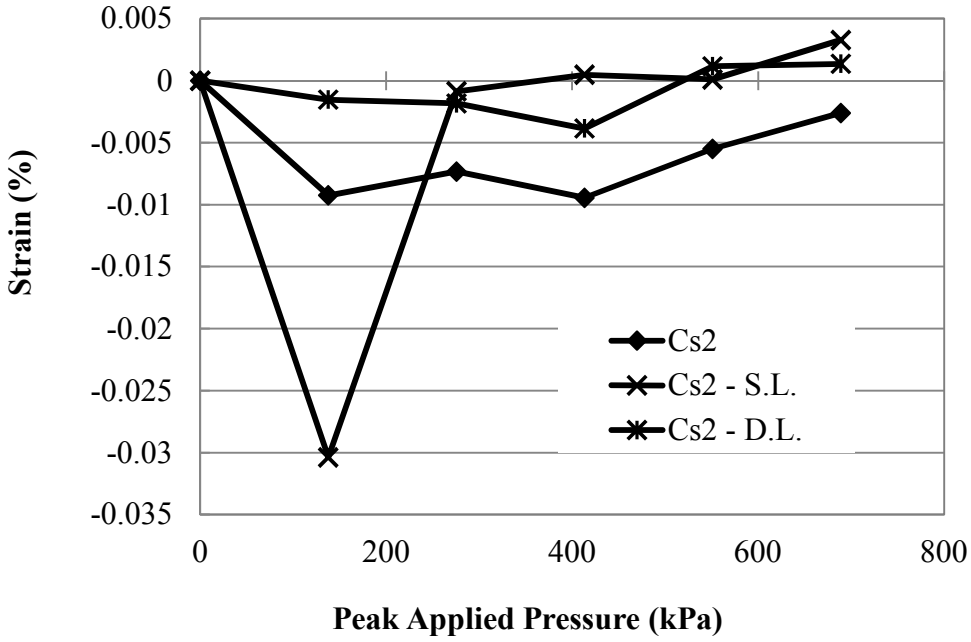

Figure 3.104 Maximum Circumferential Strains at Springline (Cs2)

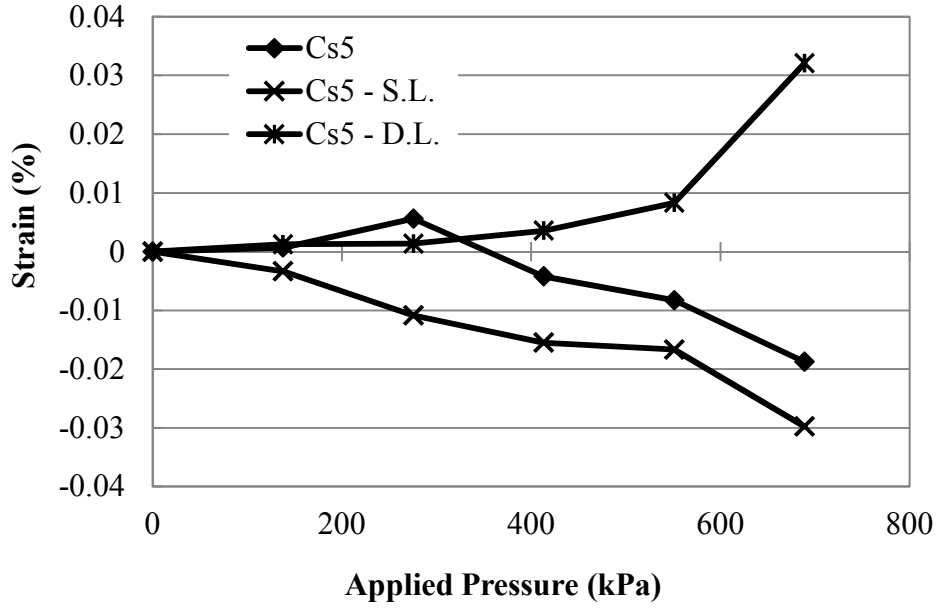

Figure 3.105 Maximum Circumferential Strains at the Crown (Cs5)

Longitudinal Strains

The largest strains consistently recorded in each test, were the longitudinal strains at the crown of the pipe. Both strains in the plastic shell on the inside and the outside of the pipe were in tension. It was unclear what the mechanism for the development of the strain was, since both sides are in tension, and in most cases, greater on the outside of the shell, which is counter to standard plate bending. It is conjectured that the corrugations of the pipe are resisting the lateral spreading and shear stresses at the interface between the backfill and the pipe caused by the concentrated load. In the sand backfill, the geogrid was only able to slightly reduce the strains in the pipe longitudinal direction (Figures 3.106 through 3.109).

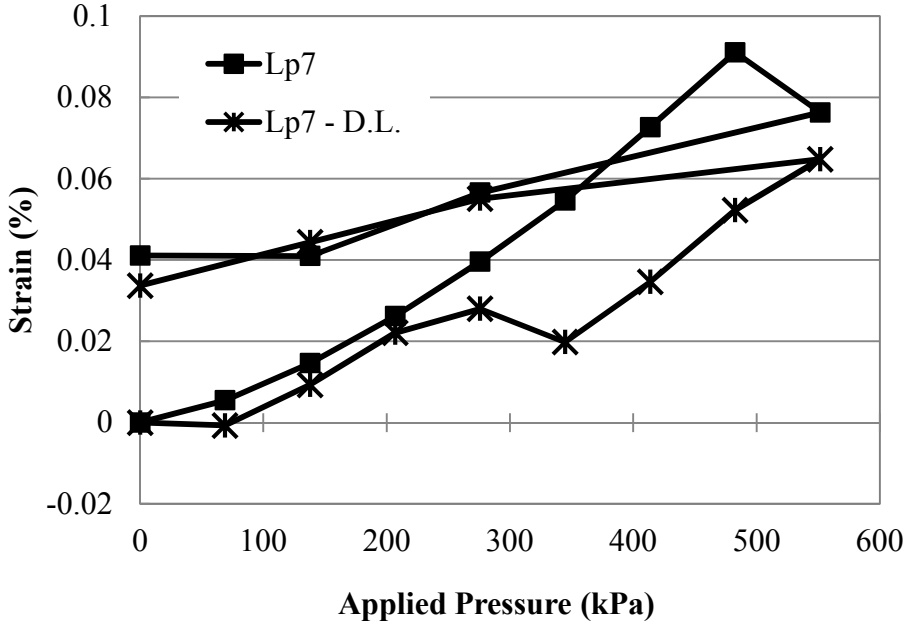

Figure 3.106 Longitudinal Strains at Crown Lp7

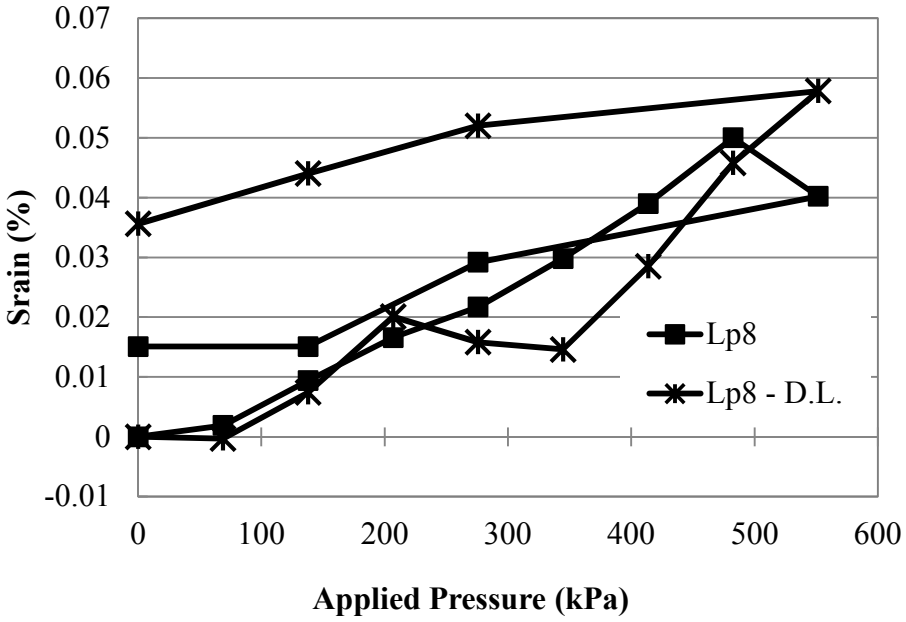

Figure 3.107 Longitudinal Strains at Crown Lp8

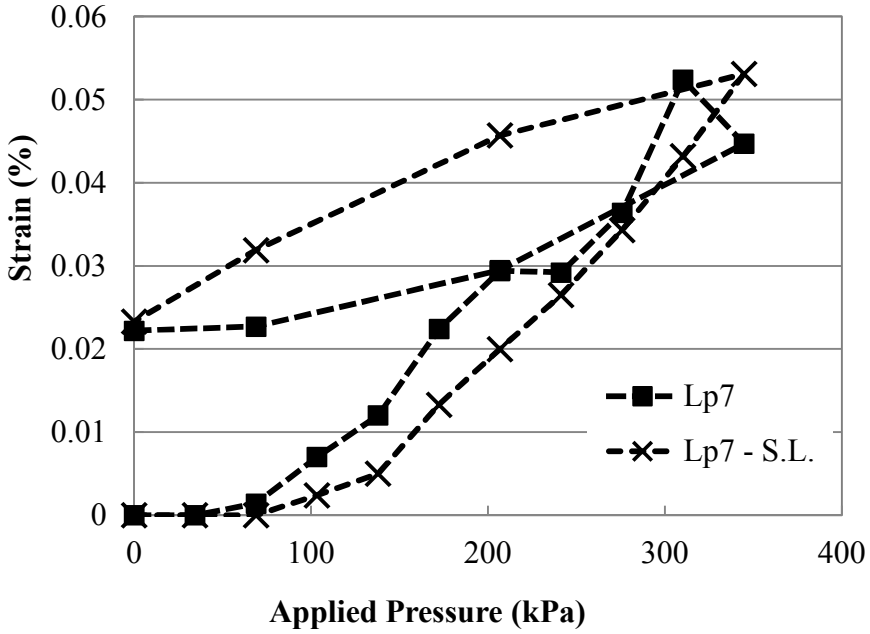

Figure 3.108 Longitudinal Strains at Crown - Lp7

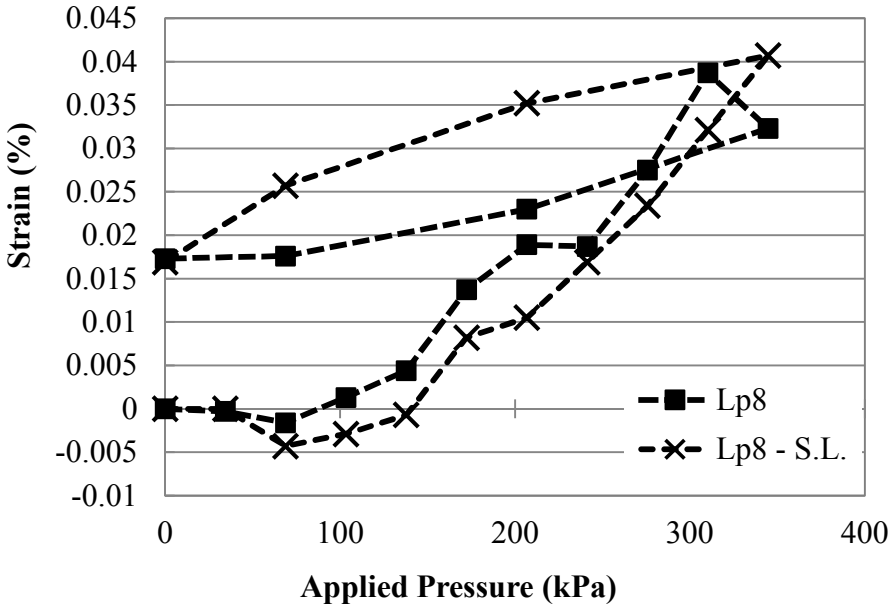

Figure 3.109 Longitudinal Strains at Crown - Lp8

In the aggregate backfill there was a significant reduction in the longitudinal strain due to the inclusion of the geogrid (Figures 3.110 and 3.111). Similar to the sand backfill condition the response of the pipe was tensile strain both on the inside and the outside of the pipe shell. Given that the longitudinal strain gauge Lp7 was on the outside of the shell and the tensile strain dropped to almost zero while the strain gauge Lp8 on the inside of the shell was still in tension, it is assumed that the geogrid reduced the tensile strain due to the lateral spreading of the backfill over the pipe.

The same pattern can be seen in cyclic loading case (Figures 3.112 and 3.113). However, during the application of the cycles with the peak pressure of 413.4 kPa there appeared to be a loss of confinement of the aggregate above the pipe and the tension in the shell dissipated quickly. Specifically on the outside of the shell there was a significant reduction in the longitudinal strain.

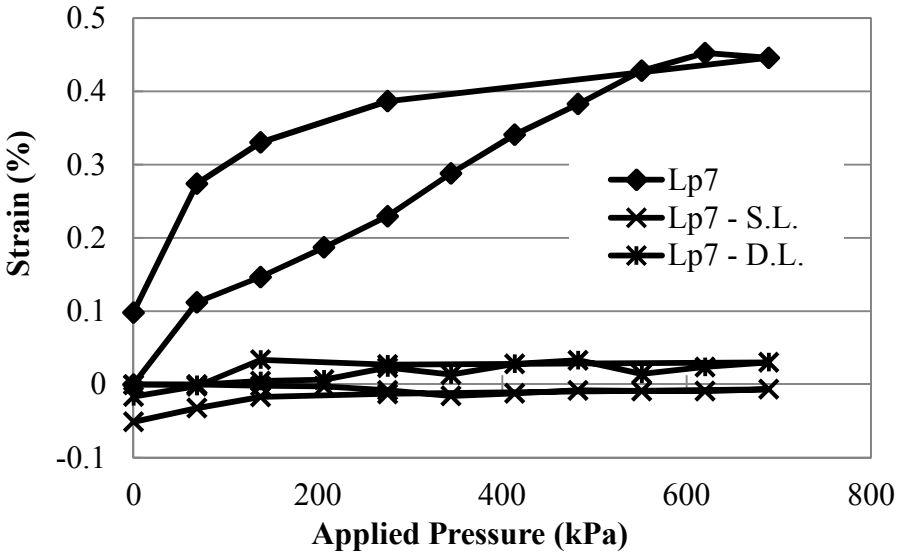

Figure 3.110 Longitudinal Strains – Plastic Lp7

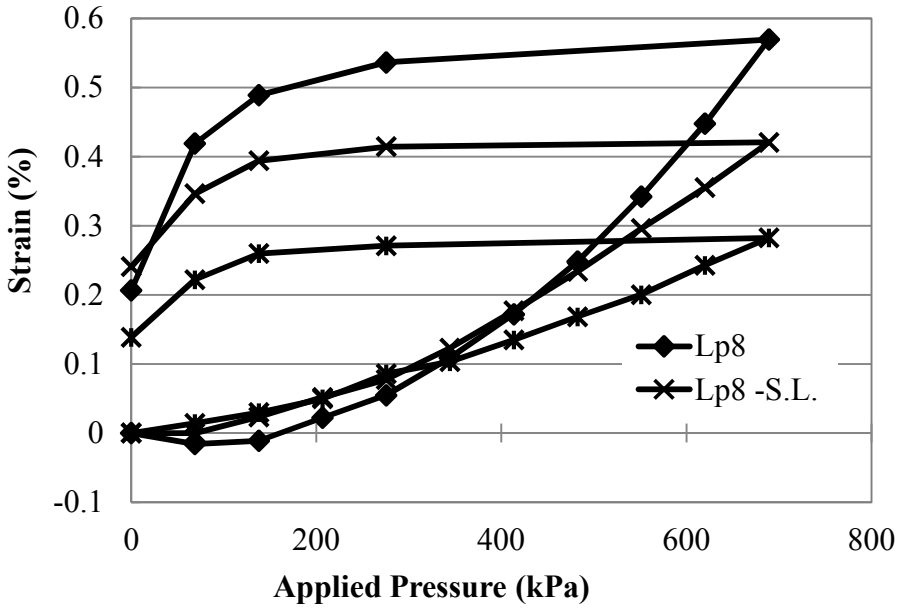

Figure 3.111 Longitudinal Strains – Plastic Lp8

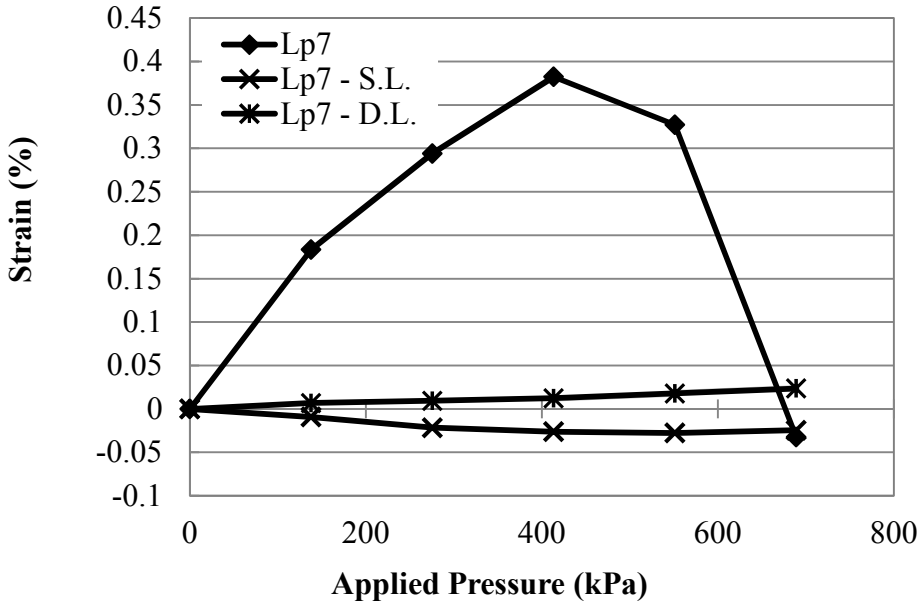

Figure 3.112 Maximum Longitudinal Strains at the Crown (Lp7)

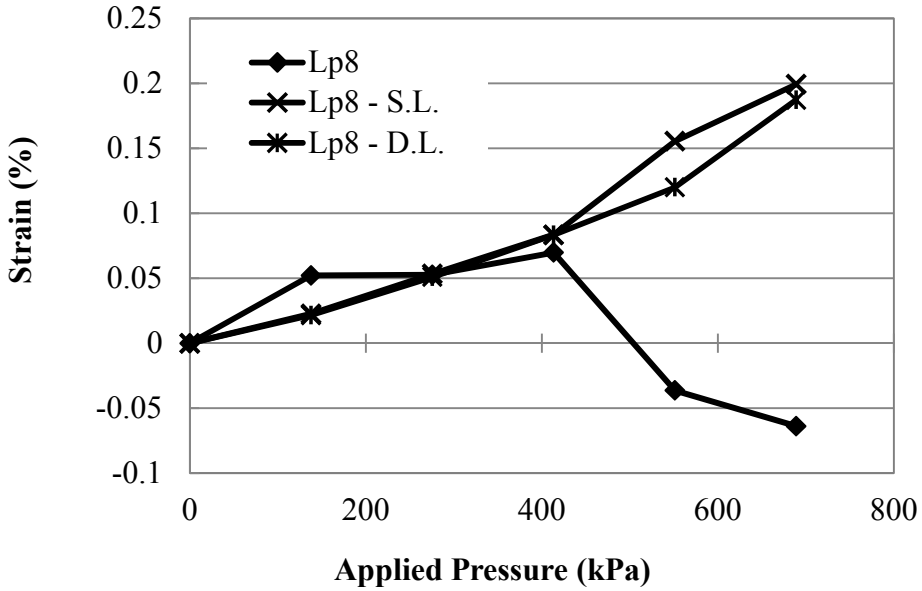

Figure 3.113 Maximum Longitudinal Strains at the Crown (Lp8)

Radial Strains

It was expected that the radial strains on the plastic rib would be tensile as the plastic rib would transfer forces from the valley to the top of the steel rib as described by Moore (2009). In the static plate load test there was no clear pattern of strain distribution that could be determined. For instance, radial strain gauge Rs4 is shown in Figure 3.114 and represents a typical radial strain plot on the steel. The radial strain gauges at the crown plastic (Rp3 and Rp4) however showed opposite, compressive and tensile strains, on either side of the rib (Figures 3.115 and 3.116). This could be an additional indication that there was shear at the interface in the longitudinal direction, bending the outstanding rib over, and thus generating compressive and tensile strains.

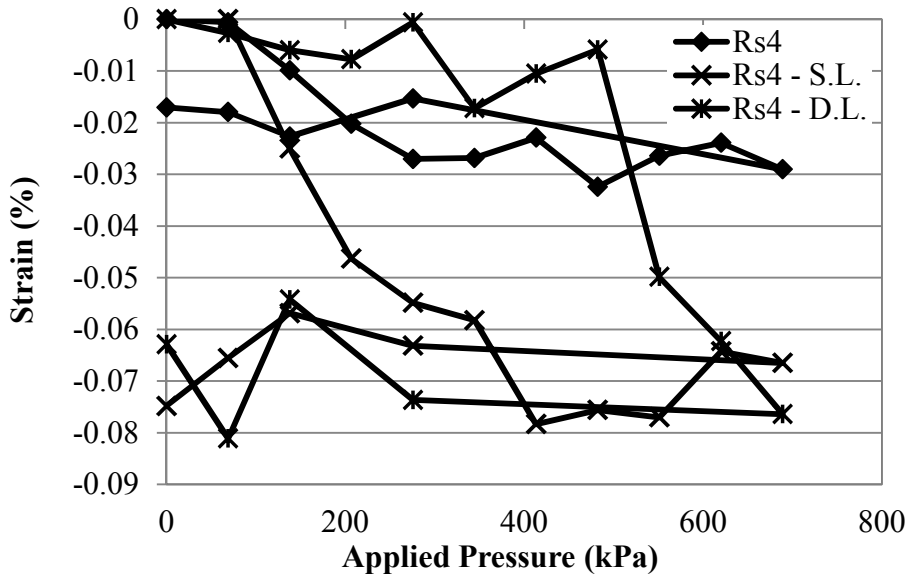

Figure 3.114 Radial Strains at Crown Rs4 in Test 5, 7, and 9

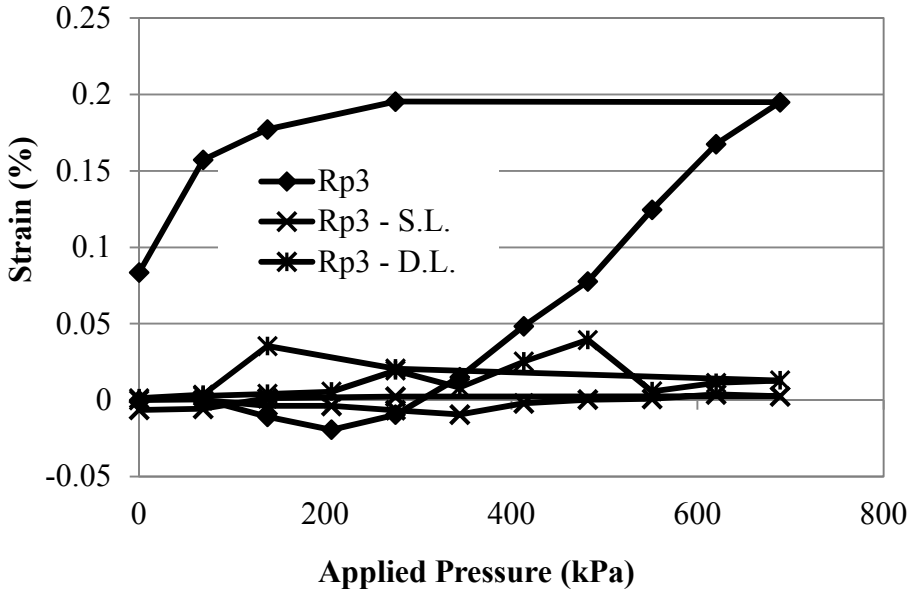

Figure 3.115 Radial Strains at Crown Rp3 in Test 5, 7, and 9

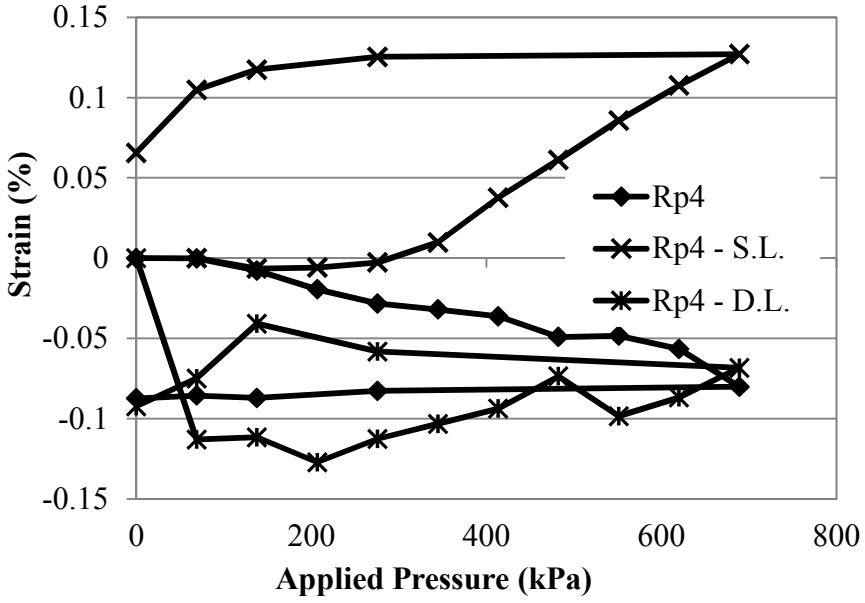

Figure 3.116 Radial Strains at Crown Rp4 in Test 5, 7, and 9

3.8.5 Geogrid Strain

Strain gauges were placed on the geogrid to determine its response to the applied load and the stiffness of the pipe soil system. The strain gauge locations which were shown in section 3.6 are shown here again for convenience (Figure 3.117). The strain gauges were placed on the top of geogrid in the following layered systems. Strain gauges that failed during the tests are not included in the following figures. The strain response of geogrid reinforcement provides insight into the function of the geogrid as described in the literature review. Knowing the function and the response of the geogrid, a strategy for maximizing the effectiveness of the geogrid can be generated. The geogrid responses also gave insight into the distribution of soil pressures in the base course and backfill.

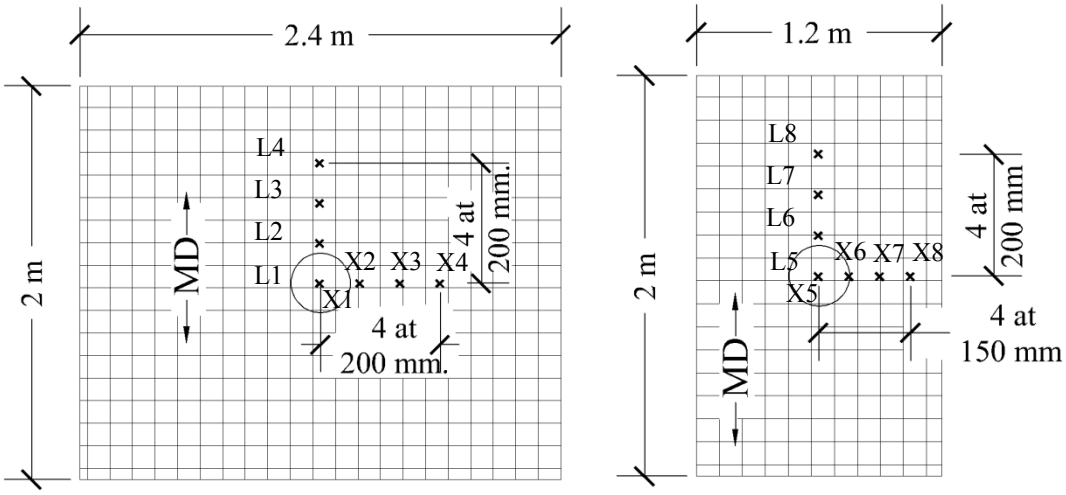

A. Upper Layer **B. Lower Layer**

Figure 3.117 Geogrid Strain Gauges on Single and Double Layers

Geogrid Strains in Test 3

Test 3 was a single layer of geogrid placed in a compacted sand backfill with a compacted sand base course. The geogrid was the length and width of the trench placed at 0.458m below the surface of the base course. The recorded strains in the machine direction and cross-machine direction of the pipe can be seen in Figures 3.118 and 3.119 respectively. A distribution of the strains in the machine and cross-machine direction can be seen in Figure 3.120. In the longitudinal direction the geogrid strain was in tension directly under the plate. The strain in the geogrid decreased as the distance from the loading plate increases until the strain reached zero and the geogrid strain became compressive. Assuming that the location of zero strain is the limit of the plate load distribution a distribution angle can be calculated and plotted (Figure 3.121). This is in general agreement with a distribution factor of 1.15 assumed by AASHTO (2012).

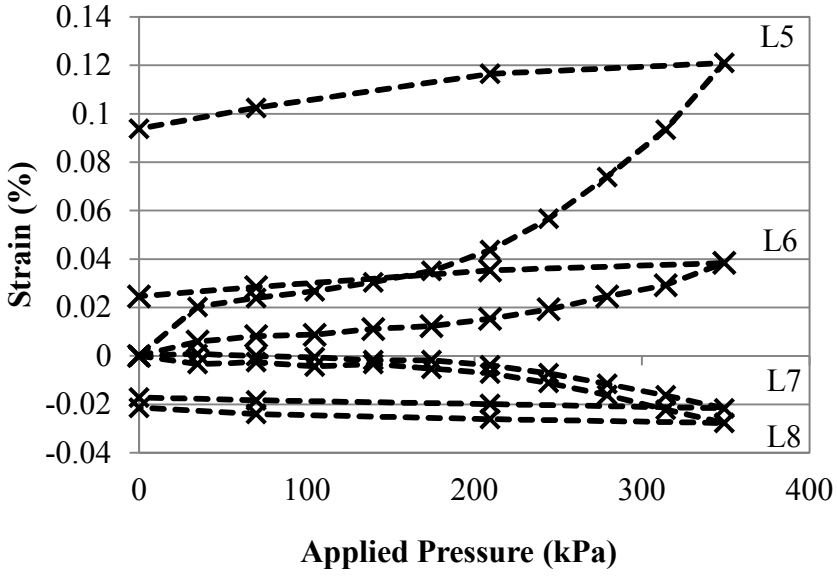

Figure 3.118 Longitudinal Strains in Geogrid

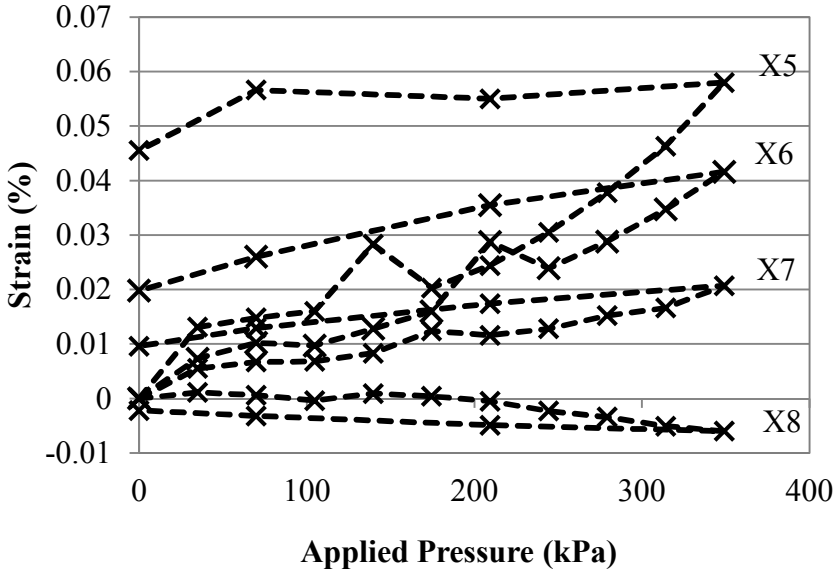

Figure 3.119 Cross-machine Direction Strains in Geogrid

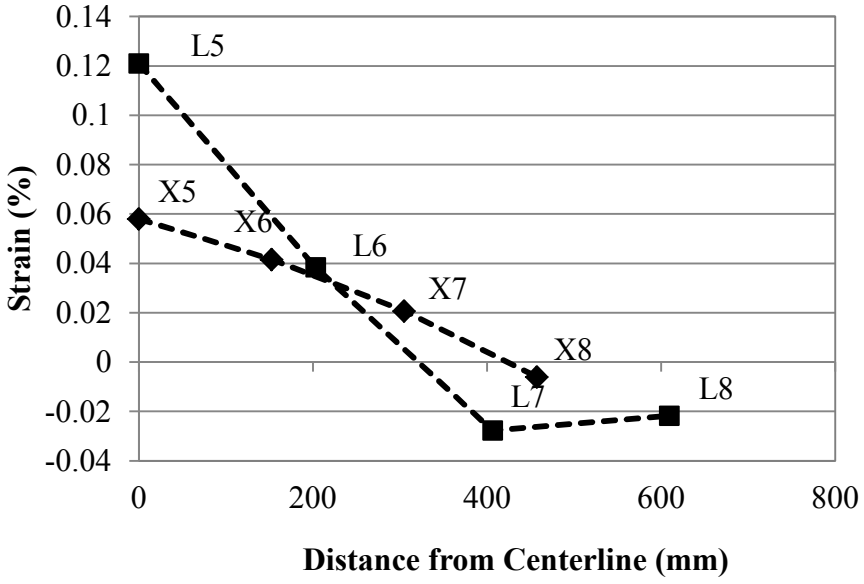

Figure 3.120 Strain in Geogrid at Maximum Applied Pressure (345 kPa)

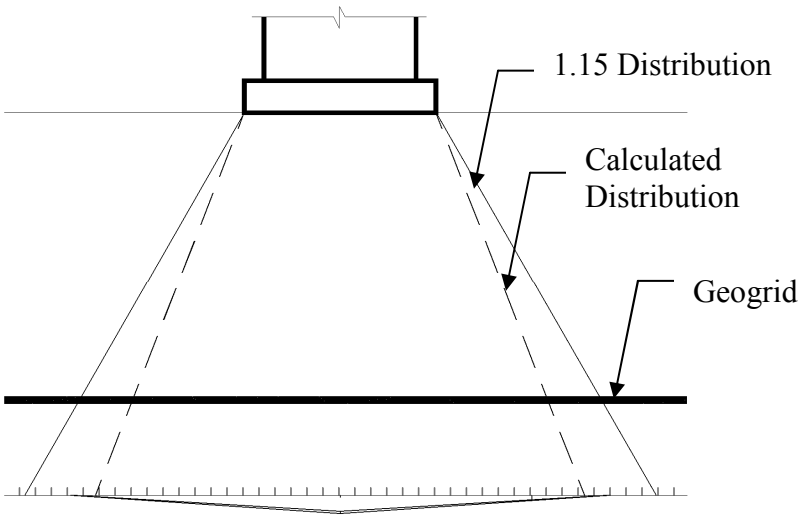

Figure 3.121 Plate Load Pressure Distributions in Test 3

Geogrid Strains in Test 4

Test 4 was two layers of geogrid placed in a compacted sand backfill with a compacted AB-3 base course. The lower geogrid was the length and width of the trench placed at 0.458 m below the surface of the base course while the upper geogrid was 0.380 m below the surface. The recorded strains in the machine direction and cross-machine direction of the geogrid, in both upper and lower layers, can be seen in Figures 3.122 through 3.125. A distribution of the strains in the machine and cross-machine direction of both layers can be seen in Figures 3.126 and 3.127. Again assuming that the location of zero strain is the limit of the plate load distribution a distribution angle can be calculated and plotted (Figure 3.128). This is in general agreement with a distribution factor of 1.15 assumed by AASHTO (2012).

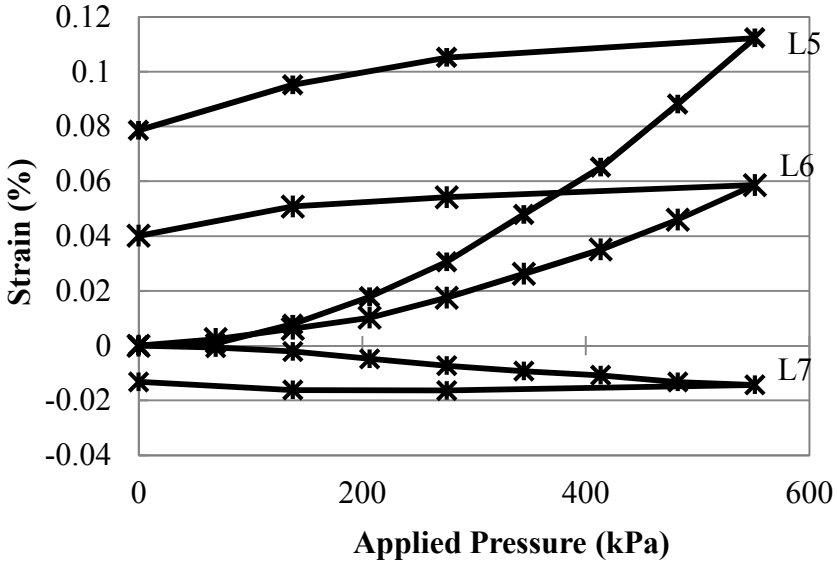

Figure 3.122 Longitudinal Strains in Geogrid – Double Layer in Test 4

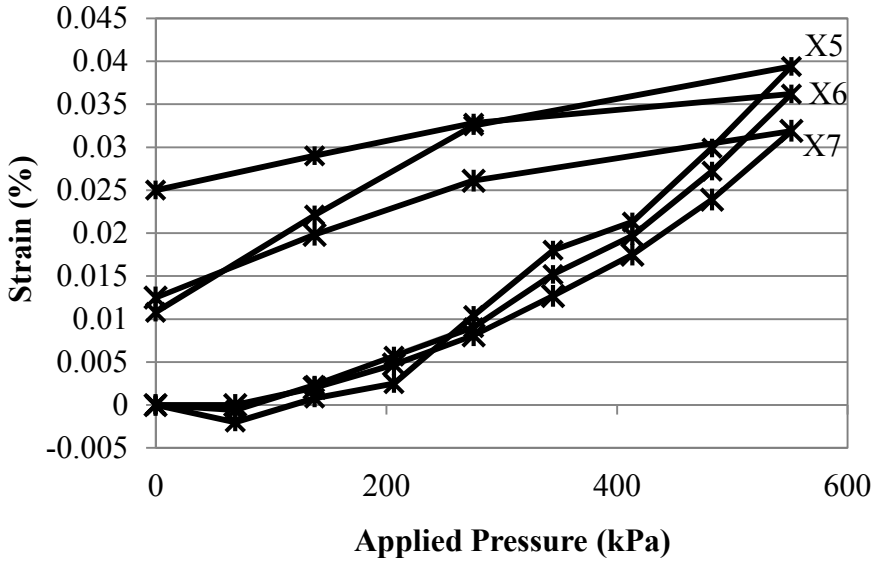

Figure 3.123 Cross Direction Strains in Geogrid – Double Layer in Test 4

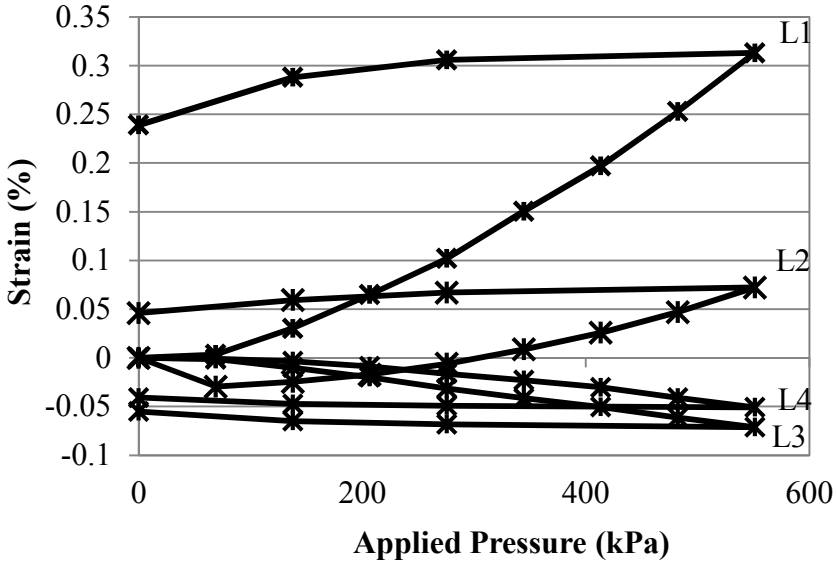

Figure 3.124 Longitudinal Strains in Geogrid – Double Layer in Test 4

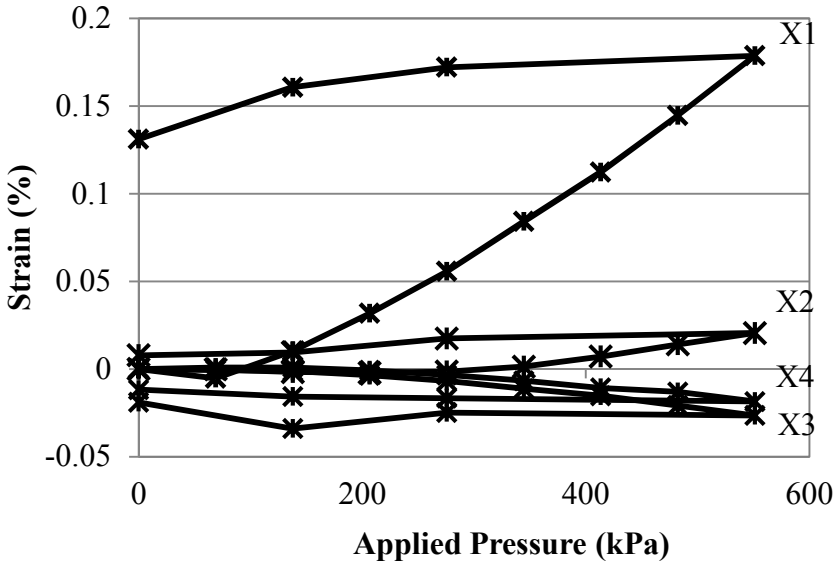

Figure 3.125 Cross Direction Strains in Geogrid – Double Layer in Test 4

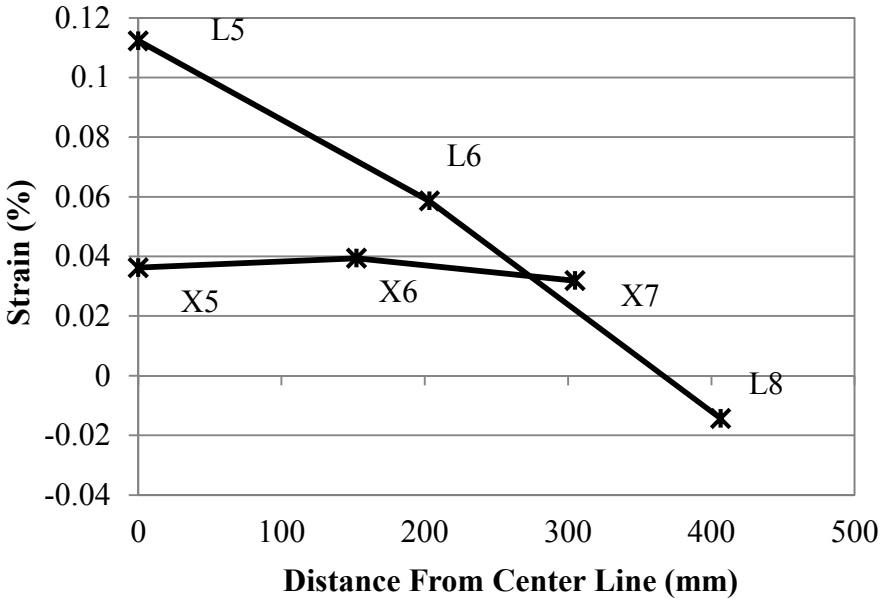

Figure 3.126 Lower Layer Geogrid Strains at Maximum Applied Pressure (689 kPa)

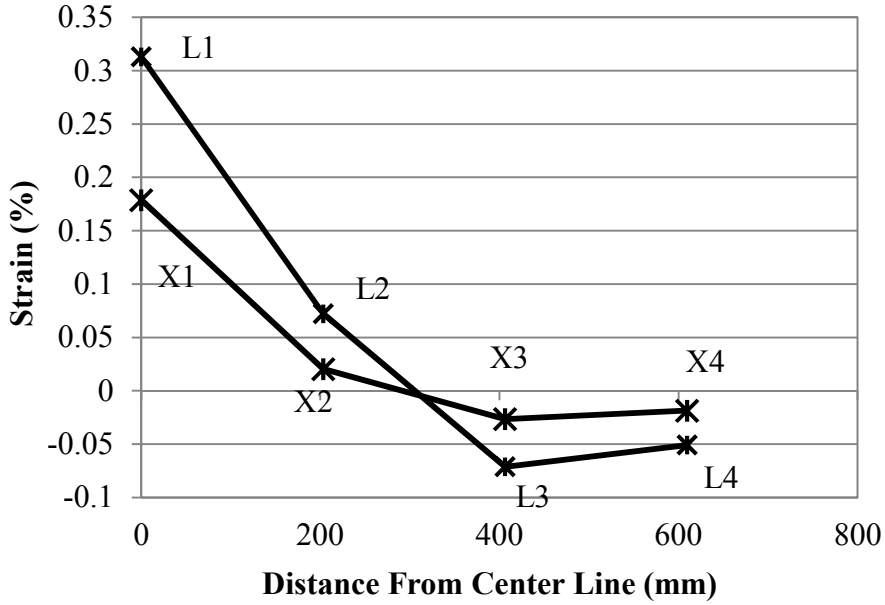

Figure 3.127 Upper Layer Geogrid Strains at Maximum Applied Pressure (689 kPa)

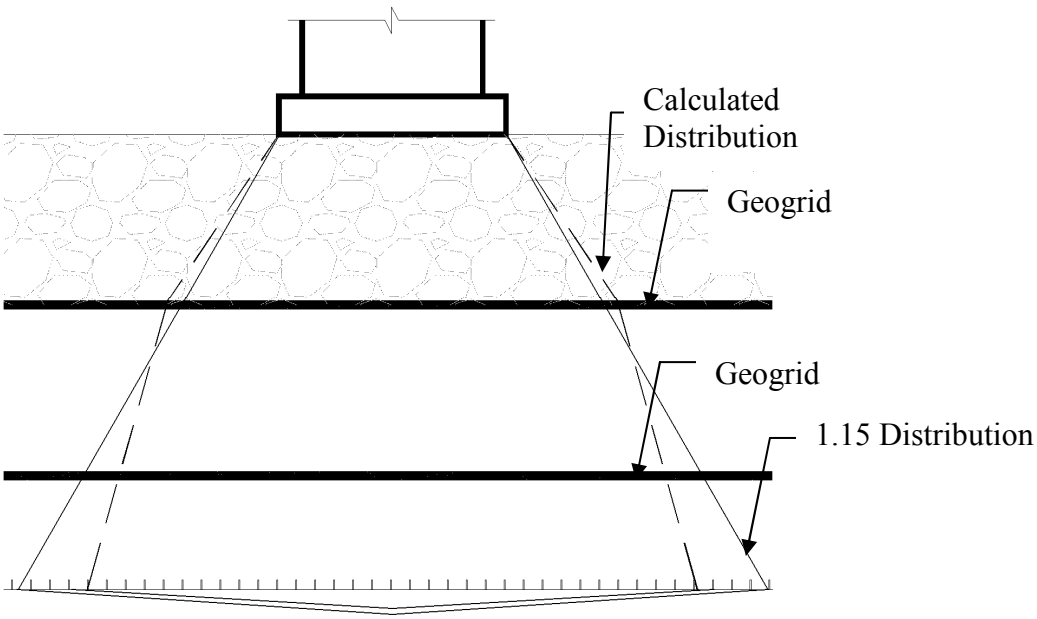

Figure 3.128 Plate Load Distributions in Test 4

Geogrid Strains in Tests 7 and 9

In tests 7 and 9 the geogrid was placed in a single layer and a double layer respectively in a crushed stone aggregate backfill. An effort was made to protect the strain gauges during each test, but the survivability of the strain gauges in the crushed stone aggregate backfill tests was much lower than in the sand backfill. Many of the strain gauges failed but a few observations can be gleaned from the strain gauge data. In the single layer test (Test 7) it appears that a portion of the strain gauges were in compression in the cross-machine direction (Figure 3.129) similar to the sand test; however in the machine direction (longitudinally) all of the strain gauges were in tension (Figure 3.130). A plot of the strain distribution of across the geogrid in the longitudinal direction and the cross-machine direction are given in Figure 3.131.

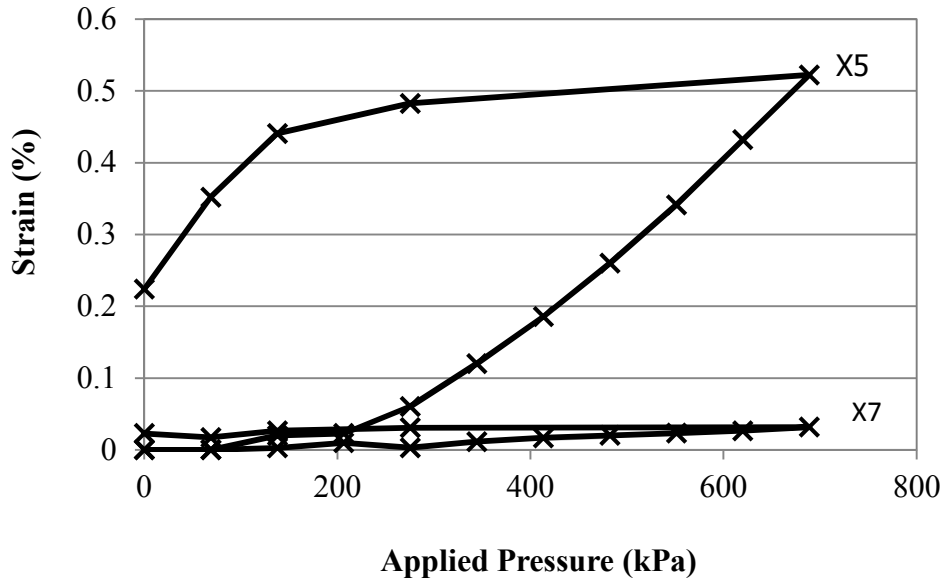

Figure 3.129 Cross Direction Strains in Geogrid – Single Layer in Test 7

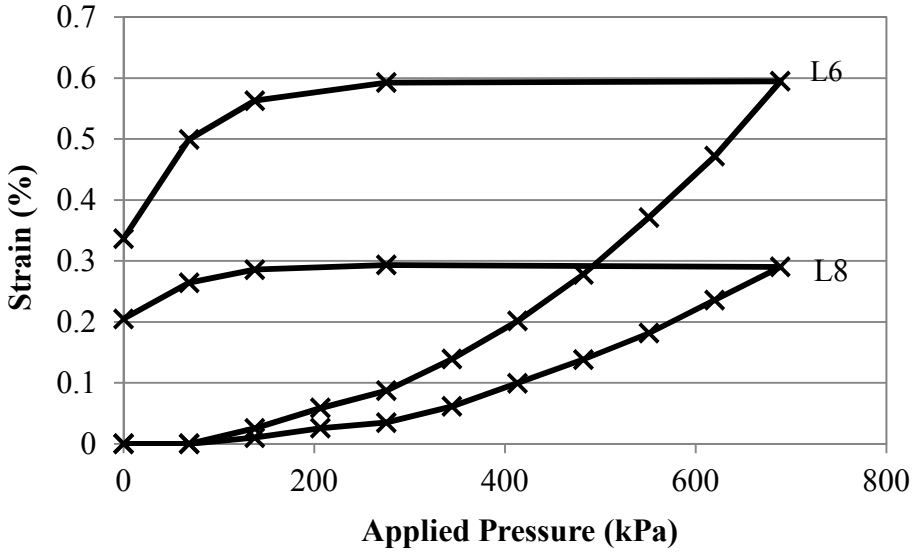

Figure 3.130 Longitudinal Strains in Geogrid – Single Layer in Test 7

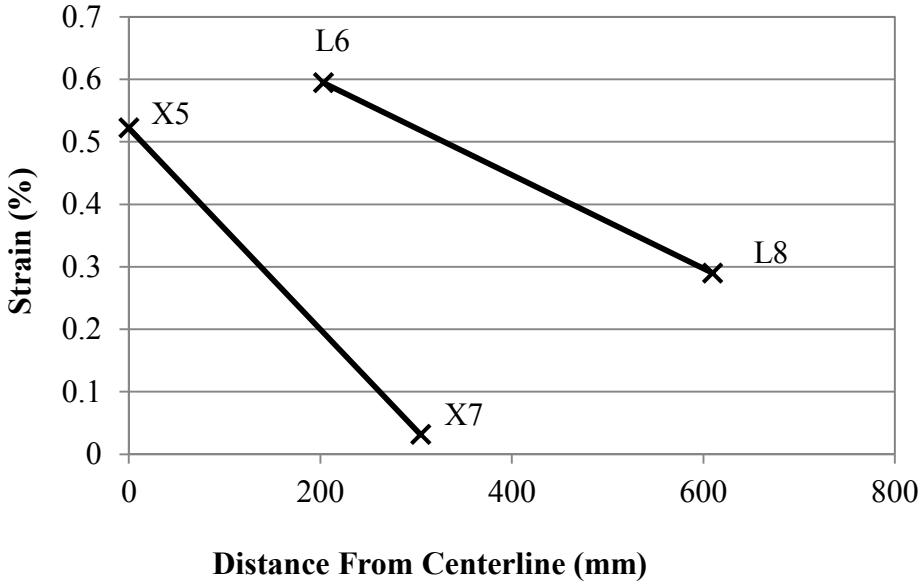

Figure 3.131 Strains in Geogrid at Maximum Applied Pressure (689 kPa) in Test 7

In the double layer test (Test 9) the longitudinal and cross-machine direction strains of the lower layer can be seen in Figures 3.132 and 3.133 respectively. The longitudinal and cross-machine direction strains of the upper layer can be seen in Figures 3.134 and 3.135 respectively. The distribution of strains across the width and length of the lower and upper layers of geogrid can be seen in Figures 3.136 and 3.137. With regards to the double layer of geogrid there are some slight differences between the behavior of the sand backfill and the crushed stone aggregate backfill. Specifically in the upper geogrid layer in the longitudinal direction the strain did not reach its peak at the center of the geogrid, at strain gauge L1. The maximum strain in the geogrid appears to be closer to the strain gauge L2. Both the upper and lower geogrid strains also measured higher strains as compared to the sand layer.

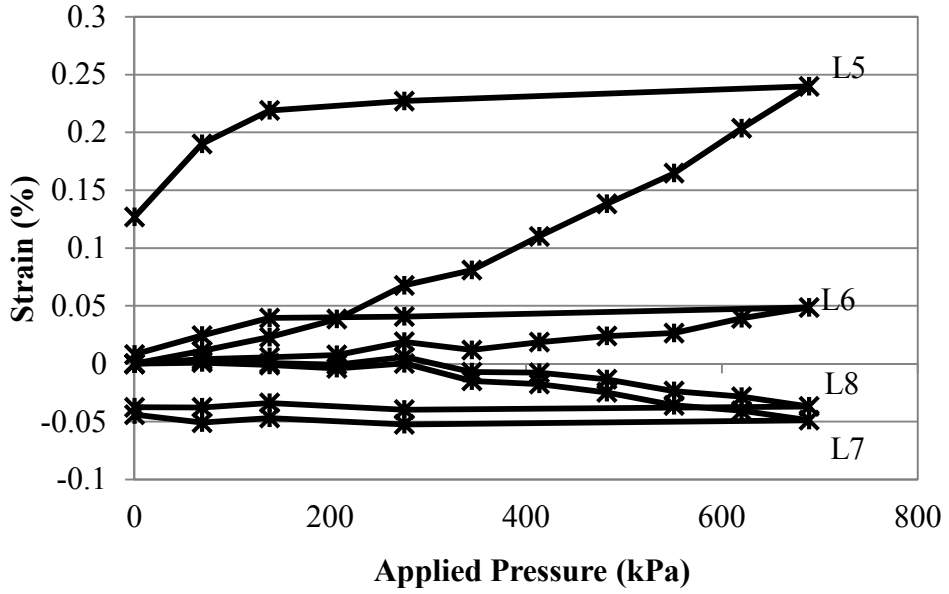

Figure 3.132 Longitudinal Strains in Geogrid – Double Layer in Test 9

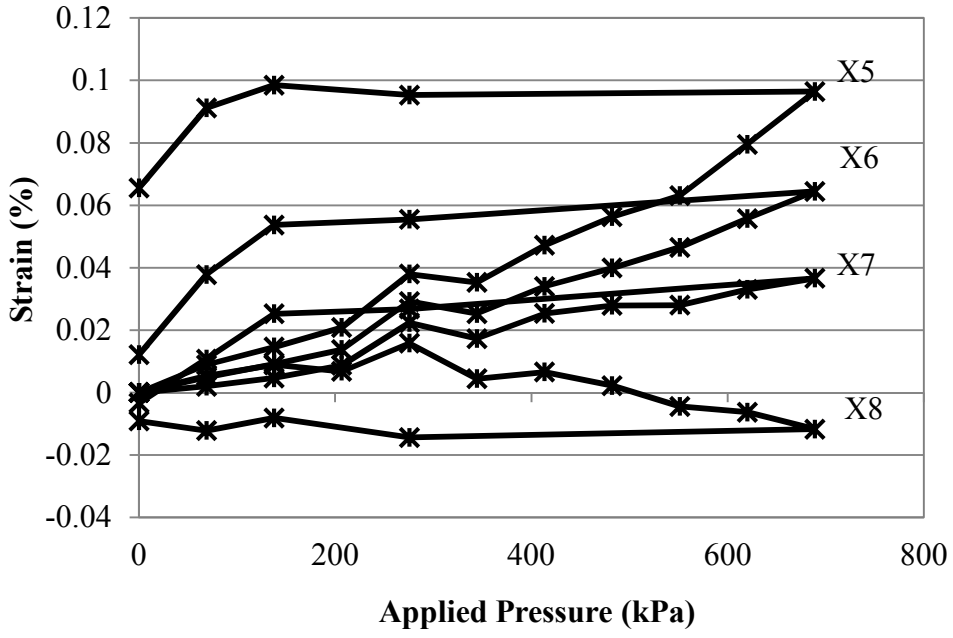

Figure 3.133 Cross-machine Direction Strains in Geogrid – Double Layer in Test 9

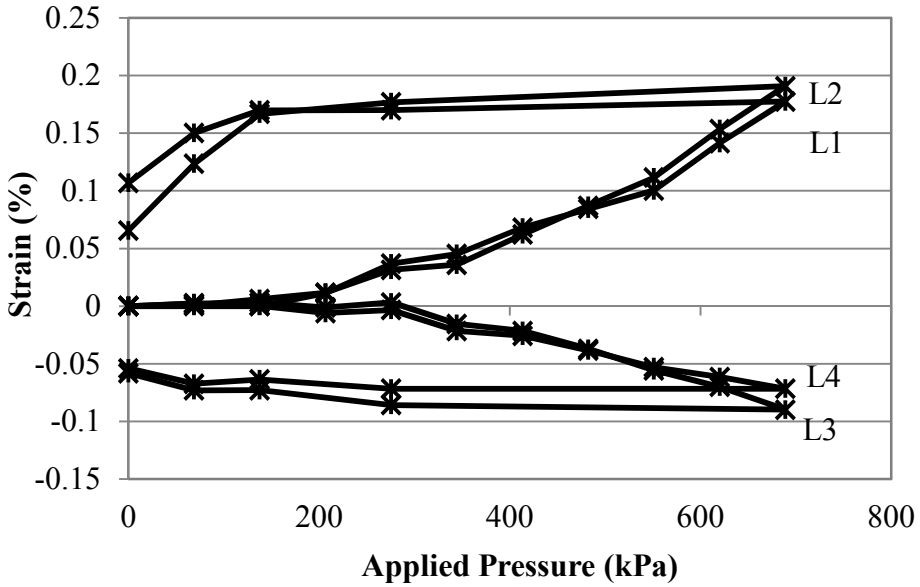

Figure 3.134 Longitudinal Strains in Geogrid – Double Layer in Test 9

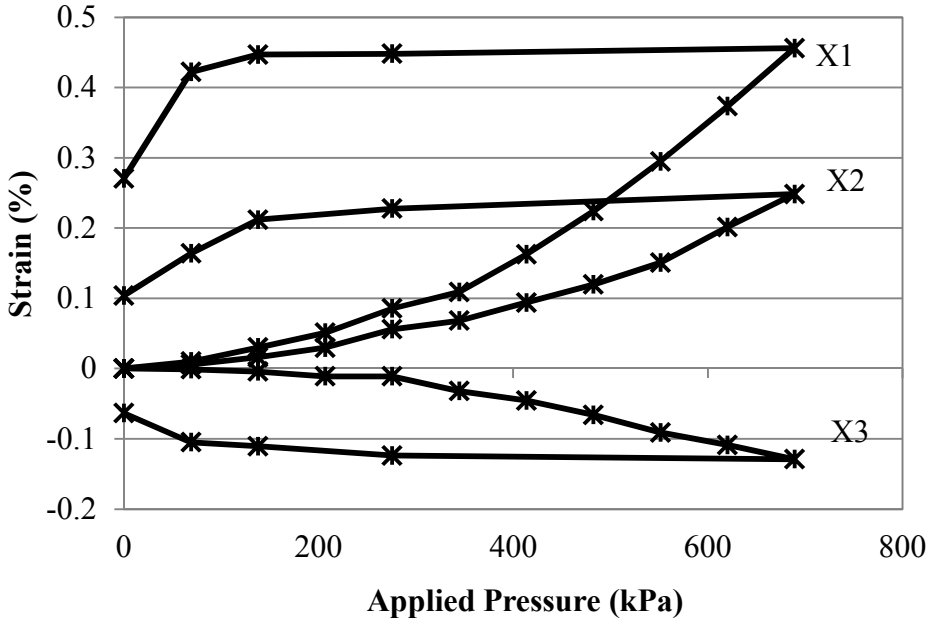

Figure 3.135 Cross-machine Direction Strains in Geogrid – Double Layer in Test 9

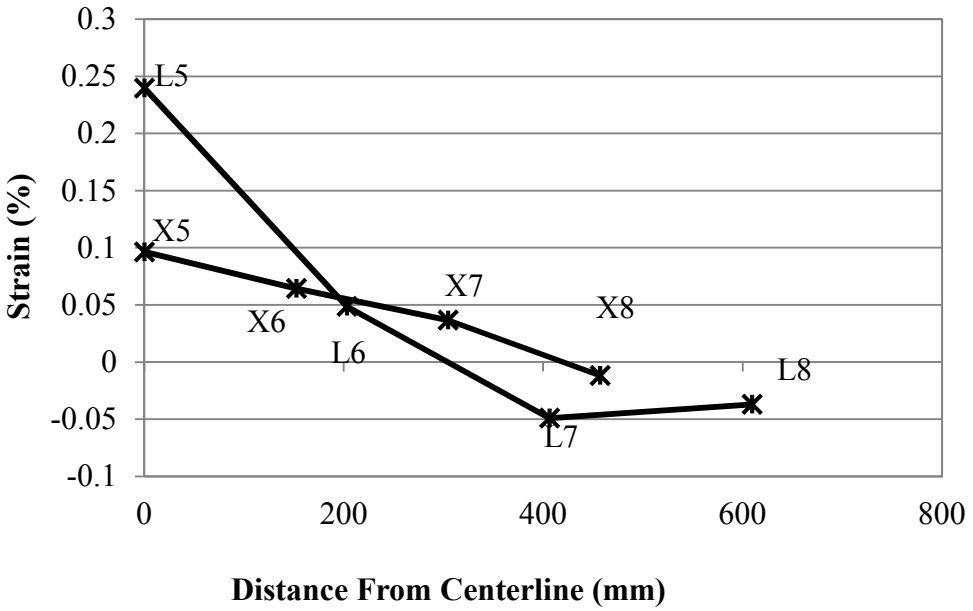

Figure 3.136 Lower Geogrid Strains at Maximum Applied Pressure (689 kPa)

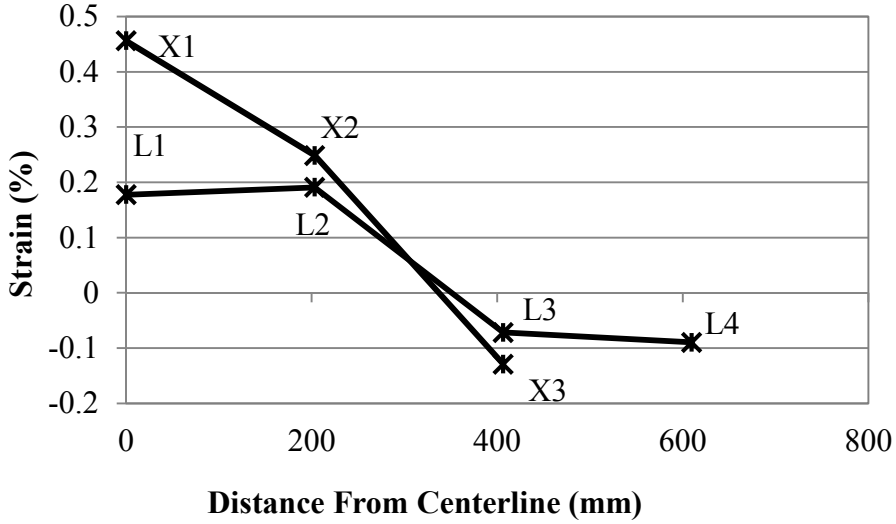

Figure 3.137 Upper Geogrid Strains at Maximum Applied Pressure (689 kPa)

3.9 Analysis of Laboratory Results

Because of the variation in test results common to geotechnical engineering and pipe design, and the limited amount of test runs possible, it is worthwhile to analyze and determine the veracity of the recorded data. Previous researchers have provided a variety of methods that can be used to verify the results. Some of the methods used here to inspect the data go back to the very foundations of pipe design. Both old and new analysis methods provide additional insight into the protection of buried pipes from surface loads. Some techniques may not be the most precise, but these simple calculations can give extremely helpful information.

3.9.1 Pipe Deflections

There have been several iterations of Spangler's original formula for the calculation of the anticipated deflection of a buried pipe. The most current, and the one used for the analysis here is provided by the NCHRP 631 report (McGrath et al. 2009). The percent deflection calculation has the familiar form of Spangler's equation but adds a second term where the deflection due to axial shortening of the pipe is included (Equation 3.1).

$$\frac{\Delta_v}{D} = \frac{q_v}{\frac{EA}{R} + .57M_s} + \frac{D_l K_b q_v}{\frac{EI}{R^3} + 0.061M_s} \qquad \textbf{3.1}$$

The deflection lag factor (D_l) and the bedding factor (K_b) are hold outs from the original equation. The terms E, A, I, and R are the modulus of elasticity, the area, the moment of inertia,

and the radius of the pipe respectively. The term q_v is the applied stress at the crown of the pipe, and the modulus of soil reaction has been replaced with the constrained modulus (M_s).

Constrained modulus tests were completed on both the dense sand and crushed stone aggregate backfills (Deep, 2012) as shown in Figure 3.138. Using the average method to compute the strain modulus as described by McGrath (1998) the computed values are shown in Table 3.8.

Table 3.8 Constrained Modulus of Backfill

Material	Constrained Modulus (MPa)
Dense Sand	21
Crushed Stone Aggregate	13.1

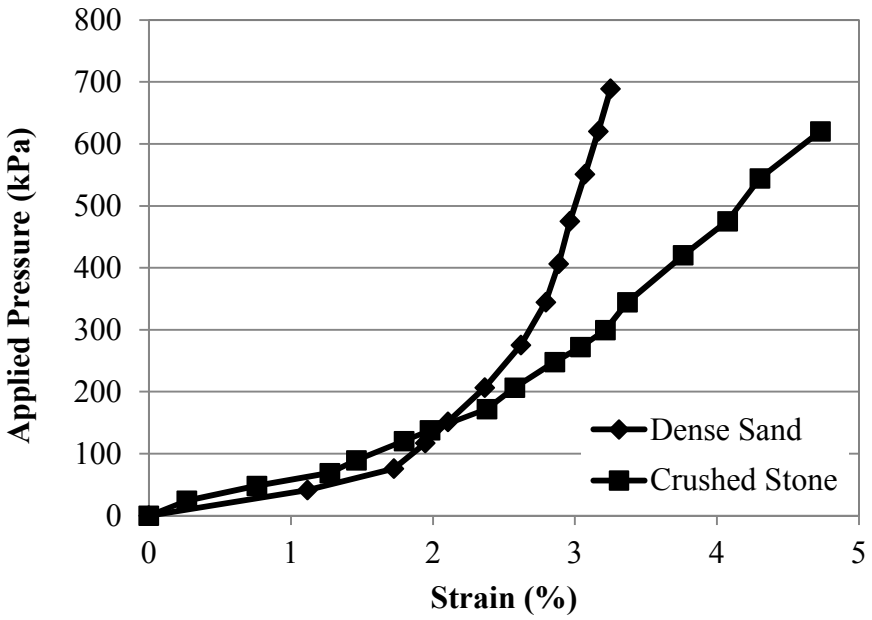

Figure 3.138 Backfill Constrained Modulus Test Data

The calculated values for the compacted Kansas River sand are very close to the prescribed values by McGrath (1998). By inspection of McGrath (1998) and Howard (1977) the constrained modulus values for the crushed stone are similar for the sand case ranging from 21 MPa to 7 MPa between the lightly compacted and dumped backfill conditions.

With these rudimentary material properties an estimation of the expected deflection of the pipe can be calculated. Since no deflection lag is expected in this short test, D_l is assumed to be 1 and the bedding factor is generally around 0.1. The applied load q_v was calculated by the applied pressure multiplied by the ratio of the loading plate diameter to the area of distribution at the pipe crowns using the 1.15 distribution angle. The left hand term of Equation 3.1 and the pipe stiffness are a very small percentage of the expected deflection and can be neglected.

At the maximum applied load based on Equation 3.1 a deflection was calculated approximately 4.5 mm for the crushed stone condition and 2.25 mm for the sand backfill condition. This approximation verifies the recorded data on the crushed stone aggregate backfill condition (4 mm), but also indicates that there may be a problem with the recorded deflection of the pipe in compacted sand (0.5 mm).

3.9.2 Earth Pressures

The earth pressures that were recorded during the tests are analyzed here and broken into two categories, vertical pressures at the crown and lateral pressures at the springline. The vertical pressures at the crown are compared with the estimated pressures as computed by the Boussinesq method (Figures 3.139 and 3.140). For the compacted sand backfill condition (Tests 1 and 2)

and the crushed stone backfill condition (Test 9) the recorded values were higher than anticipated by the elastic solution. Although the recorded values are higher than anticipated by the Boussinesq solution, there is some indication that the recorded values may be accurate. The vertical arching factor, which is the ratio of actual pressure to calculated pressure, can vary from 1.0 to 1.4 for flexible pipes.

The pressures at the springline were also recorded but are more difficult to analyze and anticipate the pressures. An examination of Spangler's assumed pressure distribution indicates that the pressure at the springline be approximately equivalent to the pressure at the crown of the pipe.

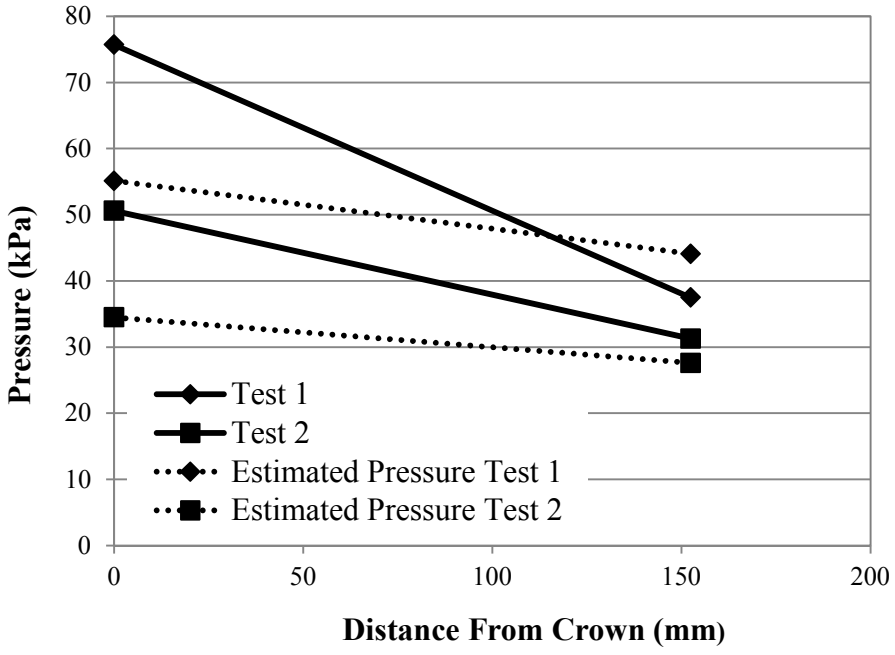

Figure 3.139 Recorded and Estimated Earth Pressures at Crown in Tests 1 and 2

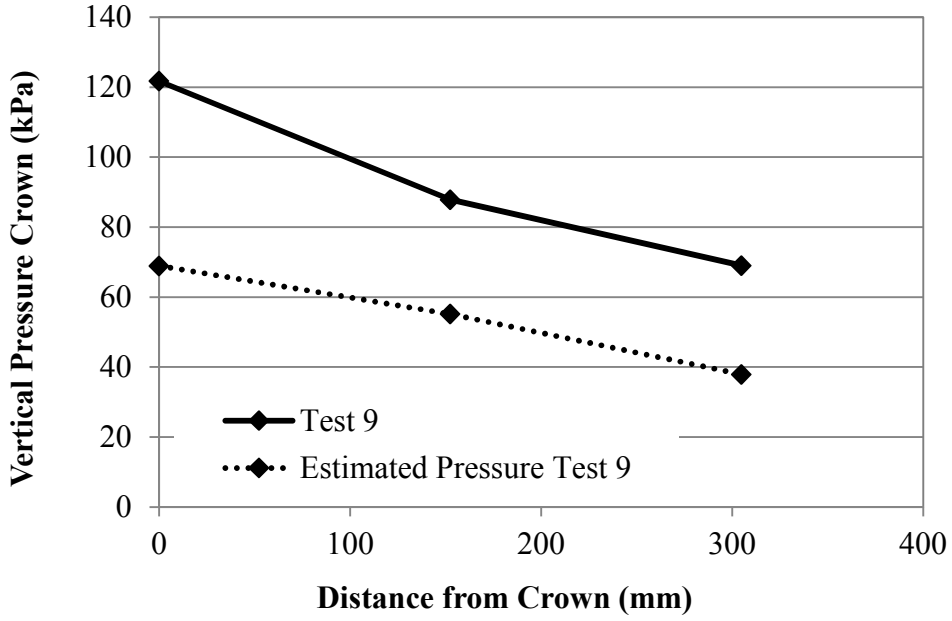

Figure 3.140 Recorded and Estimated Earth Pressures at Crown in Test 9

Spangler's original pressure distribution was based on measured laboratory data. In Spangler's solution the pressures at the spingline are proportional to horizontal movement of the pipe wall ($\Delta x/2$) times a modulus of passive resistance (e). In the Iowa formula Watkins and Spangler (1958) expressed the stiffness of the soil as the modulus of soil reaction (E') which was equivalent to the product of modulus of passive resistance and the radius (r) of the pipe. The constrained modulus (M) has been accepted as being generally equivalent to the modulus of soil reaction (E') (McGrath 1998), but can range from 0.7 to 1.4 times the constrained modulus. Using the radius of the pipe and the constrained modulus given in Table 3.8 the modulus of passive resistance was estimated to be approximately 43 MPa/m and 68.9 MPa/m for the crushed stone and sand backfill conditions. Based on the maximum horizontal deflection recorded at the maximum applied pressure it is estimated that the maximum springline pressures should be

approximately 43 kPa and 35 kPa for the crushed stone and sand backfill conditions. Spangler (1941) also described the horizontal soil pressure distribution on the pipe springline as a parabola extending from the springline at 50 degrees above and below a horizontal plane. Based on the maximum pressure and the parabolic soil distribution the assumed soil distribution is plotted versus the recorded pressures in Figures 3.141 and 3.142.

Examination of elastic methods of determining soil pressures around a buried pipe, such as Burns and Richard (1964) indicated that for a pipe with the known calculated parameters the pressure at the springline should be about 1 to 1.3 times the uniform pressure (P) applied at the surface of a buried pipe depending on if the slip or non-slip condition is used.

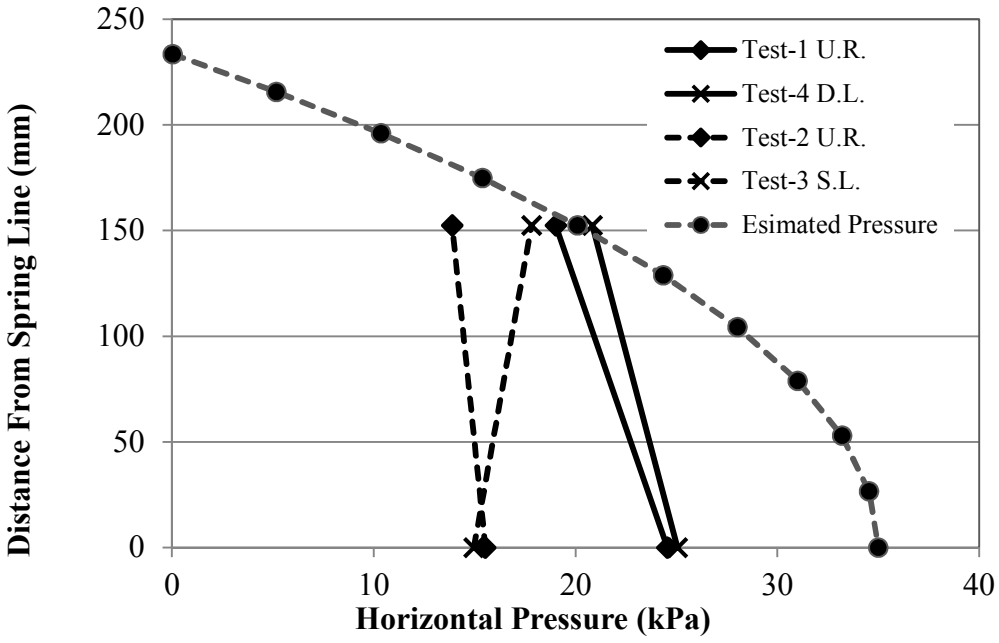

Figure 3.141 Recorded and Estimated Soil Pressure Distributions at the Springline

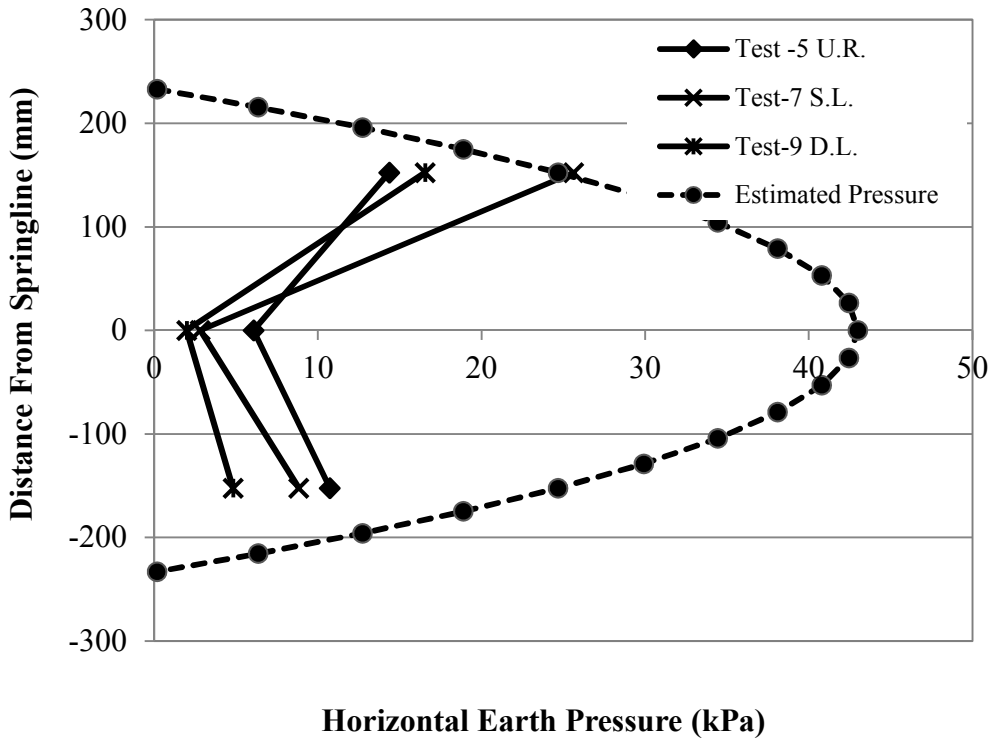

Figure 3.142 Recorded and Estimated Soil Pressure Distributions at the Springline

Also, Watkins (1966) estimated the pressure at the springline (P_y) to be proportional to the pressure at the crown (P_x) times the ratio of the pipe's long and short radii, which is approximated by Equation 3.2:

$$P_x = P_y(1+d)^3/(1-d)^3 \qquad \textbf{3.2}$$

where d is the vertical pipe deflection.

With this equation, for even small deflections, the pressure at the spring line is assumed to be larger than the pressure recorded at the crown. Arockiasamy et al. (2006) and Chaallal et

al. (2014) completed analysis of experimental and numerical experiments for flexible pipes under wheel loads. Both researchers indicated a lateral earth pressure at the springline of 0.5 to equivalent to the pressures recorded at the crown depending on the stiffness of the pipe.

Overall there appears to be enough evidence that there is a significant problem with the recorded earth pressures at the springline of the pipe, especially in the crushed stone backfill tests. Despite efforts to calibrate the pressure cells before and after the full scale laboratory tests, the recorded data at earth pressure cell S1 appears to vary significantly from accepted and observed buried flexible pipe behavior. The recorded data problems are not without precedent. Talesnick et al. (2011) showed that the ratio of particle size to cell diameter can have a significant negative effect on the pressure cell data.

3.10 Conclusions of Laboratory Results

1. The single layer of geogrid at 152.4 mm above the crown of the pipe, generally appeared to have minimal or no effect as compared to the cases that included an upper layer of geogrid. The single layer lowered the plate settlement for the sand backfill and base course condition, but for all other measured results the lower layer slightly increased or had no effect, see Table 3.9.
2. The geogrid reinforcement had the most impact on plate settlements, pipe deflections, and earth pressure attenuation in the less stiff aggregate backfill conditions (Table 3.9).

Table 3.9 Reductions (%) by Reinforcement (Single Layer or Double Layer) Compared to Unreinforced Condition

Backfill	Plate Settlement	Vertical Pipe Deflection	Earth Pressure at Crown
	SL / DL	SL / DL	SL / DL
Compacted Sand	24% / 11.2%	-12.6% / 24%	10% / 10%
Crushed Stone Aggregate	-26% / 36%	-8.2% / 55%	13.3% / 41%

3. The additional layer of geogrid directly underneath the base course decreased the measured results while the single layer alone made no significant change in the measured results for the aggregate backfill condition in the cyclic load tests. The difference in plate displacements and pipe deflections in the pipe for the single layer of geogrid is assumed to be differences in the stiffness and strength of the base course.

Table 3.10 Reductions (%) by Reinforcement (Single Layer or Double Layer) Compared to Unreinforced Condition under Cyclic Loads

Backfill	Plate Settlement	Vertical Pipe Deflection	Earth Pressure at Crown
	SL / DL	SL / DL	SL / DL
Crushed Stone Aggregate	-20% / 43%	-53% / 33%	-34% / 5%

4. The double layer of geogrid reduced the ratio of vertical to horizontal deflections. Assuming pipe deflections of the same general magnitude, the larger the ratio of vertical to horizontal deflection ratios the higher the strain in the pipe wall.

5. The geogrid appeared to have little or no reduction of the earth pressures over the pipe in the sand backfill condition. In the crushed stone aggregate condition the pressures were reduced significantly directly over the pipe and it appeared that the load was shifted away from the crown as the pressure at the outer two crown pressure cells increased.
6. At approximately 400 mm from the centerline of the plate the geogrid was in compression. This indicated that the geogrid did not act strictly as a tensioned membrane. The responses observed were confinement of the base course, lowered shear stress under the geogrid, and lowered vertical stresses in the backfill. These responses are typical for geosynthetic reinforcement of paved and unpaved roads as described by other researchers, such as Perkins et al. (2001) and Christopher et al. (2001).
7. The geogrid strain was higher in the condition with crushed stone backfill. It is assumed that the relative stiffness of the un-compacted aggregate and the efficiency of the backfill aggregate geogrid interaction increased the influence of the geogrid.
8. Longitudinal strains appeared to play a significant role in the response of the pipe to the plate loading. Other researchers, such as Klaiber et al (1996) and Phares et al. (1998), also commented on the apparent significance of strain on the pipe. The largest strain in their tests with wheel loads on buried HDPE pipes was in the longitudinal direction also. Inclusion of the geogrid appeared to significantly reduce the longitudinal strains in the pipe wall.

Chapter 4 Numerical Analysis

4.1 Overview

The emphasis of this chapter is the calibration of a numerical analysis to effectively model the laboratory tests. As discussed in the literature review there are a few items that are critical to achieve this goal. It is critical to model both the unique physical properties of the pipe and the non-linear stress strain properties of the soil materials. It is also important to consider the construction steps to capture the movement and stresses in the pipe and backfill. FLAC 3D version 4.0 (Itasca 2009) was chosen to model the laboratory tests and has been used extensively to solve geotechnical problems and can easily meet these criteria. The FLAC finite difference method is adept at effectively modeling large strain movements and modeling steps commonly required in geotechnical materials. The FLAC 3D version was important because of the strains and stresses developed in the third dimension parallel to the pipe.

As with any numerical model there are limitations of how precisely a system can be modeled and each model presents its own unique set of problems. The FLAC 3D model lends itself well to modeling the macro or large scale properties of the system. For instance, the pipes individual elements were not constructed into the model but were represented as an orthotropic uniformly thick plate. Consequently, numerical studies on the behavior of the pipe wall were also prepared to substantiate the behavior predicted in the overall model. The finite element program Abaqus was used to model the behavior of the pipe wall. Models of the tri-axial tests on

the backfill material were also run to calibrate the non-linear and plastic properties of the backfill.

4.2 Material Parameters

4.2.1 Orthotropic Pipe Stiffness

The pipe used in the full scale experiments had distinct bending and axial stiffness in the two axis of the pipe. A pipe of uniform thickness for example will have shell properties that are the same in both axes of the pipe wall. A corrugated steel pipe, by its geometry, has a unique stiffness in each direction of the pipe. Reinforced concrete and profile pipe are other examples of pipe materials that can have orthotropic properties due to the reinforcement or pipe geometry.

For the SRHDPE pipe used in this study the shell stiffness in the circumferential and longitudinal directions are significantly different. The steel reinforcement, running in the Y axis in Figure 4.1 significantly increases the stiffness in that direction compared to the thin HDPE shell in the X direction.

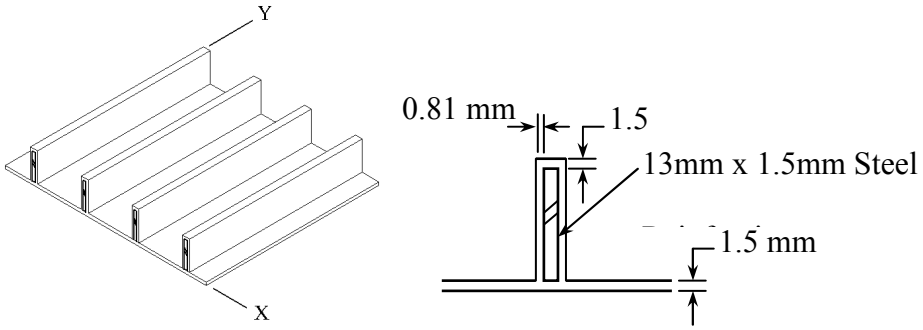

Figure 4.1 Steel Reinforced HDPE Pipe Walls of 25.4 mm on Centers

The Itasca FLAC 3D software allows for the numerical modeling of three dimensional plates, and also allows the user to model the orthotropic properties of shells. As suggested by Itasca (2009) and described by Ugural (1981) the plate rigidities for the numerical analysis can be approximated, for both bending and membrane stiffness, and entered into the FLAC 3D structural element constitutive model in a material stiffness matrix. The bending plate rigidities approximations given by Ugural (1981) are shown in Equations 4.1 through 4.4.

$$D_x = H = \frac{E_p {t_p}^3}{12(1-\nu^2)} \quad \textbf{4.1}$$

$$D_y = \frac{E_p {t_p}^3}{12(1-\nu^2)} + \frac{E'I}{s} \quad \textbf{4.2}$$

$$D_{XY} = D_x - 2G_{XY} \quad \textbf{4.3}$$

$$G_{XY} = \frac{t^3 G}{12} \quad \textbf{4.4}$$

where the plastic material properties: plastic modulus of elasticity (E_p), plastic thickness (t_p), and Poisson's Ratio (ν), are used for the plate, and the steel modulus of elasticity (E'), and steel core moment of inertia (I), are used for the equidistance spaced ribs (s), show in Table 4.1.

As noted in Section 3.2.1 the measured pipe stiffness during the parallel plate loading test (295 kPa) was lower than the stiffness calculated by Spangler's elastic solution for pipe stiffness (Equation 2.2) using the second moment area of the steel rib. This bending stiffness difference can be accounted for by geometric non-linearity, pitch of the helically wrapped corrugations, and incomplete composite action between the steel core and the plastic shell. For this reason the

initial bending stiffness was determined by using the measured pipe stiffness, the moment of inertia of the steel core (I), and back calculating an equivalent modulus of elasticity with Equation 2.2 for determining the bending stiffness in the Y direction D_y.

Table 4.1 FLAC 3D Pipe Shell Properties

E_p (MPa)	450
t_p (mm)	1.5
s (mm)	25.4
I (mm^4/mm)	10.8
E' (MPa)	200,000
$\nu_{plastic}$	0.46

For the membrane stiffness of the plate, the circumferential stiffness of the steel hoop and longitudinal stiffness of the plastic shell were assumed to be independent of each other. The membrane stiffness are based on the modulus of elasticity of the steel (E') and the plastic (E_p), and the equivalent wall area in the circumferential and longitudinal axis respectively. To maintain a consistent thickness of pipe shell (1.47 mm) in both the bending stiffness and membrane stiffness matrices, the modulus of elasticity of the pipe in the Y axis was modified to match proportions of actual steel area (7.677×10^{-4} m^2/m) to pipe area in the model (1.47×10^{-3}

m^2/m). The pipe shell-bending and membrane stiffness properties are shown in Tables 4.2 and 4.3.

To verify the accuracy of the orthotropic pipe stiffness, a simulation of a parallel plate load test was run in the finite difference program (Figure 4.2). The pipe using the estimated pipe stiffness properties was generated between two blocks of elastic material. One block was stationary while the other block moved towards it at a constant displacement per step.

Table 4.2 FLAC 3D Pipe Shell Bending Stiffness Properties

D_x (kPa-m^3)	$2.7x10^{-4}$
D_y (kPa-m^3)	1.24
G_{xy} (kPa-m^3)	$6.7x10^{-5}$
D_{xy} (kPa-m^3)	$1.3x10^{-4}$

Table 4.3 FLAC 3D Pipe Shell Membrane Stiffness Properties

E_x (kPa)	$1.03x10^6$
E_y (kPa)	$106x10^6$
G (kPa)	$253x10^3$

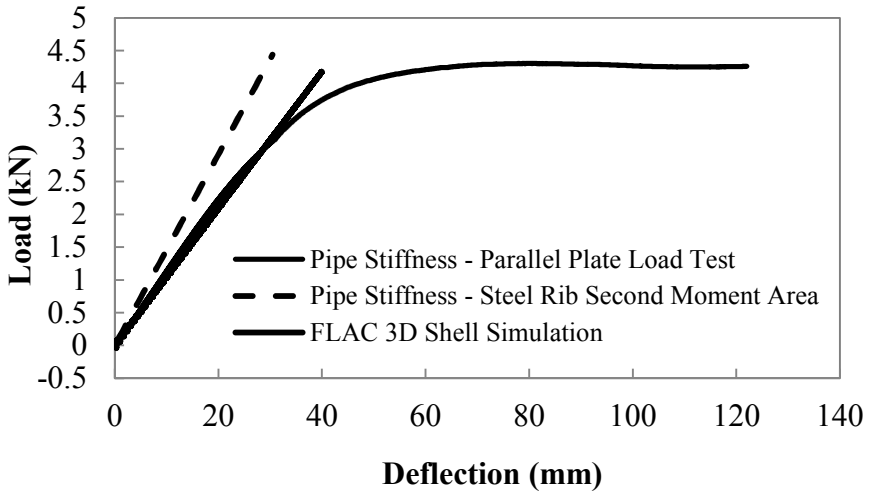

Figure 4.2 Simulated Parallel Plate Load Test Results

4.2.2 Pipe Local Buckling

The steel reinforcement of the pipe wall is encapsulated in an HDPE cover and is outstanding from the outer surface of the pipe wall. The local buckling of the pipe wall is controlled by the stress in the pipe wall and the configuration of the wall elements. The pipe wall can be seen in Figure 4.1. Since the numerical analysis will be reviewed for a wide range of loading conditions it is important to determine if there are any limit states or changes in the stiffness of the pipe wall not captured in the experimental tests. Local buckling of the pipe wall is one of those items that can affect the results of the numerical analysis.

Assuming compatibility of strain between the two materials, the material areas shown in Figure 4.1, a modulus of elasticity of steel E_s=200,000 MPa, and a long term modulus of elasticity of the plastic E_p= 450 MPa, the steel takes 99% or effectively the entire load of the cross section. To calculate the strength of the pipe wall it is important to determine if the wall

element will buckle locally before other failure modes occur; yielding or global buckling of the pipe. The critical buckling strength of plates has been given in the literature review (Bryan 1891), and restated here in Equation 4.5:

$$\sigma_{CR} = k\frac{\pi^2 E}{12(1-\mu^2)}\left(\frac{t}{w}\right)^2 \qquad \textbf{4.5}$$

where the steel modulus of elasticity (E), steel plate thickness (t) and width (w), the steel Poisson's ratio (μ), and buckling coefficient (k) are the terms of the expression.

The buckling coefficient k is a function of the width and length proportions of the plate and the edge supporting conditions. For a simply supported (S.S.) plate on all four sides (Figure 4.3), k is defined by the Equation 4.6.:

$$k = \left[m\left(\frac{w}{a}\right) + \frac{1}{m}\frac{a}{w}\right]^2 \qquad \textbf{4.6}$$

where w is the plate width, a is the plate length, and m is the buckling mode represented by an integer (1, 2, 3…..).

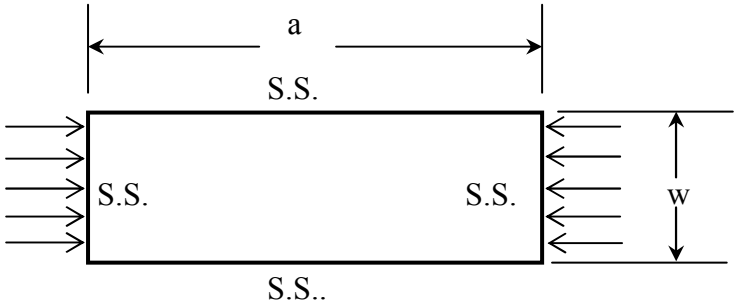

Figure 4.3 Simply Supported Plates on all four sides

The buckling coefficient for a simply supported plate with one free side (Figure 4.4) is given by Gerard and Becker (1957) with Equation 4.7:

$$k = \left[m\left(\frac{w}{a}\right) + \frac{1}{m}\frac{a}{w}\right]^2 \qquad \textbf{4.7}$$

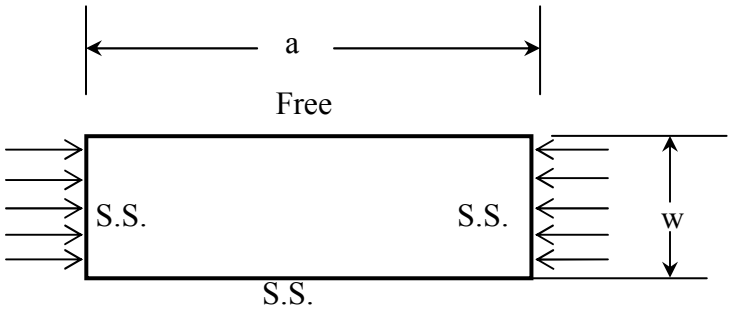

Figure 4.4 Simply Supported Plates with One Side Free

The length of the plate is assumed to be long. The values of k converge to 4 and 0.43 for the simply supported plate on all four sides and the simply supported plate with one side free, respectively. The finite element program Abaqus™ was used to analyze one rib of the pipe wall for buckling properties. The model of the section was built using plate elements with steel properties for the rib and HDPE properties for the pipe wall. The cross sectional area was built as a steel plate outstanding from an HDPE pipe wall.

Table 4.4 Material Properties for Analysis

Material	Modulus of Elasticty (MPa)	Poisson's Ratio
HDPE	450	0.46
Steel	200,000	0.25

The load was applied to the steel rib only as discussed earlier, considering strain compatibility across the section. The initial boundary conditions and loads can be seen in Figure 4.5. As in any finite element analysis, boundary conditions are important, and it was critical to recognize that the pipe wall is continous and unable to translate in its own plane as the pipe wall is inifite in the direction of the pipe.

The load was applied as a unit load, and run as a buckling analysis resulting in an Eigenvalue equal to the first mode of buckling. Analyses were completed for plate lengths ranging from 6 mm to 152 mm. The critical buckling stress given by the finite element program was equated to a buckling coefficient using Equation 4.7. Typical buckling results can be seen in Figure 4.6.

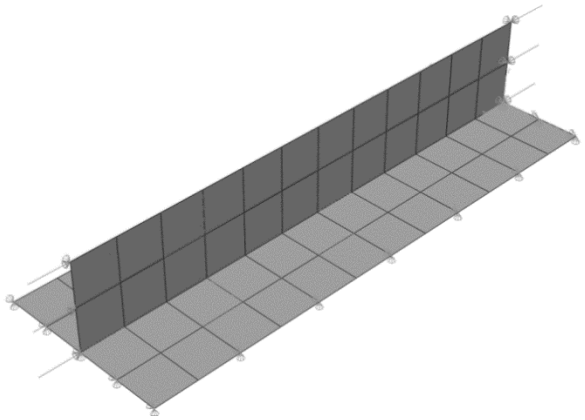

Figure 4.5 Abaqus ™ Boundary Conditions and Loads

Results of the analysis can be seen in Figure 4.7. The results show that the buckling coefficient for a range of lengths nearly matches the buckling coefficient of a simply supported plate with one free side given by the Gerard and Becker (1957) equation. The buckling coefficient of a simply supported plate is included in the figure for reference. The analysis

values are slightly lower and demonstrate that the edge condition is close but not equivalent to a simple support. The pipe wall does have some flexibility, slightly lowering the buckling coefficient. As the member length was reduced below 10 mm long (a/w< 0.6) Abaqus™ stopped analysis as the first Eigenvalue was a result of buckling of the HDPE liner.

The analysis of the buckling coefficient resulted in a buckling coefficient of 0.33, slightly less than the standard value of 0.43 for a simply supported plate with one free edge. Applying the coefficient of buckling of 0.33 to Equation 4.5, the critical buckling stress for the steel rib on the pipe is 772 MPa. This critical buckling stress is higher than the controlling yield stress for the steel rib material of 552 MPa. These results also do not include additive resistance to buckling from any soil materials between the ribs.

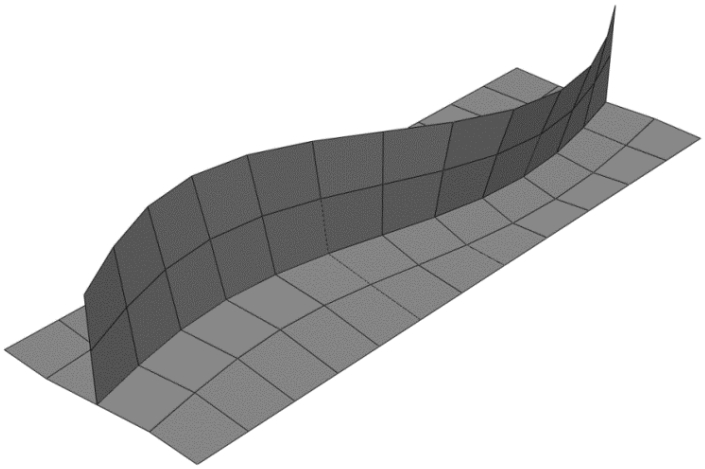

Figure 4.6 Typical Abaqus ™ Buckling Results

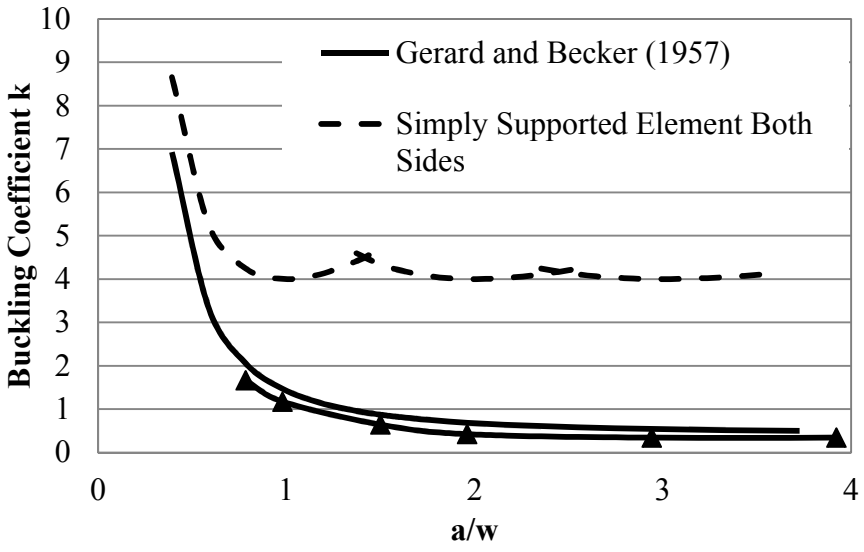

Figure 4.7 Buckling Coefficient k

These results indicate that as long as the axial stress in the pipe wall is kept below the yield stress, local buckling should not be an issue for an analysis of a simple shell (uniform thickness) of equivalent wall stiffness. In conditions where there are bending and axial load the superposition of the two stresses will also be kept below the yield stress similar to AISI's method of preventing local buckling due to bending stress. If it is desired or necessary that the pipe wall stress exceed the yield stress, it will be important to have a pipe section in the numerical analysis that reflects the yielding and local buckling of the pipe section.

4.2.3 Fat Clay

The fat clay in-situ soil was modeled as a linear elastic material, based on the CBR values ranging from 2% to 3%. Lister and Powell (1987) gave the following approximation for

modulus of elasticity for soils with a CBR (California Bearing Ratio) less than 5% (Equation 4.8). Based on the CBR of 2.5% the modulus of 25 MPa was used. The resulting bulk modulus and shear modulus based on a Poison's ratio of 0.3 are shown in Table 4.5.

$$E = 10\ x\ CBR \quad \text{in MPa} \qquad \textbf{4.8}$$

Table 4.5 Elastic Soil Properties of Fat Clay

	Fat Clay
Bulk Modulus K (MPa)	20.8
Shear Modulus G (MPa)	9.6

4.2.4 Sand and Crushed Stone

As discussed in the literature review it was important that the non-linear and plastic strain of the backfill be captured in the numerical analysis. For this reason, the Cap-Yield constitutive model from the FLAC 3D program was selected to model the sand and aggregate backfill materials. The Cap-Yield soil parameters were developed based on the results of the triaxial tests as discussed in Section 3.4.1 of the previous chapter. The Cap-Yield parameters are shown in Tables 4.6 and 4.7. A numerical analysis was run on an element to simulate a triaxial test for each confining pressure, the results of which are shown in Figures 4.8 through 4.11.

Table 4.6 Cap-Yield Soil Parameters of Kansas River Sand

Dr (%)	25	77
G^{e}_{ref} (kPa)	13472	26399
K^{iso}_{ref} (kPa)	67834	91500
R_f	0.95	0.95
m	0.81	0.74
ϕ_f	38	46
β	2	2
ν	0.2	0.45
ψ	0	2.5

Table 4.7 Cap-Yield Soil Parameters of Crushed Stone Aggregate

	Crushed Stone Aggregate
G^{e}_{ref} (kPa)	9391
K^{iso}_{ref} (kPa)	135000
R_f	0.95
m	0.77
ϕ_f	48
β	2
ν	0.38
ψ	0

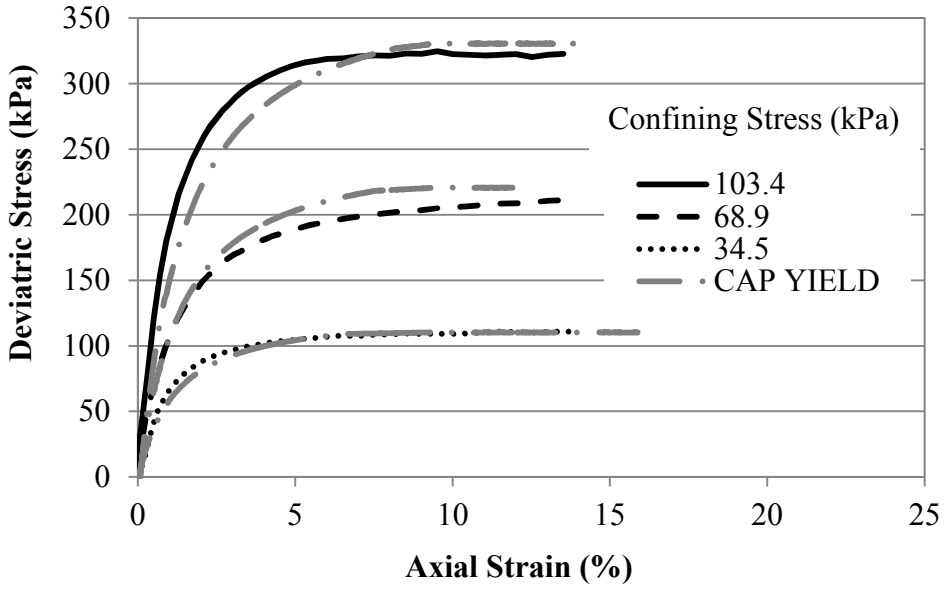

Figure 4.8 Triaxial Data and Numerical Triaxial Model - Loose Sand (Dr = 25%)

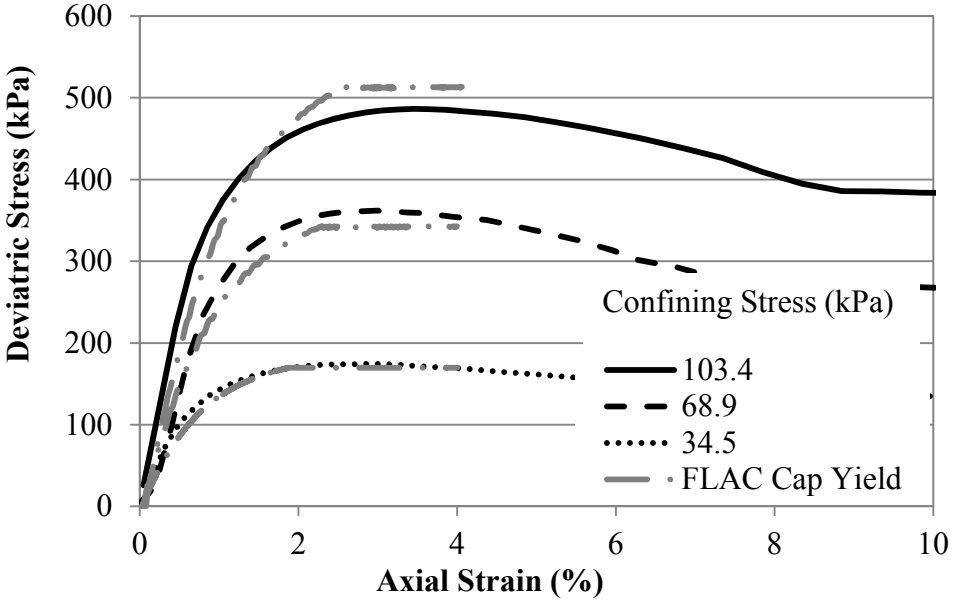

Figure 4.9 Triaxial Data and Numerical Model - Dense Sand (Dr = 77%)

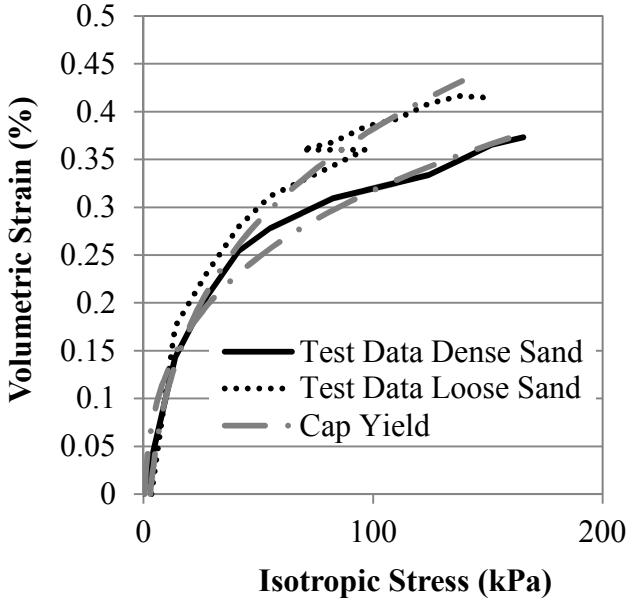

Figure 4.10 Isotropic Compression Data and Numerical Model - Dense and Loose Sand

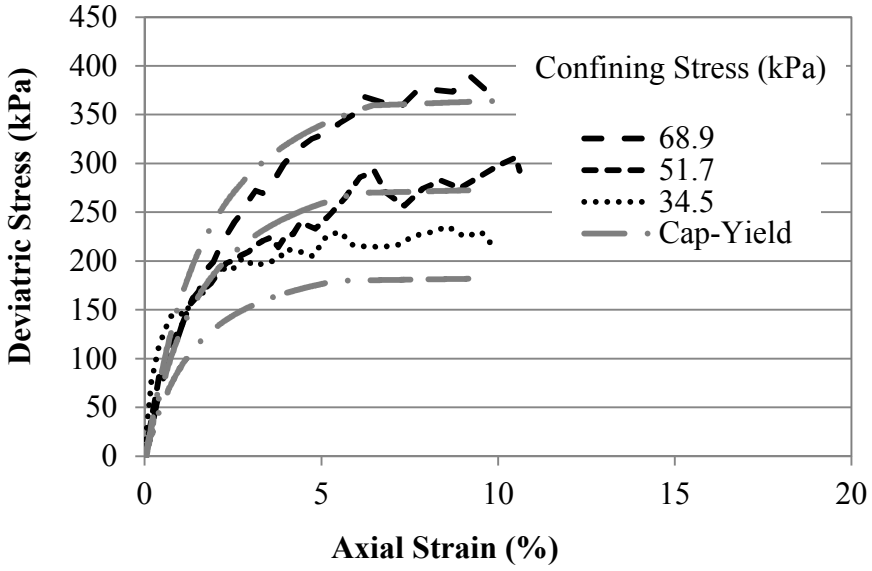

Figure 4.11 Triaxial Data and Numerical Model – Crushed Stone Aggregate

4.2.5 AB-3 Aggregate

The AB-3 aggregate used as a base course was modeled as a linearly elastic perfectly plastic material with the Mohr-Coulomb failure criterion provided by the FLAC 3D software. The friction angle and cohesion values used in the numerical models were based on triaxial shear tests on AB-3 material compacted to 95% maximum density (Figures 4.12 and 4.13). The modulus of elasticity of the compacted AB-3 material was estimated based on the application of Janbu's (1963) equation (Equation 2.18). The modulus of elasticity for the unreinforced condition was computed as 16.4 MPa assuming a minimum confining pressure of 20 kPa. The reinforced condition relied on additional confinement due to compaction of the AB-3 in the geogrid, and the modulus of elasticity was estimated at 27.25 MPa. The resulting bulk and shear modulus given in Table 4.9 are based on a Poisson's ration of 0.3.

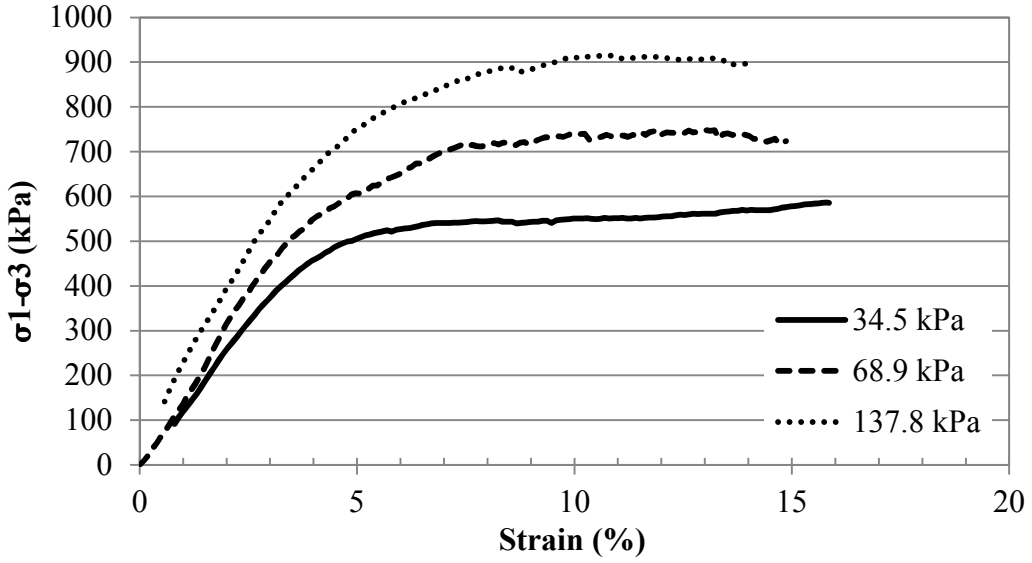

Figure 4.12 Triaxial Tests of Compacted AB-3 Aggregate

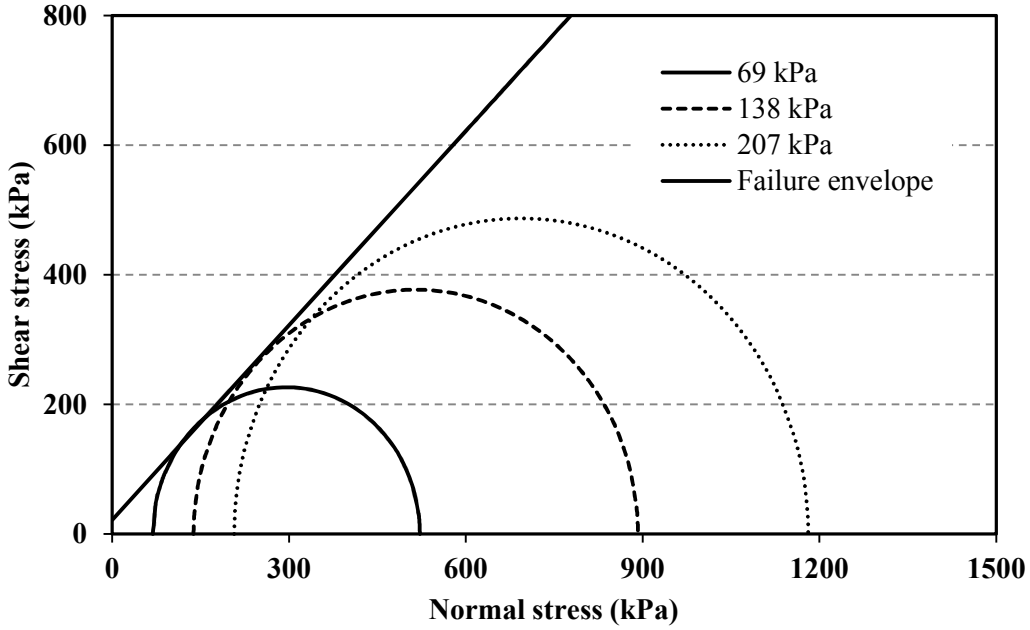

Figure 4.13 Failure Envelope of AB-3 Aggregate

Table 4.8 Properties of AB-3 Aggregate

Liquid/Plastic Limit- LL/PL	20/13
Specific Gravity G_s	2.69
Maximum Dry Unit Weight γ_{dmax} (kN/m^3)	20.6
Optimum Moisture Content w_{opt} (%)	10
Coef. of Curvature / Uniformity Cc/Cu	1.55/21
Mean Particle Size (mm)	7.0
Friction Angle ϕ	45˚
Cohesion (kPa)	22

Table 4.9 AB-3 Elastic Properties of AB-3

	AB-3	AB-3 Reinforced
Bulk Modulus K (MPa)	13.7	22.7
Shear Modulus G (MPa)	6.4	10.5

4.2.6 Geogrid

The punch-drawn polypropylene biaxial geogrid described in Section 3.6.1 was modeled in the numerical analysis with the built-in geogrid structural element. The FLAC 3D program models geogrids as a 3 node flat element that resists membrane loads only. Similar to the pipe in the model, the geogrid used was orthotropic with a different stiffness in each axis. Since the strains in the tests were all measured below 1% strain the tensile stiffness (J) at 2%, published by the geogrid manufacturer was used as a starting point and adjusted to generate the stiffness parameters in the model. Giroud (1992) and Kupec and McGown (2004) have also shown that that stiffness of a biaxial geogrid was higher under biaxial tension than in uniaxial tension. Because of the non-linear stress strain stiffness of the geogrid and the biaxial nature of the geogrid the stiffness was approximated to be twice the stiffness given by the manufacture, at 2% strain, and also considering the stiffness added to the membrane by a Poisson's ratio of 0.3.

The effective shear modulus of the geogrid was approximated based on the proposed correlation between the aperture stability modulus (ASM) and the geogrid shear modulus provided by Perkins et al. (2004). The relationship reduced to a convenient equation (Equation 4.9), where ASM is in N-mm/degree units and the shear modulus is in kPa.

$$G = 7\ ASM \quad \textbf{4.9}$$

Table 4.10 FLAC 3D Geogrid Membrane Stiffness Properties

J_M (kN/m)	660
J_{XM} (kN/m)	990
G (kPa)	4550

4.3 Numerical Model Mesh and Boundary Conditions

The numerical analysis model was created to simulate the conditions established in the laboratory tests. One quarter of the two meter by two meter by three meter geotechnical box was modeled to take advantage of the symmetry parallel and perpendicular to the length of the pipe. The box was modeled as rigid boundary conditions, perpendicular to the boundary, on the bottom, and the four sides of the soil block. The mesh size was selected on a number of criteria, foremost of which had sufficient density to successfully model the laboratory test while at the same time minimizing the model size and run times. The plastic pipe was modeled by three sided flat elements with three nodes and as such the pipe must also have a minimum number of shell elements so that the pipe was sufficiently circular in shape. The mesh was generated so that horizontal layers could be placed to simulate the installation phase of the box setup. For simplicity a uniform mesh size of 38.1 mm was selected which was also evenly divisible into the diameter of the pipe. A schematic of the mesh can be seen in Figure 4.14.

To check the validity of the mesh size the results of an elastic run was compared to the elastic solution provided by Burns and Richard (1964). The Burns and Richard solution can be used to determine pipe and soil stresses for elastic soil and elastic pipe simulations. The solution assumes that uniaxial pressures (P) are uniform, infinite, and applied at the surface one to two diameters distance from the pipe (Figure 4.15). Per Burns and Richard (1964), "the results of the method are for the applied pressure only and can be superimposed on the conditions existing before the application of the uniform surface load." The method also allows the designer to simulate full bondage or full slip between the pipe and the elastic medium.

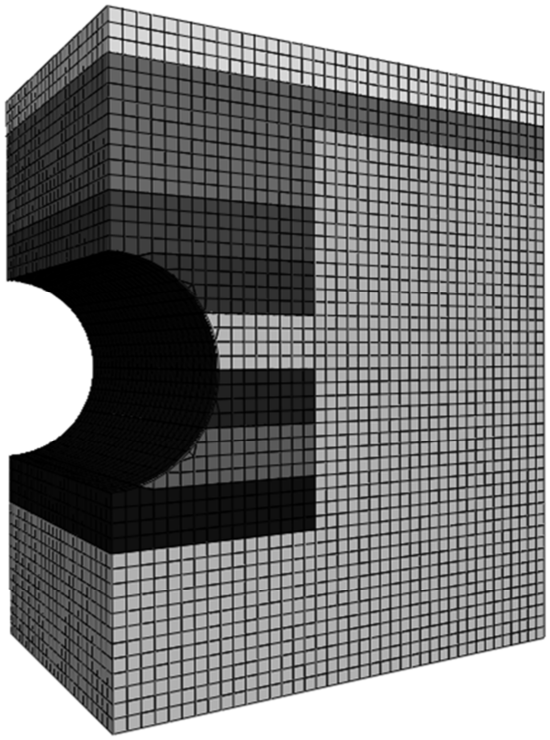

Figure 4.14 FLAC 3D Mesh

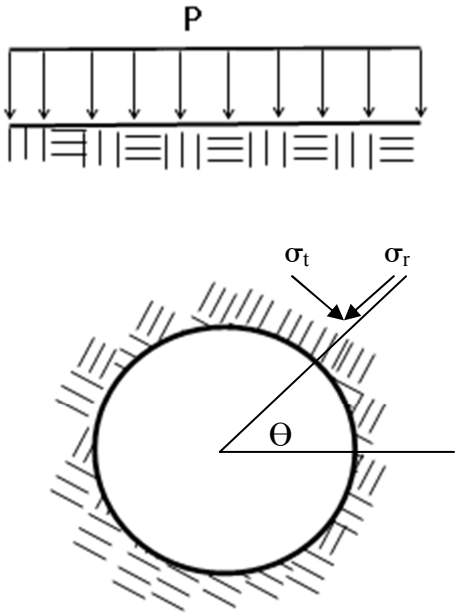

Figure 4.15 Pressure Applied to the Free-Field State (Burns and Richard 1964)

To simulate the conditions of a Burns and Richard (1964) analysis the model was built with pipe stiffness described in the previous sections and with an isotropic elastic medium, with a modulus of 25 MPa. This modulus was in the range of sand stiffness determined by the triaxial tests. The derived equations for stress in the elastic medium provided by Burns and Richard (1964) were input into a spreadsheet application. A comparison of the FLAC 3D and the elastic solution are shown in the following figures. In the pipe wall the thrust (N) and moment (M) per unit length of pipe are dimensionless and shown in Figures 4.16 and 4.17 for the no-slip and full-slip conditions. Theta (Θ) is the angle from the springline to the location on the pipe wall. In the elastic medium the radial stresses (σ_r) are forces parallel to the radius of the pipe and the tangential stresses (σ_t) are forces perpendicular to the radius (R). The dimensionless pressures in the elastic medium are shown in Figures 4.18 and 4.19, and the distance of the element (r) is dimensionless by the radius of the pipe (R).

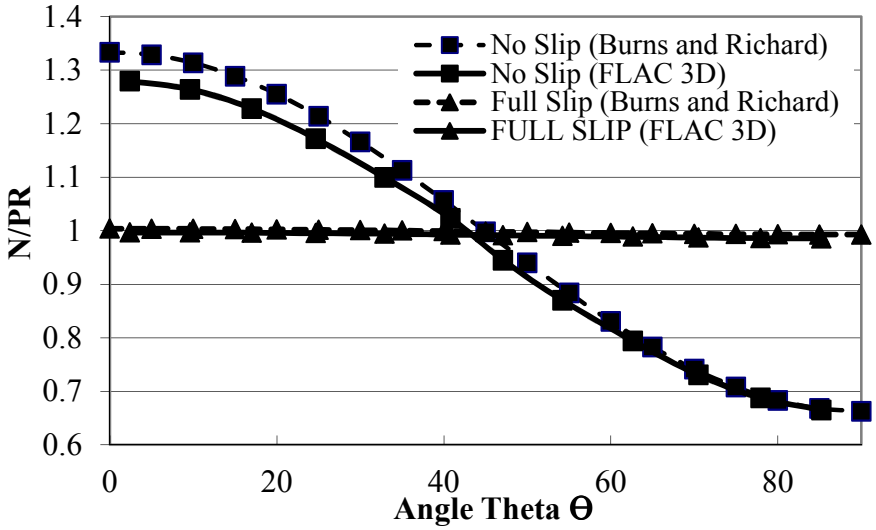

Figure 4.16 Axial Thrust in Pipe Wall

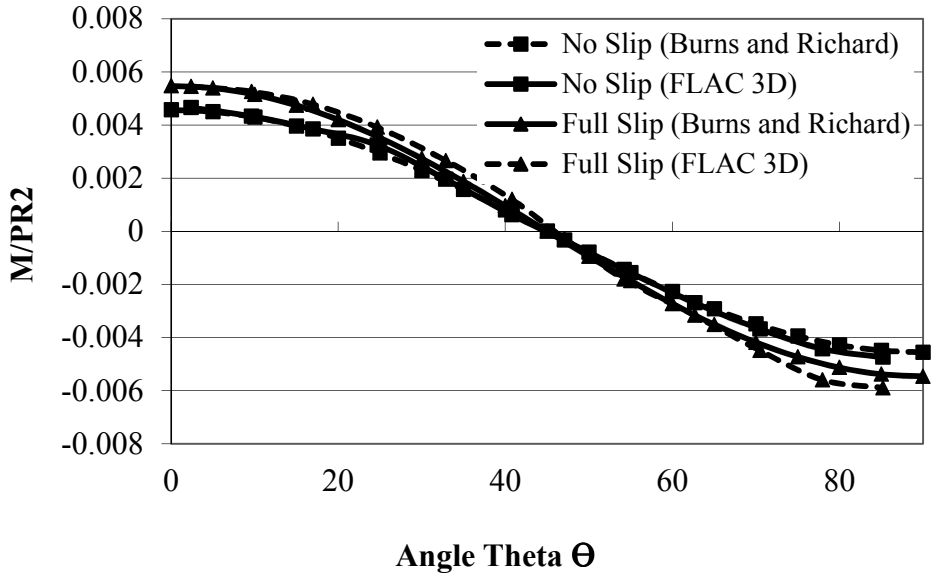

Figure 4.17 Moments in the Pipe Wall

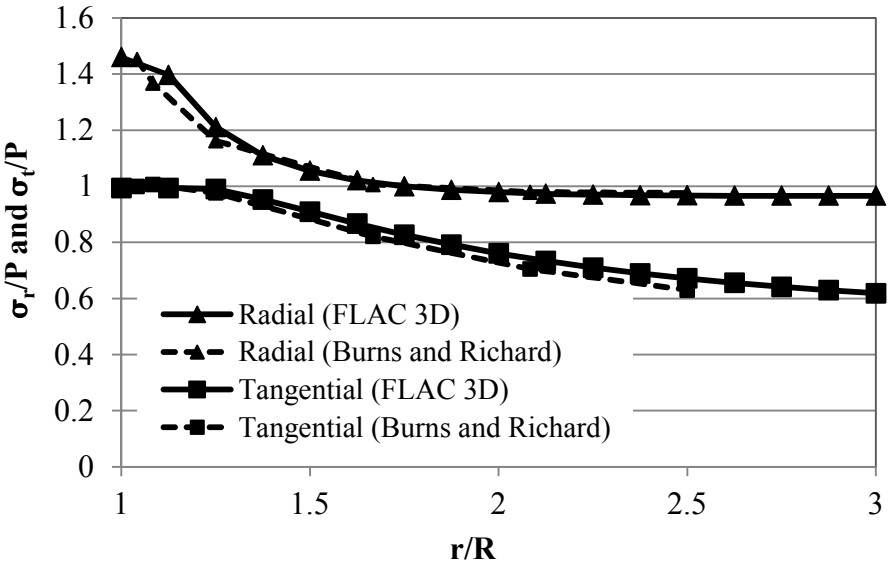

Figure 4.18 Earth Pressure at Springline with a Full Slip

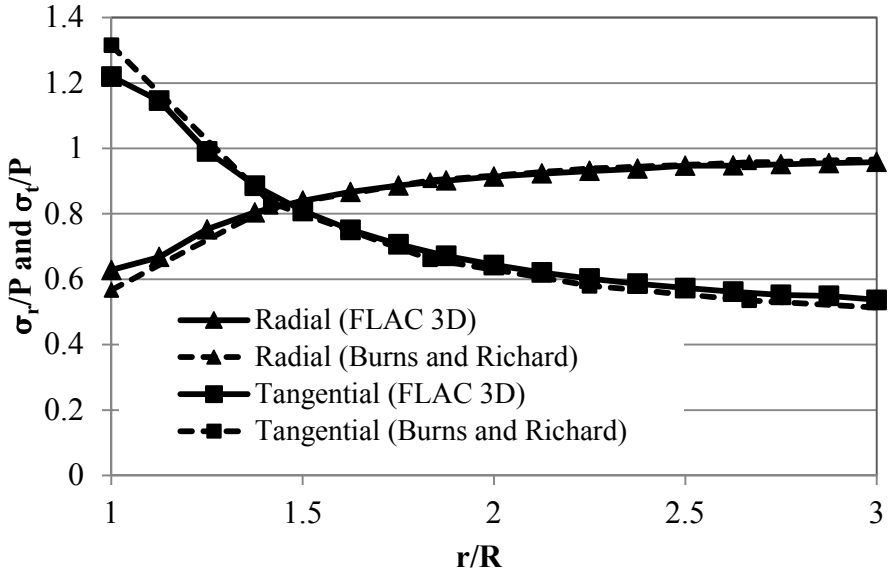

Figure 4.19 Earth Pressure at Springline with No Slip

The data points for the FLAC model were taken as the average radial and tangential stresses for the zone. The data point at the pipe wall was determined by the polynomial-fit extrapolation provided by the FLAC 3D software. Overall there appears to be a good agreement between the elastic solution and the FLAC 3D model, and the mesh density in the numerical model seems appropriate.

4.4 Numerical Simulation of Installation and Compaction

As noted in the literature review previous researchers have emphasized the importance of determining the pipe and backfill stress states due to the installation and construction process. To capture the stresses in pipe and backfill due to the effects of installation of the sand and crushed stone the numerical analysis was built similarly to the actual construction process. The bedding and each layer were placed and stressed to simulate compaction if required, and the model was run until a balanced strain was reached in succession.

4.4.1 Kansas River Sand Backfill

To simulate the stressing of the layers of soil the method described by Elshimi and Moore (2013) was selected. The basic principle of the Elshimi and Moore method is to stress the backfill layer. This method allows the soil to displace the flexible pipes alleviating some of the pressure and creating the peaking process seen in the construction of flexible pipes. The

horizontal pressure as calculated by Equation 4.10 is a gradient pressure based on the unit weight of the soil (γ), the depth of the layer (d), a passive earth pressure factor (N_ϕ) (Equation 4.11), and a kneading factor (K_n). Based on the recommendations by Elshimi and Moore (2013) a kneading factor of 2 was chosen on the basis that a rammer was used to compact the soil between the pipe and the trench wall. In this case, because the model was three dimensional, the horizontal stresses were placed in both the X and Y axes of the model. To prevent the soil from failing a temporary cohesion factor of 4 kPa was added as suggested by Elshimi and Moore (2013).

$$\sigma_h = \gamma d N_\phi K_n \qquad \textbf{4.10}$$

$$N_\emptyset = \frac{1 + sin\phi}{1 - sin\phi} \qquad \textbf{4.11}$$

While each layer was stressed, the top and bottom of the layer were fixed in the vertical axis causing the material to displace horizontally depending on the stiffness of the pipe, the backfill, and the trench wall (Figure 4.20). The pipe and backfill were analyzed with an interface element with no tensile capacity, and with a coefficient of interface friction of one. After a balance was reached and the analysis run completed the boundary condition was released and the cohesion was removed as the next layer was created. This process was repeated until all of the layers were in place. The Mohr-Coulomb constitutive model was used during the backfill process as the strains in the backfill were large and the stresses were well beyond the yield plane. The modulus of bulk and shear modulus of the backfill were chosen based on the minimum calculated secant modulus of elasticity (E_{50}) for the loose sand condition (D_r = 25%).

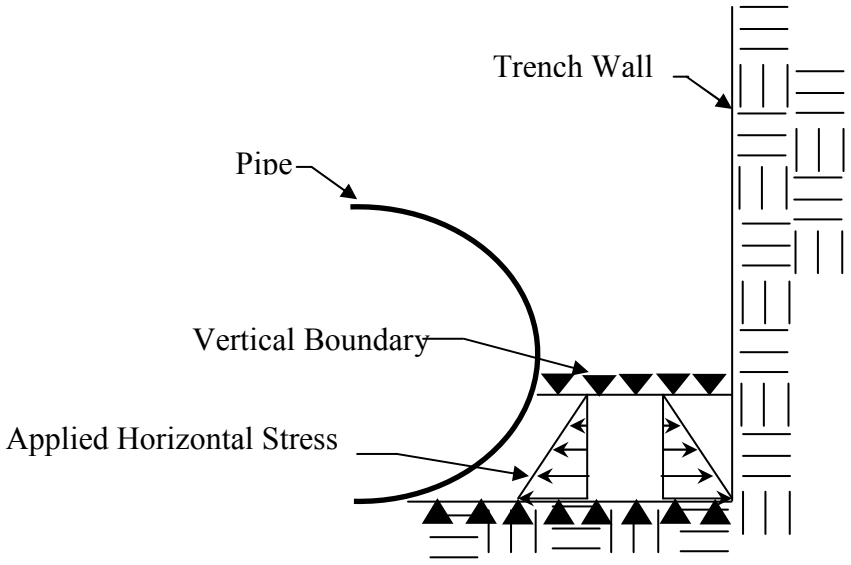

Figure 4.20 Applications of Typical Stresses to a Compacted Layer

After each step, with the compaction stress run, the next layer generated and the confining boundary conditions released, the soil layer's constitutive model was switched to the cap-yield soil model. To determine the properties of each zone in the model for the cap-yield soil model, FLAC was programed to cycle through each zone to determine the critical soil states and to generate the shear and volumetric strain tables based on the mobilized friction angle and the cap pressure respectively. The mean effective stress (p) and the deviatoric stress (q) were calculated with critical state soil mechanics by Equations 4.12 and 4.13.

The initial cap pressure (p_c) was estimated by Equation 4.14. The mobilized friction angle was calculated by Equations 4.15 and 4.16, and the initial shear stiffness of each zone was determined by Equation 4.17. The tables controlling the shear and volumetric plastic strains were generated using Equations 2.29 and 2.30.

$$p = \frac{\sigma_1 + \sigma_2 + \sigma_3}{3} \quad \textbf{4.12}$$

$$q = \frac{\sqrt{(\sigma_1 - \sigma_2)^2 + (\sigma_2 - \sigma_3)^2 + (\sigma_3 - \sigma_1)^2}}{2} \quad \textbf{4.13}$$

$$p_c = \sqrt{p^2 + q^2} \quad \textbf{4.14}$$

$$m' = {}^{q}/_{p} \quad \textbf{4.15}$$

$$\phi_m = asin((3m')/(6 + m')) \quad \textbf{4.16}$$

$$G^e = G^e_{ref}\left(\frac{p}{p_{ref}}\right)^m \quad \textbf{4.17}$$

The installation steps were run a number of times with varying friction angles ranging from the loose condition to the dense condition. The friction angles used in both the Mohr-Coulomb constitutive model and to calculate the horizontal gradient pressure in Equations 4.10 and 4.11 were changed. The resulting pipe deflection for a soil friction angle of 46° was most similar to the results recorded in the full scale laboratory test (Figure 4.21).

The pipe deflection results were also very sensitive to the pipe stiffness (D_y). Small adjustments in the pipe stiffness caused the pipe to behave very differently. If the pipe was made stiffer the pipe would not deflect or peak. If the pipe stiffness was lowered the pipe would deflect, but not peak. The pipe shape would become square with no peaking. The pipe stiffness of 1.36 kPa-m^3 used was 10% higher than what was back calculated by the parallel pipe test method (Table 4.2). It was not surprising that there was some difference in the pipe stiffness between the parallel plate load test and the full scale test. The parallel plate load test was on a 0.356 m long sample that was cut from a full piece of which the steel reinforcing ends were loose. In the full scale tests the pipes were complete from bell to spigot, with no steel reinforcement and free ends.

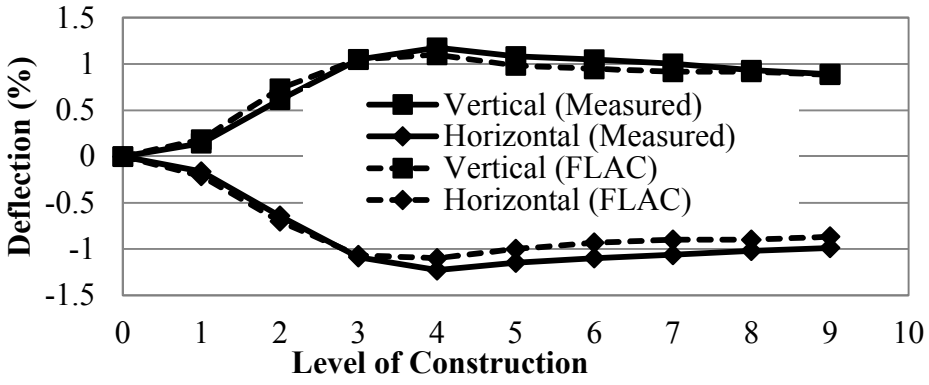

Figure 4.21 Measured and Computed Pipe Deflections during Installation

The earth pressures in the numerical analysis were also recorded at each step to determine if the method used resembled the recorded values in the laboratory test (Figure 4.22). Earth pressure cells C_3, C_4, S_3, S_4, and S_5 were not included in the first full scale test with sand backfill.

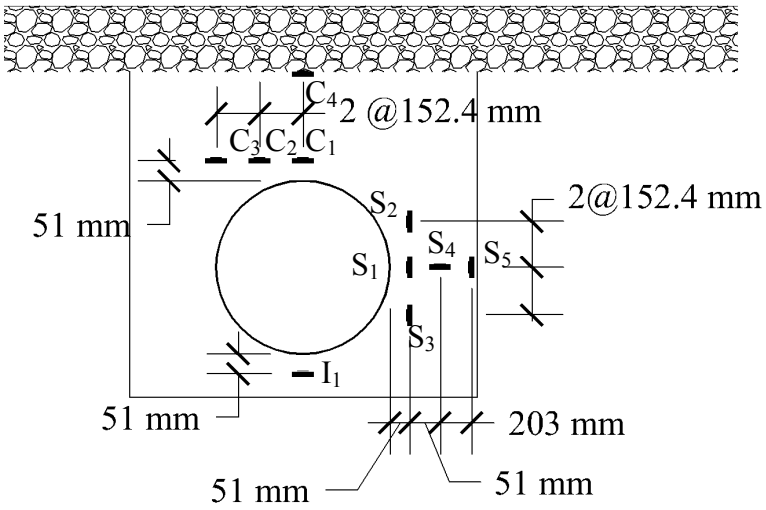

Figure 4.22 Earth Pressure Cell Locations

Because of the way that the numerical mesh was laid out, the stresses reported at S_1 and S_2 are the average of the stresses of the zones above and below the desired location, at the springline and the shoulder. The applied horizontal pre-stress at each installation level (Figure 4.20) caused a significant change in horizontal pressure from the top of one installed layer to the bottom of the next. It is unclear how accurate this is as it is expected that compaction of the next layer would soften this distinct transition, however the resulting average of the two stresses matched fairly closely the stresses measured at earth pressure cells S_1 (Figure 4.23) and S_2 (Figure 4.24). The vertical pressures in the cells C_1 and C_2 are shown in Figures 4.25 and 4.26 respectively.

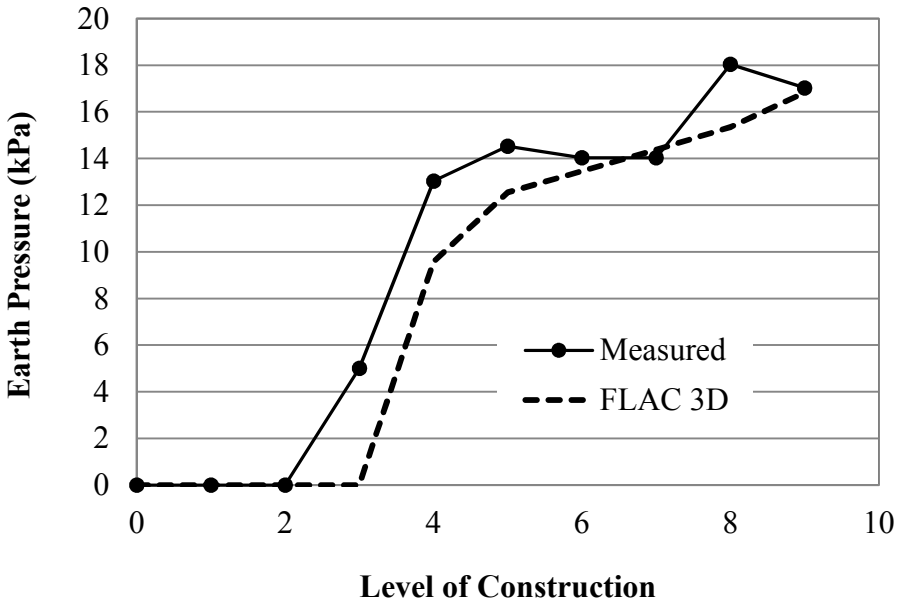

Figure 4.23 Earth Pressure at Spring Line (S_1)

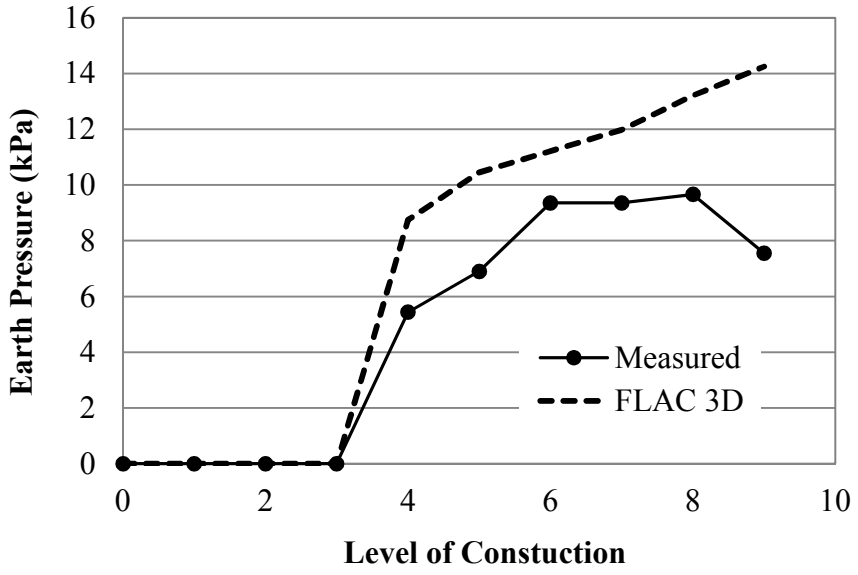

Figure 4.24 Earth Pressure at Shoulder (S_2)

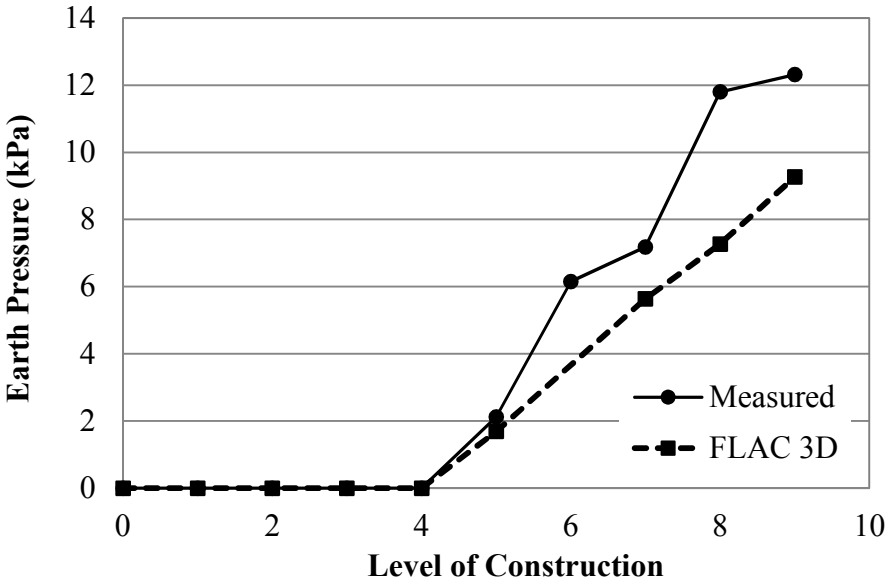

Figure 4.25 Earth Pressure at Crown (C_1)

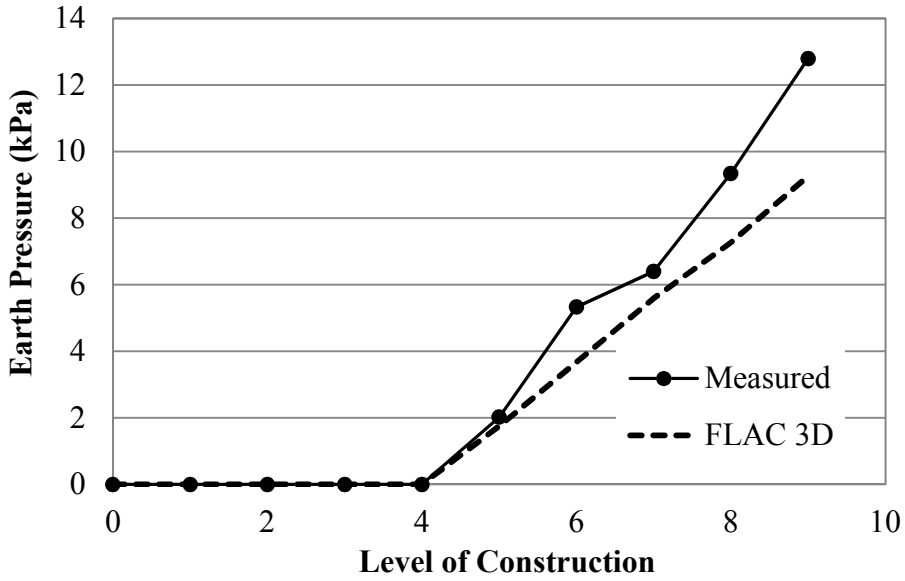

Figure 4.26 Earth Pressure at Crown (C_2)

4.4.2 Crushed Stone Aggregate Backfill

The analysis of the construction and installation process for the crushed stone aggregate backfill was attempted similar to the sand backfill. Each layer of the crushed stone backfill was added and the model was run to equilibrium. The same pipe stiffness fine-tuned in the sand backfill analysis was used. It was noted that during the installation there was a peaking of the pipe of approximately 0.2% or about 1.2 mm (Figure 3.16). A series of numerical analysis was run varying the frictional strength values of the backfill and the bulk and shear moduli from the recorded triaxial values to zero. The resulting peaking in the analysis was, at the maximum, one fifth of the actual recorded values. It is assumed that there was some dynamic action of the backfill being poured or dumped into the trench. Analysis of the plate loading tests indicated that the modeling of the installation process in the crushed stone aggregate backfill condition

resulted in a high stiffness at the springline that resulted in a calibrated model that did not match the laboratory data. Since the pipe returned to its original circular shape after the installation of the backfill, it was decided to generate the backfill in one step. The Cap-Yield model parameters where calculated per equations 4.12 through 4.17.

4.5 Numerical Results of Plate Loading Tests

The plate loading tests were analyzed by taking the completed analysis of the installation of the backfill and base course and applying the plate loads to the surface in the steps described in Table 3.6. The plate was modeled with a modulus of elasticity of 200 GPa and with only a vertical degree of freedom. Each step was run until equilibrium was met before proceeding to the next step. The concentration of the pipe loading in the aggregate backfill was chosen as the less stiff backfill resulted in the highest benefit by including the geosynthetic.

4.5.1 Base Course Compaction

During the analysis of the double reinforced conditions it quickly became apparent that the reduction in pipe deflections and distribution of the soil pressures around the pipe was not simply attributable to the presence of geogrid. Placing the geogrid in the numerical analysis model, with the properties as described in Section 4.2.6 resulted in the same pipe displacements as the unreinforced condition.

An investigation of current and past research of numerical analysis of geogrid reinforced base courses shows that there is a precedent for this type of behavior especially in continuum analysis. There are a number of ways, in which this issue has been resolved. Wathugala et al (1996), Erickson and Drescher (2001), and Leng and Gabr (2003) showed in numerical parametric studies that geogrid stiffness is one the most important parameters for reducing surface displacements. In the studies the geogrid stiffness was increased by a factor of ten or more to assist in simulating measured values (Kwon et al. 2005).

Another method of reducing the surface displacements and strains at the bottom of the base course is considering the residual stress in the base course layer. Perkins (2004), Kwon et al. (2008), and Kwon et al. (2009) indicated that increasing the confining pressure in the base course layer as a result of the residual stress due to compaction decreased the displacement in the base course. This method has been used predominantly in the investigation of cyclic loading of the base courses. The basis for the amount of residual stresses estimated in the base course was the result of discrete element models (Kwon et al. 2009).

Other investigators treated the geogrid reinforcing as an apparent cohesion in the geogrid reinforced layer, which has the combined properties of the soil and geogrid as a composite material based on the Schlosser and Long (1974) concept. Nquyen et al. (2011) and Wu et al. (2013) proposed equations for the apparent cohesion provided by the geogrid reinforcement. The equation proposed by Wu et al. (2013) was used for this study (Equation 4.18):

$$c_r = \left[0.7^{\frac{s_v}{s_{ref}}}\right] \frac{T_f}{2s_v} \sqrt{K_p} + c \qquad \textbf{4.18}$$

where T_f is the tensile strength of the geogrid, s_v is the vertical spacing of the reinforcements, K_p is the coefficient of passive earth pressure, and c is the cohesion of the base course. The reference spacing, S_{ref} is based on Equation 4.19.

$$s_{ref} = 6d_{max} \quad \textbf{4.19}$$

where d_{max} is the maximum particle size.

Both the residual stress method and the composite method were investigated for the condition of the upper layer of geogrid reinforcement. For the apparent cohesion method the combined cohesion of the base course was assumed to be 100 kPa based on Equation 4.17. For the residual stress method a series of analyses were run with a residual stress in the base course ranging from 20 kPa to 60 kPa. This range was based on the suggested values by Perkins et al. (2004) and Kwon et al. (2009).

A comparison of the two methods is shown in Figure 4.27 by plotting the displacement of the mesh at the centerline of the model. The displacements at the surface, at the interface of the base course and the backfill, and at the top of the pipe are compared. The recorded displacements at the surface and of the vertical pipe deflection were 8.8 mm and 1.8 mm respectively.

While the pipe deflection is not precisely the displacement at the top of the pipe, due to movement at the bottom of the pipe, there is a strong correlation as the displacement at the bottom of the pipe is small by comparison.

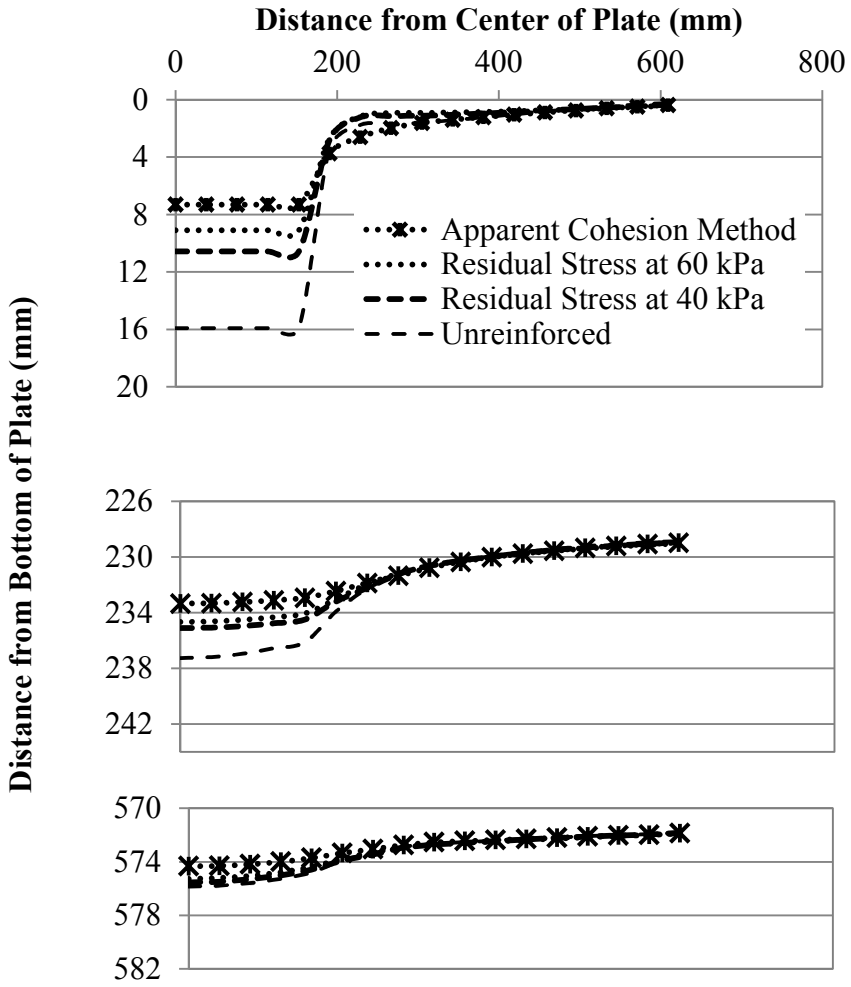

Figure 4.27 Vertical Displacement at Center Line of model

The residual stress method worked well near the surface of the test model. An assumed residual stress in the base course of 40 kPa resulted in a significant decrease in the surface displacement nearly matching the recorded values, 10.6 mm versus 8.8 mm. At the bottom of the base course the displacement indicated by the analysis decreased from 9 mm to 6.5 mm by including the geogrid and the residual stress. At the top of the pipe the displacement did not closely match the recorded values when the residual stress method was used. An expanded view of the displacement at the crown of the pipe (Figure 4.28) shows the displacement of the soil at

the top of the pipe. Because of the importance of the displacement of the pipe to the study the apparent cohesion method was used for the analysis of the experimental data and the parametric study.

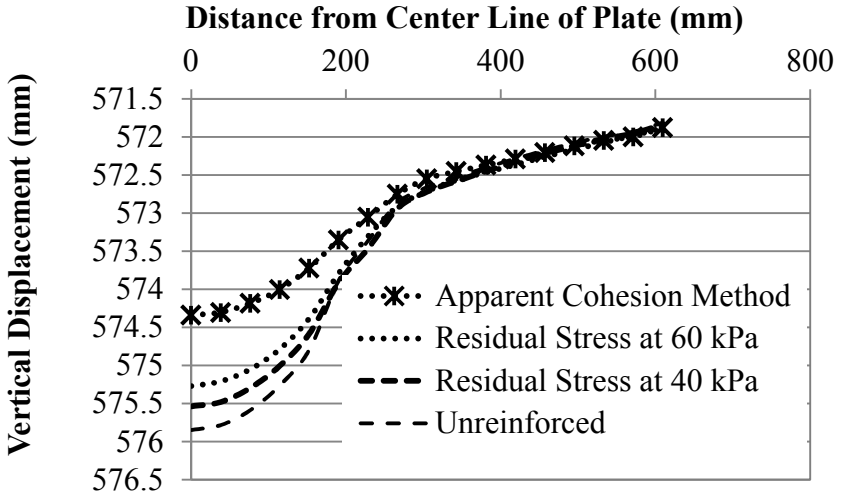

Figure 4.28 Vertical Displacements at the Crown of the Pipe

4.5.2 Plate Load Tests on Aggregate Backfill

Given that the most benefit from the inclusion of the geogrid was in Tests 5 through 10, the primary focus of the comparison and calibration of the numerical methods was for the condition of crushed stone aggregate backfill. Following are comparisons of the numerical test results with the experimental data for plate settlements, pipe deflections, earth pressures, pipe strains, and geogrid strains.

Plate Settlements and Pipe Deflections

As noted in Section 4.5.1 it was surmised that plate displacements and pipe deflections that matched the experimental data, would result in pipe strains and earth pressures that would also match the experimental data. A comparison of the experimental and numerical plate displacements can be seen in Figure 4.29. A comparison of the pipe vertical and horizontal deflections can be seen in Figures 4.30 and 4.31.

Overall the displacements of the pipe and settlements of the plate matched well with the experimental data. The magnitude of the maximum displacements and permanent displacements appeared to match well. The permanent displacements of the pipe and plate indicate that the Cap-Yield soil model captured the permanent strain reasonably well. For the single reinforced system and the unreinforced system there was less difference in the displacements as compared to the experimental data.

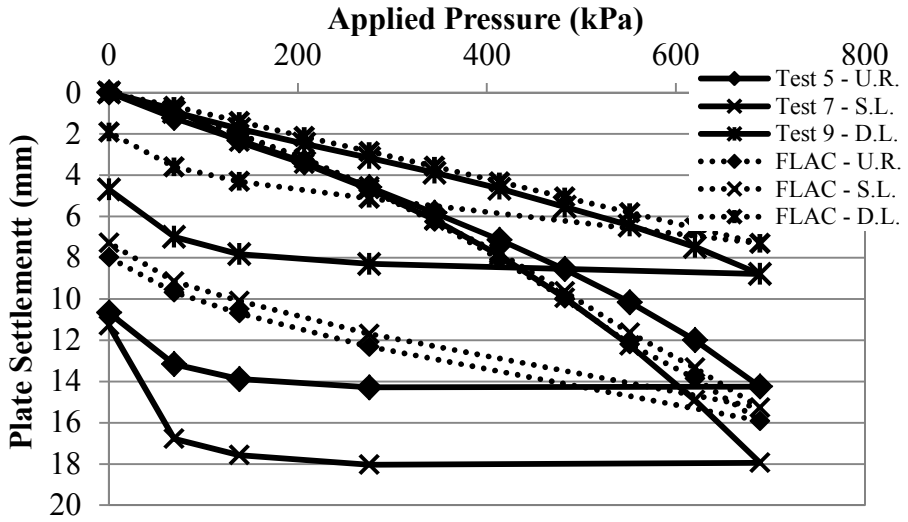

Figure 4.29 Vertical Settlements of the Loading Plate

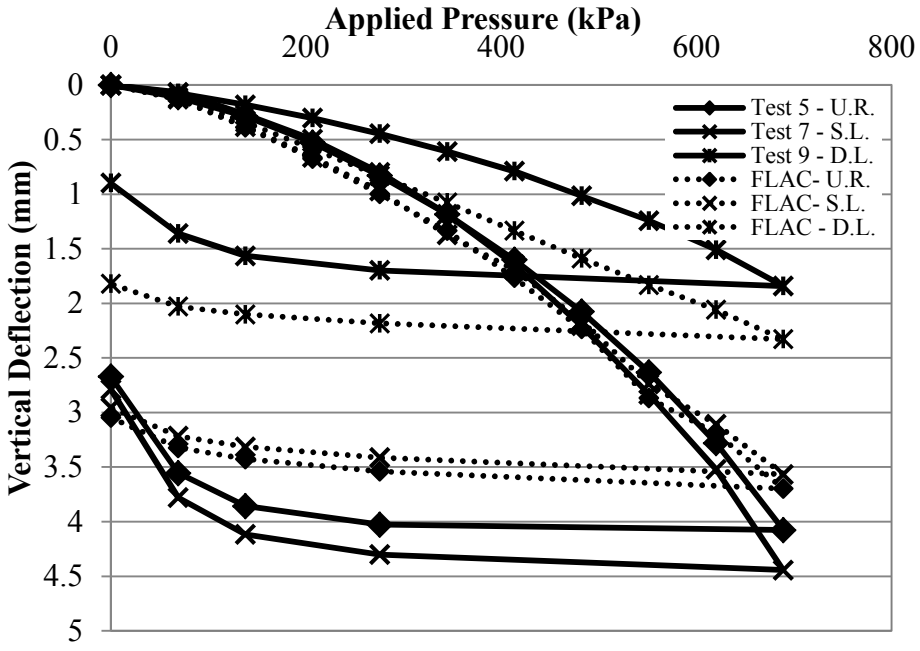

Figure 4.30 Vertical Deflections of the Pipe

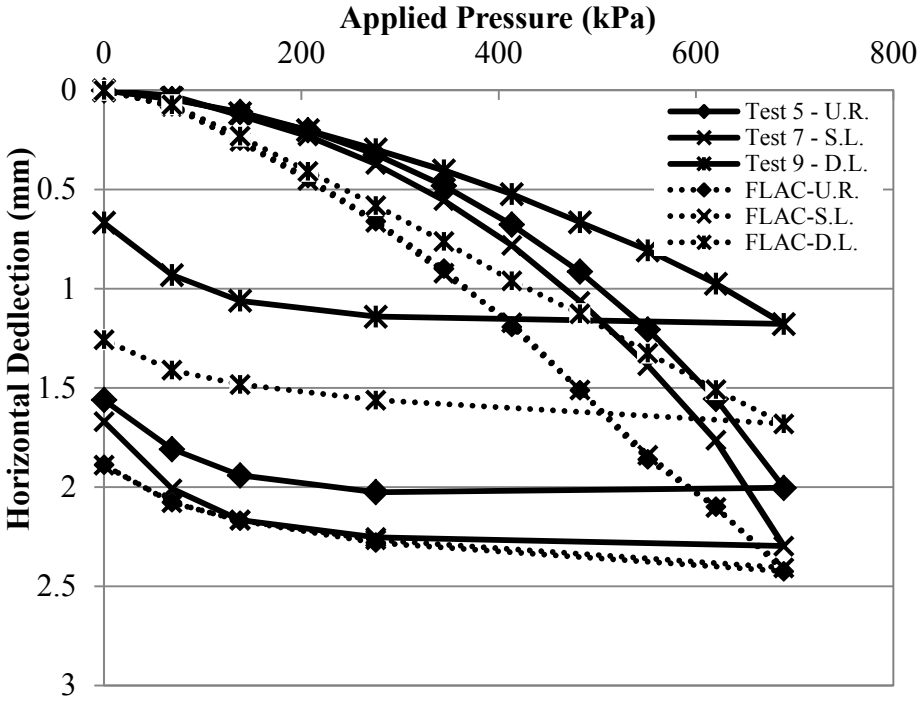

Figure 4.31 Horizontal Deflection of the Pipe

Earth Pressures

The earth pressure in the numerical analysis, at the same locations as the earth pressure cells in the experimental tests are plotted and compared to the experimental data. The earth pressures at the crown (C_1, C_2, C_3, and C_4) are shown in Figures 4.32 through 4.34 for each applied load step, and the distribution of earth pressures at the maximum applied load are shown in Figure 4.35. The magnitude of the earth pressures was within an acceptable range as compared to the experimental data. As discussed in Chapter 3 there were some difficulties with the accuracy of the earth pressure data possibly due to the size of the aggregate in relation to that of the earth pressure cell. The distribution of the pipe stresses looked reasonable with exception of the single layer experimental data, in which there was a significant drop in the pressure as compared to the numerical data.

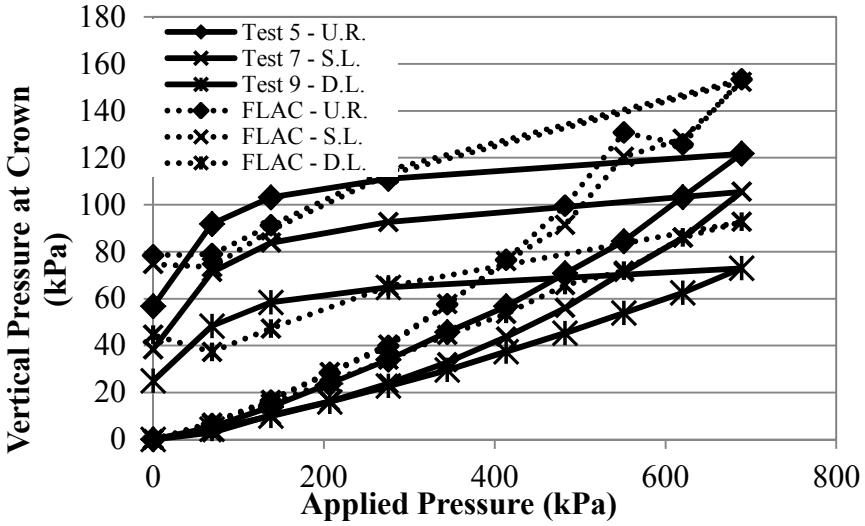

Figure 4.32 Vertical Pressures at the Crown (C_1)

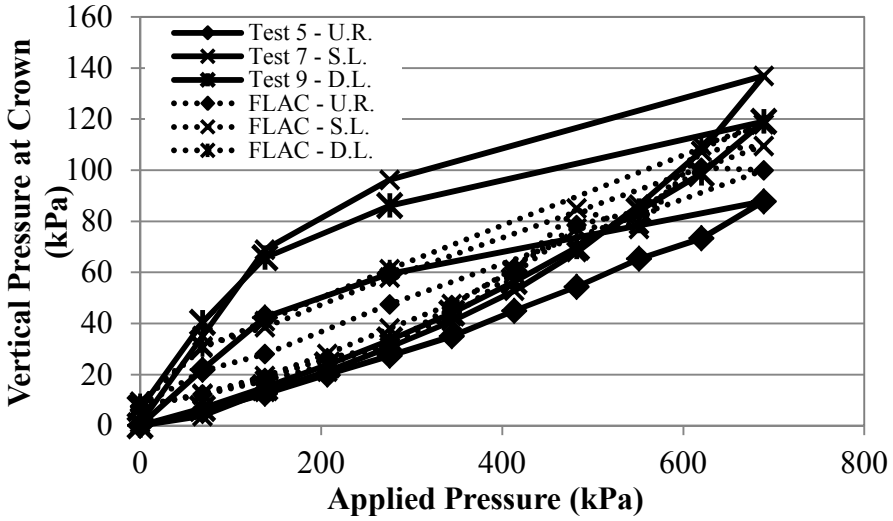

Figure 4.33 Vertical Pressures at the Crown (C_2)

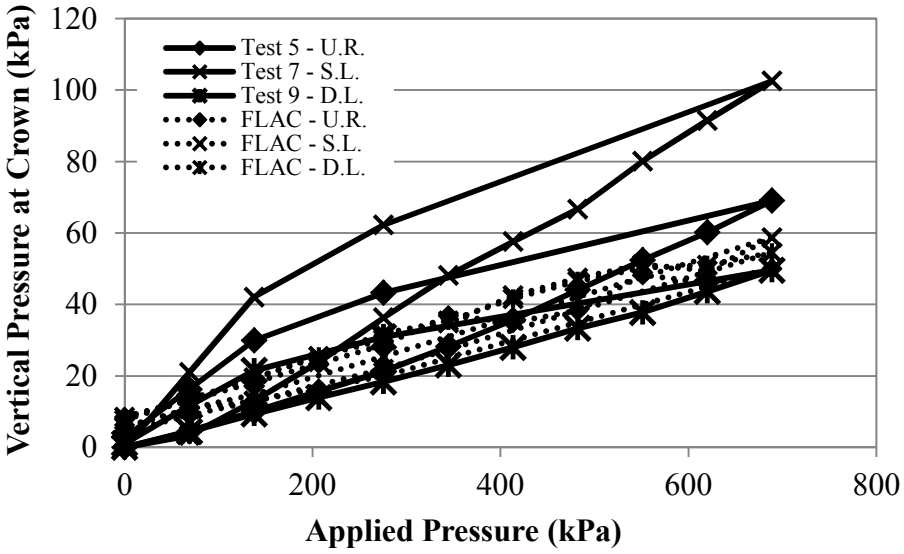

Figure 4.34 Vertical Pressures at the Crown (C_3)

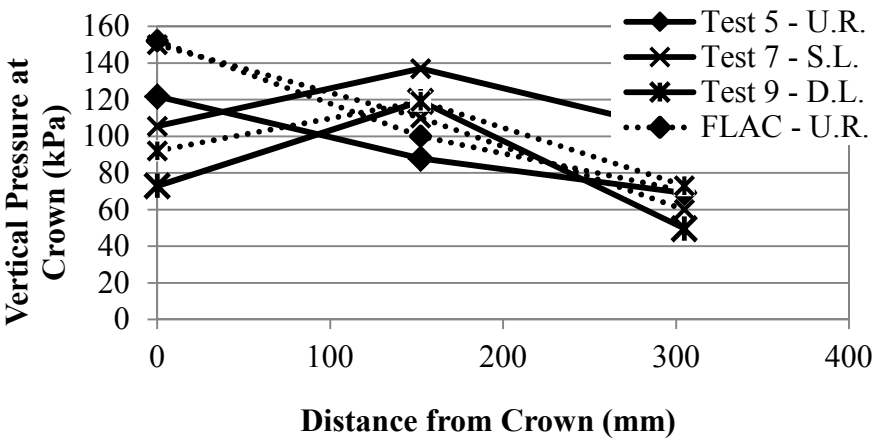

Figure 4.35 Distributions of Vertical Pressures at the Crown

The pressures at the interface between the base course and the backfill material, directly under the plate (C_4) are shown in Figure 4.36. The problem of the accuracy of the earth pressure cell appeared to be exacerbated by the proximity to the pressure plate for the experimental unreinforced condition. It is assumed that the stress at 225 mm below the plate should not record a pressure as applied at the surface.

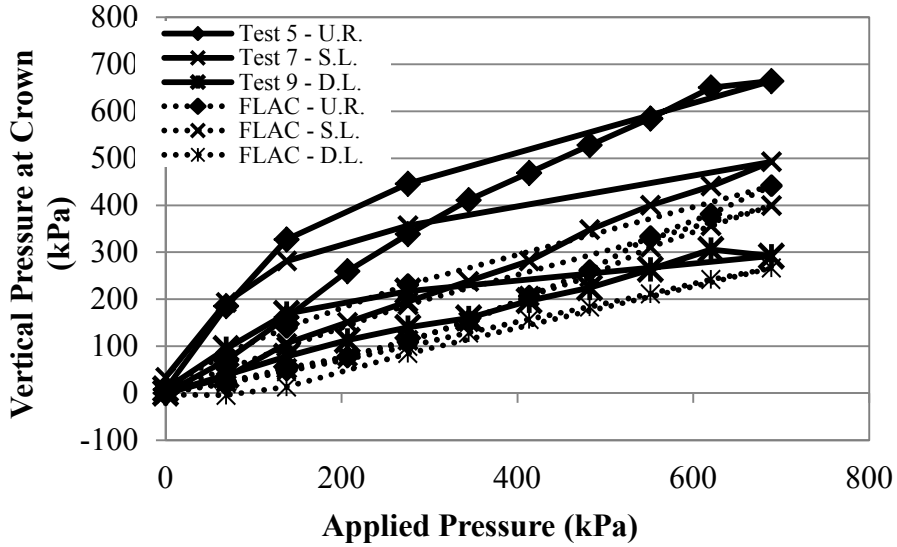

Figure 4.36 Vertical Pressures at Crown (C_4)

Similarly, at the springline the earth pressure cells recorded data that showed a similar magnitude of vertical pressures (Figure 4.37).

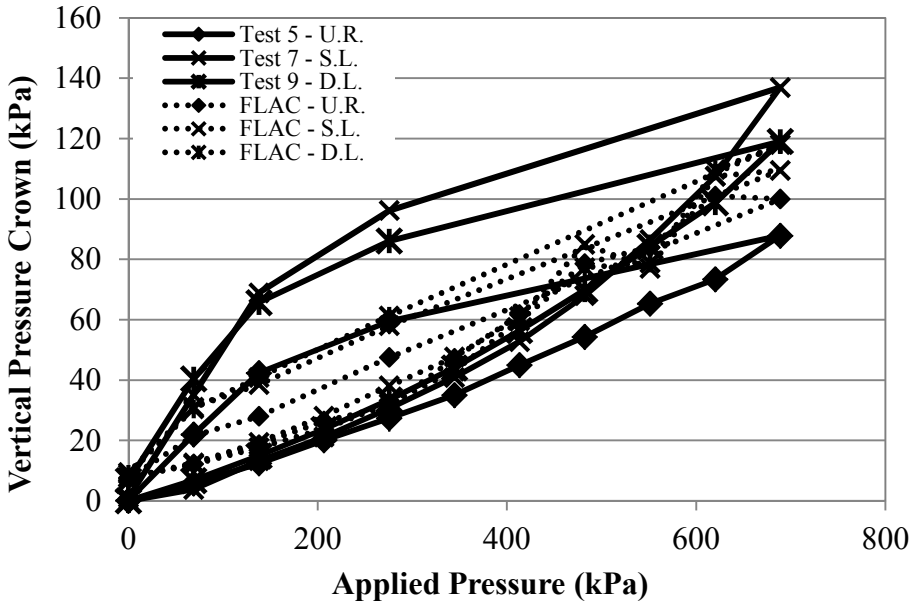

Figure 4.37 Vertical Pressures at Springline

As noted in Chapter 3 there appeared to be significant accuracy issues with the earth pressures cells that were oriented to record horizontal pressures. The results of the numerical analysis are shown here while the experimental data has not been included. The numerical analysis showed the same non-linear shape of the response to the applied load, and the reduction of the load. In each case the earth pressure response of the experimental data was off from the numerical data by a constant factor. This matched observations made by Talesnick et al. (2011). The lateral earth pressures at the haunch, the springline, and the shoulder are shown in Figures 4.38 through 4.40. In each case there is little difference in the calculated pressures between the single layer case and the unreinforced case. The inclusion of the double layer of geogrid lowered

the pressures at all locations by a factor of one and a half. The distribution of the horizontal pressures can be seen in Figure 4.41. This distribution is rational in that it is the distribution described by Spangler (1941) with additional pressure at the shoulder due to the near surface load. The earth pressures at the trench wall are shown in Figure 4.42.

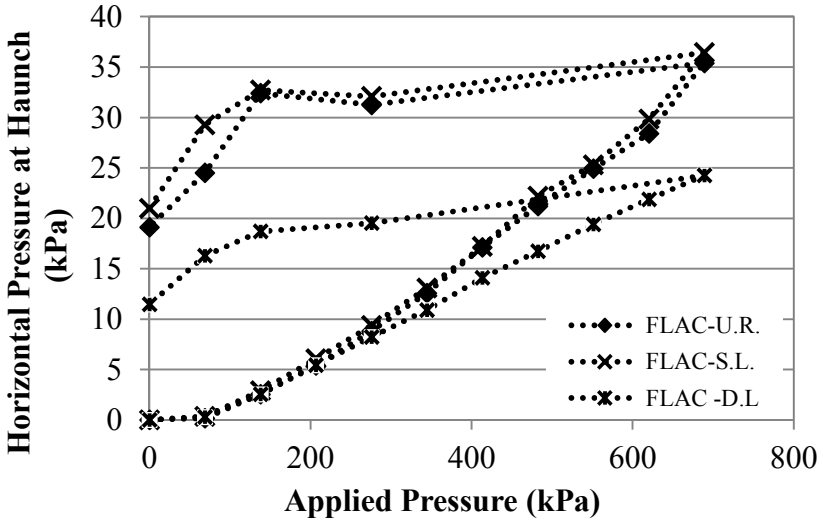

Figure 4.38 Horizontal Pressures at Haunch

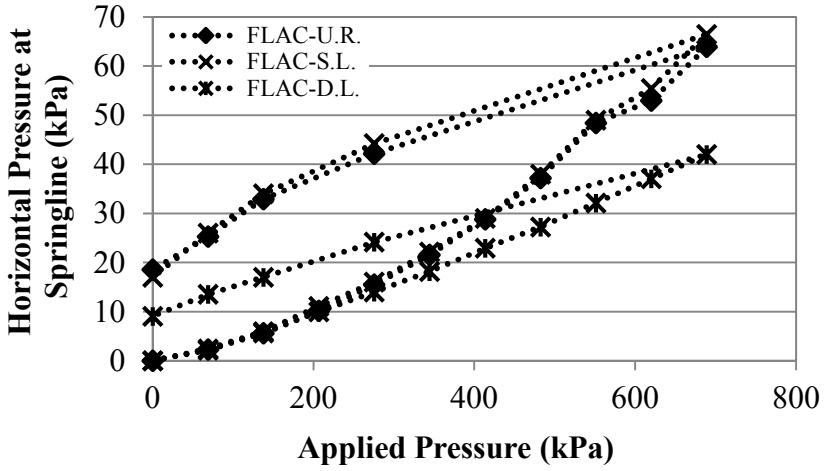

Figure 4.39 Horizontal Pressures at the Springline

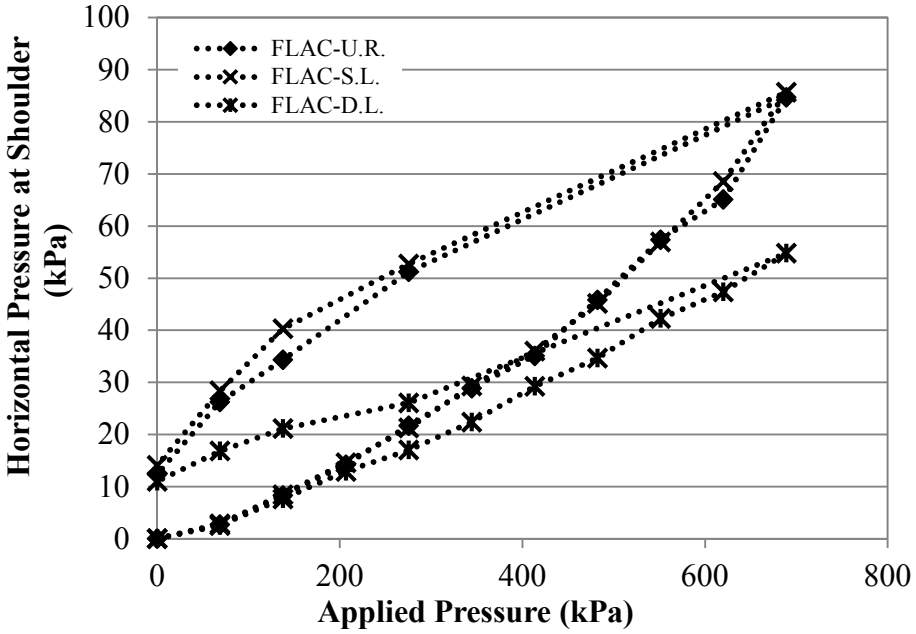

Figure 4.40 Horizontal Pressures at the Shoulder vs. Applied Pressure

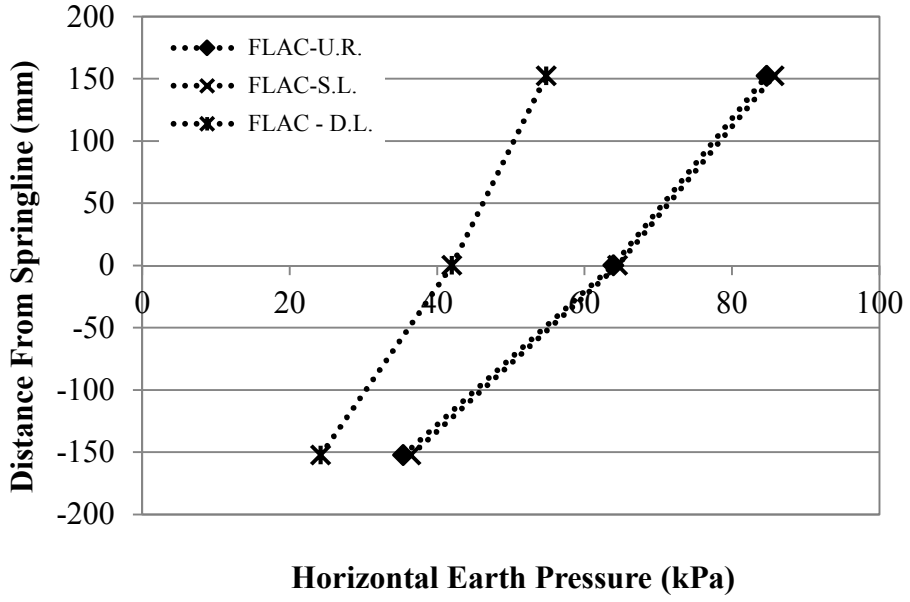

Figure 4.41 Distributions of Horizontal Pressures at the Springline

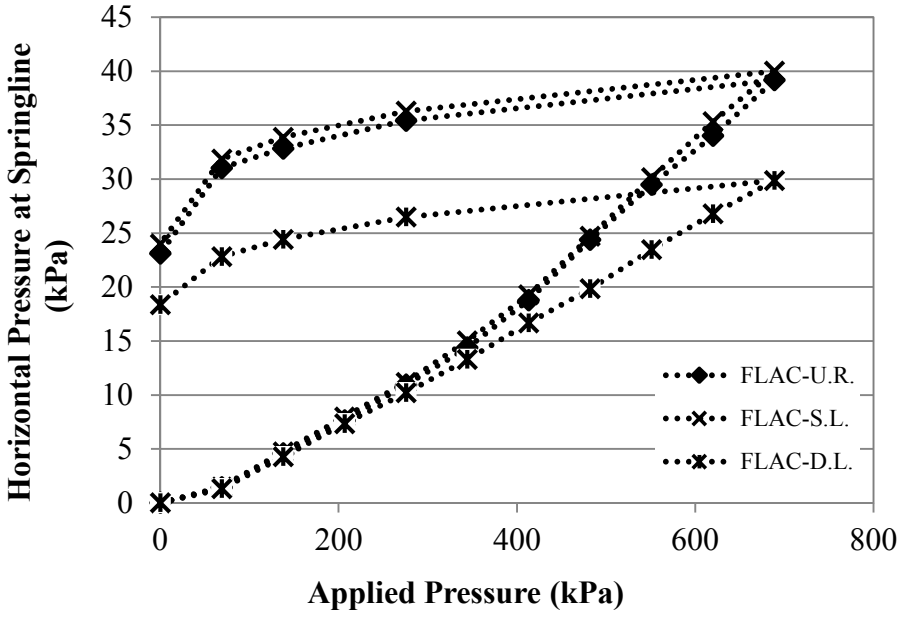

Figure 4.42 Horizontal Pressures at the Trench Wall

Pipe Strains

The experimental results of the pipe strain were difficult to interpret as most data resulted in very minute and seemingly random strains. The calculated strains that are compared to the experimental data are based on the strains calculated from the moment and thrust diagrams for the pipe, directly under the loading plate, as shown in Figures 4.43 and 4.44. The strains from the experimental data were recorded at the crown, the springline, and the invert. On the figures 0, 90, and 180 degrees represent the locations at the crown, the springline, and the invert respectively. As shown in the figures, the maximum thrust and moments recorded were at 45 degrees from the crown, near the shoulder of the pipe. Thrust was compressive at all locations and the moment in the pipe wall transitioned from the positive moment at the crown to the

negative moment at the shoulder, and back to the positive moment at the invert. Both the thrust and moment in the pipe wall were reduced in the case of the two layers of geosynthetic and actually increased slightly for the singly reinforced condition. The maximum strain, at the shoulder, was reduced by 40% by including the two layers of geogrid.

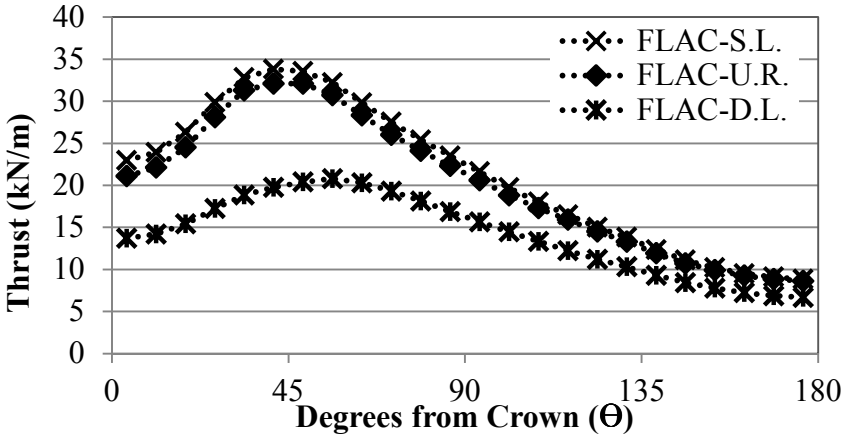

Figure 4.43 Thrust in Pipe Wall at Maximum Applied Pressure

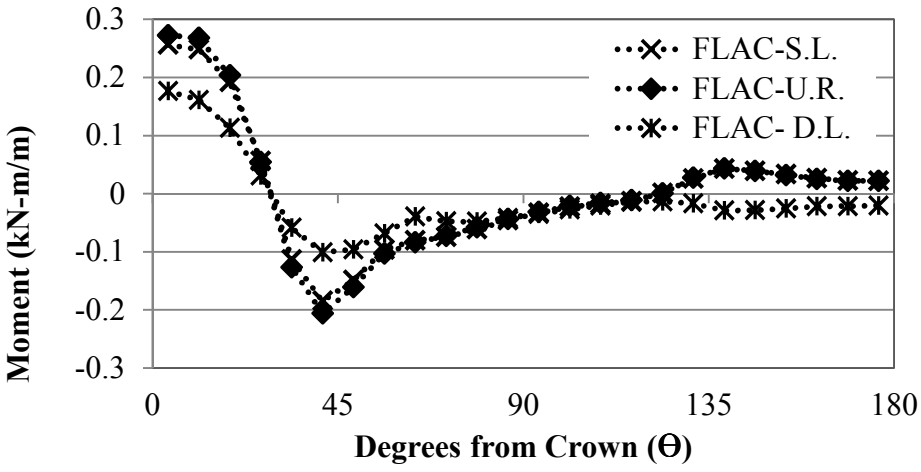

Figure 4.44 Moment in Pipe Wall at Maximum Applied Pressure

Strains were also calculated in the longitudinal direction on the inside and the outside of the pipe at the crown, springline, and invert. Both the inside and outside of the pipe wall were in tension. It was hypothesized in Chapter 3 that the lateral tension in the pipe wall was a result of the horizontal strain in earth fill above the pipe and soil structure interaction. In addition to lateral displacement of the soil, bending in the pipe wall due to non-uniform displacement along the length of the pipe occurred. The strains were calculated by using the basic relationship between moment of inertia, area, and modulus of elasticity of the pipe wall. In the longitudinal direction the plastic wall only had a thickness of 1.5 mm and a modulus of elasticity of 450 MPa. The strains on the inside and outside of the pipe wall were calculated by summing the thrust and bending moments in the pipe wall.

The recorded strains and the calculated strains for each load step are shown in Figures 4.45 and 4.46. The strains on the outside of the pipe (Lp7) on Tests 7 and 9 were not included as it appeared that the strain gauge was no longer working after Test number 5. It should also be noted that the longitudinal strains were some of the highest strains recorded on the pipe.

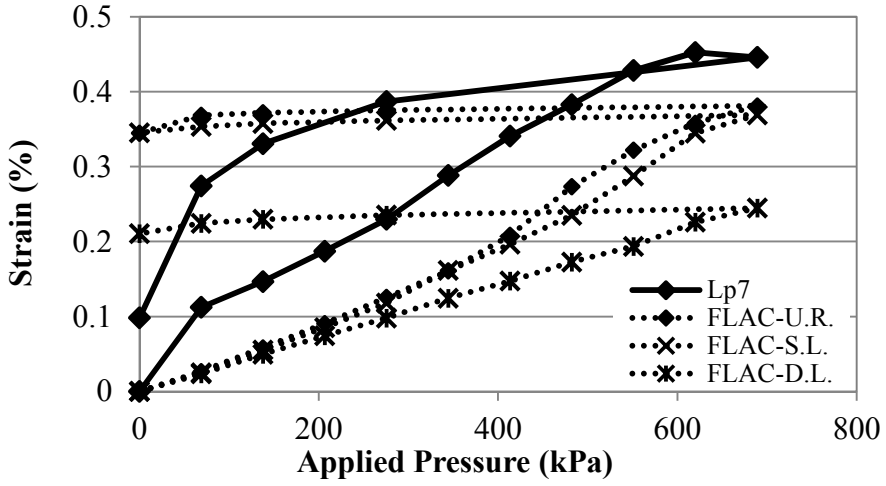

Figure 4.45 Longitudinal Strains at Crown on the Outside of Pipe

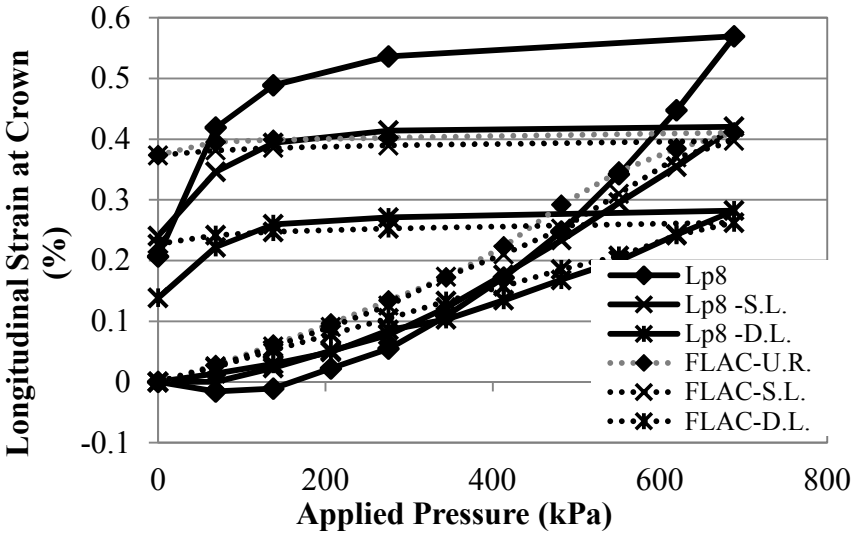

Figure 4.46 Longitudinal Strains at Crown on Inside of Pipe

Finally, the strain in the longitudinal axis due to thrust along the crown of the pipe at the maximum applied load is shown in Figure 4.47.

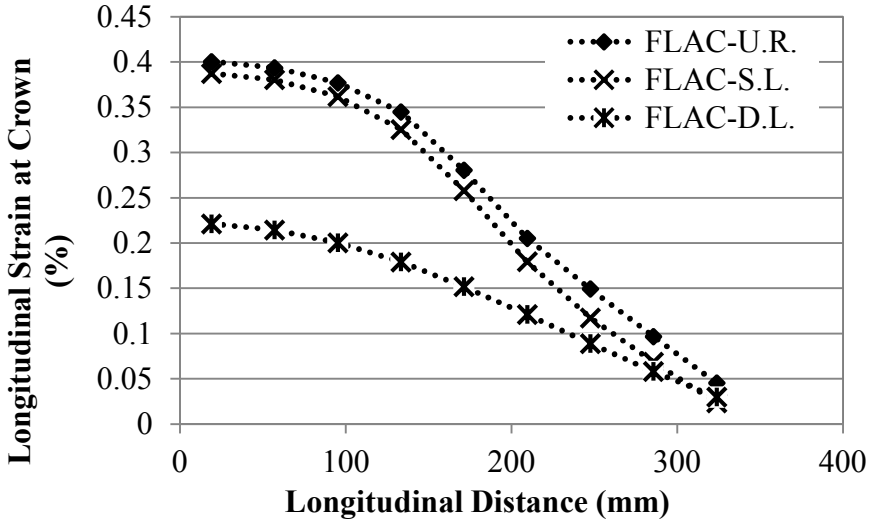

Figure 4.47 Longitudinal Strains at the Crown under the Maximum Applied Plate Load

Geogrid Strains

The geogrid strains were also determined by the numerical model and compared to the experimental data. For the double layer of geogrid condition (i.e. Test 9), the response of the model matched the experimental data well. In the cross-machine direction (Figure 4.48) the response of the upper geogrid layer over each step matched very well. In the machine direction, parallel with the axis of the pipe, the geogrid strains (Figure 4.49) did not match quite as well with the strains directly under the pipe, which were significantly higher in the FLAC model than recorded in the experiment. The strain distributions for the machine direction and the cross-machine direction at the maximum applied pressure can be seen in Figures 4.50 and 4.51.

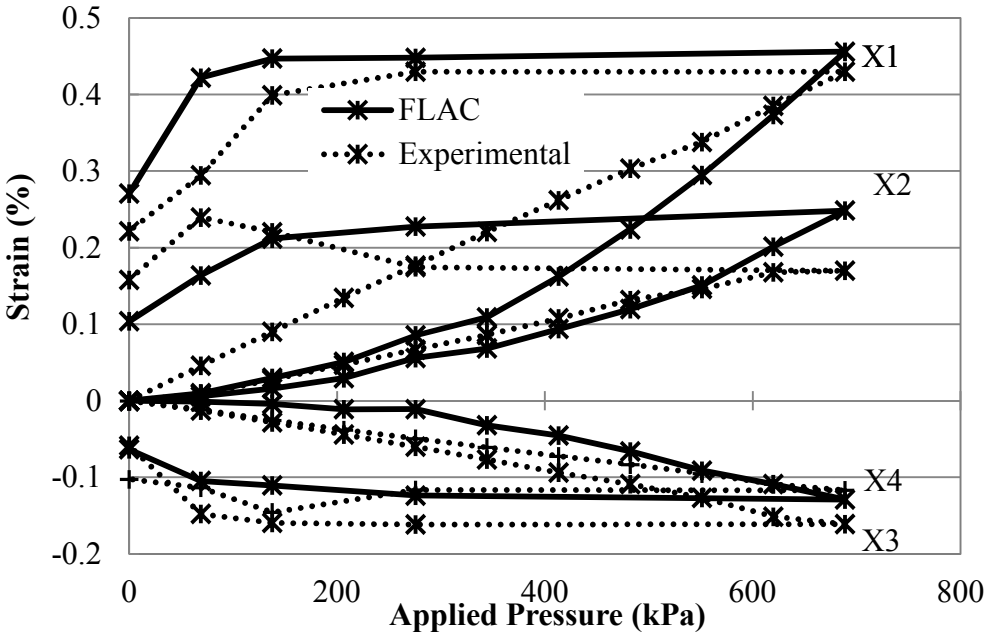

Figure 4.48 Geogrid Strain Top Layer Cross Direction

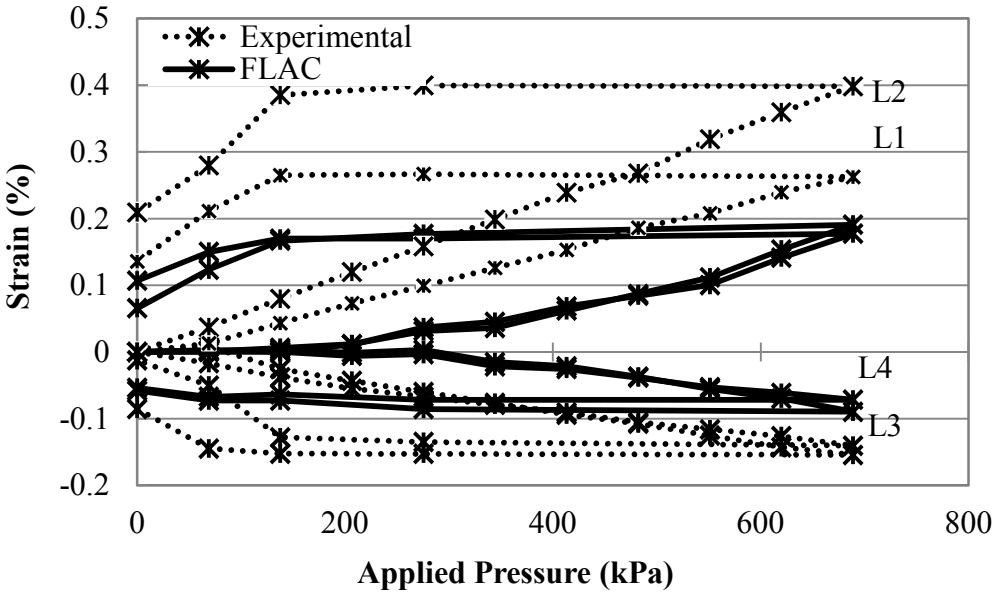

Figure 4.49 Strain of Top Geogrid Layer in the Longitudinal Direction

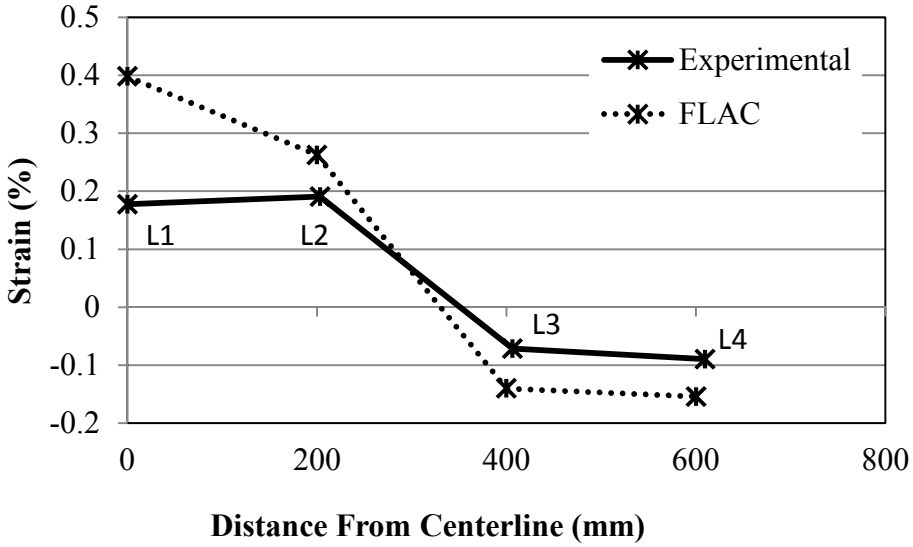

Figure 4.50 Strain of the Top Geogrid Layer in the Machine Direction under Maximum Applied Pressure

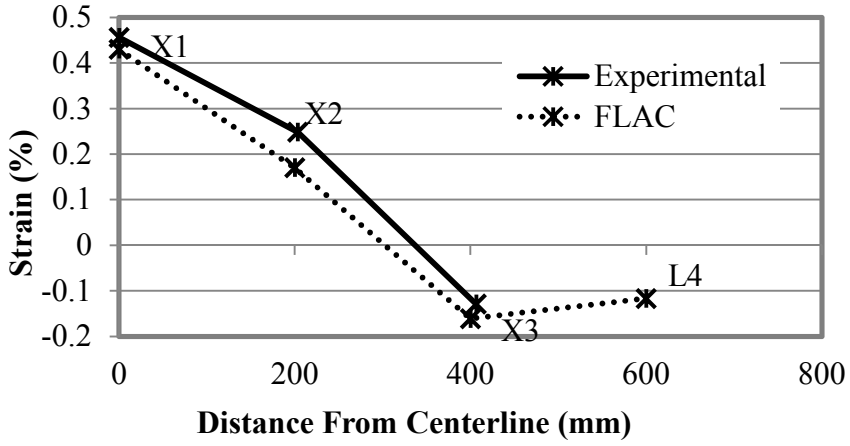

Figure 4.51 Strain of Geogrid in Cross-Machine Direction under the Maximum Applied Pressure

The strains of the lower geogrid layers in the numerical data did not match as well as the upper geogrid layers. The geogrid strains in the machine and cross-machine direction are shown in Figures 4.52 and 4.53. The strains at the maximum applied pressure are shown in Figures 4.54 and 4.55.

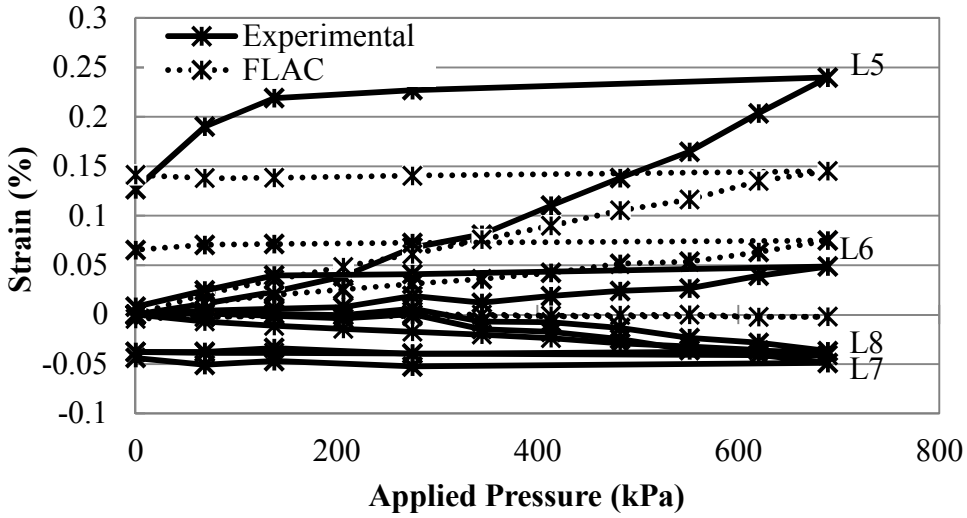

Figure 4.52 Strain of Lower Geogrid in the Machine Direction

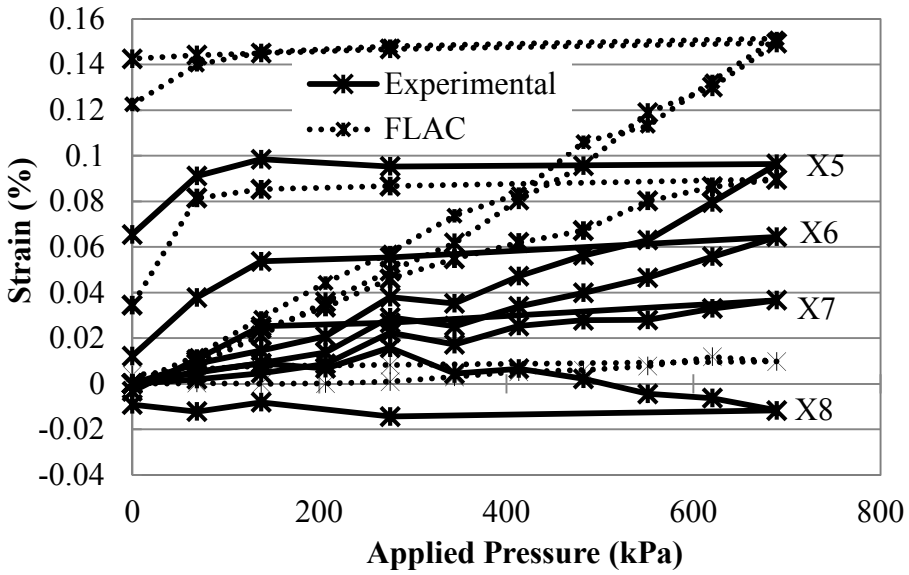

Figure 4.53 Lower Geogrid Strain of Lower Geogrid in the Cross-Machine Direction

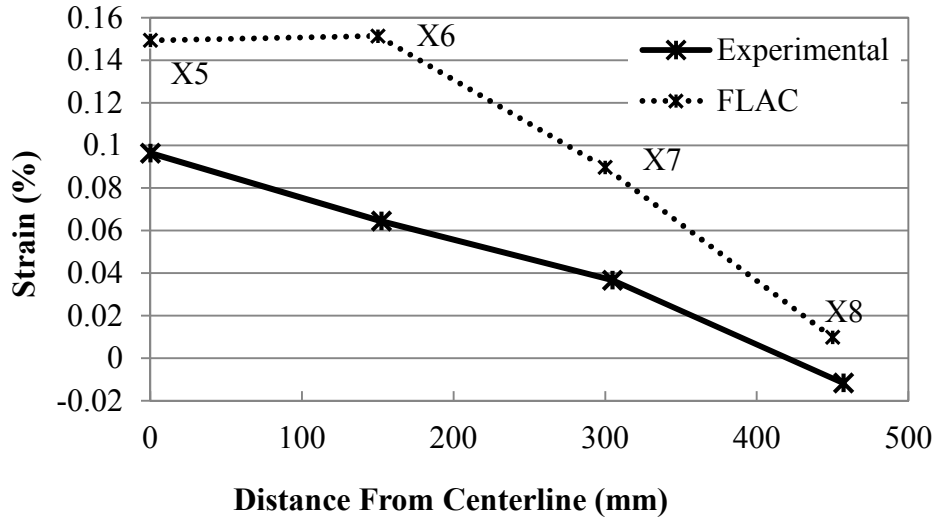

Figure 4.54 Strain of Lower Geogrid Layer under the Maximum Applied Pressure

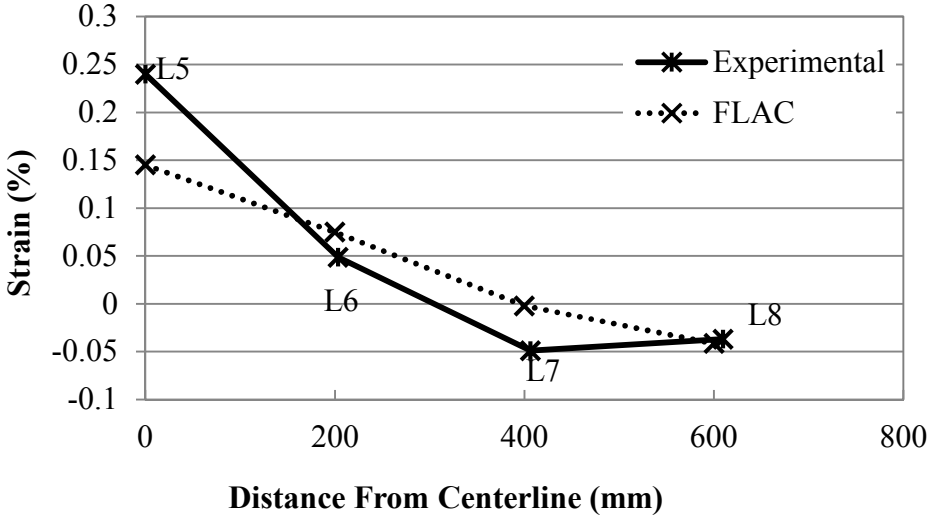

Figure 4.55 Strain of the Lower Geogrid Layer under the Maximum Applied Pressure

Chapter 5 Parametric Study

5.1 Introduction

The numerical analysis presented in Chapter 4 was based on the experimental tests conducted in the laboratory. Due to the limitations of large-scale tests, limited tests were conducted. To evaluate the effects of a few key influence factors on the benefits of using geosynthetics to protect pipes, a parametric study was developed based on the literature review, the experimental results, and the calibrated numerical models. The numerical model of the test section was used as the baseline for the parametric study. This chapter starts with this introduction, the selection of parameters, the results of the parametric study, and finally the conclusions from the parametric study.

5.2 Selection of Parameters

Relative stiffness of the pipe to the soil backfill is an important parameter for pipe design. Division of pipe products into rigid and flexible pipes is generally done according to the bending stiffness of the pipe wall. Rigid pipes resist soil loads by resisting bending while flexible pipes

have a low bending stiffness and rely on the resisting forces at the springlines of the pipe provided by the soil.

With the introduction of plastic pipes, the hoop stiffness of the pipe and the axial stiffness of the pipe wall, conventionally ignored with more rigid pipes, became an important aspect of design and analysis. McGrath (1998) introduced the Bending Stiffness Factor (S_b) and the Hoop Stiffness Factor (S_H) based on the parameters for the elastic solution proposed by Burns and Richards (1964). These factors in Equations 5.1 and 5.2 are dimensionless and have been conveniently used to describe pipe behavior:

$$S_B = \frac{M_s R^3}{EI} \qquad \textbf{5.1}$$

$$S_H = \frac{M_s}{EA/R} \qquad \textbf{5.2}$$

where M_s is the constrained modulus of the soil, E, A, I, and R are the modulus of elasticity, the area, the moment of inertia, and the radius of pipe wall respectively.

McGrath (1998) focused on the relationship between the Hoop Stiffness Factor and the ratio of the load on the pipe to the calculated soil prism load (i.e., a Vertical Arching Factor (VAF)), based on the full slip interface or no slip interface, as shown in Figure 5.1. McGrath (1998) also showed the importance of these two parameters in the calculation of vertical pipe deflection (ΔY). McGrath provided a deflection calculation that included a term for both bending stiffness and hoop stiffness as shown in Equation 5.3:

$$\Delta Y = \frac{W}{\frac{EA}{R} + 0.57M_s} + \frac{D_L K W}{\frac{EI}{R^3} + 0.061M_s} \qquad \textbf{5.3}$$

where W is the soil prism weight per unit length, D_L is the deflection lag factor, and K is the bedding constant.

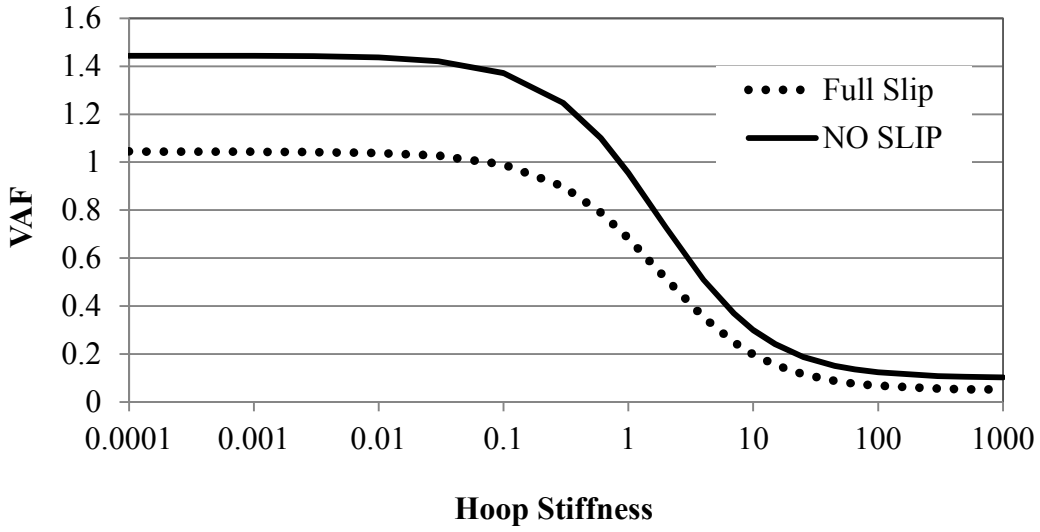

Figure 5.1 Vertical Arching Factor vs Hoop Stiffness Factor (McGrath 1998)

For the parametric study, the bending stiffness and the hoop stiffness of the pipe were parametrized by adjusting the stiffness matrix of the pipe wall in the numerical analysis. The calibrated model was the basis for the parametric study and all other parameters of the model were unchanged. The relevant results of the parametric study were plotted versus the Bending Stiffness Factor (S_B) and the Hoop Stiffness Factor (S_H) based on the constrained modulus (M_s)

of the crushed stone aggregate, which was 13.1 MPa from the plate loading tests. The pipe wall parameters are given in Table 5.1.

Table 5.1 Pipe Parameters

Nominal Pipe Diameter (m)	0.61
Moment of Inertia (Steel Only) (mm^4/mm)	10.5
Modulus of Elasticity Steel E_s (GPa)	200
Steel Yield Strength F_y (MPa)	522
Pipe Wall Area (Steel Only) (mm^2/mm)	0.752
Modulus of Elasticity HDPE E_p (MPa)	441

The pipe bending stiffness parameters selected in the parametric study were based on the range of pipe stiffness in available pipe products. The SRHDPE pipe, used as the basis of the study in the calibrated model, had a pipe stiffness ($P/\Delta Y$) of 327 kPa based on the parallel plate load test. This pipe stiffness is towards the minimum pipe stiffness of pipe products available in the literature (Figure 5.2). In the parametric study, the pipe stiffness was increased by a factor of 4, 16, and 256 to simulate other types of pipe. The pipe stiffness and pipe bending stiffness factors (S_B) in four numerical analyses are shown in Table 5.2

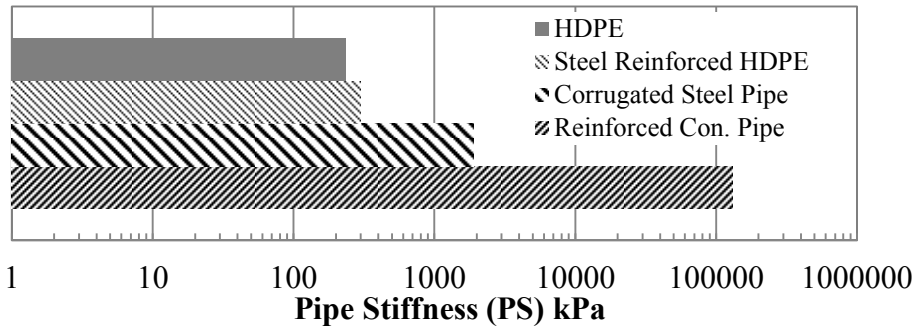

Figure 5.2 Pipe Stiffness of different Pipe Materials

Table 5.2 Bending Stiffness Parameters

Analysis	PS (kPa)	S_B
1	327	190
2	1310	47
3	5240	12
4	83827	1

The hoop stiffness factor of the pipe in the experiments and the calibrated numerical model was 0.026 based on the constrained modulus (M_S) of 13.1 MPa. Based on McGrath's (1998) suggestion for the Vertical Arching Factor as shown in Figure 5.1, the hoop stiffness factor was selected for the parametric study ranging between 0.001 and 10 as shown in Table 5.3. Each pipe stiffness parameter was used for both the unreinforced and reinforced conditions. The baseline sections for the parametric study are the unreinforced conditions and reinforced sections of Tests 5 and 9, which had a single layer of geogrid at the interface of the base course and in situ soil (Figure 5.3). The parameters for the in situ soil, the backfill, and the geogrid are

the same as those discussed in Section 4.2 of Chapter 4. The loads were applied in increments of 68.9 kPa up to 689 kPa and unloaded in 4 increments as described in the experimental program.

Table 5.3 Hoop Stiffness Factors

Analysis	PS_H (kPa)	S_H
1	13,100,000	0.001
2	503,846	.026
3	131,000	0.1
4	26200	0.5
5	13100	1
6	5240	2.5
7	2620	5
8	1310	10

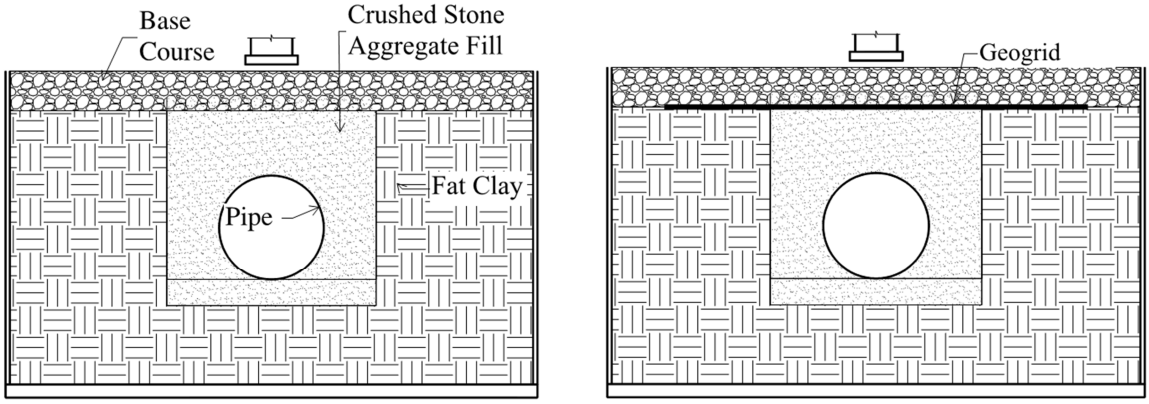

a. Unreinforced Condition **b. Reinforced Condition**

Figure 5.3 Unreinforced and Reinforced Sections for the Parametric Study

5.3 Effect of Pipe Stiffness

The effects of the pipe stiffness on pipe displacements, plate settlements, earth pressures, and pipe moments and thrusts were evaluated in the parametric study as the relative pipe stiffness (PS) of 1, 4, 16, and 256 times the stiffness of the SRHDPE pipe. In the following figures (Figures 5.4, 5.5, 5.8, 5.10, 5.12, 5.14, and 5.15) the legend shows the results based on each run, where PS 4 for example is the run where the pipe stiffness was 4 times the SRHDPE pipe. In those figures the following descriptor R label indicated the reinforced condition.

5.3.1 Pipe Deflections and Plate Settlements

Figures 5.4 and 5.5 present the vertical and horizontal deflections of the pipe at different relative stiffness and reinforced condition. With increasing pipe stiffness (PS) both the vertical and horizontal pipe deflections decreased. The vertical deflections are equivalent to 0.6% to 0.04 % of the pipe diameter, which are much smaller than the failure criterion of 5% suggested by AASHTO 2012.

As the pipe stiffness increased, the geogrid had less effect on both the vertical and horizontal pipe deflections. As can be seen in Figure 5.6 and 5.7, when the pipe deflections are plotted versus the relative pipe stiffness for the reinforced and unreinforced conditions, the geogrid has little to no effect at the maximum pipe deflections as the relative pipe stiffness approaches that of a concrete pipe, which is approximately 256 times the pipe stiffness of the tested SRHDPE pipe (PS 256).

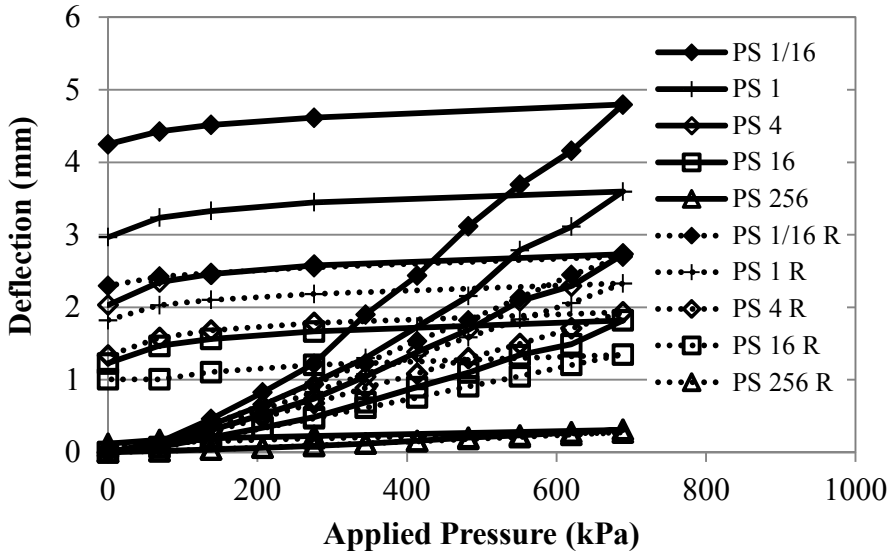

Figure 5.4 Pipe Vertical Deflections versus Applied Pressure

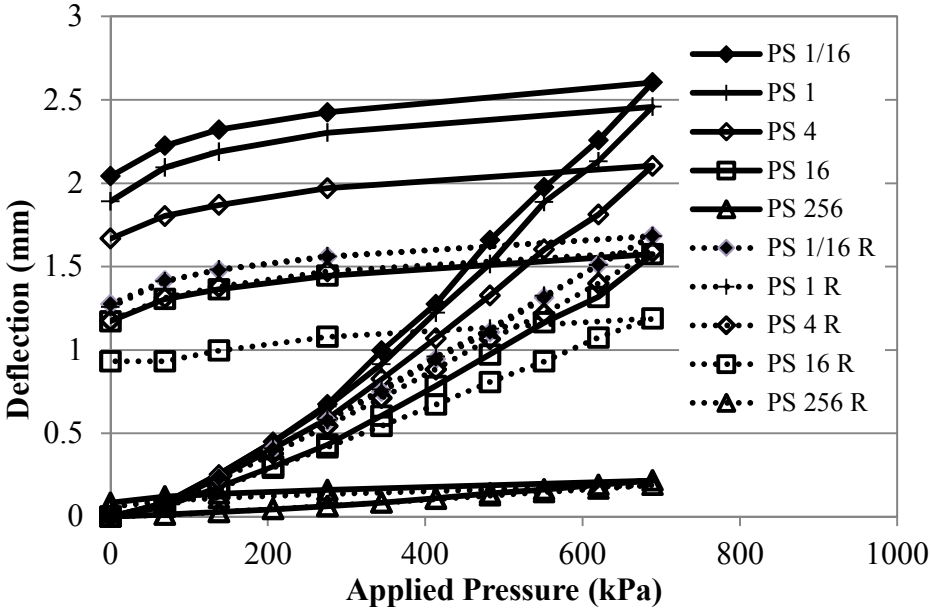

Figure 5.5 Pipe Horizontal Deflections versus Applied Pressure

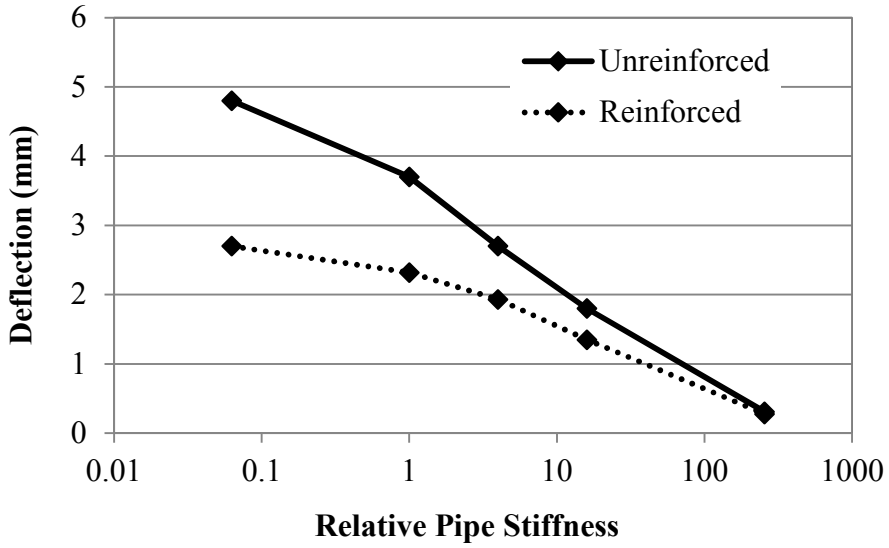

Figure 5.6 Maximum Vertical Pipe Deflections vs. Relative Pipe Stiffness

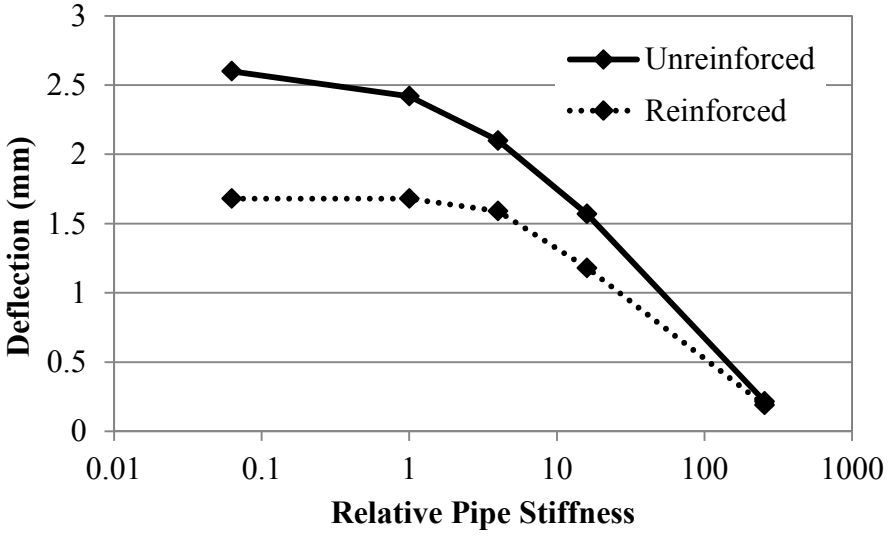

Figure 5.7 Maximum Horizontal Pipe Deflections vs. Relative Pipe Stiffness

Plates on the surface of the base course for the reinforced condition had a consistent reduction in the maximum settlements of approximately 7 mm over the range of examined

relative pipe stiffness as compared with that for the unreinforced condition as shown in Figures 5.8 and 5.9.

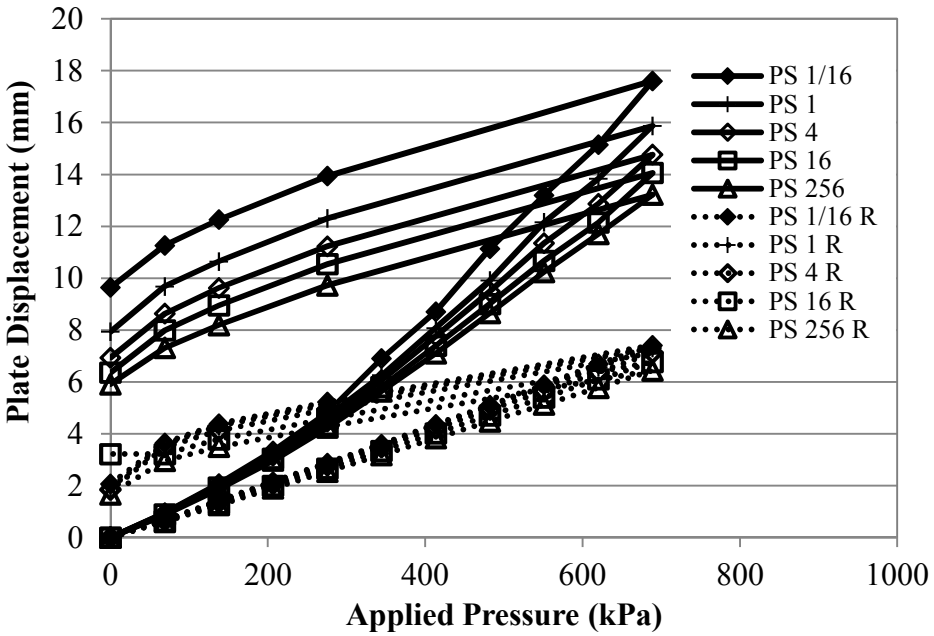

Figure 5.8 Plate Settlements versus Applied Pressure

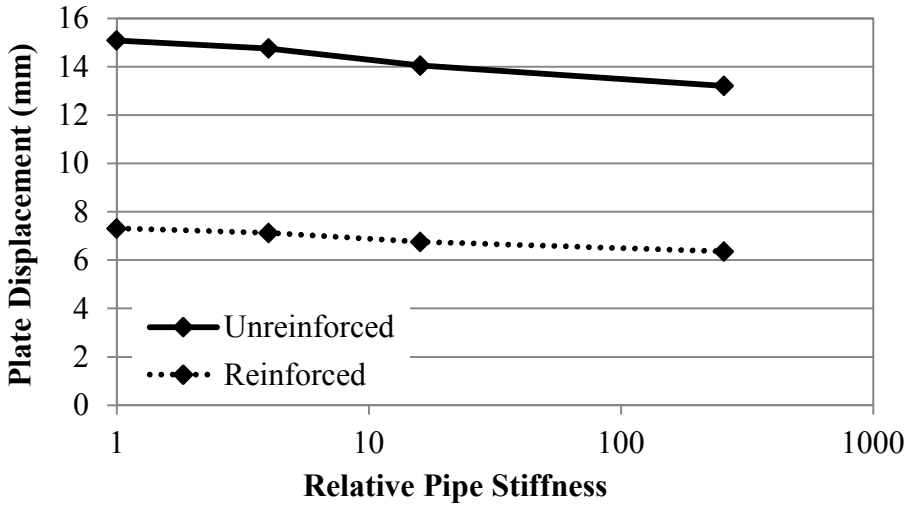

Figure 5.9 Maximum Plate Settlements vs. Relative Pipe Stiffness

5.3.2 Earth Pressures

Earth pressures at the crown and springline of the pipe are important for the safety and design of pipes. This parametric study investigated the effect of the relative pipe stiffness on the earth pressures at these locations under an applied plate pressure. For the unreinforced condition the pressures at the crown of the pipe (Figure 5.10) varied from 135 to 160 kPa. For the reinforced condition there was more variation with an apparent trend of increasing pressure, from 93 to 135 kPa, with the increasing relative pipe stiffness (Figure 5.11). Pressures at the spring line for the applied pressures are plotted in Figure 5.12. At the pipe stiffness of the SRHDPE pipe, the reduction of earth pressures, between the unreinforced and reinforced condition, was approximately 21 kPa, or a reduction of 33%. For increasing pipe bending stiffness the effectiveness of the geogrid was reduced, matching the deflection results.

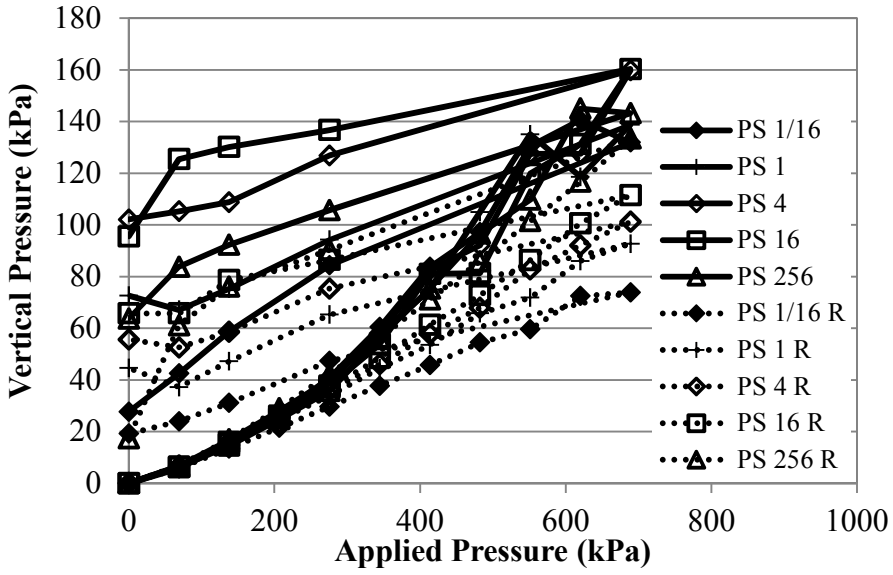

Figure 5.10 Vertical Pressures at Crown vs. Relative Pipe Stiffness

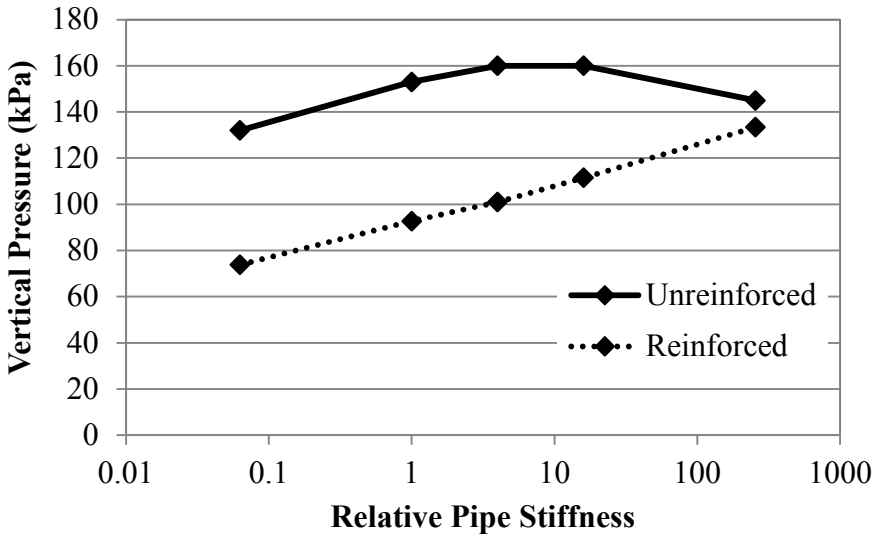

Figure 5.11 Maximum Vertical Pressures at Crown vs. Relative Pipe Stiffness

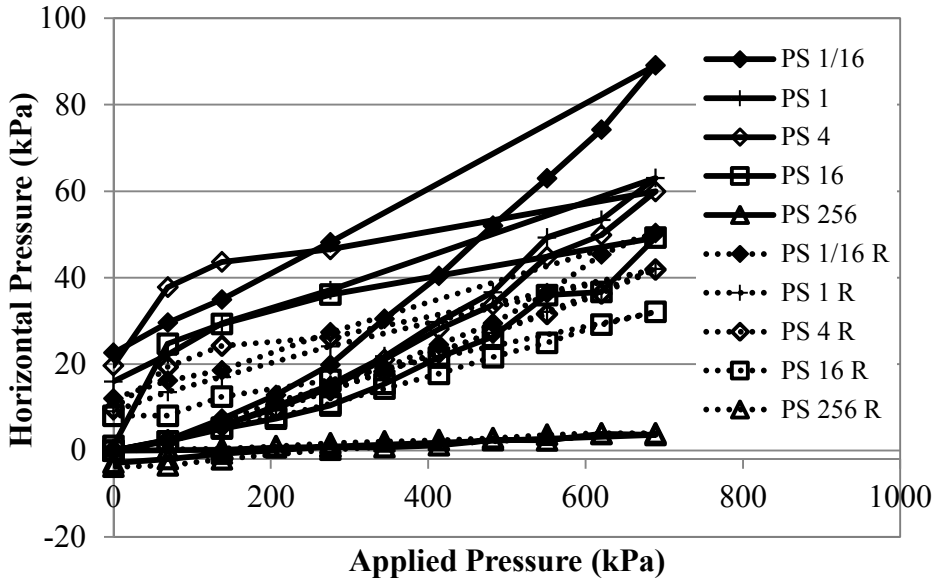

Figure 5.12 Horizontal Pressures at the Springline

At the highest pipe stiffness, approximately that of a concrete, the horizontal pressure for the unreinforced and reinforced case dropped nearly to zero, which is consistent with the recognized mechanics of rigid pipes (Figure 5.13).

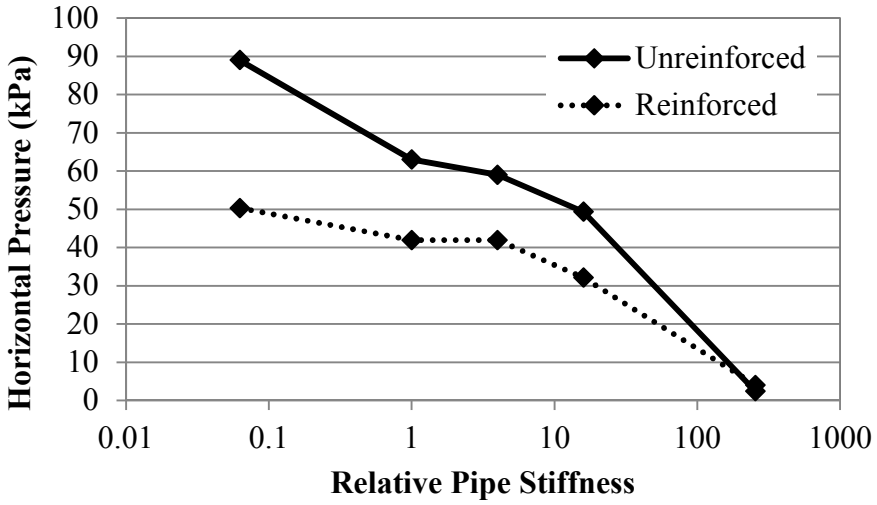

Figure 5.13 Maximum Horizontal Pressure at Springline vs Relative Pipe Stiffness

5.3.3 Pipe Moments and Thrusts

Pipe moments and thrusts are two important parameters used to evaluate pipe structural capacities. To investigate the effects of relative pipe stiffness on these two parameters, the thrust and moments were calculated at the maximum applied plate load around the circumference of the pipe from the crown to the invert given by the angle theta (Θ). Moments in the pipe wall around the circumference increased as the pipe stiffness increased, with the maximum positive moments being at the crown of the pipe, and the maximum negative moments between the shoulder and

the springline (Figure 5.14). For the unreinforced case the maximum thrusts in the pipe wall decreased and shifted away from the shoulder towards the springline of the pipe, with increased bending stiffness. For the reinforced condition the maximum thrust also shifted towards the spring line, but the magnitude of the thrust remained constant with an increased degree of pipe stiffness (Figure 5.15).

The pipe moment and thrust plotted versus the relative pipe stiffness are shown in Figures 5.16 and 5.17. The difference between the maximum moment of the unreinforced condition and the reinforced condition were constant over the range of pipe stiffness run in the parametric study (Figure 5.16). The difference in the maximum thrusts in the pipe wall between the reinforced and unreinforced condition decreased as pipe stiffness increased. As the pipe stiffness approached the pipe stiffness of a concrete pipe, 256 times the pipe stiffness of the SRHDPE pipe there was little difference between the reinforced and the unreinforced condition.

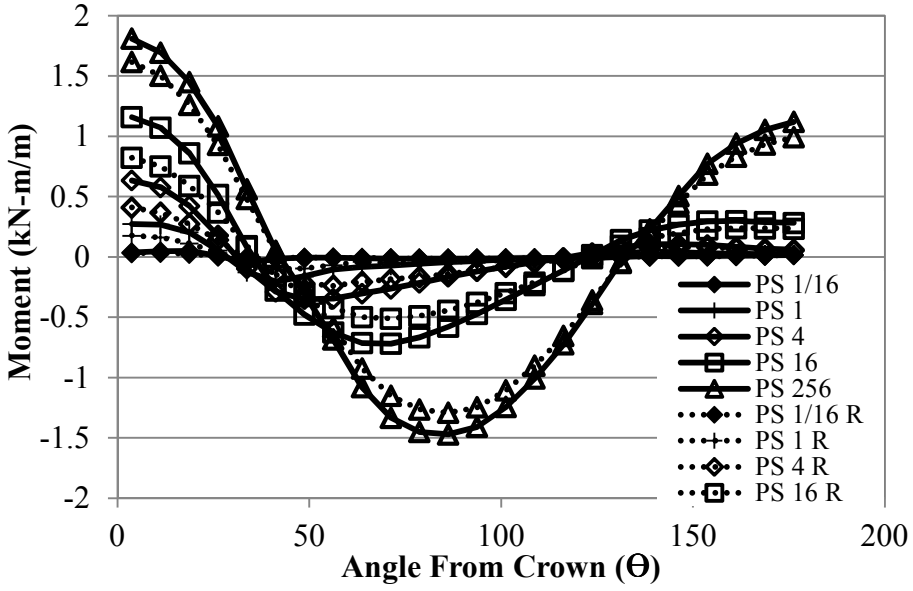

Figure 5.14 Pipe Moments at the Maximum Applied Plate Load

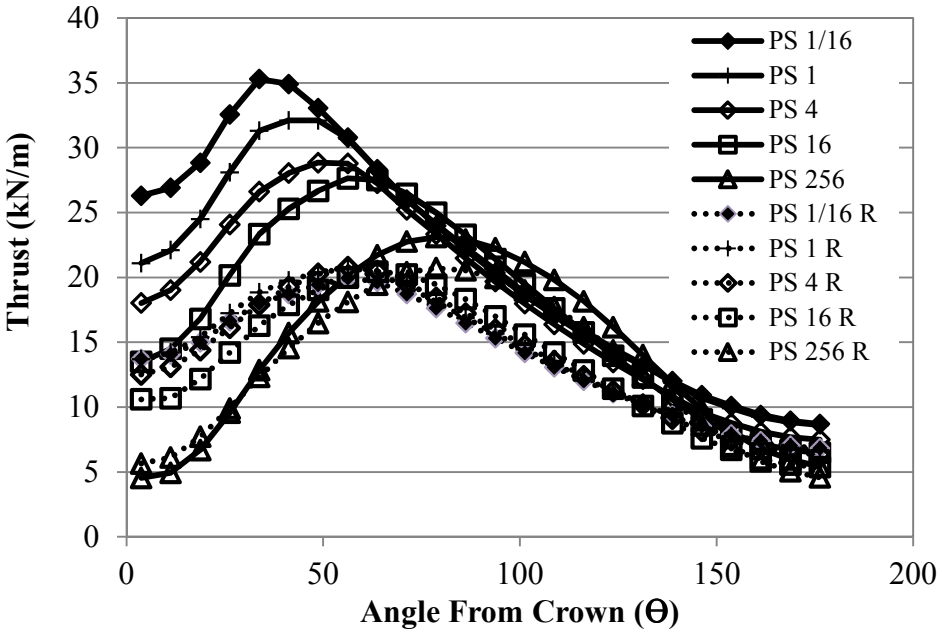

Figure 5.15 Pipe Thrusts at the Maximum Applied Plate Load

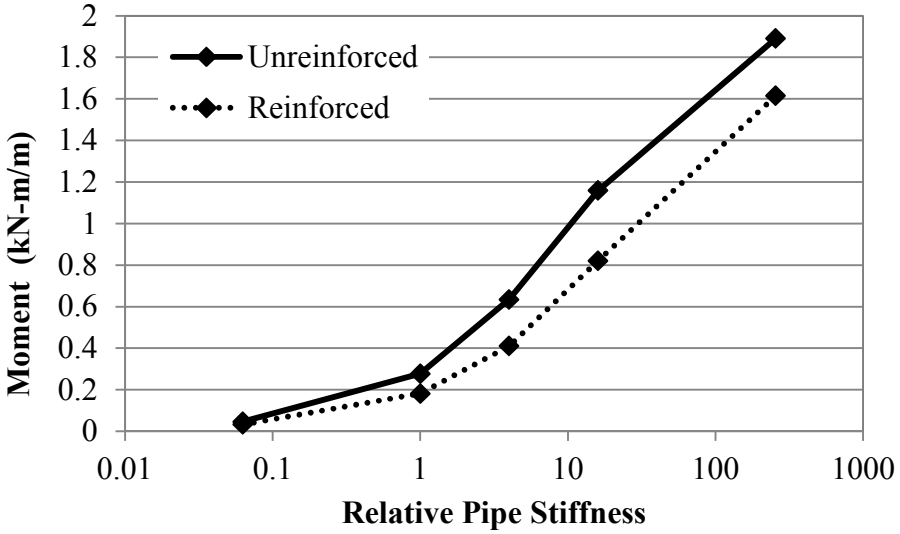

Figure 5.16 Maximum Moments vs Relative Pipe Stiffness

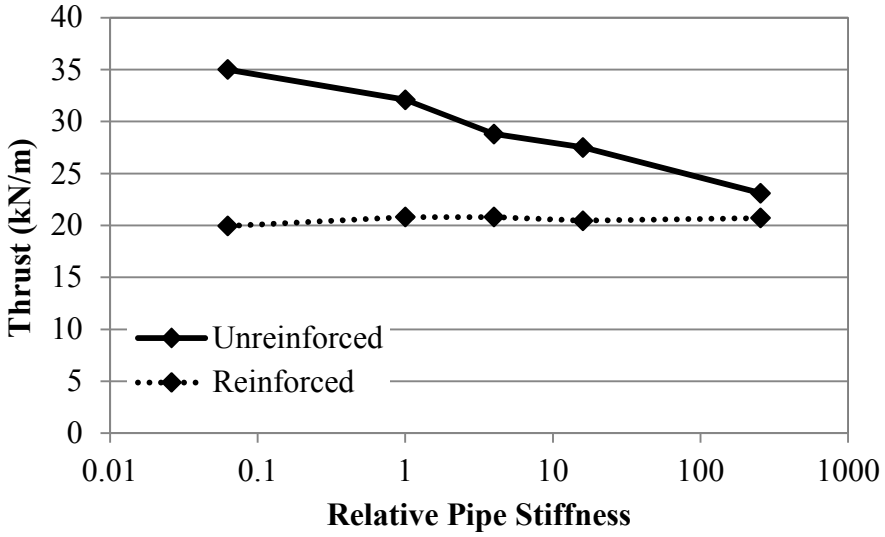

Figure 5.17 Maximum Thrusts vs. Relative Pipe Stiffness

5.3.4 Geogrid Strain

The geogrid strains in the principal axis of the geogrid sheet were calculated in the parametric study at the maximum applied pressures and shown in Figures 5.18 and 5.19. The maximum strains were 0.4% in tension at the center of the geogrid directly under the loading plate and 0.2% in compression approximately 400 mm from the loading plate. This distribution of strains from tension to compression is similar to the typical distributions of strain for geogrids that are confining a base course layer. There was very little change in both the distribution and magnitude of the strains in the geogrid.

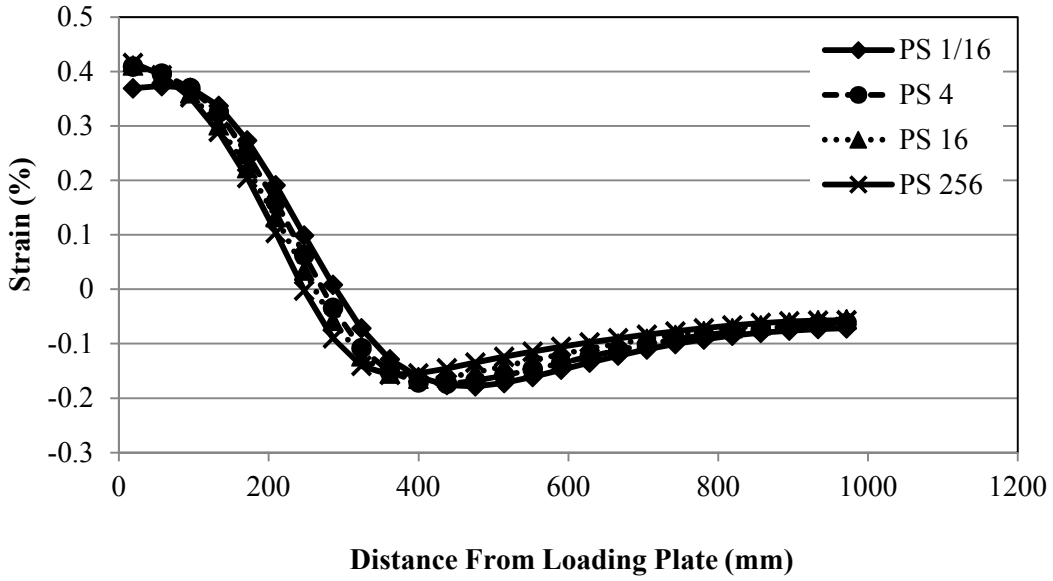

Figure 5.18 Distribution of Machine Direction Geogrid Strains at the Maximum Applied Pressure

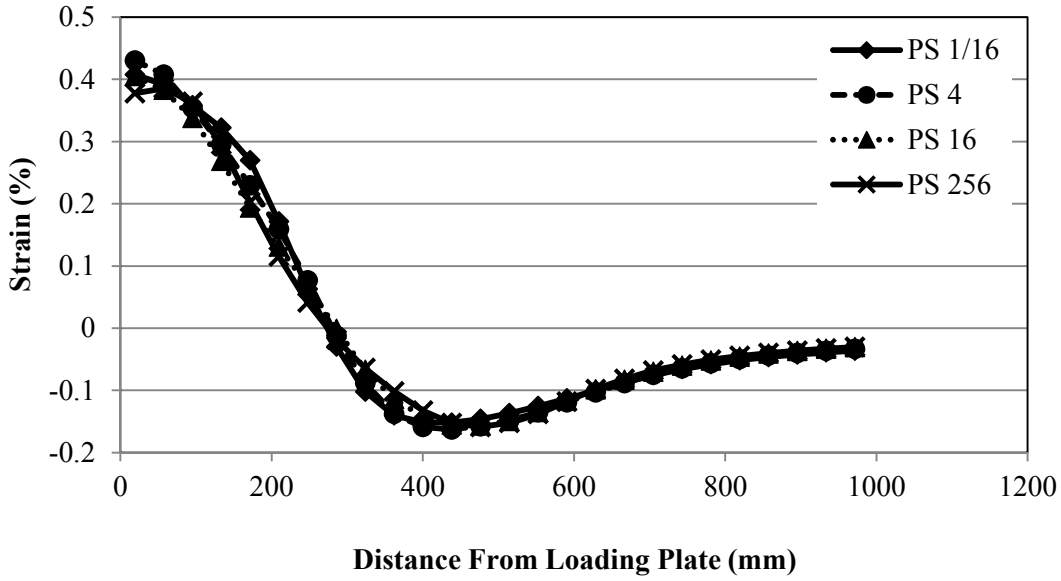

Figure 5.19 Distribution of Cross-machine Direction Geogrid Strains at the Maximum Applied Pressure

5.4 Effect of Pipe Hoop Stiffness

The effects of the pipe hoop stiffness on pipe displacements, plate settlements, earth pressures, pipe moments and thrusts, and geogrid strains were investigated in the parametric study. To be consistent with the conventional design practices, the numerical results are given with respect to the hoop stiffness factor (S_H), which is a non-dimensional ratio of the constrained modulus of the backfill to the axial stiffness of the pipe wall as defined in Equation 5.2.

5.4.1 Pipe Deflections and Plate Settlements

The vertical pipe displacements of the pipe parameterized to the pipe hoop stiffness factors are presented in Figures 5.20 for the unreinforced (UR) and Figure 5.21 for the reinforced condition (R). In both conditions the deflection of the pipe increased as the ratio of soil modulus to pipe wall stiffness increased. The unreinforced condition resulted in vertical pipe displacements in the range of 3 to 27 mm, while the reinforced condition resulted in reduced vertical pipe displacements in the range of 2.5 to 7.5 mm.

The maximum vertical pipe deflections versus the ratio of soil to hoop stiffness at the maximum applied plate load indicates a minor benefit from the geogrid until the pipe wall hoop stiffness factor increased to a hoop stiffness factor of approximately one or greater, at which point the benefit from the geogrid became pronounced (Figure 5.22).

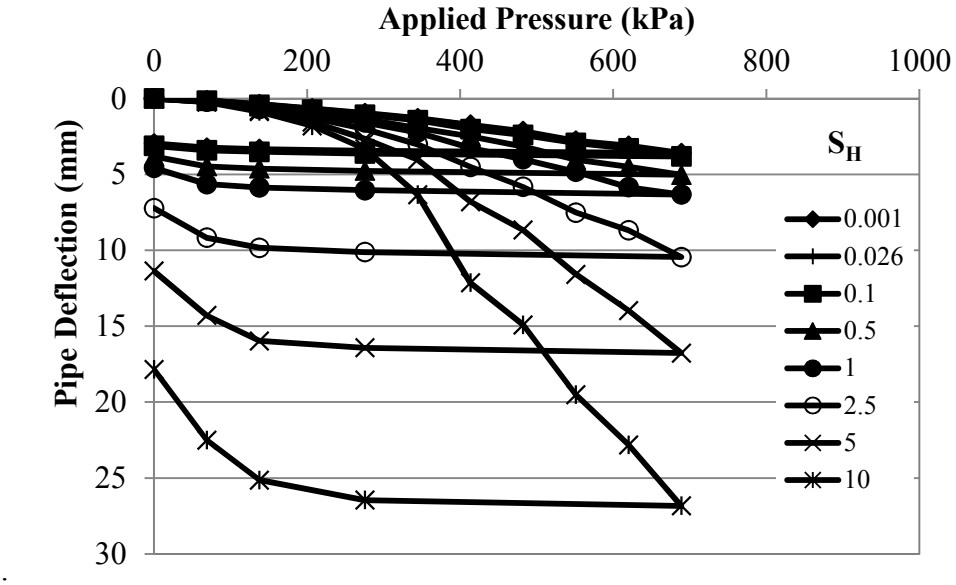

Figure 5.20 Pipe Vertical Deflections under an Unreinforced Condition

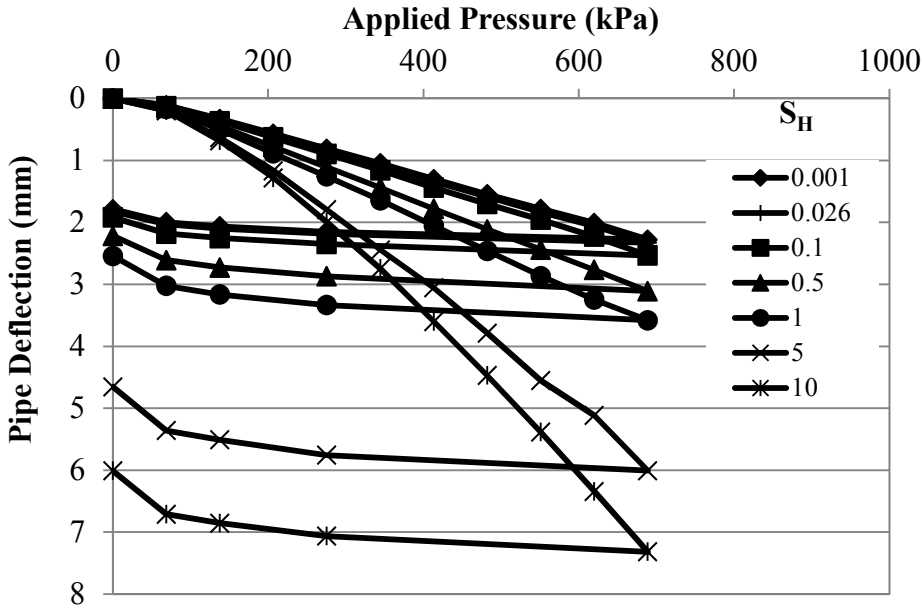

Figure 5.21 Pipe Vertical Deflections under a Reinforced Condition

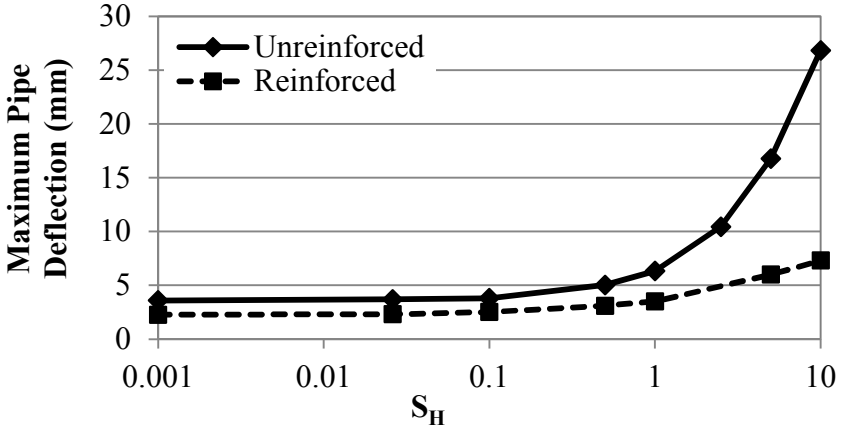

Figure 5.22 Maximum Vertical Pipe Deflections versus Hoop Stiffness Factor

Figures 5.23 and 5.24 show both the plate settlements for the unreinforced and reinforced conditions. The maximum plate displacements within the range of hoop stiffness factors are shown in Figure 5.25. The plate displacements showed similar performance to the pipe deflection with the most benefit occurring at the higher pipe stiffness factors. The maximum permanent plate displacements were obtained after the plate load was removed and are shown in Figure 5.26.

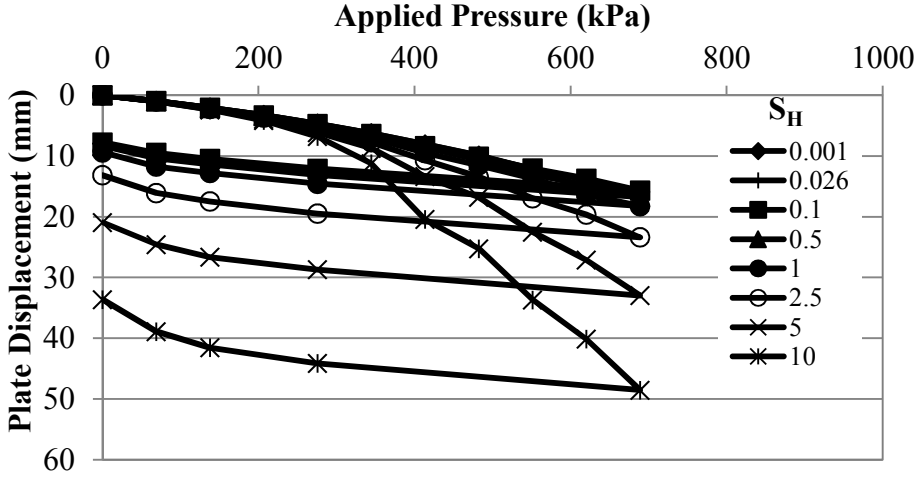

Figure 5.23 Vertical Plate Displacements under an Unreinforced Condition

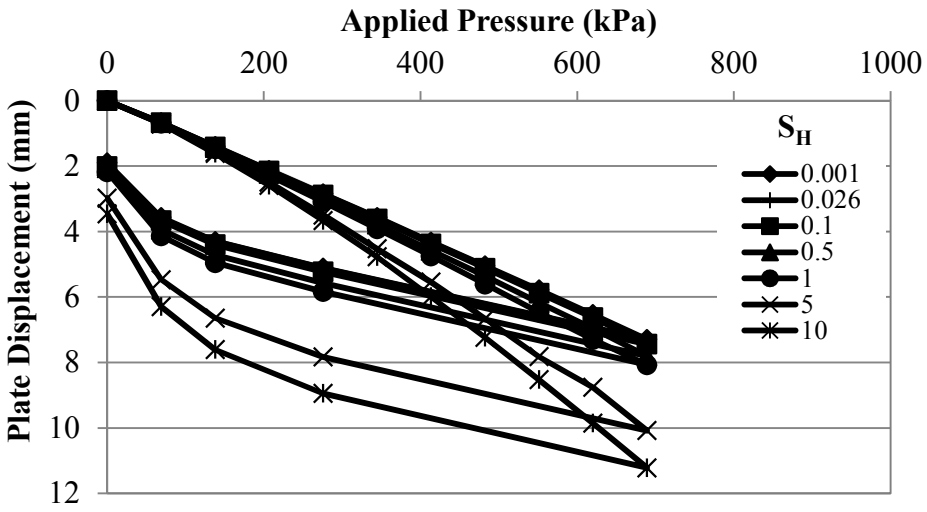

Figure 5.24 Vertical Plate Displacements under a Reinforced Condition

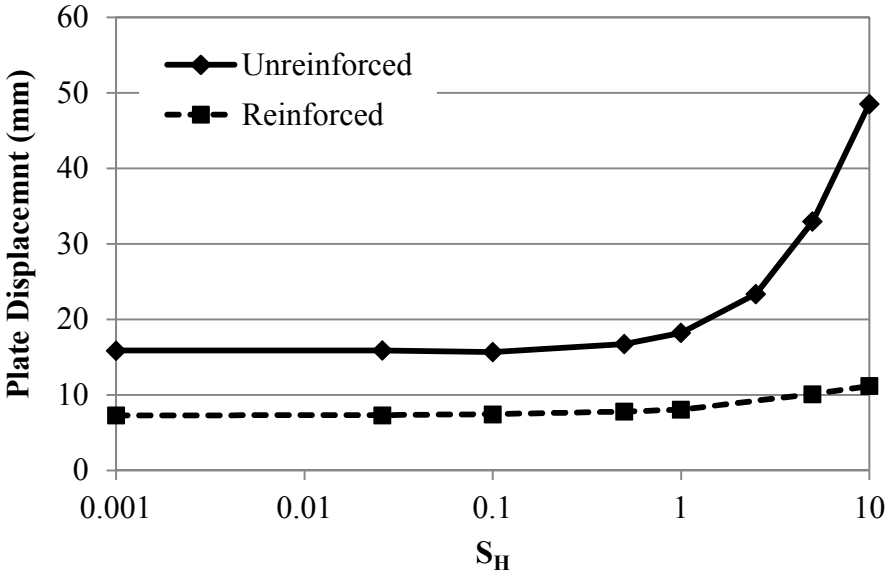

Figure 5.25 Maximum Plate Displacements at Surface versus Ratio of Soil to Pipe Hoop Stiffness

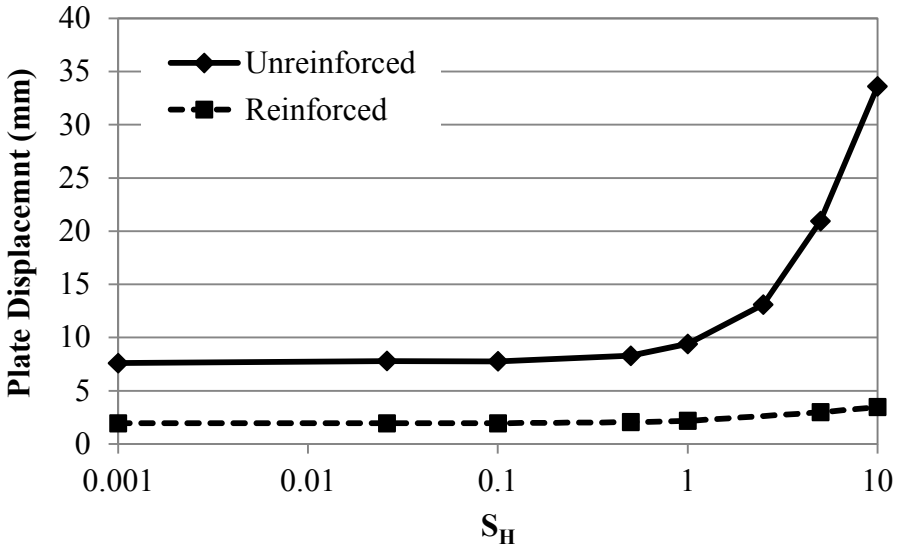

Figure 5.26 Permanent Plate Displacements versus Ratio of Soil to Pipe Hoop Stiffness

The distributions of vertical displacements on the surface of the base course, at the bottom of the base course, and at the crown of the pipe are presented in Figure 5.27. These distributions are given at the highest hoop stiffness (0.001) and the lowest hoop stiffness (10). At the hoop stiffness greater than one, the displacement increased significantly. The consequences of the displacements of the soil above the pipe in the unreinforced condition can be seen in the following plots of pipe displacements, surface displacements, and distribution of soil stresses around the pipe.

The horizontal deflections of the pipe decreased with an increased hoop stiffness factor in both unreinforced and reinforced conditions (Figures 5.28 and 5.29). The difference in the horizontal deflection due to the geogrid reinforcement was constant over the range of examined hoop stiffness factors (Figure 5.30).

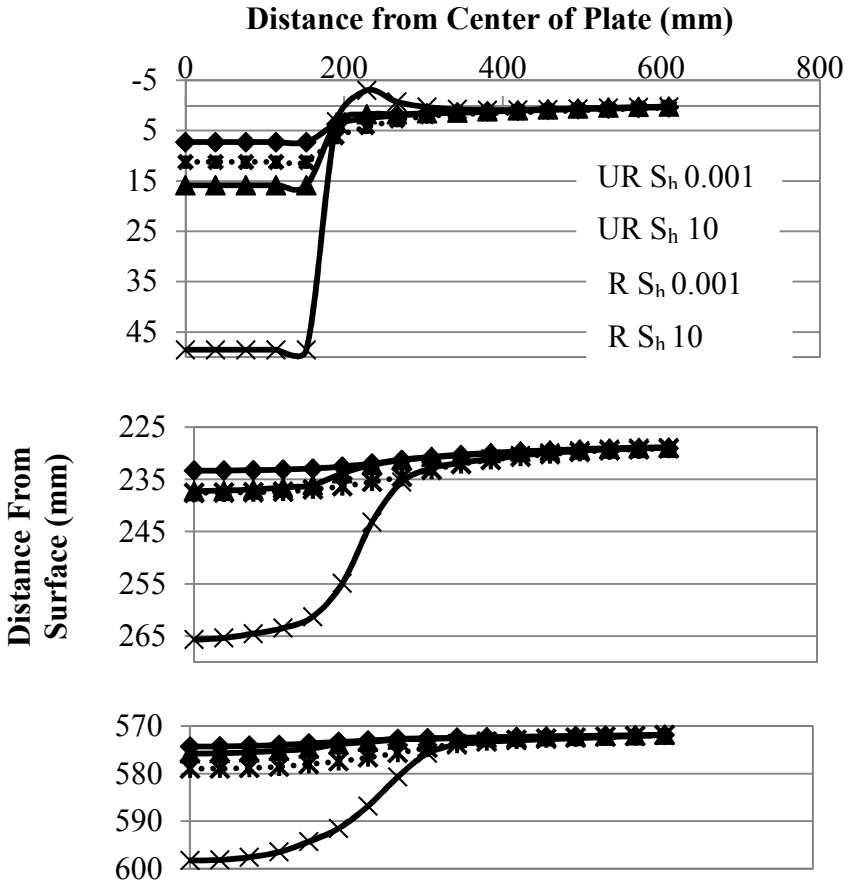

Figure 5.27 Vertical Soil Displacements between Loading Plate and Crown of Pipe

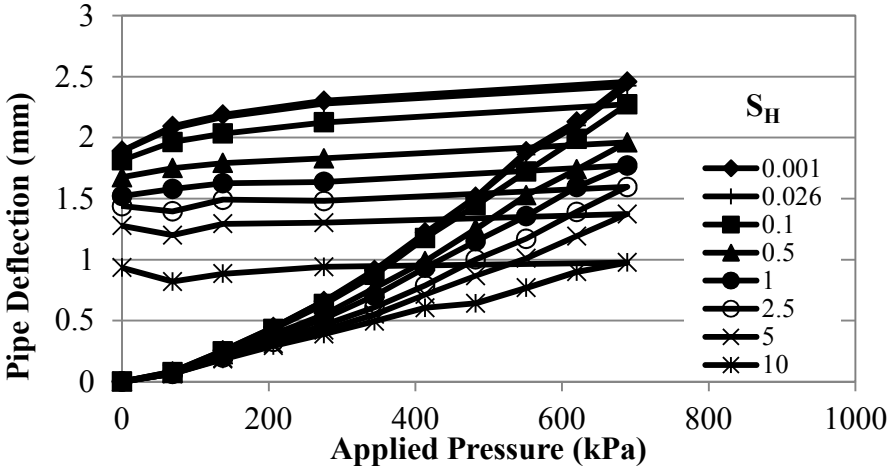

Figure 5.28 Horizontal Pipe Deflections under an Unreinforced Condition

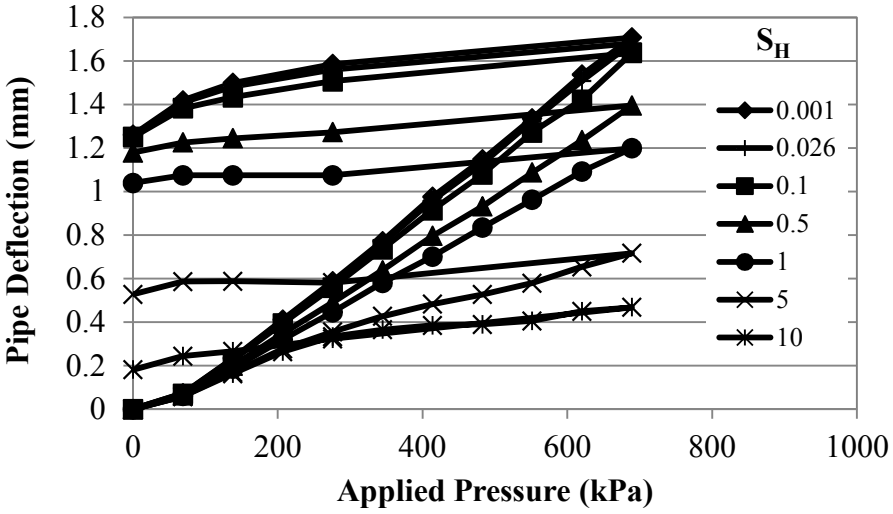

Figure 5.29 Horizontal Pipe Deflections under a Reinforced Condition

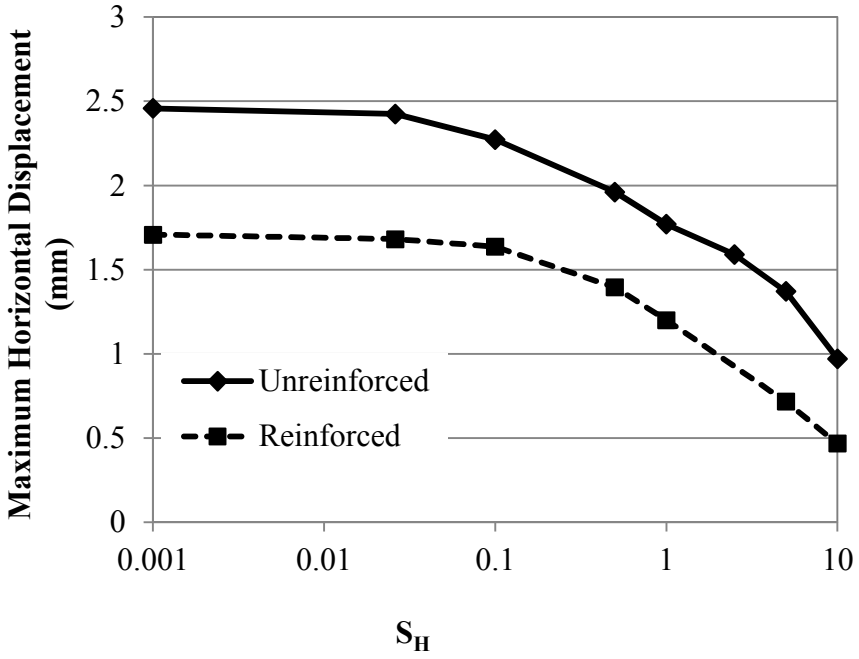

Figure 5.30 Maximum Horizontal Pipe Deflections versus Ratio of Soil to Pipe Hoop Stiffness

5.4.2 Earth Pressures

Figures 5.31 and 5.32 show the earth pressures at the crown of the pipe for the unreinforced and reinforced conditions. An increase in the hoop stiffness factor (the ratio of soil modulus to the pipe wall axial stiffness) resulted in lower pressures at the crown of the pipe, which corresponded to the increased vertical deflection of the pipe (Figure 5.33). The distribution of vertical pressures at the bottom of the base course is shown in Figures 5.34 and 5.35 for the hoop stiffness factors of 0.001 and 10, respectively. These two figures indicate that in both conditions the geogrid distributed the pressure over a wider area. The vertical pressures at the crown of the pipe for the hoop stiffness factors are shown in Figures 5.36 and 5.37. In both cases the pressure concentration at the crown was reduced by the inclusion of the geogrid in the base course.

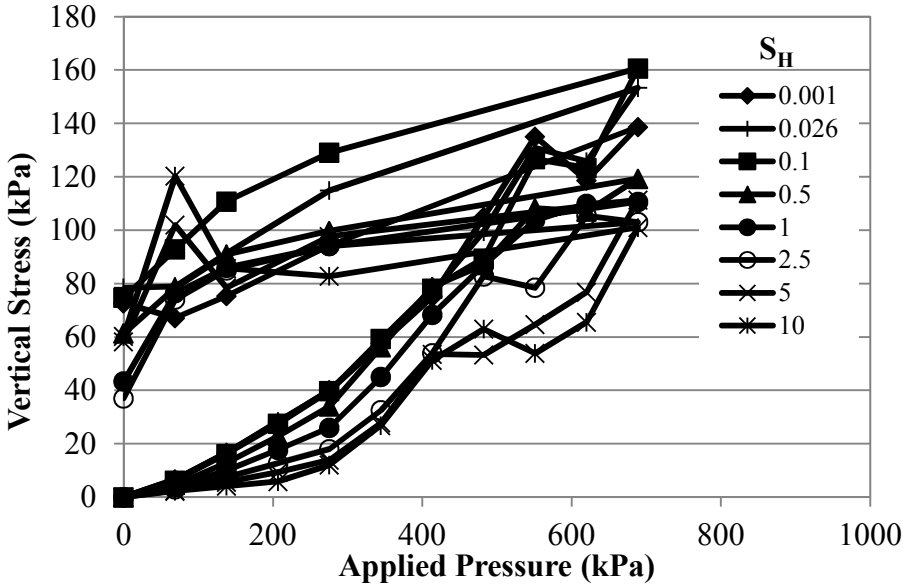

Figure 5.31 Vertical Pressures at Crown of Pipe under an Unreinforced Condition

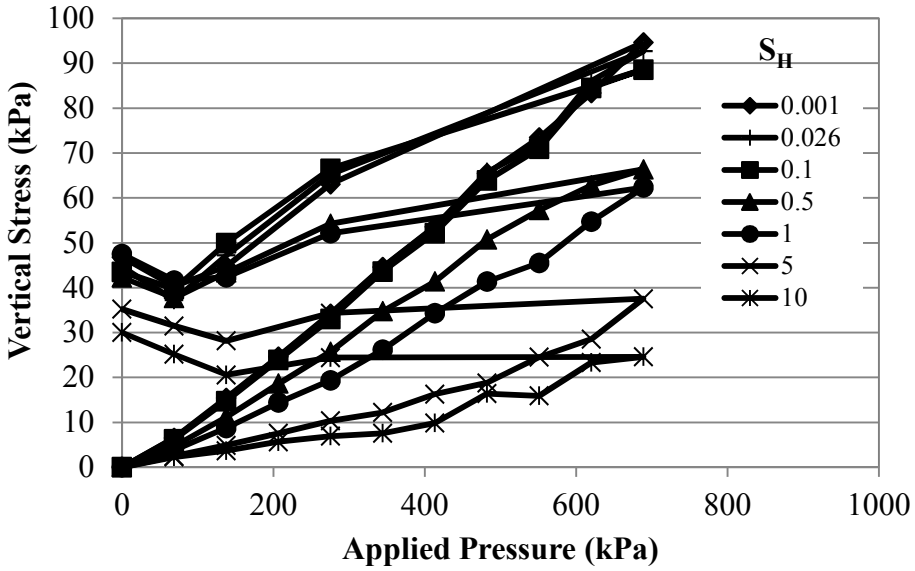

Figure 5.32 Vertical Pressures at the Crown under a Reinforced Condition

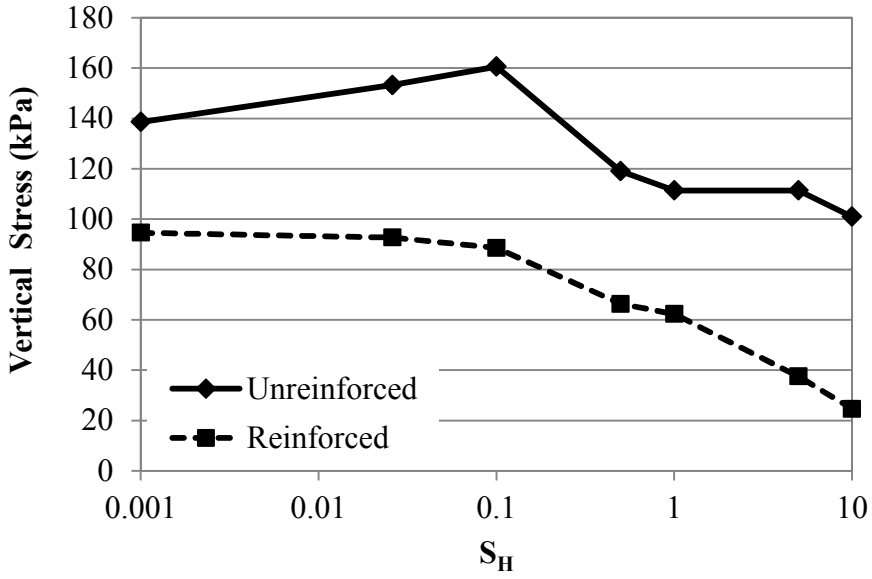

Figure 5.33 Vertical Crown Pressure vs Ratio of Soil to Pipe Hoop Stiffness

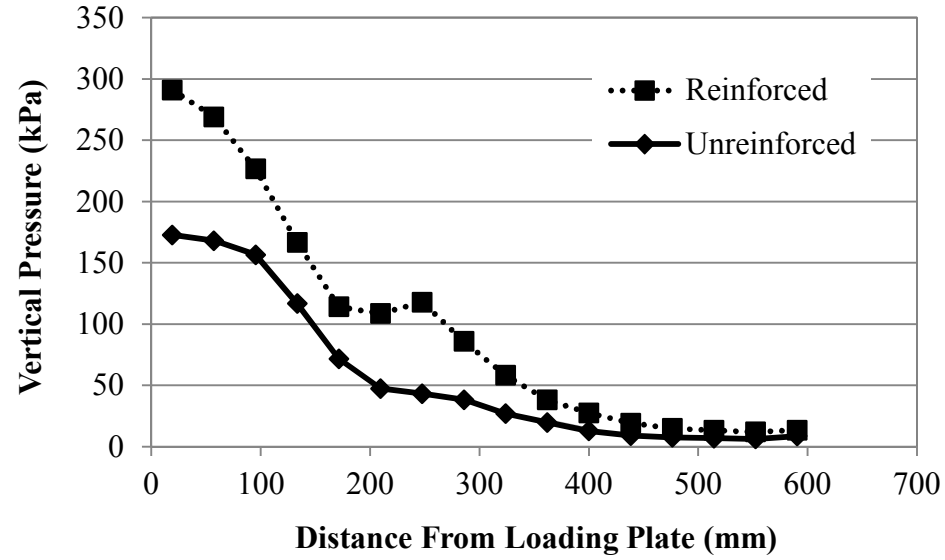

Figure 5.34 Vertical Pressure Distributions at the Bottom of the Base Course ($S_H = 0.001$)

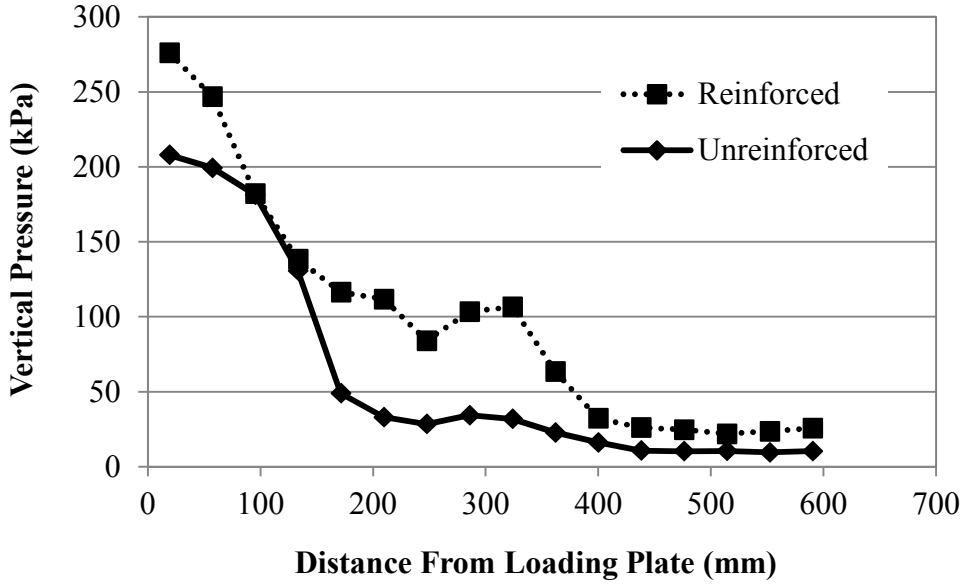

Figure 5.35 Vertical Pressure Distributions at the Bottom of Base course (S_H =10)

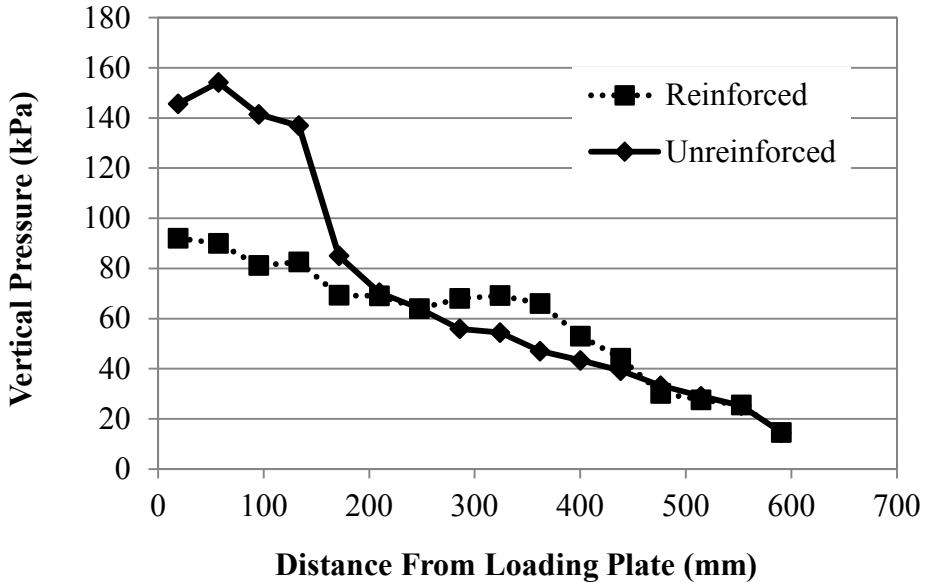

Figure 5.36 Vertical Pressure Distributions at the Crown of the Pipe (S_H = 0.001)

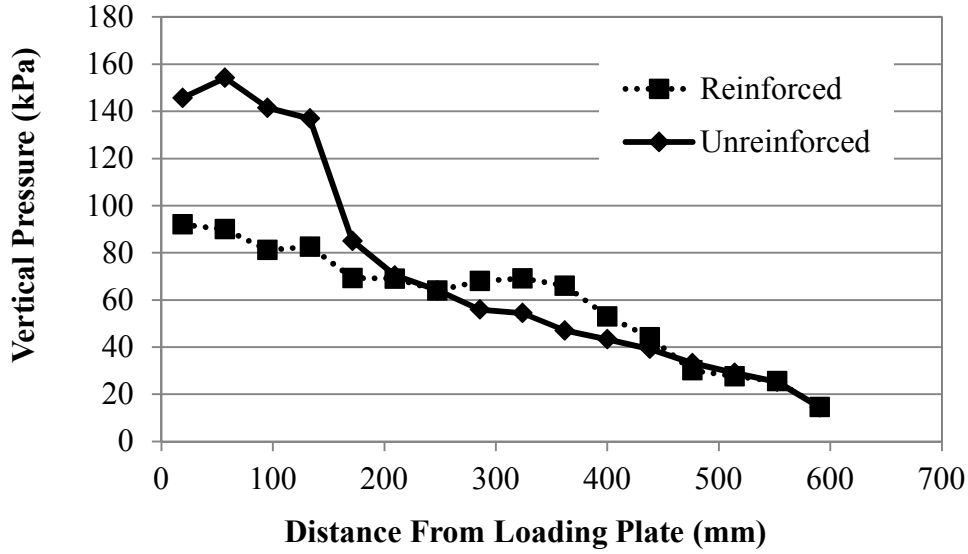

Figure 5.37 Vertical Pressure Distributions at the Crown of the Pipe with Pipe Hoop Stiffness Factor of 10

Horizontal pressures at the springline are shown in Figures 5.38 and 5.39. The horizontal pressures at the spring line decreased with the increased hoop stiffness factor. The reductions in the horizontal pressures at the spring line were consistent between the hoop stiffness factor of 0.001 and 1. When the hoop stiffness factors were greater than one, the horizontal pressure at the springline increased markedly as compared to the reinforced condition (Figure 5.41).

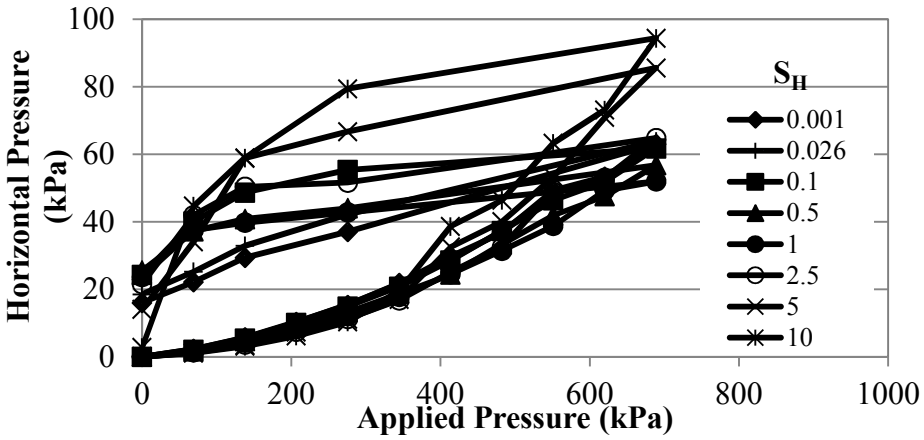

Figure 5.38 Horizontal Pressures at Springline under an Unreinforced Condition

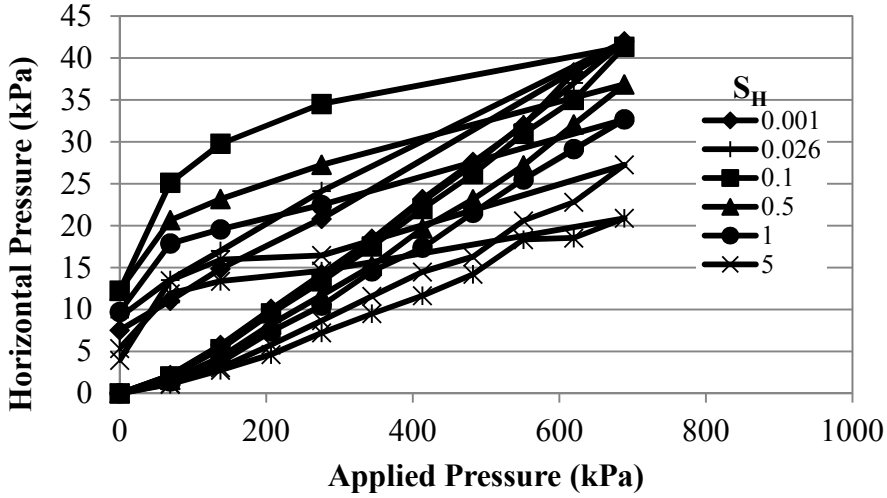

Figure 5.39 Horizontal Pressures at Springline under a Reinforced Condition

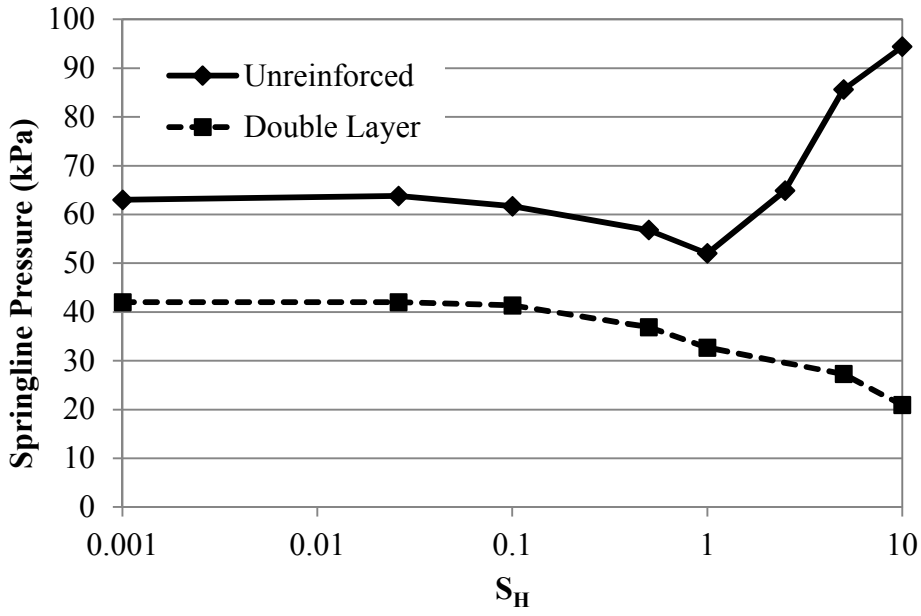

Figure 5.40 Maximum Horizontal Pressures at the Springline versus Ratio of Soil to Pipe Hoop Stiffness

5.4.3 Pipe Moments and Thrusts

The unreinforced and reinforced conditions resulted in similar distributions of bending moments in the pipe wall at the maximum applied plate pressure as shown in Figures 5.41 and 5.42. The magnitudes of the moments in the unreinforced condition were significantly higher than those in the reinforced condition. The moments were distinctly higher when the hoop stiffness factor was 1.0 or greater (Figure 5.43). The moments of the pipe with respect to the hoop stiffness factors corresponded well with the behavior of the pipe deflections.

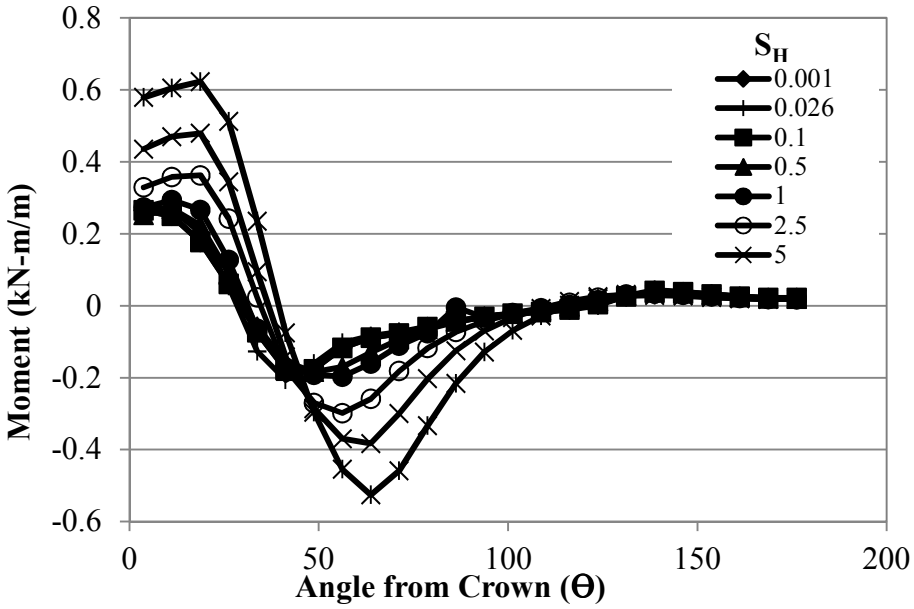

Figure 5.41 Bending Moments in the Pipe Wall for Varying Hoop Stiffness at the Maximum Applied Pressure under an Unreinforced Condition

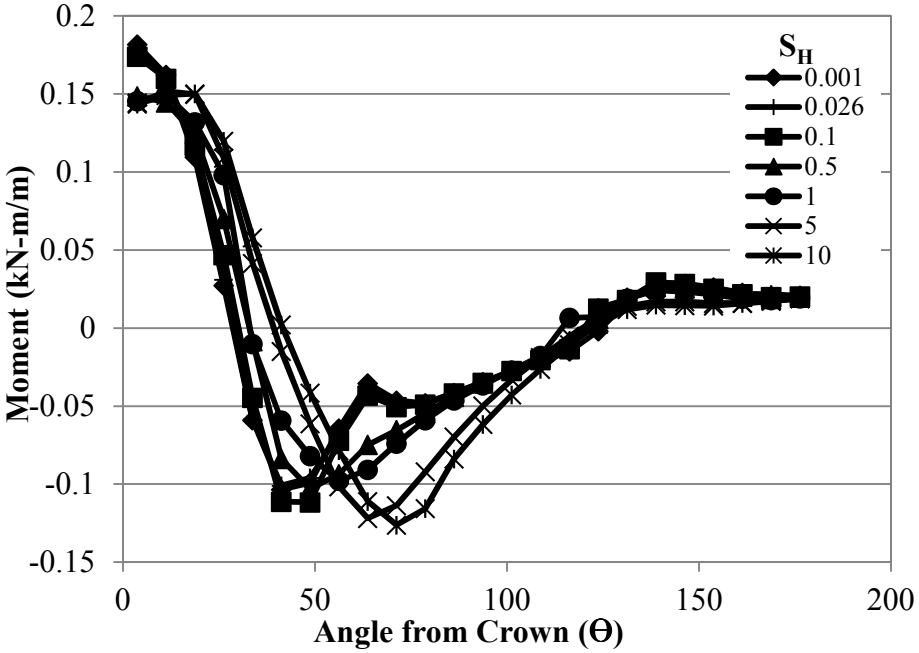

Figure 5.42 Bending Moments in the Pipe Wall for Varying Hoop Stiffness under a Reinforced Condition

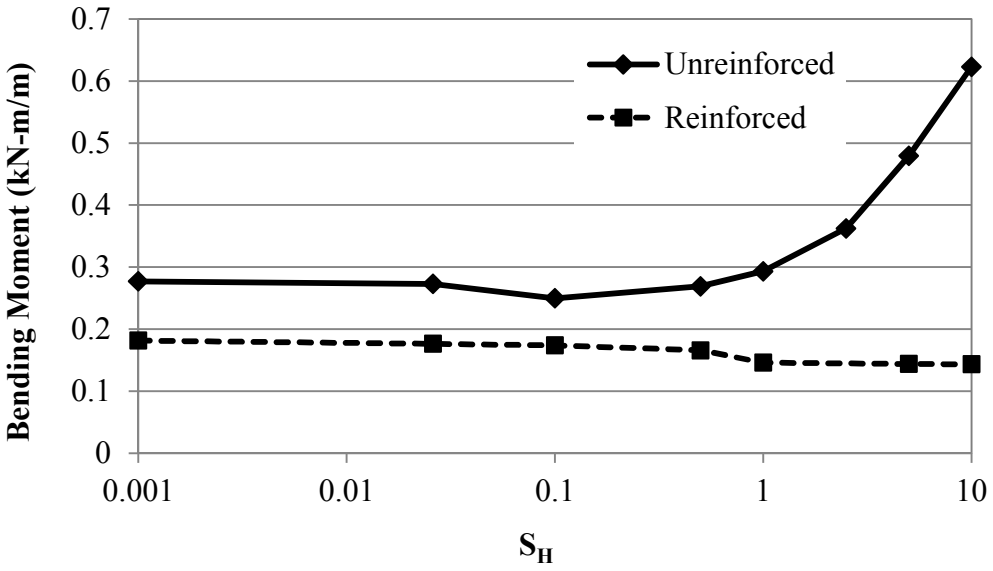

Figure 5.44 Maximum Bending Moments vs. Ratio of Soil to Pipe Hoop Stiffness

As the ratio of the soil stiffness to axial stiffness of the pipe (i.e., the hoop stiffness factor) increased, the thrust in the pipe as shown in Figure 5.44 and Figure 5.45 decreased as anticipated according to McGrath's (1998) VAF as shown in Figure 5.1. The thrust decreased at all locations of the pipe with the thrust in the reinforced condition significantly lower. The thrust at the maximum applied plate pressure versus the hoop stiffness at the crown and at the shoulder, as shown in Figures 5.46 and 5.47, shows a fairly uniform drop in the thrust over a wide range of hoop stiffness. However, at the shoulder of the pipe, there was an increase in the thrust at the shoulders of the pipe when the hoop stiffness factor was 1.0 or greater for the unreinforced condition.

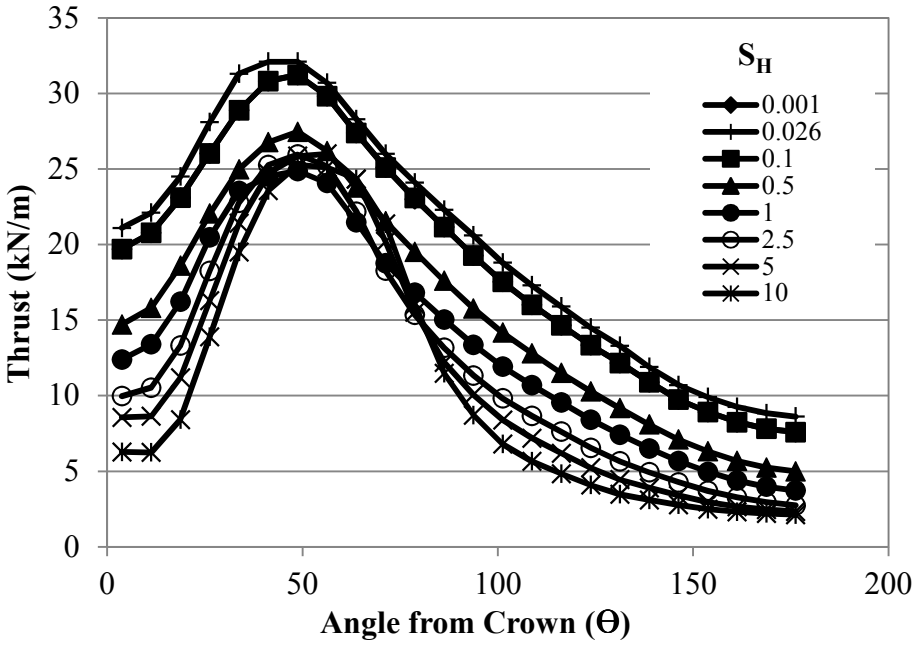

Figure 5.44 Thrust in Pipe for Varying Hoop Stiffness under an Unreinforced Condition

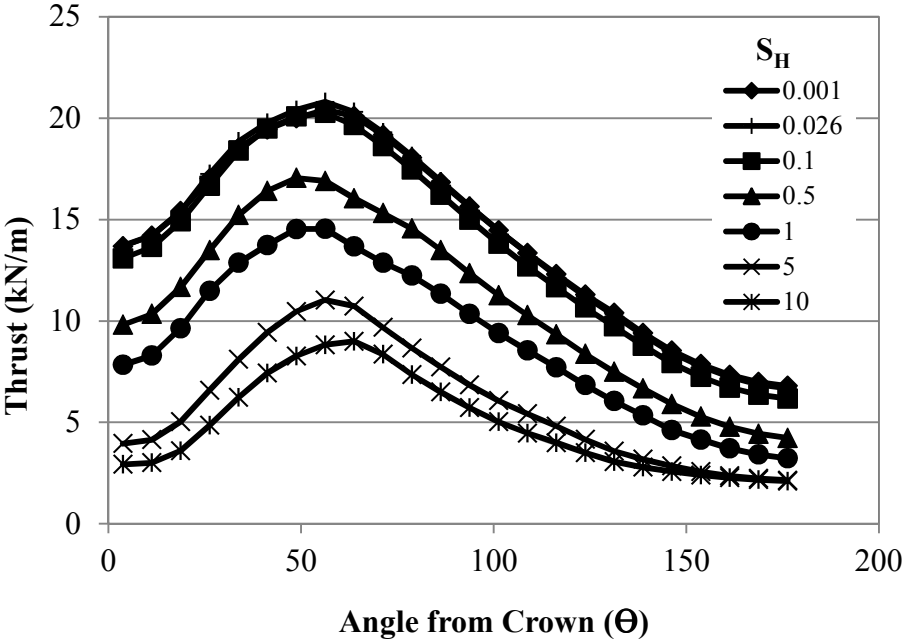

Figure 5.45 Thrust in Pipe for Varying Hoop Stiffness under a Reinforced Condition

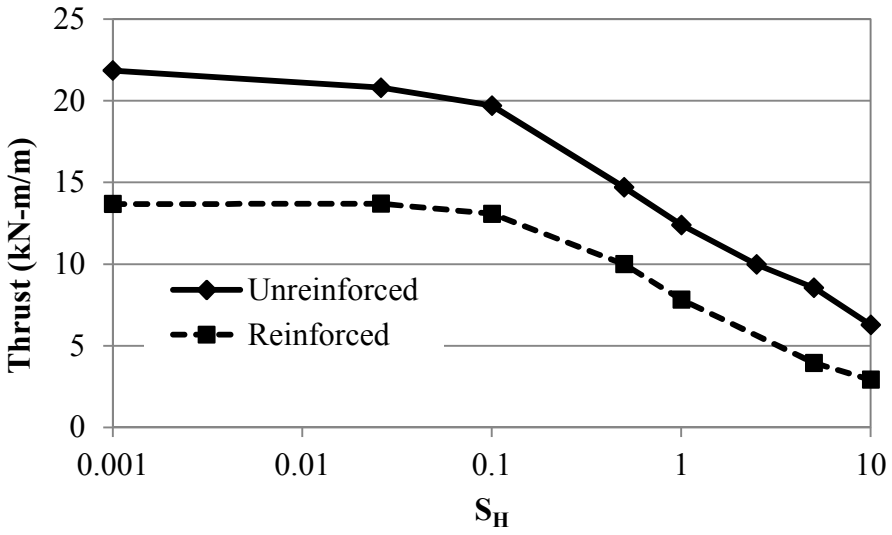

Figure 5.46 Thrust at Crown vs Ratio of Soil to Pipe Hoop Stiffness

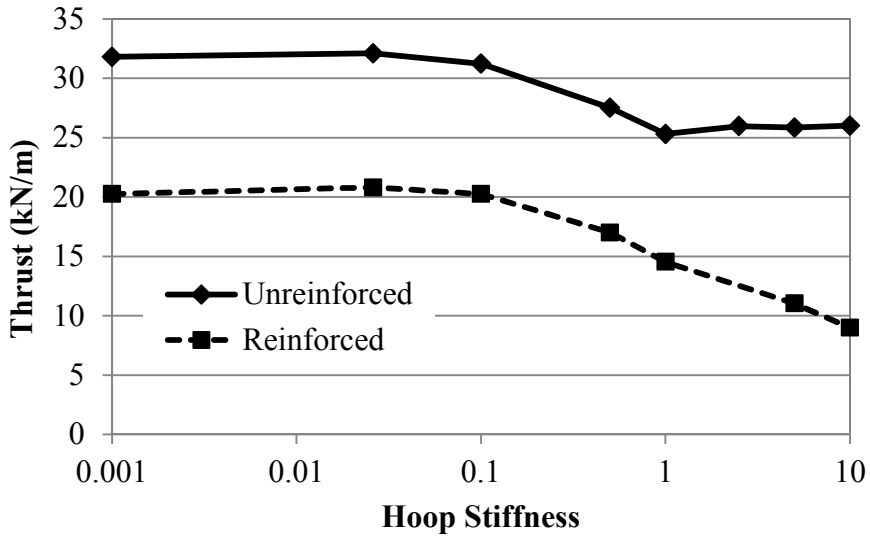

Figure 5.47 Thrust at Shoulder vs. Ratio of Soil to Pipe Hoop Stiffness

Longitudinal strains at the crown of the pipe were determined for the reinforced and unreinforced conditions over the range of hoop stiffness factors run in the parametric study as

shown in Figure 5.48. For hoop stiffness factors between 0.001 and 1 the difference in longitudinal strain were constant. The reduction in longitudinal strain was approximately 33% from 0.42% strain to 0.27%. For hoop stiffness factors greater than 10 the longitudinal strain for the unreinforced condition dropped so that there was almost no difference in strains between the two conditions. It is assumed that for the high hoop stiffness factor the greater deflection of the pipe reduced the vertical and horizontal stresses in the backfill directly over the crown, resulting in lower strains in the pipe wall.

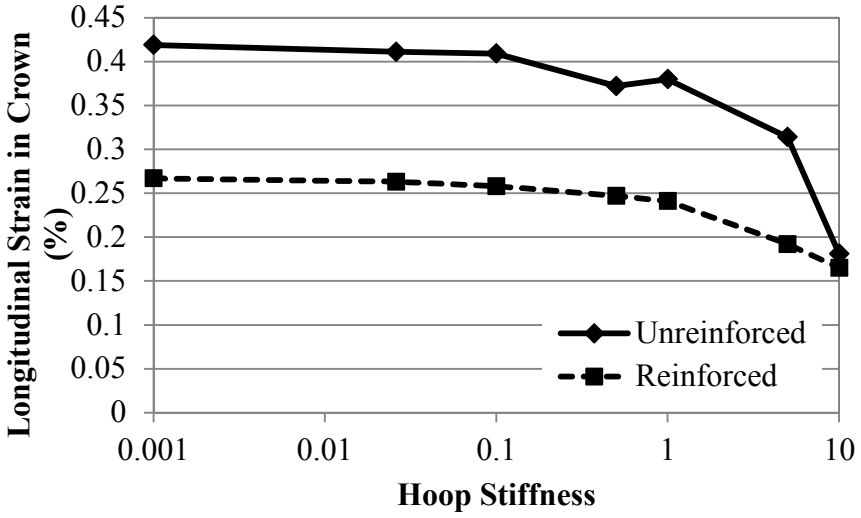

Figure 5.48 Longitudinal Strains at Crown vs. Ratio of Soil to Pipe Hoop Stiffness

5.4.4 Geogrid Strain

To examine the contribution of geogrid, the geogrid strains under loading were computed. Figures 5.49 and 5.50 both show that geogrid strains did not vary significantly with

the hoop stiffness factors similar to the changes in pipe stiffness. As the hoop stiffness factor increased, the strain in the geogrid did increase slightly. At a hoop stiffness factor of 1.0 and greater, there appeared to be a larger increase in the geogrid strain, and a redistribution of strains in both axes of the geogrid sheet. As noted, the geogrid distribution of strains matched the typical distribution of strains for geogrid confinement in a base course.

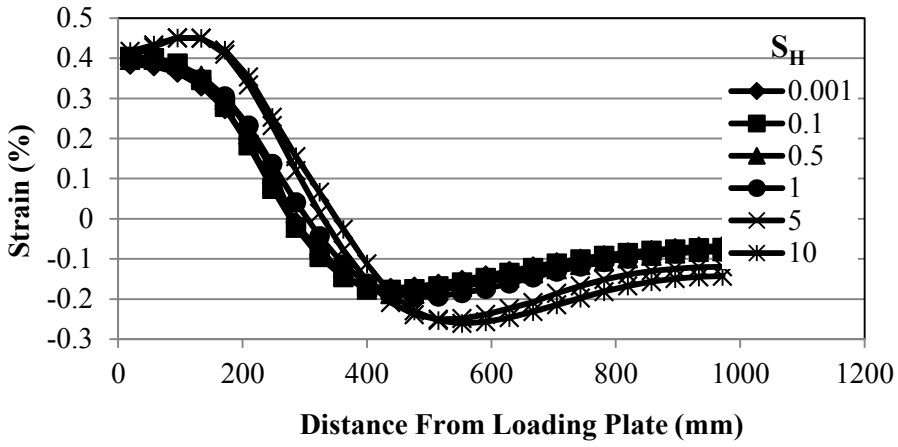

Figure 5.49 Distribution of Machine Direction Geogrid Strains at the Maximum Applied Pressure

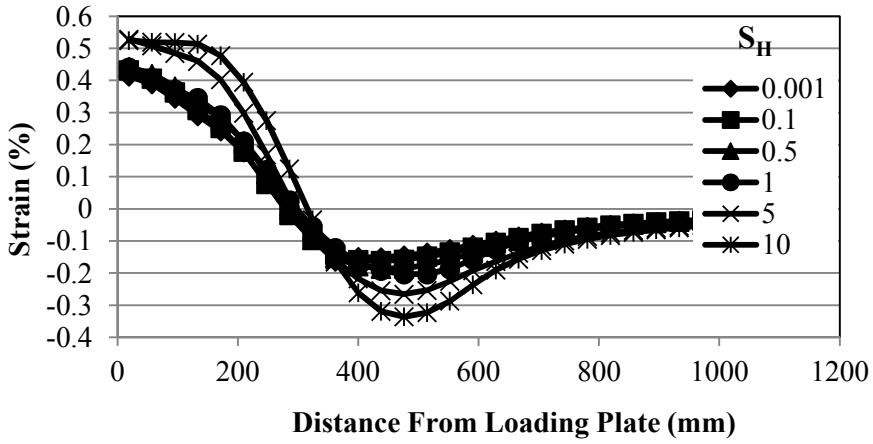

Figure 5.50 Distribution of Cross-machine Direction Geogrid Strains at the Maximum Applied Pressure

5.5 Conclusions

The parametric study on the effects of the bending stiffness and hoop stiffness revealed both anticipated and insightful results into the application of geogrid reinforcement with respect to pipes. The parametric results were obtained based on the numerical parametric study of wheel loads over shallowly buried pipes in trenches. The following conclusions can be drawn from this parametric study:

1. The pipe stiffness is a good indication of the effectiveness of the geogrid in reducing deflections and strains in the pipe. Pipes with high bending stiffness, such as a concrete pipe, had little improvement by the inclusion of a geosynthetic layer.
2. The reduction in the pipe moments was consistent to the degrees of pipe stiffness investigated between the unreinforced and reinforced conditions. The reduction in the thrust increased as the pipe stiffness decreased over the range of pipe stiffness investigated.
3. For the range of the pipe hoop stiffness factors from approximately 0.001 to 1.00, the improvements in reduced pipe deflection, plate settlements, and reduced earth pressures provided by the geogrid were constant. At the higher hoop stiffness factors (i.e., greater than 1), the improvements in pipe performance were increased significantly by the inclusion of the geogrid.
4. It appears that at a hoop stiffness factor of less 1.0, the benefit from the geogrid is a function of the stiffness of the geogrid reinforced layer. At a hoop stiffness factor

greater than 1.0, the benefit appears to be a function of both the stiffness of the geogrid layer and the geogrid reinforced layer preventing the redistribution of soil pressure around the pipe.

5. The differences in the magnitudes of strains and deflections between the reinforced and unreinforced conditions will be a function of the backfill stiffness and the reinforced layer. It is assumed that the improvements provided by the geogrid will be greater for backfills with a lower modulus.

Chapter 6 Conclusions and Recommendations

6.1 Introduction

Experiments were completed on a buried steel-reinforced HDPE pipe (SRHDPE) in a trench condition subjected to a near surface load. Static and cyclic plate loads were applied on the surface simulating a point or wheel load with compacted sand and crushed stone aggregate backfills. For these tests, conditions of unreinforced and geogrid-reinforced base courses and backfills were examined. Based on the literature review and experimental tests, numerical models were calibrated to the unreinforced and geogrid reinforced static plate loading tests of the SRHDPE pipe in a crushed stone-filled trench. The calibrated numerical models were then used to perform a parametric study investigating the effects of the pipe hoop stiffness and the pipe bending stiffness on the performance of the buried pipes and loading plates under the unreinforced and reinforced conditions.

6.2 Experimental Study

The following conclusions can be made based on the experimental tests on shallowly buried SRHDPE pipes subjected to static and cyclic loading with and without geogrid reinforcement:

1. The longitudinal strains in the pipe were higher than expected and were not simply a result of bending in the pipe wall. The longitudinal strain on the inside and the outside of the pipe wall at the crown were in tension. Incidentally, the longitudinal strains at the crown were the highest strains recorded in the pipe during the tests.
2. A single layer of geogrid at 152.4 mm above the crown of the pipe in the backfill, generally had no significant impact on the reduction of vertical pressures, deflections, or strains in the cross section of the pipe. This geogrid layer, however, did reduce the longitudinal strains in the pipe wall at the crown of the pipe.
3. The double layer of geogrid, the first layer at 152.4 mm above the crown of the pipe, and the second layer at the interface between the base course and the backfill, did have an impact on the reduction of pipe deflections, stresses in the backfill, and strains in the pipe wall in both the compacted sand and crushed stone aggregate backfills. Compared with the single layer system, the upper layer geogrid was more effective in improving the performance of the pipe.
4. The geogrid reinforcement had the most impact on the plate settlements, the pipe deflections, which were both lowered, and the attenuation of earth pressures in the less stiff aggregate backfill conditions as compared to the stiffer compacted sand condition. The geogrid strains were also higher in the condition with the crushed stone backfill.
5. At approximately 400 mm from the centerline of the plate, the geogrid was in compression. This result indicated that the geogrid did not act strictly as a tensioned membrane but more in line with base course confinement.

6. The results of the cyclic plate load tests confirmed the results of the static plate load tests. Similar to the static plate load tests the single layer of geogrid above the pipe did not significantly impact the pipe deflection and earth pressures when comparing the reinforced and unreinforced conditions. The pipe deflections were higher in the cyclic plate load tests as compared to the static load test. Similar to the static plate load tests in the cyclic plate load tests the highest strains recorded in the experiments were recorded in the longitudinal direction in the pipe wall.

6.3 Numerical Calibration

The following conclusions can be made from the numerical calibration of the test sections of the crushed stone aggregate backfill from the experimental study:

6. The Cap-Yield model was a reasonable method of modeling the non-linear response of the soil to the stresses and strains around the pipe. The calibrated model indicated that this constitutive model worked well.
7. Modeling the benefit of the geogrid below the compacted AB-3 layer was difficult. Displacements on the surface and at the bottom of the base course in the numerical model matched the measured results by assuming some additional residual stresses considering the base course compaction. However the displacements of the soil near the pipe crown in the model did not match the measured experimental displacements.

The apparent cohesion method used in the calibrated method gave good results, but limited the scope of potential parametric studies.

8. The three dimensional numerical model was able to capture the longitudinal strain in the crown of the pipe and confirm that the strain can be determined by superposition of bending strains and strains caused by the horizontal spreading of the soil above the pipe.

6.4 Parametric Study

The following conclusions can be made from the parametric study considering two important parameters of the pipe bending and hoop stiffness under unreinforced and geogrid-reinforced conditions was conducted: The geogrid appeared to have two functions, firstly lowering the applied load on the pipe, thus reducing deflections and strains, and secondly confining the backfill materials above the pipe and resisting the redistribution of soil pressures around the pipe.

1. The inclusion of the geogrid layer did not have much effect on the performance (i.e. deflections, thrust, and bending moments) of pipes with the high pipe stiffness (PS), such as concrete pipes.
2. When the pipe hoop stiffness factors varied from approximately 0.001 to 1.0, the difference in pipe deflections, loading plate settlements, pipe thrusts and moments

between the unreinforced and reinforced conditions were constant. When the hoop stiffness factors were greater than 1.0, the inclusion of the geogrid significantly increased the degree of improvement in the pipe performance.

3. The magnitude of reduction in pipe deflections and strains and the magnitude in reduction of plate settlements when the base course was reinforced with geogrid as compared to the unreinforced base course appeared to be a function of the relative stiffness of the backfill and the base course. Therefore in backfills with a lower modulus it is expected that there will be greater improvement (difference in vertical pipe deflections between the reinforced and unreinforced conditions) by including a geogrid in the base course.
4. When the hoop stiffness factor was greater than 1.0, the difference in pipe deflections, plate displacements and pipe strains, between the unreinforced and reinforced condition appeared to be a function of pipe hoop stiffness, backfill stiffness, and the stiffness of the geogrid reinforced base course. The benefit of the geogrid (reduction in pipe deflections) increased as the hoop stiffness factor increased. The geogrid reinforced base course also resulted in more uniform distributions on vertical earth pressures at the crown of the pipe. For the unreinforced condition at the highest applied plate pressures the vertical earth pressures were concentrated at the crown and the horizontal pressures increased as the pipe transferred more earth pressure to the spring-line.

6.5 Recommendations

This Ph.D. study primarily focused on SRHDPE pipes with two specific backfill materials under loading at the center of the pipe. The following tasks are recommended for possible future studies:

1. Experimental studies of geogrid-reinforced base courses with unreinforced HDPE pipes of low hoop stiffness, having hoop stiffness factors ranging from 1 to 100, should be performed to verify the findings of this study.
2. Experimental and numerical studies, with test conditions similar to the ones reported in this study, should be conducted with lower modulus backfills, which can verify and expand the findings of this study. The further studies can help establish the relationship between the modulus of the backfill, the stiffness and strength of the geogrid reinforced base course, and the magnitude in improvements in the pipe, which decreased deflections and pipe strains.
3. A study should be performed to investigate the effect of the locations of the applied plate loads relative to the location of the pipe. Misalignment of the load from the crown to the shoulder may show more benefit of the geogrid than the applied load directly over the pipe.

References

AASHTO (American Association of State Highway and Transportation Officials). (2012). *AASHTO LRFD bridge design specifications*, Washington, DC.

AISI (American Iron and Steel Institute). (1983). *Handbook of Steel Drainage & Highway Construction Products*, Washington, DC.

Armco Handbook of Drainage and Construction Products. (1955). ARMCO Drainage and Metal Products, Inc., Middletown, OH.

Arockiasamy, M., Chaallal, O., and Limpeteeprakarn, T. (2006). "Full-scale field tests on flexible pipes under a live load application." *Journal of Performance of Constructed Facilities,* 20(1), 21-27.

ASCE (American Society of Civil Engineers). (1982). *Gravity Sanitary Sewer Design and Construction,* No. 60, New York, NY.

ASCE (American Society of Civil Engineers). (2013). *2013 Report Card for America's Infrastructure,* ASCE, New York , NY.

AWWA (American Water Works Association). (1999). *Fiberglass Pipe Design (M45),* Denver, CO.

Bathurst, R.J., and Knight, M.A. (1998). "Analysis of geo-cell reinforced-soil covers over large span conduits." *Computers and Geotechnics*, 3(22), 205-219.

Bauer, G.E. (1994). “The control of settlement using geogrids.” *Vertical and Horizontal Deformations of Foundations and Embankments, Geotechnical Special Publication No. 40*, A.T. Yeung and G.Y. Félio, eds., Vol. 1, ASCE, New York, NY, 491-501.

Bishop, R.R., and Lang, D.C. (1984). “Design and performance of buried fiberglass pipes – a new perspective.” *Pipeline Materials and Design,* B.J. Schrock, ed., ASCE, New York, 1-12.

Brown, F.A., and Lytton, R.L. (1984) “Design criteria for buried flexible pipe.” *Pipeline Materials and Design,* B.J. Schrock, ed., ASCE, New York, 36-47.

Bryan, G.H. (1891). “On the stability of a plane plate under thrusts in its own plane, with applications to the buckling of the sides of a ship.” *Proc. of the London Mathematical Society,* Vol. 22, London, 54-67.

Bueno, B.S., Viana, P.M.F., and Zornberg, J.G. (2005). "A novel construction method for buried pipes using geosynthetics." *Proc., Geo-Frontiers 2005*, ASCE, Austin, TX, 4155-4161.

Burns, J.Q., and Richard, R.M. (1964). “Attenuation of stresses for buried cylinders.” *Proc. of the Symposium on Soil Structure Interaction*, University of Arizona, Tucson, AZ, 378-392.

Carlström B., and Molin, J. (1966). *Kunststoffe*, 12, 895-898.

Chaallal, O., Arockiasamy, M., and Godat, A. (2014). “Numerical finite-element investigation of the parameters influencing the behavior of flexible pipes for culverts and storm sewers under truck load.” *Journal of Pipeline Systems Engineering Practice,* 6(2), 04014015.

Christopher, B.R., Berg, R.R., and Perkins, S.W. (2001). *Geosynthetic Reinforcements in Roadway Sections,* NCHRP Report 20-7, Transportation Research Record, Washington, DC.

Cole, B.W., and Timblin, T.O. (1981). "Strain calculations for FRP pressure pipe." *Proc. of the International Conference on Underground Plastic Pipe.* B.J. Schrock, ed., New Orleans, LA, 130-147.

Dhar, A.S., and Moore, I.D. (2006). "Evaluation of local bending in profile-wall polyethylene pipes." *Journal of Transportation Engineering,* 132(11), 898-906.

Dhar, A.S., Moore, I.D., and McGrath, T.J. (2004). "Two-dimensional analyses of thermoplastic culvert deformations and strains." *Journal of Geotechnical and Geoenvironmental Engineering,* 130(2), 199-208.

Duncan, J.M. (1976). "Finite element analysis of buried flexible metal culvert structures." *Laurits Bjerrum memorial volume: contributions to soil mechanics*, L. Bjerrum, N. Janbu, F.A. Jørstad, & B. Kjærnsli, eds., Norges geotekniske institutt, Oslo, 213-222.

Duncan, J.M. (1978). "Soil culvert interaction method for the design of metal culverts." *Transportation Research Record,* 678, 53-59.

Duncan, J.M. (1979). "Behavior and design of long-span metal culverts." *Journal of the Geotechnical Engineering Division,* 105(3), 399-418.

Duncan, J.M., Byrne, P., Wong, K.S., and Mabry, P. (1980). *Strength, stress-strain and bulk modulus parameters for finite element analyses of stresses and movements in soil masses*, Geotechnical Engineering Report No. UCB-GT-80-01, College of Engineering Office of Research Services, University of California, Berkley, CA.

Duncan, J.M., and Chang, C.Y. (1970). "Nonlinear analysis of stress and strains in soils." *Journal of the Soil Mechanics and Foundations Division*, 96(5), 1629-1653.

Duncan, J.M., and Seed, R.B. (1986). “Compaction induced earth pressures and Ko- conditions.” *Journal of Geotechnical Engineering,* 112(1), 1-22.

Duns, C.S., and Butterfield, R. (1971). “Flexible buried cylinders part I – static response.” *International Journal of Rock Mechanics and Mining Sciences,* 8(6), 577-627.

Elshimi T.M., and Moore, I.D. (2013). “Modeling the effects of backfilling and soil compaction beside shallow buried pipes.” *Journal of Pipeline Systems Engineering Practice,* in press.

Erickson, H., and Drescher, A. (2001). *The Use of Geosynthetics to Reinforce Low Volume Roads,* Dept. of Civil Engineering Report No. MN/RC-2001-15, University of Minnesota, Minneapolis, MN.

Fernando, N.S.M., and Carter, J.P. (1998). “Elastic analysis of buried pipes under service patch loading.” *Journal of Geotechnical and Geoenvironmental Engineering*, 124(8), 720-728.

Forrestal, M.J., and Herrmann, G. (1965). “Buckling of a long cylindrical shell surrounded by an elastic medium.” *International Journal of Solids and Structures,* 1(3), 297-309.

Gassman, S.L., Schroeder, A.J., and Ray, R.P. (2005). "Field performance of high density polyethylene culvert pipe." *Journal of Transportation Engineering,* 131(2), 160-167.

Gerard, G., and Becker, H. (1957). *Handbook of Structural Stability: Buckling of Flat Plates,* National Advisory Committee for Aeronautics, Washington, DC.

Giroud, J.P. (1992). “Biaxial Tensile State of Stress in Geosynthetics.” *Geotextiles and Geomembranes,* 11(3), 319-325.

Giroud, J.P., Ah-line, C., and Bonaparte, R. (1985). "Design of unpaved roads and trafficked areas with geogrids." *Polymer Grid Reinforcement,* Thomas Telford Limited, London, 116-127.

Giroud, J.P., Bonaparte, R., Beech, J.F., and Gross, B.A. (1990). "Design of Soil Layer-Geosynthetic Overlying Voids." *Geotextiles and Geomembrane.* 9(1), 11-50.

Giroud, J.P., and Han, J. (2004). "Design method for geogrid-reinforced unpaved roads. I. development of design method." *Journal of Geotechnical and Geoenvironmental Engineering,* 130(8), 775-786.

Giroud, J.P., and Han, J. (2004). "Design method for geogrid-reinforced unpaved roads. II. calibration and applications." *Journal of Geotechnical and Geoenvironmental Engineering,* 130(8), 787-797.

Giroud, J.P., and Noiray, L. (1981). "Geotextile-reinforced unpaved road design." *Journal of the Geotechnical Engineering Division,* 107(9), 1233-1254.

Greatorex, C.B. (1981). "The relationship between the stiffness of a GRP pipe and its performance when installed." *Proc. of the International Conference on Underground Plastic Pipe,* B.J. Schrock, ed., New Orleans, LA, 117-129.

Hafez, H., and Abdel-Sayed, G. (1983). "Finite element analysis of soil-steel structures." *The Canadian Journal of Civil Engineering,* 10(2), 287-294.

Hashash, N., and Selig, E.T. (1990). "Analysis of the performance of a buried high density polyethylene pipe." *Structural Performance of Flexible Pipes,* S.M. Sargand, G.F. Mitchell, and J.O. Hurd, eds., Balkema, Rotterdam, 95-103.

Howard, A.K. (1977). *Modulus of Soil Reaction Values for the Buried Flexible Pipe,* Engineering and Research Center, Bureau of Reclamation, Denver, CO.

Hsuan, G.Y., and McGrath, T.J. (1999). *HDPE Pipe: Recommended Material Specifications and Design Requirement,* NCHRP Report 429, Transportation Research Record, Washington, DC.

Itasca. (2009). *FLAC3D Fast Lagrangian Analysis of Continua in 3 Dimensions, Users Guide,* Version 4.0, Itasca Consulting Group, Inc., Minneapolis, MN.

Janbu, N. (1963). "Soil compressibility as determined by oedometer and triaxial tests." *European Conference on Soil Mechanics and Foundation Engineering*, Germany, 19-25.

Janson, L. (1981). "Plastic gravity sewer pipes subjected to constant strain by deflection." *Proc. of the International Conference on Underground Plastic Pipe.* B.J. Schrock, ed., New Orleans, LA, 104-117.

Janson, L. (1985). "The relative strain as a design criterion for buried uPVC gravity sewer pipes." *Advances in Underground Pipeline Engineering: Second International Conference,* J.K. Jeyapalan, and M. Jeyapalan, eds., ASCE, New York, NY, 278-283.

Jeyapalan, J.K. (1983). "Geofabric stabilization of soft backfill materials for plastic sewer pipe installation." *Proc. of Pipelines in Adverse Environments II*, ASCE, New York, NY, 188-198.

Jeyapalan, J.K., and Abdelmagid, A.M. (1984). "Importance of relative pipe soil stiffness ratio in plastic pipe design." *Pipeline Materials and Design,* B.J. Schrock, ed., ASCE, New York, NY, 48-66.

Jeyapalan, J.K., Ethiyajeevakaruna S.W., and Boldon, B.A. (1987). "Behavior and design of buried very flexible plastic pipes." *Journal of Transportation Engineering,* 113(6), 642-657.

Jeyapalan, J.K., and Watkins, R. (2004). “Modulus of soil reaction (E’) values for pipeline design.” *Journal of Transportation Engineering,* ASCE, 103(1), 43-48.

Kang, J., Parker, F., and Yoo, C.H. (2008). “Soil-structure interaction of deeply buried corrugated steel pipes part 1: Embankment Installation.” *Engineering Structures,* 30(2), 384-392.

Katona, M.G. (1990). “Minimum cover heights for corrugated plastic pipe under vehicle loading.” *Transportation Research Record*, 1288, 127-135.

Katona, M.G., Mlynarski, M., and McGrath, T.J. (2007). *CANDE-2007: Culvert Analysis and Design Solution Methods and Formulations,* Final Report to the National Cooperative Highway Research Program, Washington, DC.

Katona, M.G., Smith, J.M., Odello, R.S., and Allgood, J.R. (1976). *CANDE: a modern approach for the structural design and analysis of buried culverts*, Federal Highway Administration Report No. FHWA-RD-77-5, Washington, DC.

Kawabata, T., Uchida, K., Hirai, T., Mohri, Y., Ling, H.I., and Koyama, N. (2003). "Experiments on buried pipe using backfill of cover with geosynthetics." *Proc. of the ASCE International Conference on Pipeline Engineering and Construction*, ASCE, Baltimore, MD, 1271-1278.

Kazemian, S., Barghchi, M., Prasad, A., Maydi, H., and Huat, B.K. (2010). "Reinforced pavement above trench under urban traffic load: Case study and finite element (FE) analysis." *Scientific Research and Essays*, 5(21), 3313-3329.

KDOT (Kansas Department of Transportation). (2007). *Standard specification for state and bridge construction,* Topeka, KS.

Kennedy, J.B., Laba, J.T., and Shaheen, H. (1988). "Reinforced soil-metal structures." *Journal of Structural Engineering*, 6(114), 1372-1388.

Khatri, D.K. (2012). *Experimental Evaluation of the Behavior of Steel Reinforced High Density Polyethylene (SRHDPE) Pipes*. M.S. Thesis, University of Kansas, Lawrence, KS.

Klaiber, F.W., Lohnes, R.A., Wipt, T.J., and Phares, B.M. (1996). *Investigation of High Density Polyethylene Pipe for Highway Applications*: *Phase 1*, Engineering Research Institute Final Report, Iowa State University, Ames, IA.

Koerner, R.M. (2005). *Designing with Geosynthetic,* Fifth Ed., Pearson Prentice Hall, Upper Saddle River, NJ.

Konder, R.L. (1963). "Hyperbolic stress-strain response: cohesive soils." *Journal of the Soil Mechanics and Foundations Division,* ASCE, 89(1), 115-143.

Kupec, J., and McGown, A. (2004). "The biaxial load-strain behavior of biaxial geogrids." *Proc. 3rd Asian Regional Conference on Geosynthetics GeoAsia 2004.* Korean Geosynthetics Society, Seoul, Korea, 349-356.

Kwon, J., Tutumuler, E., and Al-Qadi, I. (2009). "Validated mechanistic model for geogrid base reinforced flexible pavements." *Journal of Transportation Engineering,* 135(12), 915-926.

Kwon, J., Tutumuler, E., and Kim, M. (2005). "Development of a mechanistic model for geosynthetic-reinforced flexible pavements." *Geosynthetics International,* 12(6), 310-320.

Kwon, J., Tutumuler, E., and Koneietzky, H. (2008). "Aggregate base residual stresses affecting geogrid reinforced flexible pavement response." *International Journal of Pavement Engineering,* 9(4). 275-285.

Leng, J., and Gabr, M.A. (2003). "Numerical analysis of the stress-deformation response in reinforced unpaved road sections." *Proc. of the Transportation Research Board Annual Meeting,* (CD-ROM), Transportation Research Record, Washington, DC.

Leonhardt, G. (1978). *Belastungsannahmen bei erdverlegten GFK-Rohren*, AVK, Freudenstadt.

Lister, N.W., and Powell, W.D. (1987). "Design practice for bituminous pavements in the United Kingdom." *6th International Conference of Structural Design of Asphalt Pavements,* Vol. 1, Ann Arbor, MI, 220-231.

Lundvall, J.F., and Turner, J.P. (1997). *Mitigation of roadway settlement above buried culverts and pipes*, Wyoming Department of Transportation Report FHWA/WY -97/01, Cheyenne, WY.

Luscher, U. (1966). "Buckling of soil-surrounded tubes." *Journal of Soil Mechanics Foundations Division,* 92(6), 221-228.

Marston, A. (1930). *The Theory of Loads on Closed Conduits in Light of the Latest Experiments,* Bulletin No. 96, Iowa State College, Ames, IA.

Marston, A., and Anderson, A.O. (1913). *The Theory of Loads on Pipes in Ditches and Tests of Cement and Clay Drain Tile and Sewer Pipe*, Bulletin No. 31, Iowa Engineering Experiment Station, Ames, IA.

Masada, T., and Sargand, S.M. (2007). "Peaking deflections of flexible pipe during initial backfilling process." *Journal of Transportation Engineering*, 133(2), 105-111.

McGrath, T.J. (1998). *Design method for Flexible Pipe*, A Report prepared for the Polyethylene Pipe Design Task Group of the AASHTO Flexible Culvert Liaison Committee, Simpson Gumpertz, & Heger, Inc., Arlington, MA.

McGrath, T.J., Moore, I.D., and Hsuan, G.Y. (2009). *Updated Test and Design Methods for Thermoplastic Drainage pipe*, NCHRP Report 631, Transportation Research Record, Washington, DC.

McGrath, T.J., and Sagan, V.E. (2000). *Recommended LRFD Specifications for Plastic Pipe and Culverts*, NCHRP Report 438, Transportation Research Record, Washington, DC.

McGrath, T.J., and Sagan, V.E. (2001). "Design of profile wall thermodynamic pipe for local buckling." *Transportation Research Record,* 1170, 209-219.

McGrath, T.J., Selig, E.T., and DiFrancesco, L.C. (1994). "Stiffness of HDPE pipe in ring bending." *Buried Plastic Pipe Technology: 2nd Volume,* ASTM STP 1222, D. Eckstein, ed., American Society for Testing Materials, Philadelphia, PA.

McGrath, T.J., Selig, E.T., Webb, M.C., and Zoladz, G.V. (1999). *Pipe Interaction with Backfill Envelope*, National Science Foundation and the Federal Highway Administration Final Report FHWA-RD-98-191, Dept. of Civil and Environmental Engineering, University of Massachusetts, Amherst, MA.

Meyerhoff, G.G., and Baikie, L.D. (1963). "Strength of steel culvert sheets bearing against compacted sand backfill." *Highway Research Record,* (30), 1-19.

Moghaddas Tafreshi, S.N., and Khalaj, O. (2008). "Laboratory tests of small-diameter HDPE pipes buried in reinforced sand under repeated-load." *Geotextiles and Geomembranes*, 26(2), 145-163.

Moghaddas Tafreshi, S.N., and Khalaj, O. (2011). "Analysis of repeated-load laboratory tests on buried plastic pipes in sand." *Soil Dynamics and Earthquake Engineering*, 31(1), 1-15.

Moon, K.K., Cho, S.H., Yun, I.J., and Won, J.H. (2010). "Three-dimensional responses of buried corrugated pipes and ANN-based method for predicting pipe deflections." *International Journal for Numerical and Analytical Methods of Geomechanics,* 36(1), 1-16.

Moore, I.D. (1987). "The elastic stability of shallow buried tubes." *Geotechnique,* 37(2), 151-161.

Moore, I.D. (1989). "Elastic buckling of buried flexible tubes - a review of theory and experiment." *Journal of Geotechnical Engineering,* 115(3), 340-358.

Moore, I.D. (1994). "Profiled HDPE pipe response to parallel plate loading." *Buried Plastic Pipe Technology: 2nd Volume,* ASTM STP 1222, D. Eckstein, ed., American Society for Testing Materials, Philadelphia, PA.

Moore, I.D. (2009). *DuroMaxx Pipe Assessment,* Final Report Submitted to Contech Construction Products, Inc., West Chester, OH.

Moore, I.D., and Brachman, R.W. (1994). "Three-dimensional analysis of flexible circular culverts." *Journal of Geotechnical Engineering,* 120(10), 1829-1844.

Moore, I.D., and Hu, F. (1995). "Response of profiled high-density polyethylene pipe in hoop compression." *Transportation Research Record,* 1914, 29-36.

Moore, I.D., and Laidlaw, T.C. (1997). "Corrugation buckling in HDPE pipes – measurements and analysis." *Proc. of the 76th Annual Meeting of the Transportation Research Board*, Transportation Research Board, Washington, DC.

Moore, I.D., and Selig, E.T. (1990). "Use of continuum buckling theory for evaluation of buried plastic pipe stability." *Buried Plastic Pipe Technology,* ASTM STP 1093, G.S. Buczala, and M.J. Cassady, eds., American Society for Testing Materials, Philadelphia, PA.

Moore, I.D, Selig, E.T., and Haggag, A. (1988). "Elastic buckling strength of buried flexible culverts." *Transportation Research Record,* 1191, 57-64.

Moore, I.D., and Taleb, B. (1999). "Metal culvert response to live loading: performance of three-dimensional analysis." *Transportation Research Record*, 1656, 37-44.

Mruk, S.A. (1990). "The durability of polyethylene piping." *Buried Plastic Pipe Technology,* ASTM STP 1093, G.S. Buczala, and M.J. Cassady, eds., American Society for Testing Materials, Philadelphia, PA.

NCSPA (National Corrugated Steel Pipe Association). (2008). *Corrugated Steel Pipe Design Manual.* National Corrugated Steel Pipe Association, Dallas, TX.

Nquyen, M.D., Yang, K-H, and Lee, S-H. (2011). "Comparison of the prediction of geosynthetic-reinforced soil shear strength by difference approaches." *Proc. of the 14th Conference on Current Researches in Geotechnical Engineering in Taiwan,* Taoyuan, Taiwan.

Palmeira, E.M., and Andrade, H.K.P.A. (2010). "Protection of buried pipes against accidental damage using geosynthetics." *Geosynthetics International*, 17(4), 228-241.

Pearson, A.E., and Milligan, G.W.E. (1991). "Model tests of reinforced soil in conjunction with flexible culverts." *Proc. of the International Reinforced Soil Conference*, Glasgow, 365-369.

Perkins, S.W. (2001). *Mechanistic-Empirical Modeling and Design Model Development of Geosynthetic Reinforced Flexible Pavements*, Department of Civil Engineering Final Report, Montana State University, Bozeman, MT.

Perkins, S.W., Christopher, B.R., Cuelho, E.L., Eiksund, G.R., Hoff, I., Schwartz, C.W., Svanø, G., and Want, A. (2004). *Development of Design Methods for Geosynthetic Reinforced Flexible Pavements,* Final Report to the Federal Highway Administration No. DTFG61-01-X-00068, Montana State University, Bozeman, MT.

Peterson, D.L., Nelson, C.R., Li, G., McGrath, T.J., and Kitane, Y. (2010). *Recommended Design Specifications for Live Load Distributions to Buried Structures*, NCHRP Report 647, Transportation Research Board, Washington, DC.

Phares, B., Wipf, T., Klaiber, F., and Lohnes, R. (1998). "Behavior of high-density polyethylene pipe with shallow cover." *Transportation Research Record*, 1624, 214-224.

PHMSA (Pipelines and Hazardous Materials Safety Administration). (2011). "State of the National Pipeline Infrastructure." <http://opsweb.phmsa.dot.gov/pipelineforum/docs/Secretarys Infrastructure Report_Revised per PHC_103111.pdf > (Oct. 31, 2011).

Rajkumar, R., and Ilamparuthi, K. (2008). "Experimental study on the behavior of buried flexible plastic pipe." *Electronic Journal of Geotechnical Engineering*, 13(C), 1-10.

Reddy, D.V. (2002). *Long-term Performance of Buried High Density Polyethylene Plastic Piping,* A Report prepared for the Florida Department of Transportation, Florida Atlantic University, Boca Raton, FL.

Roark, R.J. (1943). *Formulas for Stress and Strain*, McGraw-Hill, New York.

Sargand, S.M., Masada, T., White, K.E., and Altarawneh, B. (2002). "Profile-wall high-density polyethlyene pipes 1050 mm in diameter under deep soil cover." *Transportation Research Record,* 1814, 109-123.

Schanz, T., Vermeer, P.A., and Bonnier, P.G. (1999). "The hardening soil model: formulation and verification." *Beyond 2000 in Computational Geotechnics – 10 Years of PLAXIS,* R. Brinkgreve, ed., Amsterdam, Netherlands, 1-16.

Schlosser, F., and Long, N.T. (1974). "Recent results in French research on reinforced earth." *Journal of the Construction Division*, 100(3), 223-237.

Seed, R.B., and Duncan, J.M. (1986). "FE analysis: compaction-induced stresses and deformations." *Journal of Geotechnical Engineering,* 112(1), 23-43.

Selig, E.T. (1988). "Soil parameters for design of buried pipelines." *Pipeline Infrastructure,* B.A. Bennett, ed., ASCE, New York, NY, 99-116.

Selig, E.T., DiFrancesco, L.C., and McGrath, T.J. (1994). "Laboratory test of buried pipe in compression." *Buried Plastic Pipe Technology: 2nd Volume,* ASTM STP 1222, D. Eckstein, ed., American Society for Testing Materials, Philadelphia, PA, 119-132.

Spangler, M.G. (1941). *The Structural Design of Flexible Pipe Culverts*, Bulletin No. 153, Iowa Engineering Station, Ames, IA.

Spangler, M.G. (1947). "Underground conduits – an appraisal of modern research." *Transactions of the American Society of Civil Engineers,* Paper 2337, Vol. 113.

Spangler, M.G. (1951). *Soil Engineering*, International Textbook Co., Scranton, PA.

Spangler, M.G., Mason, C., and Winfrey, R. (1926). *Experimental determinations of static and impact loads transmitted to culverts,* Iowa State College, Ames, IA.

Suleiman, M.T., Lohnes, R.A., Wipf, T.J., and Klaiber, F.W. (2003). "Analysis of deeply buried flexible pipe." *Transportation Research Record*, 1849, 124-134.

Taleb, B., and Moore, I.D. (1999). "Metal culvert response to earth loading performance of two-dimensional analysis." *Transportation Research Record,* 1656, 24-36.

Talesnick, M.L., Xia, H.-W., and Moore, I.D. (2011). "Earth pressure measurements on buried HDPE pipe." *Geotechnique*, 61(9), 721-732.

Ugural, A.C. (1981). *Stresses in Plates and Shells*, McGraw-Hill, New York.

Von Karman, T., Sechler, E.E., and Donnell, L.H. (1932). "The strength of thin plates in compression." *Transactions of the American Society of Civil Engineers,* 54, 53-57.

Wathugala, G.W., Huang, B., and Pal, S. (1996). "Numerical simulation of geosynthetic-reinforced flexible pavements." *Transportation Research Record*, 1534, 58-65.

Watkins, R.K. (1960). "Failure conditions of flexible culverts embedded in soil." *Highway Research Proceedings,* 39, 361-371.

Watkins, R.K. (1966). *"*Structural design of buried circular conduits*", Buried circular conduits and behavior of foundations; 8 reports,* Highway Research Record*,* 1-16.

Watkins, R.K. (1971). "Response of corrugated steel pipe to external soil pressures." *Highway Research Record,* 37, 86-96.

Watkins, R.K. (1985). "Longitudinal stresses in buried pipes." *Proc. of the International Conference on Advances in Underground Pipeline Engineering,* J.K. Jeyapalan, ed., ASCE, New York, NY, 409-417.

Watkins, R.K., Dwiggins, J.M., and Altermatt, W.E. (1987). "Structural design of buried corrugated polyethylene pipes." *Transportation Research Record,* 1129*,* 12-20.

Watkins, R.K., and Spangler, M.G. (1958). "Some characteristics of the modulus of passive resistance of soil: a study of similitude." *Proc. of the Highway Research Board*, 37, 576-583.

Watkins, R.K., Szpak, E., and Allman, W.B. (1974). *Structural design of polyethylene pipes subjected to external loads,* Utah State University, Logan, UT.

White, H.L., and Layer, J.P. (1960). "The corrugated metal conduit as a compression ring." *Proc. of the Highway Research Board,* 39, 389-397.

Winter, G. (1946). "Strength of thin steel compression flanges." *Transactions of the American Society of Civil Engineers,* 111, 527-544.

Wolf, E.W., and Townsend, M. (1970). *Corrugated metal pipe: Structural design criteria and recommended installation practice*. U.S. Govt. Print. Off., Washington, DC.

Wu, J.T.H., Pham, T.Q., and Adams, M.T. (2013). *Composite Behavior of Geosynthetic Reinforced Soil Mass,* Dept. of Civil Engineering Report No. FHWA-HRT-10-077, University of Colorado-Denver, Denver, CO.

Yang, X. (2010). *Numerical Analyses of Geocell-Reinforced Granular Soils Under Static and Repeated Loads*. Ph.D. Dissertation, University of Kansas, Lawrence, KS.

Zaman, M., and Laguros, J.G. (1990). “Predicting the bahavior of buried pipes using a mixed finite element approach.” *Structural Performance of Flexible Pipes, Proc. of the First National Conference on Flexible Pipes,* G.F. Mitchell, J.O. Hurd, and S.W. Sargand, eds., Columbus, OH, 163-169.

Zhang, C., and Moore, I.D. (1997). “Nonlinear mechanical response of high density polyethylene. Part II: uniaxial constitutive modeling.” *Polymer Engineering and Science.* 37(2). 414-420.